The lateral confinement of microwave surface waves

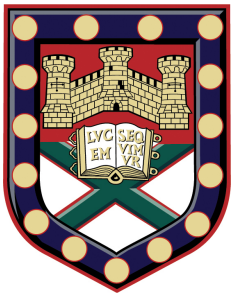

Elizabeth Martine Gerber Brock

Department of Physics and Astronomy

University of Exeter

A thesis submitted for the degree of

Doctor of Philosophy

December 2013

The lateral confinement of microwave surface waves

Elizabeth Martine Gerber Brock

December 2013

Supervised by Alastair Hibbins

Submitted by Elizabeth Martine Gerber Brock, to the University of Exeter as a thesis for the degree of Doctor of Philosophy in Physics, December 2013.

I certify that all material in this thesis which is not my own work has been identified and that no material has previously been submitted and approved for the award of a degree by this or any other University.

(Signature) .....

‘Try again, fail again. Fail better.’ Samuel Beckett

Acknowledgements

I would like to thank my supervisor, Professor Alastair Hibbins, for all his hard work and advice throughout my PhD. No one knows better than him that I do not always communicate well so I thank him for sticking with it. I have been fortunate indeed to work with a Professor who has always been quick to grasp the subtle concepts of physics which I have struggled to understand.

I would like to thank Professor Euan Hendry for contributions to my work, my conversations with him have always been a source of inspiration. I would like to thank Professor Roy Sambles for his relentless energy, it has also been a source of inspiration and sometimes even awe. In particular I would like thank Professor Sambles for asking the fundamental questions and for encouraging me to do the same. I would like to thank Dr Ian Hooper for repeatedly hitting me with 'the physics stick'. I would like to thank my mentor Professor Tim Naylor for listening to me and guiding me through a few grey areas. A large thank you also goes to Nick Cole, as well as the other technicians at the University of Exeter. They play a leading role in any experimental PhD and are appreciated not only for their fantastic technical ability but also the tireless patience they exhibit when working with students who sometimes don't really know what kit or sample they need to make until after chatting to them.

I would like to thank my new boss at the Met Office, Dr Jacqueline Sugier for hiring me. Having an exit strategy from academia gave me great peace of mind. The encouragement I received from her and my co-workers to complete this thesis while working has been priceless.

I would like to thank my family and especially my friends who have been with me through the good and the bad times, I would not have produced a thesis without their advice and support. I also would not have started the unlikely sport of Dragon Boating or most recently Marathon Kayaking without them so let's face it dear reader, they have a lot to answer for! I would like to dedicate this thesis to them.

I would also like to thank Dr Kent McClymont. Thank you.

Abstract

Surface waves and their applications have been extensively studied by the photonics and radio engineering communities throughout the whole of the twentieth century. This thesis details briefly the history of both approaches and highlights their significance with regard to the subject of this thesis; laterally confining a surface wave in the microwave regime. Detailed within are the experimental, analytical and numerical methods used to ascertain what, if any, effect a change in the dimension of a guiding structure has on the dispersion of a mode supported by a metamaterial.

The method of experimentally determining the dispersion of a microwave surface wave is discussed. The insensitivity of a mode supported on a one-dimensional corrugated array to the lateral width of the supporting array, even when the width is much less than the wavelength of radiation incident upon it, is investigated. Spatial dependent reduction of group velocity associated with a microwave surface wave is also detailed. Local electric-field and phase measurements are used to probe this condition. In particular, the measurement of phase associated with the supported microwave surface wave is shown to indicate the trapping location of a surface wave more accurately when compared to local electric-field measurement. The channelling of surface waves via the addition of dielectric overlayers to a metamaterial surface is investigated. By progressively narrowing the width of the channel, the interaction of the electric fields associated with the mode supported in the channel with the bordering dielectric overlayer increases. This investigation leads to a discussion of the electric field overlap between two regions of differing surface impedance.

Contents

Glossary of Terms

Table 1: Glossary of Terms, in order of appearance.

Name of Constant	Symbol
Grating Periodicity	λ_g
Angle of Diffracted Light	ϕ_N
Angle of Incident Light	θ
Order of Diffraction	N
Wavelength	λ
Angular Frequency	ω
Wavevector	k
Plasma Frequency	ω_P
Surface Plasma Frequency	ω_{SP}
Speed of Light	c
Total Wavevector	k_0
Permittivity	ϵ
Permeability	μ
Electric Field	$\underline{\mathtt{E}}$
Electric Field Displacement	$\underline{\mathtt{D}}$
Magnetic Field Induction	$\underline{\mathtt{H}}$
Magnetic Field Intensity	$\underline{\mathtt{B}}$
Electron Charge	e
Effective mass of electron	m
Charge on an electron	q
Modal Index	n
Refractive Index	n_{ref}
Group Velocity	v_g
Relaxation Time	τ
Conductivity	σ
Skin Depth	δ_s
Penetration Depth	δ_z
Pitch	d
Height	h
Radius	r
Thickness	t
Capacitance	C
Inductance	L
Impedance	Z
Surface impedance	Z_S
Reactance	χ
Resistance	R
Impedance of Free Space	η
Impedance Inside a Groove	ζ
Separation Distance	d_1
Area	A
Voltage	V
Current	I

Table 2: Glossary of Terms, continued.

Name of Constant	Symbol
Lateral Width	L
Phase	Φ
Length of Exposed Probe Wire	l
Propagation Distance	P
Total Phase	$\Sigma\Phi$
Total Phase Difference	$\Sigma\Phi_{\texttt{Diff}}$
Limiting Frequency	$f_{\texttt{res}}$
Overlap Integral	Q
Group Velocity	v_g
Group Delay	d_g
Charge	$\texttt{Q}$
Abbreviations and acronyms	
Surface Plasma	SP
Surface Plasmon Polariton	SPP
Vector Network Analyser	VNA
Double Negative Media	DNG
Single Negative Media	SNG
Double Positive Media	DPS
Single Positive Media	SPS
Perfect Electric Conductor	PEC
Perfect Magnetic Conductor	PMC
Transverse Magnetic	TM
Transverse Electric	TE
Finite Element Method	VNA
Radio Frequency	RF
Local Oscillator	LO
Intermediate Frequency	IF
Total Internal Reflection	TIR
Motorised Stage	XYZ
Photonic Crystal	PhC

Chapter 1

Introduction

1.1 Purpose of Research

The focus of this thesis is the investigation of laterally confined microwave surface waves supported on structures that gain their electrical properties from geometric design rather than their constituent material properties. Applications associated with surface waves include wireless communication devices and the reduction of monostatic reflections from an object under radar surveillance via the control of surface waves excited on the surface of that object. Another application includes beam steering of the radiation emitted by patch array antennas through the control of the surface waves scattering off the patch arrays. Rather counter intuitive to the focus of this thesis, the excitation of surface waves can also be undesirable. When excited along substrates of microwave antennas, surface waves can distort the radiation pattern of the antenna and reduce its overall efficiency.

The control of surface waves and an understanding as to how small a limit a surface wave can be confined to is clearly a topic worthy of study, even if it is not a new one. For over one hundred years the study of surface waves has received a large amount of attention from both engineers studying radio waves and physicists investigating extraordinary optical phenomena on gratings. The obvious difference in wavelength regimes that define both areas of research resulted in two very different paths to the same conclusion: in the optical regime an electromagnetic mode can be excited and confined to an interface between air and metal. In the microwave regime, confinement of a surface wave to an interface is achieved by surface structure.

Analysis of surface waves supported by a variety of different surface structures is studied. Specifically, this thesis explores the limits to which a microwave surface wave can be confined before the dispersive properties of the mode are changed. Given the large period of time over which surface wave phenomenon have been

scrutinised, it is surprising to note that studies regarding the lateral confinement of surface waves, the slowing light properties of microwave surface waves and investigations as to the channelling of these modes have yet to be exhausted. This work details some of the more recent advancements in the field of microwave surface wave research and strives to contribute to it.

1.2 Outline of Thesis

This thesis is organised as follows. Chapter 2 outlines literature relevant to this thesis, providing a historical review of microwave surface wave studies to date. This includes material specifically relevant to laterally confining microwave surface waves.

Chapter 3 details the experimental methods used throughout this thesis. Detailed are the methods used to experimentally determine the dispersion of a microwave surface wave. The techniques used to excite microwave surface waves are also detailed. Numerical and analytical techniques used to support experimental measurements are included in this discussion. Chapter 4 explores the lateral confinement of microwave surface waves. Highlighted is the lateral insensitivity of the mode supported on a one-dimensional array of corrugations, even when the geometry of the supporting structure is made much less than that of the incident radiation.

Chapter 5 details microwave surface waves supported on a tapered geometry metasurface. Local electric field and phase measurements associated with the supported mode are recorded. Conclusions as to the slowing and trapping of a wave due to lateral confinement are made; phase measurements are preferred as an indicator of the trapping location.

Chapter 6 discusses the channelling of a microwave surface wave between two dielectric overlayers. This chapter shows that the mode is supported in a region between the overlayers and in the overlayers themselves.

Finally, Chapter 7 reiterates the findings of this thesis and suggests possible future avenues of research in light of this study.

Chapter 2

Background

2.1 Introduction

Surface waves and their applications have been extensively studied by the photonics and radio engineering communities throughout the whole of the twentieth century. This chapter details briefly the history of both approaches and highlights their significance with regard to the subject of this thesis; a surface wave in the microwave regime. The conditions required to support a surface wave are reviewed from the basic principles of Maxwell's equations and applied to metals in the microwave regime. The concept of resonances associated with subwavelength surface structure at microwave frequencies in contrast to an intrinsic resonant condition associated with the bulk free electrons of a metal at visible frequencies is included in this discussion.

2.2 Historical Review

Rather counter intuitively to the focus of this thesis, the excitation of surface waves can be undesirable. When excited along substrates of microwave antennas, surface waves distort the radiation pattern of the antenna and reduce its overall efficiency. Further, when excited within the substrates associated with microwave integrated circuits there is an increase in cross-talk between components, decreasing the sensitivity of the device [1].

For over one hundred years the study of surface waves has received a large amount of attention from both engineers studying radio waves and physicists investigating extraordinary optical phenomena on gratings. It wasn't until a publication by U. Fano in 1941 [2] that the two studies were linked. The obvious difference in wavelength regimes that define both areas of research resulted in two very different paths to the same conclusion. An outline of these routes is now

included in a small narrative, collated from the earlier literary efforts of Stratton [3], Zucker [4] and Glory [5].

2.2.1 Radio Engineering

In 1907 Zenneck [6] proposed that a planar interface between two semi-infinite media such as ground and air could support an electromagnetic wave which is exponentially attenuated in the direction orthogonal to the interface. This hypothesis was based on early investigations by Cohn [7] and Uller [8] in 1903 on the guiding of an electromagnetic wave on a plane interface separating a dielectric and a good conductor.

In Zenneck's analysis a wave with a forward tilt, following a flat (planar) earth and attenuated in the vertical as well as the horizontal direction was shown to be a valid solution of Maxwell's equations. It was then proposed as a possible explanation for observed radio transmission. However, definitive proof of excitation of such a wave bound to a surface via a radio antenna was actually attempted by Sommerfeld in 1909 [9], wherein he laid out three possible components of an electromagnetic surface wave excited by a vertical antenna; two free space waves and one main 'surface' wave component.

It is apparent from the literature reviewed that this attempt failed due to a mathematical error. Studies conducted by Weyl in 1919 [10] contradicted the predictions of Sommerfeld. Although the solutions of the total electric field as defined by Sommerfeld and Weyl match in the special case where the co-ordinate under consideration is at the interface between a conducting earth and a dielectric (free space), as soon as some vertical component is considered there is a discrepancy between the two studies. Norton preformed his own analysis of the possible excitation of a surface wave using a vertical antenna emitting radio waves in 1935 [11]. In this paper it was pointed out that Sommerfeld's original paper in 1909 contained an incorrect sign, resulting in incorrect predictions of transmission of radio waves at a radial and vertical distances from the emitting antenna. Experimental results obtained by Burrows in 1936 [12] confirmed the Weyl-Norton analysis by measuring transmission at 150 MHz over Seneca Lake, New York. The vertical antenna was varied in height above the lake and a receiver placed 1.8 km away from the transmitting antenna.

Experimental data obtained by Burrows and the theoretical values Weyl-Norton of radio wave intensity at a given height from the earth were found to agree well. In contrast to these results, the predictions outlined by Sommerfeld were more than a thousand times greater than the observed experimental values. Controversy as to the original analysis preformed by Sommerfeld was further ignited when Norton

pointed out that this mathematical error had not been repeated in Sommerfeld's 1926 paper (of the same name as the 1909 paper). However, when the analysis presented in 1926 was compared to experimental data, it was found to be correct only when the conductivity of the earth was considered to be large. In fact, Sommerfeld's mathematical error in the form of an incorrect square root of a complex error function was later outlined by Neissen in 1937 [13].

Sommerfeld's earlier work on the propagation of surface waves on a single wire in 1899 [14] stood the test of time somewhat better and was an inspiration for the analysis preformed by Goubau [15] on surface waves propagating on a dielectric coated wire. However, credit for the first deliberate study of surface waves excited in the microwave regime should go to Toraldo di Francia in 1942 [16] for his work concerning evanescent waves excited via a diffraction grating.

Francia's 1942 paper is referred to by Zucker (1952) [4] and Guerra (1995) [17] who credit the Italian publication as being the first to examine surface waves deliberately. Toraldo is credited with proving their existence and illustrating the role they play in diffraction [4] and for specifically showing that the period of evanescent waves diffracted from a grating directly correlates with the period of the grating upon which they are excited [17].

A copy of the referenced publication has not yet been found which is unfortunate because it pre-dates the paper originally accredited to have been the first study of surface waves in 1944 [18], discussed shortly. In 1949, Francia and Schaffner [19] expanded on the 1942 paper to show diffracted evanescent microwaves could excite a propagating surface wave. Ulrich and Tacke [20] later undertook a similar experiment with a laser incident on a prism upon a wire mesh.

Indeed, optical investigations using diffraction gratings were the means by which the photonics community first gained awareness of surface waves. As such, the genesis of surface wave understanding via extraordinary optical phenomena will now be discussed.

2.2.2 Photonics

The study of the properties and transmission of photons is a topic commonly known as 'Photonics'. Its rich history spans many centuries and has moved from the study of photons at frequencies associated with visible light to those no longer observed by the human eye in the ultraviolet. In 1821 Joseph von Fraunhoffer used a diffraction grating to measure the wavelength of visible light (λ_0) and verified

the grating equation:

$$\lambda_g(\sin\phi_N - \sin\theta) = N\lambda_0 \tag{2.1}$$

where N is the order of diffraction, θ is the angle of incident light, ϕ_N the angle of diffracted light and λ_g is the period of the grating. Optical phenomena associated with diffracting grating experiments were to follow over eighty years later.

In 1902 Wood [21] published a paper detailing the extraordinary response of a metallic ruled diffraction grating when the surface of that grating was radiated with a white light source. The reflection spectra not only exhibited extreme bright and dark bands, the spacial distance between these bands was notably smaller than expected. The origin of the extreme bright bands was later explained by Lord Rayleigh [22] in 1907 as a result of the scattered field at specific wavelengths becoming evanescent and energy redistributing amongst the other propagating orders. However, the positions of the dark bands in the spectra were observed by Strong [23] to be modified when the metallic composition of the diffraction grating was changed. Therefore the effect could not be the result of grating periodicity.

The consequence of this was not realised until Fano [2] proposed that, in fact, the origin of the two dark and bright neighbouring bands were a consequence of the excitation of a pair of surface waves travelling along the surface of the grating. These waves are bound to the surface and decay exponentially in the direction perpendicular to the grating. Although Fano recognised that the solutions provided by Sommerfeld may not have been suitable to compare to a field excited by a radio antenna (by citing Weyl) he drew parallels between his own mathematical treatment of surface waves with those already derived by Sommerfeld. From the perspective of this author this added to the confusion as to the correct accreditation for the discovery of surface waves.

The momentum of the pair of surface waves proposed by Fano exceeds that of a wave propagating in free space, i.e. it is a non-radiating mode decaying exponentially from the interface to which it is bound. As a result, a free space wave cannot simply excite such a surface wave as the momentum of the two modes are not matched.

Teng and Stern (1967) [24] used an optical grating to provide enhanced momentum so that the surface mode and the incident electron beam used in their experiment could couple together, resulting in peaks in the out-coupled radiation. The out-coupled radiation was polarised so that if the propagating component of the surface wave was in the plane of this page, the magnetic component of the radiation would oscillate in and out of the page. This polarisation convention is known

as transverse magnetic and is further detailed in section 2.3.1 of this chapter.

A reflection experiment was then conducted. The same grating was bombarded by an electron beam, incident on that grating at the specific angles and frequency at which the out-coupled radiation in the previous experiment had been emitted. Teng and Stern's hypothesis was that if indeed the free electrons of the metal were coherently interacting as a plasma and a surface wave was excited, there would be a lack of amplitude of reflection at a given frequency for a given angle of incidence (corresponding to the aforementioned peaks).

The hypothesis proved correct and for the first time the momentum (k) and angular frequency (ω) of a surface wave supported on a grating surface was obtained. This surface wave was termed a 'surface plasmon' and, just as Zenneck originally hypothesised, is a non-radiative mode that decays exponentially from the interface between a dielectric and a metal. The energy of that mode is concentrated at the interface.

2.2.2.1 Applications Associated with Surface Plasmons

The potential applications of surface plasmons are still a very much active area of research and include miniaturized photonic circuits, enhancement of Raman spectroscopy and sensing. A photonic circuit would rely on using the subwavelength channelling properties of surface plasmons. Such a circuit would convert light into surface plasmons, which would then propagate along subwavelength channels to be processed by logic elements. Another application would be to use the electric field enhancement of the surface plasmon at the dielectric-metal interface to manipulate light-matter interactions and boost non-linear phenomena. For example surface-enhanced Raman spectroscopy (SERS) relies on massive signal enhancement from structures much smaller than the wavelength of light. This enhancement could be greatly increased if these structures were supporting surface plasmons. A third application would be to use the field enhancement associated with surface plasmons as a sensor to indicate minute changes in the surrounding medium, ideal for sensing changes in biomolecules. These applications are further elaborated upon in the following publications [25, 26, 27].

2.2.2.2 Dispersion: Relating Frequency and Wavevector

The limiting frequency of a surface plasmon is governed by the surface plasma frequency ω_{SP} and is therefore dependent on the behaviour of the electrons at the surface of the metal. Above the plasma frequency (ω_p) the surface electrons are unable to respond to the incident electromagnetic field, therefore the surface wave excitation is limited to ω_{SP} (where $\omega_{SP} = \frac{\omega_p}{\sqrt{2}}$). The relationships between

frequency (ω) and momentum (k) of an electromagnetic mode is given by $\omega = ck$ and is often called the dispersion relation. When an electromagnetic mode is travelling in free space the momentum associated with it, 'k' is referred to as the wavevector which can be separated into contributions in each dimension:

$$k_0^2 = k_x^2 + k_y^2 + k_z^2 \tag{2.2}$$

where $k_0 = 2\pi/\lambda_0$ and λ_0 is the wavelength of the incident wave. The three components of k_0 determine the propagation and nature of attenuation (or loss) suffered by that mode and is elaborated upon further in section 2.4.1.1 of this chapter. This thesis maintains the coordinate system where the propagation of the mode is always described to be positive in the x-direction. Therefore the component of momentum of the surface mode will further be described as the in-plane wavevector or 'k_x'.

Figure 2.1 depicts the dispersion of an optical surface wave on a flat metal sheet.

The three bands of colour represent three different frequency regimes including microwave (yellow), infrared (red) and visible (purple) of wavelengths 10^{-2} m, 10^{-5} m and 0.5 x 10^{-6} m. The behaviour of a photon travelling in free space is represented by the solid black line with a constant gradient, the surface mode is represented with the solid black line with a frequency dependent gradient. The black dashed line represents the limiting frequency of the surface wave. In this diagram that frequency is governed by the bulk response of electrons at the surface of the metal, the surface plasma frequency (ω_{SP}).

As the mode approaches ω_{SP}, the electric fields associate with the surface wave become more confined to the interface upon which it is supported. Notice that in the microwave regime the dispersion of the mode has diverged from the light line (where $\omega = ck$) an infinitesimal amount. Therefore in this frequency regime the mode can be described as 'unconfined' and resembles a free space photon.

Physically, this can be understood by examining the extent of penetration of the electric field into the two media bordering the interface of air and metal. Specifically note the vertical extent of the electric field into the metal at visible and microwave frequencies, as seen in schematic (a) and (b) (respectively) inset in Figure 2.1. The exponential decay of the electric field into the metal at visible frequencies is obvious whereas it is distinctly lacking in the schematic depicting the vertical extent of the fields into both bordering mediums at microwave frequencies.

As there is a greater concentration of field close to the interface at visible frequencies in comparison to the microwave regime, the surface wave is described as 'confined'. The physical origin of this lack of penetration is further elaborated

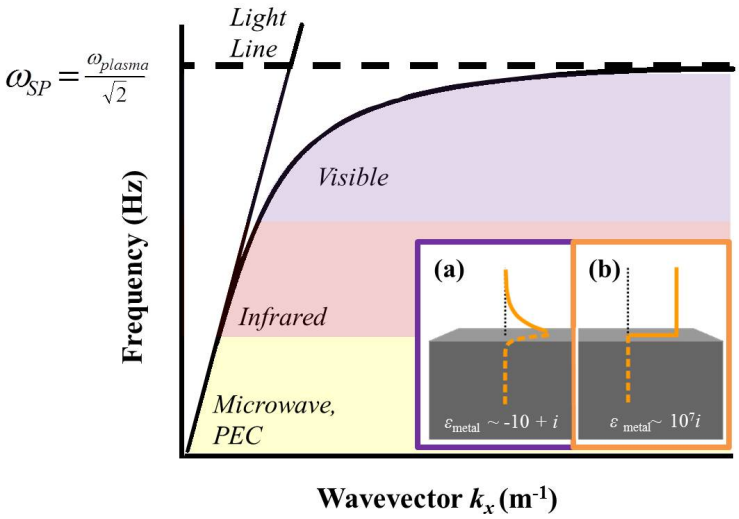

Figure 2.1: Dispersion of a surface wave (solid black curve) associated with the coherent oscillation of bulk electrons within a metal. Also included is dispersive behaviour of a free space photon (solid black line) and the limiting frequency of the mode (dashed black line). Inset: Schematic representation of the electric field associated with a surface wave penetrating into the surrounding region. The solid orange line represents the vertical extent of the electric field of the surface wave into air and is contrasted with the dashed orange line representing the penetration of the electric field into the metal. Inset (a) vertical electric field penetration into the metal at visible frequencies. (b) vertical electric field penetration into the metal at microwave frequencies. Reproduced with permission from Hibbins et al. (2005) [28]. Below each inset is the approximated relative permittivity of the metal ($\epsilon_{\texttt{metal}}$). Inset (b) shows the decay of the electric field into the dielectric relative to the penetration depth of the electric field into the metal in each case. Therefore the length of decay into the dielectric region in (a) is not directly comparable to the corresponding length in schematic(b).

on in Sections 2.3.1.1 and 2.4.

2.2.3 Microwave Surface Waves and their Early Applications

Confined microwave surface waves have been explored by the radar engineering community for a number of years. The original hypothesis that surface waves were responsible for radio transmission was debunked by both experimental evidence of Burrows [12] and analysis by Weyl [10] and Norton [11]. In 1937 Wise [29] proved the transmission of radio waves could not be due to a surface wave of the form proposed by Zenneck in 1907 as a vertical dipole could not excite such a solution, ending the subject in terms of radio wave propagation.

However, it was discovered quite accidentally by Cutler in 1944 [18] during his efforts to increase the transmission of radar antennas that a surface wave such as

described by Zenneck could in fact be excited on a metal at microwave frequencies. Cutler originally wanted to reduce the reflections he observed from radiation emitted from the side of the flat antenna feed he was using to interact with a near-parabolic reflector dish. Radiation emitted from the side of the antenna feed instead of in the forward direction are known as side lobes. In general this feature results in a non-directive antenna beam pattern and as such is an undesirable property. The flat metallic feed is also known as a flat reflector, which reflects the signal initially fired at the dish from a waveguide source back to the dish and is designed to increase the gain of the antenna in a certain direction [30].

When used together, the dish and the feed were designed to achieve an antenna that could be used to survey high altitude aircraft from its position on the ground via a beam pattern polarised in the vertical direction. The military significance of such a device in a time when World War II raged across the globe was not lost on Cutler, who was then under contract with the US Air Force.

By indenting the surface of the flat metallic feed with closely spaced corrugations that were one quarter of the wavelength of the operating frequency in depth he hoped to reduce the distorting effects of the side lobes. However, what he observed was a pronounced maximum field at the corrugated surface which decreased by several orders of magnitude when moved no more than a wavelength away from the corrugations. This is indicative of the evanescent field decay associated with surface waves in the vertical direction away from the supporting interface; Cutler had discovered microwave surface waves on a corrugated sheet. This was two years after the referred to publication by Toraldo di Francia (1942) [16]. Cutler's final solution to his antenna problem was to cut the corrugations deeper to negate the effects of side lobe reflections, however, this experiment is considered to be the first investigation of a microwave surface wave supported on an array of quarter wavelength corrugations embedded in a metal sheet.

Figure 2.2 details the initial boundary conditions of surface waves first outlined by (a) Zenneck in 1907 [6] and the genesis of this understanding of surface waves as regards antenna theory as detailed by Zucker [31] (b) and in another paper by Barlow and Cullen (1953) [32] presenting a unified picture of the various forms of surface waves known at the time.

Indeed, antenna theory and microwave circuitry were the main topics of research as regards surface waves in the 1950s in the pursuit of guiding electromagnetic radiation. In 1950 Goubau [15] investigated surface waves on metallic rods which were smooth (as in Sommerfeld's initial analysis [14]) or coated with a dielectric layer over a modified surface. By patterning the surface of the rod with a spiralling groove in the same way a common screw is patterned (or 'threaded') and adding a dielectric overlayer Goubau showed that the radial extent of the electric

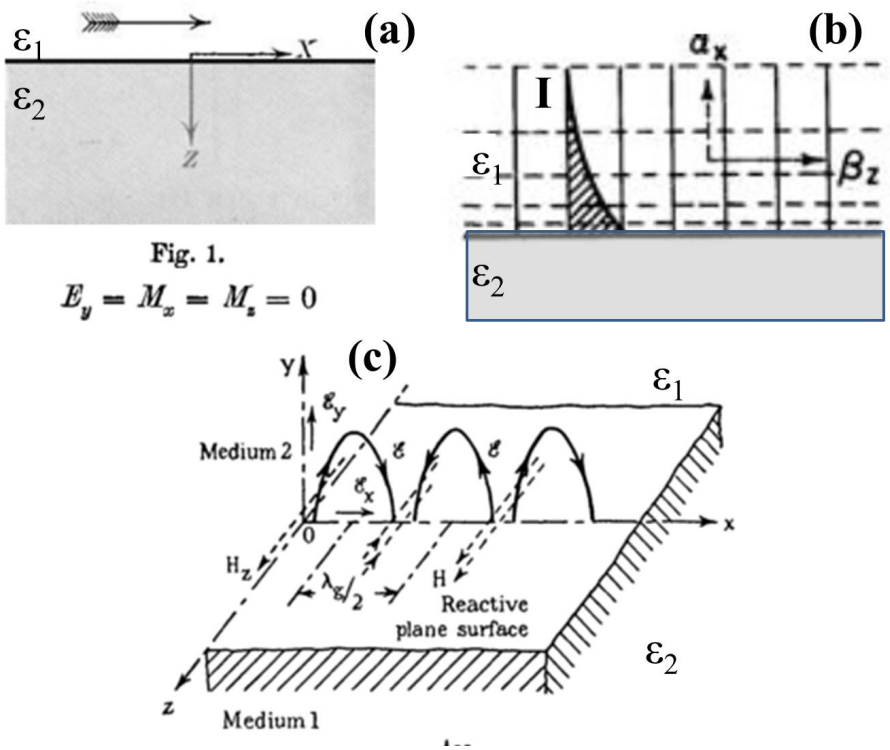

Figure 2.2: Figures reproduced (with modifications) from historical publications detailing surface waves where ϵ_1 indicates the permittivity of the dielectric layer and ϵ_2 indicates the permittivity of the conducting surface layer. (a) Zenneck's original paper [6] hypothesising the field solution of a transverse magnetic surface wave and the arrow representative of the direction of the propagating mode. Underneath are the electric (**E**) and magnetic (**M**) field components required to be zero for such a mode to be supported. (b) Zucker (1952) [31] representation of the phase and amplitude variation of the electric field associated with a surface wave. Shaded region represents amplitude decay (I) as a function of distance from the interface between ϵ_1 and ϵ_2 media, solid vertical lines represent lines of constant phase and dashed horizontal lines represent lines of constant amplitude (c) The orientation of the electric and magnetic fields what is described as a Zenneck wave as defined by Barlow and Cullen in 1953 [32].

field associated with the supported mode was controlled. The radial extent of this electric field was also shown to be less than the radial extent of the electric fields on the smooth uncoated rod. As a result low loss methods of transporting radio frequency signals (transmission lines) could feasibly be designed.

This analysis was extended by Attwood in 1951 [33] by investigating dielectric layers on plane conducting sheets and exciting a confined surface wave to this interface. Surface wave application to transmission lines using corrugated metal sheets were further studied in 1951 by Rotman [34] who modified Cutler's original formulas by using a different approximation for the field distribution in the gaps between the corrugations. This approach was extended to the study of antennas in 1954 by R.S. Elliot [35] where a corrugated rectangular waveguide used as a

feed to a corrugated surface was analysed.

2.2.3.1 Corrugated Waveguides and Horn Antennas

The study of waveguides with corrugations originated with Slater in 1941 [36] when, during his analysis of magnetron oscillators, he derived an approximate theory for wave propagation between parallel conducting plates with the interior of one plate being corrugated in the transverse dimension. Goldstein [37, 38] and Walkinshaw [39, 40] extended this to rectangular and circular waveguides, respectively. This, as well as an in depth discussion of waveguide modes and propagation of electromagnetic radiation in a waveguide is summarised in a book titled 'Microwave Engineering' by Pozar [41] and will not be further elaborated on in this thesis.

Corrugations can be used to guide a mode from a confined waveguide into free space by texturing the inner surface of a tapered guide known as a feedhorn (horn) antenna. Diffraction from the aperture of the antenna results in undesirable radiation which distorts the Gaussian beam profile of the radiating device. It was realised by Kay in 1964 [42] that corrugations inside a horn antenna could be used to reduce such diffraction as they present the same boundary conditions to all polarizations of waveguide mode within the device. This tapers the field distribution at the aperture of the antenna in all planes so that the same boundary conditions are enforced on the emitted waveguide mode on all four walls of the aperture, eliminating spurious diffraction.

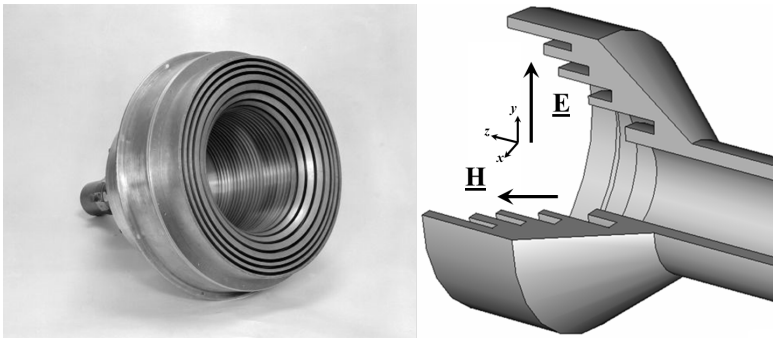

Figure 2.3: Photograph of a corrugated scalar horn antenna (left) and a schematic representation (right) of the interior cross section of the same antenna. The scale of the schematic (modified diagram from CST AG) does not represent the dimensions of the photographed horn on the left, a corrugated feed horn antenna designed by the Commonwealth Scientific and Industrial Research Organisation (CSIRO).

Figure 2.3 shows a photograph of a corrugated horn antenna designed by CSIRO in comparison to a schematic of the inside of the same horn to illustrate the corrugations within a feed horn antenna. The dimensions of the schematic are for illustrative purposes only. Olver and Clarricoats [43, 44] further analysed

corrugated feed horn antennas such as the ones depicted in Figure 2.3 in 1984. Corrugated feed horn antennas remain an active area of research as the properties inherent with this design such as low sidelobes and high beam symmetry are desired on smaller scales to operate at higher frequency regimesand has been designed by McKay et al. (2013) [45]. However, the physics of a mode confined within a waveguide is not the subject of this work therefore this historical review now continues to follow the genesis of the surface wave mode.

Barlow and Cullen [32, 46] and Harvey [47] summarise the excitation and support of surface waves via quarter wavelength grooves or dielectric overlayers via a property known as surface impedance (Z_s). Z_s is defined as the ratio between the tangential components of electric and magnetic fields associated with the surface wave. In fact the impedance model was used by Wait [48] to provide a link between the surface waves of Zenneck, Sommerfeld, Norton, and Goubau [6, 14, 11, 15].

Further study of surface wave applications including increasing the directivity and decreasing the gain of the antenna is summarised in Zucker (1952) [49]. As an aside it is noted that the property of directivity is the ratio of the radiation intensity in a given direction from the antenna to the radiation intensity averaged over all directions.

In the concluding remarks Zucker notes that while a Zenneck wave is almost impossible to excite on a metallic sheet in the microwave regime due to a negative permittivity, at optical frequencies it should be easily supported. To the surprise of this author a parallel is drawn between the surface wave observed by Wood and Fano and the mode supported by a dielectric overlayer on a metallic sheet or an array of corrugations in the microwave regime. To the best knowledge of this author this is notably the first parallel drawn between the field of photonics and microwave engineering concerning the electromagnetic modes studied in each field actually being attributed to one in the same phenomenon. A more rigorous approach was used by Pendry et al. (2004) [50, 51] to explain the link between microwave surface waves and those in the visible regime (Figure 2.1) via the concepts of ‘Metamaterials’ and ‘effective’ permittivity and permeability.

2.2.4 Metamaterials

In terms of electromagnetic materials, a metamaterial is one whose electromagnetic properties are due to its geometric design and not the constituent properties of its chemical composition. By altering the structure of a metamaterial its electric and magnetic properties as defined by complex permittivity (ϵ), the ratio between electric field $\underline{\mathbf{E}}$ and electric displacement $\underline{\mathbf{D}}$ as stated in equation 2.3, and permeability (μ) the ratio between magnetic induction $\underline{\mathbf{H}}$ magnetic field intensity $\underline{\mathbf{B}}$ are altered. It is common to classify a material into four possible subcategories depending on the sign of ϵ and μ associated with it i.e. ($+\epsilon$, $+\ \mu$), ($-\ \epsilon$, $-\ \mu$), ($+\epsilon$, $-\mu$) and ($-\epsilon$, $+\mu$). These four categories are referred to as double positive media (DPS), double negative media (DNG) and single negative media (SNG) respectively. Most naturally occurring materials are classified as DPS but some do display characteristics of SNGs depending on the frequency regime under consideration i.e. a metal at visible frequencies has negative ϵ whereas it is otherwise positive. While there are no naturally occurring DNG materials, research in the field of metamaterials has resulted in the design and realisation of both DPS and DNG materials.

There are two theoretical and two experimental publications which have notably galvanised the field of metamaterials over a number of years including Veselago (1968) [52], Pendry (2000) [53], Smith et al. (2000) [54] and Shelby et al. (2001) [55]. Veselago proposed the use of DNG materials to achieve negative refractive index materials and hypothesised that a slab of such material could be used to focus light from a point source. Pendry re-iterated that result years later when he proposed using DNG materials as 'superlenses'. He further elaborated on this in the aformentioned citation by noting such superlenses transmitted evanescent waves without loss, surprisingly resulting in the perfect recreation of an image.

Both Smith et al. and Shelby et al. experimentally realised artificial DNG using split ring resonators (SRR), a structure first proposed by Pendry et al. (1999) [56]. The former investigated the transmission response of a structure that exhibited SNG properties and DNG properties over a range of frequencies, resulting in transmission minima and maxima respectively. The latter arranged the SRR structure into a prism and observed negative refraction of incident radiation in comparison to a prism composed of a DPS medium.

A summary of these seminal publications can be found here [57, 58]. Research topics inspired by these papers are cloaking, high refractive index materials and other artificial magnetism topics. Further, the idea of a metamaterial has been extended to include 'metasurfaces' where one dimension of the metamaterial in question is so much less than that of the other dimensions it is considered to be infinitesimal. Therefore the metasurface is considered two dimensional [59]. Also,

the dispersive properties of the metasurface must be able to be described by a sheet impedance as is discussed in Section 3.4.3.4.

What is of particular interest to this thesis is the work proposed by Pendry et al. (2004) [50] who further realised that individual resonances created by a metal sheet perforated with holes of some depth could in fact provide a means to an 'effective permittivity'.

2.2.5 The Effective Medium Approach

Pendry recognised that an infinitely thick metallic slab perforated with a square array of infinitely deep square holes could be described as a metamaterial surface with each hole acting as a resonant element. Consider Figure 2.4. As in Figure 2.1, the three bands of colour represent three different frequency regimes including microwave (yellow), infrared (red) and visible (purple). The behaviour of a photon travelling in free space is represented by the solid black line with a constant gradient and the surface mode is represented with the solid black curve with a frequency dependent gradient. The black dashed line represents the limiting frequency of the surface wave.

In contrast to Figure 2.1 this limiting frequency occurs in the regime denoted as 'microwave' and not at ω_{SP}. In this case the limiting frequency is governed by the resonant condition of a subwavelength element in an array of similar elements, in this case a square hole array. Individual resonances interact as an array, providing an overall resonant response and the mechanism by which a microwave surface wave is supported. The geometrical design of these elements dictate the frequency regime in which the limiting frequency occurs. For the specific case of a square array of deep square holes, below the waveguide cutoff frequency of that hole incident electric field will decay evanescently into the hole.

Schematic (b) in Figure 2.4 shows the electric field interaction at microwave frequencies with an array of square holes of infinite depth perforating an infinitely thick metallic slab. The electric field will exponentially decay into the holes at frequencies below the cutoff frequency of the waveguide mode supported in the square holes. Further, decay below the surface of the perforated metal results in the medium being described by an effective permittivity as now the electric field can extend beneath the interface of metal and air (into the square hole) or is screened by the non-perforated region of the metal sheet. The same logic was also applied to a sheet of quarter wavelength grooves [51], with the resonance supported by each element interacting coherently and supporting a surface wave limited by a geometrically designed resonance. This is fully discussed in Section 2.5.1.

Figure 2.4 depicts the dispersion of such a mode, termed a 'spoof' or 'pseudo'

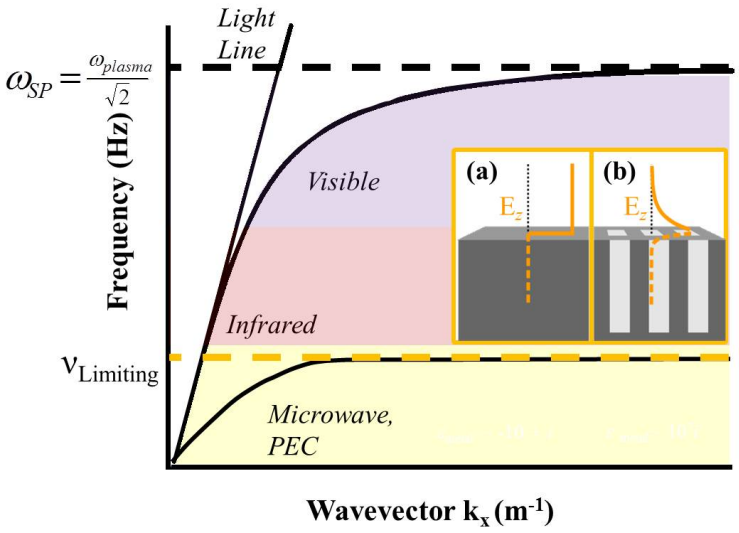

Figure 2.4: Dispersion of a surface wave associated with a metal slab of infinite depth, perforated with subwavelength holes (curved black line) which are also infinitely deep. Solid dashed line represents limiting frequency. Insets: penetration of vertical electric field (orange) into (a) metal (b) an array of infinitely deep square holes at microwave frequencies. Modified from Hibbins et al. (2005) [28].

surface plasmon. Experimental verification of this pseudo mode was given by Hibbins *et al.* (2005) [28] and the support and manipulation forms the main discussion in this thesis.

2.3 The Dispersion of a Surface Wave

A surface wave is an electromagnetic mode which exists on interface of two dissimilar media, decaying exponentially into each medium. It propagates along the interface between the two media and is non-radiative therefore the mode is subject to losses from the bordering media only. A surface plasmon (SP) can be described as such and is a longitudinal oscillation of charge along the interface between the aforementioned two media.

Figure 2.5 is a schematic representation of the electric field associated with a surface plasmon. Notice the similarity in the field profile of the schematic shown in Figure 2.5 to the wave described as a Zenneck wave in Figure 2.2 (c) in Barlow and Cullen [32] on a completely different surface and at microwave frequencies. This is because they are one in the same phenomenon as described by Zenneck in 1907 [6].

We will now describe how a surface wave can be supported on a planar interface between a metal and a dielectric. This is extended to consider the permittivity of the metal and how its behaviour changes in different frequency regimes. The

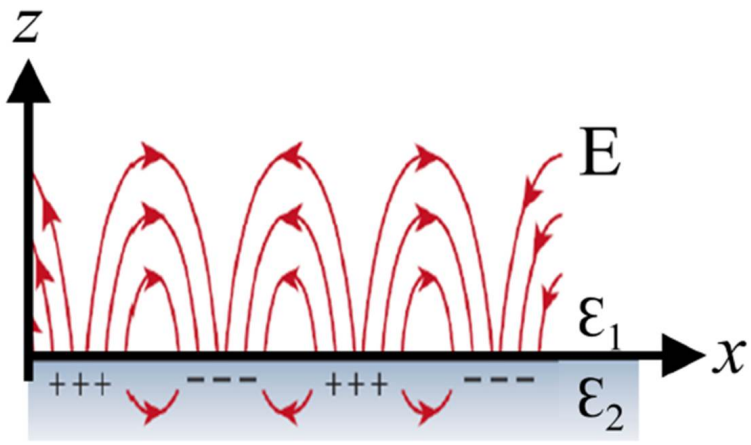

Figure 2.5: Schematic representation of the electric field associated with a surface wave confined to the interface between a dielectric (ϵ_1) and a conductor (ϵ_2) at optical frequencies, adapted from 'The Optical Response of Short-Pitch Surface-Relief Gratings' by Dr I. Hooper [60].

consequences of these changes in relation to the confinement of the electric field associated with the surface wave is discussed and a method for supporting a confined surface mode in the microwave regime is detailed. Further to this is a small illumination as to the description of a surface wave as an inhomogeneous plane wave.

2.3.1 Derivation of the Dispersion Relation

Primarily let us consider the initial conditions required for a surface wave to be supported on an planar interface between two semi-infinite homogeneous media at visible frequencies. Polarisation charge must be trapped at this interface for a surface wave to exist. Therefore a component of the electric field ($\underline{\mathbf{E}}$) must be normal to the interface so that the displacement ($\underline{\mathbf{D}}$) of the electric field will be induced. The relationship between $\underline{\mathbf{E}}$ and $\underline{\mathbf{D}}$ is described as

$$\underline{\mathbf{D}} = \epsilon_{rel}\epsilon_0\underline{\mathbf{E}} \tag{2.3}$$

where $\epsilon = \epsilon_{rel}\epsilon_0$, ϵ_{rel} represents the relative permittivity of the medium and ϵ_0 represents the permittivity of free space.

Crucially, the displacement $\underline{\mathbf{D}}$ of the electric field is continuous across such an interface. If we assume the two media in question are air (where ϵ_{rel} is positive) and metal (ϵ_{rel} is large and negative) then the direction of $\underline{\mathbf{E}}$ will change and 'trap' polarisation charge at the surface. Subsequently, to excite a surface wave the incident wave must be polarised so that its magnetic component traverses the plane of incidence and its electric field component is parallel to the plane of

incidence, a transverse magnetic (TM) polarisation.

The orientation of a TM wave is illustrated in Figure 2.6 where the plane of incidence is in the xz-plane.

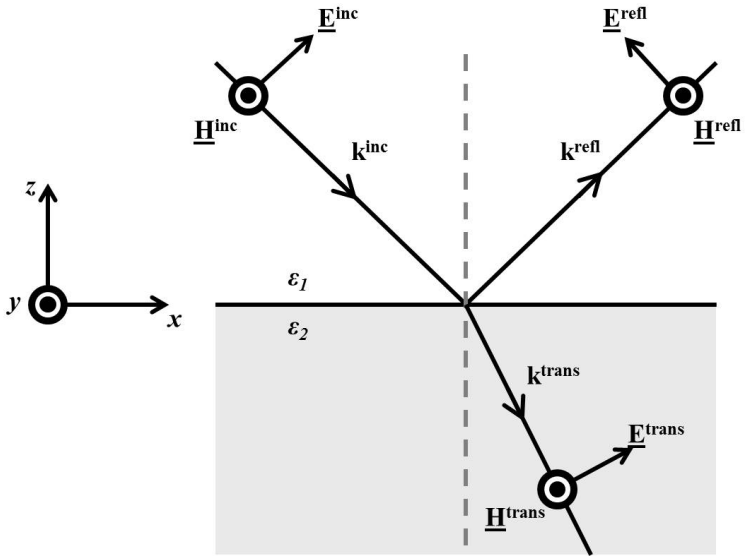

Figure 2.6: Transverse magnetic polarised plane wave incident on a metal-dielectric interface. The interface between air (medium 1) with permittivity ϵ_1 and a metal (medium 2) with permittivity ϵ_2 is planar.

An incident plane TM wave is detailed in Figure 2.6. The spatial and temporal components of electric ($\underline{\mathbf{E}}$) and magnetic fields ($\underline{\mathbf{H}}$) can therefore be described as

$$\underline{\mathbf{E}} = [E_x, 0, E_z]\, e^{i(k_x\hat{x}+k_z\hat{z}-wt)} \tag{2.4}$$

$$\underline{\mathbf{H}} = [0, H_y, 0]\, e^{i(k_x\hat{x}+k_z\hat{z}-wt)} \tag{2.5}$$

In the absence of free charge, Maxwell's equation defining the relationship between the electric and magnetic field is:

$$\underline{\nabla} \wedge \underline{\mathbf{H}} = \epsilon \frac{\delta \underline{\mathbf{E}}}{\delta t} \tag{2.6}$$

Equation 2.6 can be applied to the fields defined in equations 2.4 and 2.5 to obtain the following relations:

$$\underline{\nabla} \wedge \underline{\mathbf{H}} = (ik_x H_y \hat{z} - ik_z H_y \hat{x})\, e^{i(k_x\hat{x}+k_z\hat{z}-wt)} \tag{2.7}$$

$$\epsilon \frac{\delta \underline{\mathbf{E}}}{\delta t} = (\epsilon(i\omega E_x \hat{x} + i\omega E_z \hat{z})\, e^{i(k_x\hat{x}+k_z\hat{z}-wt)} \tag{2.8}$$

By equating the vector components of equations 2.7 and 2.8 the following

relation is obtained:

$$H_y = \frac{\epsilon\omega E_x}{k_z} = -\frac{\epsilon\omega E_z}{k_x} \tag{2.9}$$

where ϵ is the permittivity of the medium, k_x is the component of the wavevector (k_0) in the x-direction and ω is the angular frequency.

The component of k which notes the direction of travel of a confined surface wave is often noted as the 'in-plane' wavevector. As such k_x has been described in this thesis as the in-plane wavevector. We consider the permability (μ) of both media 1 and 2 to be equal to 1. Hence expressions for the incident (inc), reflected ($refl$) and transmitted ($trans$) fields are:

$$E_1^{inc} = E_{x1}^{inc}[1, 0, \frac{-k_x}{k_{z1}}]\ e^{i(k_x\hat{x}+k_{z1}\hat{z}-wt)} \tag{2.10}$$

$$E_1^{refl} = E_{x1}^{refl}[1, 0, \frac{+k_x}{k_{z1}}]\ e^{i(k_x\hat{x}+k_{z1}\hat{z}-wt)} \tag{2.11}$$

$$E_2^{inc} = E_x^{trans}[1, 0, \frac{-k_x}{k_{z2}}]\ e^{i(k_x\hat{x}+k_{z2}\hat{z}-wt)} \tag{2.12}$$

$$H_1^{inc} = E_{x1}^{inc}[0, \frac{\epsilon\omega}{k_{z1}}, 0]\ e^{i(k_x\hat{x}+k_{z1}\hat{z}-wt)} \tag{2.13}$$

$$H_1^{refl} = E_{x1}^{refl}[0, \frac{-\epsilon\omega}{k_{z1}}, 0]\ e^{i(k_x\hat{x}+k_{z1}\hat{z}-wt)} \tag{2.14}$$

$$H_1^{trans} = E_x^{trans}[0, \frac{\epsilon\omega}{k_{z2}}, 0]\ e^{i(k_x\hat{x}+k_{z2}\hat{z}-wt)} \tag{2.15}$$

Components of $\underline{\mathtt{E}}$ and $\underline{\mathtt{H}}$ which are tangential to the interface must be conserved, irrespective of medium. Further, the fields under consideration are associated with the surface wave solution to Maxwell's equations. A surface wave is an eigenmode of a metal-air interface; it is a mode that can be supported by the system. Therefore it must exist as a solution of the equations with no exciting field, and therefore we can set the incident field, E_x, to zero. These boundary conditions result in the following relations for the electric and magnetic field components in $\hat{x}$ and $\hat{y}$ with the incident field set to zero.

$$E_{x1} = E_{x2} \quad and \quad H_{y1} = H_{y2} = H_y \tag{2.16}$$

Therefore equation 2.9 is modified to:

$$H_y = \frac{-\epsilon_1\omega E_{x1}^{refl}}{k_{z1}} = \frac{\epsilon_2\omega E_{x2}^{Trans}}{k_{z2}} \tag{2.17}$$

and

$$H_y = \frac{-\epsilon_1}{k_{z1}} = \frac{\epsilon_2^{Trans}}{k_{z2}} \tag{2.18}$$

Also, as E_x is conserved so is k_x. Therefore the expression for k_0 (as seen for a free space wave in equation (2.2) can be rewritten as:

$$k_x^2 + k_{a,z}^2 = \epsilon_a k_0^2 \tag{2.19}$$

Where 'a' describes a specific medium which is, in turn, non-magnetic so $\mu = 1$. The expression for the refractive index $n_{ref} = \sqrt{\mu\epsilon}$ reduces to $n_{ref} = \sqrt{\epsilon}$. Further, we consider the incident radiation to be TM polarised. As a result, $k_y = 0$. Therefore equation 2.18 is expressed as:

$$\frac{-\epsilon_1}{\sqrt{\epsilon_1 k_0^2 - k_x^2}} = \frac{\epsilon_2}{\sqrt{\epsilon_2 k_0^2 - k_x^2}} \tag{2.20}$$

An expression for the propagating component of k_x can now be determined:

$$\epsilon_1^2(\epsilon_2 k_0^2 - k_x^2) = \epsilon_2^2(\epsilon_1 k_0^2 - k_x^2) \tag{2.21}$$

$$(\epsilon_2^2 - \epsilon_1^2)k_x^2 = \epsilon_1\epsilon_2 k_0^2(\epsilon_2 - \epsilon_1) \tag{2.22}$$

Resulting in

$$k_x^2 = k_0^2 \frac{\epsilon_1\epsilon_2}{(\epsilon_2^2 + \epsilon_1^2)} = k_{SW} \tag{2.23}$$

where k_{SW} is the wavevector of the surface wave. In this instance $k_0 < k_{SW}$. Therefore, the excitation of a surface wave is only attainable if the radiation coupling to the surface has an excess of momentum via evanescent decay from either diffraction or prism coupling [60, 61].

The wave vector normal to the interface k_z can be expressed via consideration of Equation 2.19 to be given by

$$k_{a,z} = (\epsilon_a k_0^2 - k_x^2)^{(1/2)} \tag{2.24}$$

where 'a' denotes the medium under consideration and $k_y = 0$. By considering that $k_0 < k_x$, k_z as given by Equation 2.24 must be imaginary so decays exponentially away from the interface. This equation describes an inhomogeneous plane wave, where the planes of equal amplitude are orthogonal to planes of equal phase. The electric field amplitude decays away from the supporting interface while the mode propagates along the interface. The electric field loops in Figure 2.5 result from substitution of Equations 2.23 and 2.24 into Equations 2.10, 2.11 and 2.12.

2.3.1.1 Surface Waves in Different Frequency Regimes

A graphical representation of the behaviour of k_x with respect to the frequency of radiation has previously been shown schematically in Figure 2.1 to describe the behaviour of the surface electrons associated with a metal medium at visible frequencies using the Drude model. The surface mode closely resembles that of a grazing photon until the frequency associated with the surface plasma frequency ($\omega_{SP} = \frac{\omega_p}{\sqrt{2}}$) is approached where ω_p is the plasma frequency . At this point, the value of $k_x >> k_0$ and the gradient of the dispersion changes so that the surface mode is asymptotic to ω_{SP} of the metal. ω_p is defined thus

$$\omega_p = \frac{ne^2}{m\epsilon_0} \tag{2.25}$$

where n, e and m represent electron density, electric charge and the effective mass of an electron. While exact values of the plasma frequency are obviously specific to material, in general ω_p lies in the ultraviolet region of the electromagnetic spectrum. Subsequently, the surface mode supported at microwave frequencies resembles a grazing photon.

At visible frequencies the permittivity of the medium is large and real. Therefore the comparatively small contribution of the imaginary component of ϵ_2 is neglected. However, the behaviour of the permittivity of a metal is highly dependent upon the frequency regime in which the metal is being irradiated. So much so that at microwave frequencies the imaginary component of ϵ is both large and orders of magnitude greater than the real part.

Extending equation 2.23 to include real and imaginary components of ϵ_{rel} and k_x provides insight as to the behaviour of the surface wave for a range of frequencies and has been included for completeness. This derivation has been adapted from Yang et al. (1991) [62] and [63].

The relative permittivity ϵ_{rel} and in-plane wavevector (k_x) can be described thus

$$\epsilon_{rel} = \epsilon_r + i\epsilon_i \quad and \quad k_x = k_{xr} + ik_{xi} \tag{2.26}$$

where the subscripts 'i' and 'r' denote the real and imaginary components of equation 2.26. Medium 1 is air and can be considered to be without charge so has a permittivity $\epsilon_{rel} = \epsilon_1$ without any imaginary contributions. Therefore:

$$\frac{k_x^2}{k_0^2} = \frac{k_{xr}^2 - k_{xi}^2 + 2ik_{xi}k_{xr}}{k_0^2} = \frac{\epsilon_1\epsilon_2}{\epsilon_1 + \epsilon_2} = \frac{\epsilon_1(\epsilon_{2r} + i\epsilon_{2i})}{\epsilon_1 + \epsilon_{2r} + i\epsilon_{2i}} \tag{2.27}$$

To separate the real and imaginary components of k_x with respect to the permittivity associated with both media the right hand side of Equation 2.27 is mul-

tiplied by its complex conjugate, producing:

$$\frac{\epsilon_1\epsilon_{2r}(\epsilon_1+\epsilon_{2r})+\epsilon_1\epsilon_{2i}^2+i\epsilon_1^2\epsilon_{2i}}{(\epsilon_1+\epsilon_{2r})^2+\epsilon_{2i}^2} \tag{2.28}$$

The real parts of k_x and ϵ are now describe as:

$$\frac{k_{xr}^2-k_{xi}^2}{k_0^2}=\frac{\epsilon_1\epsilon_{2r}(\epsilon_1+\epsilon_{2r})+\epsilon_1\epsilon_{2i}^2)}{(\epsilon_1+\epsilon_2 r)^2+(\epsilon_{2i})^2}= \quad R \tag{2.29}$$

While the imaginary parts can be described as:

$$\frac{2k_{xi}k_{xi}}{k_0^2}=\frac{\epsilon_1^2\epsilon_{2i}}{(\epsilon_1+\epsilon_2 r)^2+(\epsilon_{2i})^2}= \quad I \tag{2.30}$$

Therefore from equation 2.30 the following statement can be made:

$$\frac{k_{xi}^2}{k_0^2}=\frac{I^2k_0^2}{4k_{xr}^2} \tag{2.31}$$

Equation 2.31 can be substituted back into equation 2.29 and gives the following expression:

$$\frac{k_{xr}^2}{k_0^2}-\frac{I^2k_0^2}{4k_{xr}^2}-R=0 \tag{2.32}$$

Which yields the following quadratic equation with $\frac{k_{xr}^2}{k_0^2}$ as the subject:

$$\frac{k_{xr}^4}{k_0^4}-R\frac{k_{xr}^2}{k_0^2}-\frac{I^2}{4}=0 \tag{2.33}$$

Similarly a quadratic equation with $\frac{k_{xi}^2}{k_0^2}$ as the subject can be obtained.

$$-\frac{k_{xi}^4}{k_0^4}-R\frac{k_{xi}^2}{k_0^2}+\frac{I^2}{4}=0 \tag{2.34}$$

Solving equations 2.37 and 2.38 for expressions of the real and imaginary component of k_x in with respect to the permittivity gives the following.

$$\frac{k_{xr}^2}{k_0^2}=\frac{\epsilon_1(\epsilon_r^2+\epsilon_{2r}^2+\epsilon_1\epsilon_{2r}+\sqrt{(\epsilon_r^2+\epsilon_{2r}^2+\epsilon_1\epsilon_{2r})^4-\epsilon_1\epsilon_{2i}^2}}{2((\epsilon_1+\epsilon_{2r})^2+\epsilon_{2i}^2)} \tag{2.35}$$

$$\frac{k_{xi}^2}{k_0^2}=\frac{\epsilon_1(-(\epsilon_r^2+\epsilon_{2r}^2+\epsilon_1\epsilon_{2r})-\sqrt{-(\epsilon_r^2+\epsilon_{2r}^2+\epsilon_1\epsilon_{2r})^4+\epsilon_1^2\epsilon_{2i}}}{2((\epsilon_1+\epsilon_{2r})^2+\epsilon_{2i}^2)} \tag{2.36}$$

Equations 2.35 and 2.36 can be simplified by representing the terms $\epsilon_r^2+\epsilon_{2r}^2+\epsilon_1\epsilon_{2r}$ as equal to ϵ_e^2, an arbitrarily named constant, so that they can be represented

thus:

$$\frac{k_{xr}^2}{k_0^2} = \frac{\epsilon_1(\epsilon_e^2 + \sqrt{\epsilon_e^4 - \epsilon_1\epsilon_{2i}^2}}{2((\epsilon_1 + \epsilon_{2r})^2 + \epsilon_{2i}^2)} \tag{2.37}$$

$$\frac{k_{xi}^2}{k_0^2} = \frac{\epsilon_1(-\epsilon_e^2 - \sqrt{-\epsilon_e^4 + \epsilon_1^2\epsilon_{2i}}}{2((\epsilon_1 + \epsilon_{2r})^2 + \epsilon_{2i}^2)} \tag{2.38}$$

Equation 2.37 is indicative of a quantity known as the modal index n expressed as

$$n = \frac{c}{v_g} = \frac{\lambda_0}{\lambda_x} \tag{2.39}$$

where λ_0 is the wavelength of the free space mode ($\lambda_0 = \frac{2\pi}{k_0}$), λ_x is the wavelength of the surface wave ($\lambda_x = \frac{2\pi}{k_x}$) and v_g is the group velocity of the mode. Equation 2.38 describes the non-radiative damping of the mode and can be used to express the propagation length of a surface wave along a supporting interface as a function of permittivity.

2.4 Permittivity of a Metal

Having detailed complete expressions for the wavevector associated with a surface wave with respect to the permittivity of the supporting media (Equations 2.37 and 2.38), the frequency dependent nature of the permittivity with respect to the metal medium is reviewed and related to the confinement of a surface wave to the interface between a metal and a dielectric. The concept of confinement has previously been discussed in Section 2.2.2.2.

2.4.1 Permittivity as a Function of Frequency

The confinement of an electromagnetic mode is characterised by the extension of the electric field from the interface between the two supporting media. As such, the confinement of a surface wave supported by a metal-air interface varies with frequency due to the nature of the permittivity of the metal medium.

There is an absence of charge in the air medium therefore ϵ_1 remains constant and equal to ϵ_0. However, the metal is composed of conduction electrons. Their response to an incident electromagnetic field can be characterised using the Drude free-electron model [64] so that the real and imaginary parts of the permittivity are described thus:

$$\epsilon_r = 1 - \frac{\omega_p^2\tau^2}{(1 + \omega^2\tau^2)} \tag{2.40}$$

$$\epsilon_i = \frac{\omega_p^2 \tau}{\omega(1+\omega^2\tau^2)} \tag{2.41}$$

where τ is the collision time and ω_P is the plasma frequency.

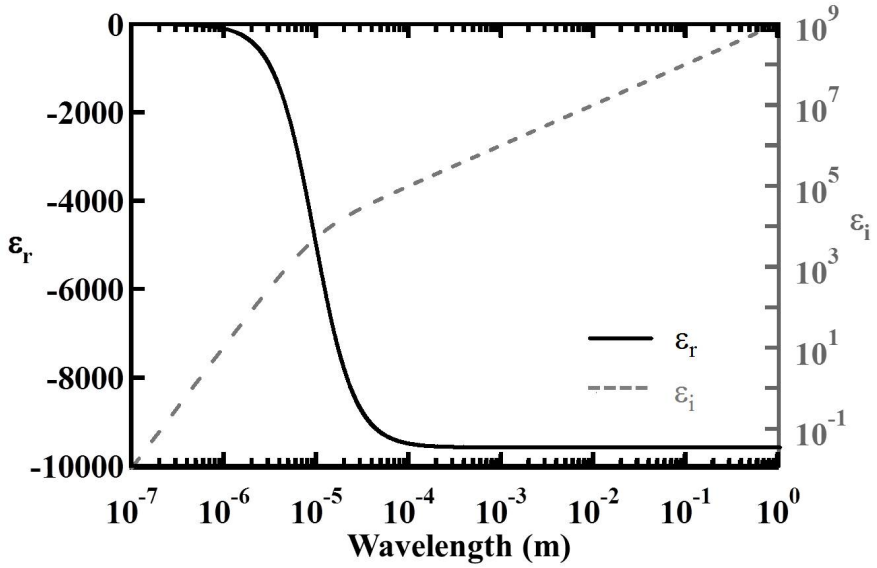

Figure 2.7: Real (black) and imaginary (grey) permittivity as defined by the Drude electron-free model for aluminium. In this case $\omega_p = 1.93\text{x}10^{16}$ radians and $\tau = 5.07\text{x}10^{-15}$ seconds, values obtained from reference [64]

Figure 2.7 represents the behaviour of the real and imaginary components of the permittivity for aluminium as a function of wavelength. It is clear that at microwave frequencies (wavelength $\simeq 0.001$ m) ϵ_r has reached a constant, steady value that is many orders of magnitude smaller than ϵ_i.

Consider a perfect electrical conductor (PEC), where the electric fields are completely screened so do not penetrate into the PEC surface and conductivity (σ) of the PEC is infinite. The imaginary component of the permittivity ϵ_i associated with a PEC is considered to be infinite and larger than ϵ_r. By inspection of Figure 2.7 it is clear to see why metals at microwave frequencies are often approximated as PECs as ϵ_i is very large and positive.

Further consider the following relation of σ at all frequencies

$$\sigma = \frac{nq^2\tau}{m(1+i\omega\tau)} \tag{2.42}$$

where n is electron density, m the mass of an electron, q is the charge of an electron and τ is relaxation time. At microwave frequencies $\omega << \frac{1}{\tau}$ so the imaginary component of σ is negligible while the real part is large, resulting in an almost perfect conductor of electric field (PEC).

The frequency dependence of the permittivity associated with a metal has direct consequences as to the penetration of electric field associated with a surface wave supported on a metal-air interface and subsequently the confinement of the mode.

2.4.1.1 Skin Depth and Penetration Depth

The decay of a surface wave in a direction normal to the interface (in the $\hat{z}$-direction in Figure 2.6) into the surrounding media defines how confined the electric and magnetic fields associated with the mode are with respect to the interface which supports the mode. An indication of the confinement of the mode to the supporting interface is the rate at which the intensity of the fields decreases as a function of distance from the supporting interface. The more confined the mode, the faster the rate of decay of the fields from the supporting interface. A description of this confinement is found via the 'skin depth' (δ_s) of a material, i.e. the distance normal to the interface at which the amplitude of the electric field reduces to $\frac{1}{e}$ in comparison to its value at the interface [41]. Skin depth is related to imaginary k_{zi} thus

$$\delta_s = \frac{1}{k_{zi}} = \sqrt{\frac{2}{\omega\mu\sigma}} \tag{2.43}$$

where σ is the conductivity of the material of the penetrated medium. This should not be confused with the 'penetration depth' (δ_z) which is the distance normal to the interface at which the intensity of the electric field drops to $\frac{1}{e}$ where

$$\delta_z = \frac{1}{2kzi} \tag{2.44}$$

Besides the obvious mathematical differences, δ_s of a material is associated with the conductivity and therefore any free charge of the medium. However, δ_z describes more general absorption into a medium. For instance, while the rate of decay of the fields associated with a surface wave into a metallic surface might be described by δ_s the rate of decay of those same fields into a dielectric such as air should be described by δ_z due to lack of free charges in the medium.

The electric field of a surface wave normal to the interface is imaginary and has previously been described by Equation 2.24. Therefore k_z will be described by its imaginary component k_{zi}. If Equation 2.24 is rewritten as a factor of k_0 and then separated in terms of the real and imaginary parts of epsilon, an expression for k_{zi} can be found:

$$\frac{k_z}{k_0} = \sqrt{(\epsilon_r + \epsilon_i) - \frac{k_x^2}{k_0^2}} \tag{2.45}$$

$$\frac{k_z}{k_0} = \sqrt{\left(\epsilon_r - \frac{\epsilon_1\epsilon_e^2}{(\epsilon_1+\epsilon_{2r})+\epsilon_{2i}^2}\right) + i\left(\epsilon_i - \frac{\epsilon_1^2\epsilon_{2i}}{(\epsilon_1+\epsilon_{2r})^2+\epsilon_{2i}^2}\right)} \tag{2.46}$$

Then, as in equations 2.37 and 2.38, a quadratic with $\frac{k_i z}{k_0}$ as the subject is used to gain an expression for k_{zi}.

$$\frac{k_{zr(a)}^2 - k_{zi(a)}^2 + 2ik_{zr(a)}k_{zi(a)}}{k_0^2} = \left(\epsilon_{r(a)} - \frac{\epsilon_1\epsilon_e^2}{(\epsilon_1+\epsilon_{2r})+\epsilon_{2i}^2}\right) + i\left(\epsilon_{i(a)} - \frac{\epsilon_1^2\epsilon_{2i}}{(\epsilon_1+\epsilon_{2r})^2+\epsilon_{2i}^2}\right) \tag{2.47}$$

$$\frac{k_{zi}}{k_0} = \sqrt{\frac{\epsilon_r - \frac{\epsilon_1\epsilon_e^2}{(\epsilon_1+\epsilon_{2r})^2+\epsilon_{2i}^2} - \sqrt{\left(\epsilon_r - \frac{\epsilon_1\epsilon_e^2}{(\epsilon_1+\epsilon_{2r})^2+\epsilon 2i^2}\right)^2 + \left(\epsilon_i - \frac{\epsilon_1\epsilon_{2i}^2}{(\epsilon_1+\epsilon_{2r})^2+\epsilon 2i^2}\right)^2}}{-2}} \tag{2.48}$$

Equations 2.48 and 2.44 can be combined to provide a frequency dependent penetration depth:

$$\delta_z = \frac{1}{2k_{zi}} = \frac{\lambda_0}{2\pi}\,\frac{k_0}{2k_{zi}} \tag{2.49}$$

where λ_0 is the wavelength of a free space wave.

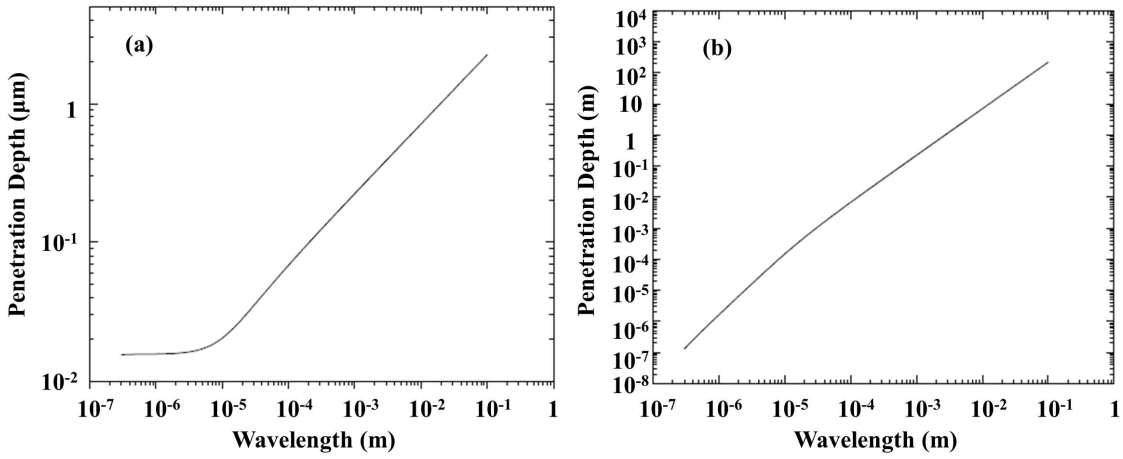

Figure 2.8: Penetration depth (δ_z) as a function of frequency associated with the electric field of the surface wave decaying in the z-direction in (a) medium 2 (aluminium) and (b) medium 1 (air). Adapted from from 'Electromagnetic surface wave mediated absorption and transmission of radiation at microwave frequenciesDr M Lockyear' by Dr M. Lockyear [63].

Figure 2.8 represents the skin depth of the electric field associated with the surface wave in (a) medium 2 (aluminium) and (b) medium 1 (air). The values of δ_z differ between these two media severely at microwave frequencies. For instance

at 30 GHz $\delta_z = 0.7$ μm in aluminium whereas $\delta_z = 18.5$ m in air. However, when the wavelength under consideration is in nanometers (visible light), inspection of Figures 2.8 (a) and (b) shows that although penetration into aluminium is less than at microwave frequencies, the ratio between the values of δ_z is far more comparable and in fact only differs by an order of magnitude [28].

2.5 Microwave Surface Waves on Metallic Structures with Subwavelength Patterning

In the optical regime the skin depth of the electric field into the metal is comparable to the skin depth into the air. However, in the microwave regime, this component extends many wavelengths into the air medium and the surface wave is no longer confined to the interface between the air and metal. Since the 1950s, it has been known that the addition of surface structure or a dielectric overlayer will act to confine a surface wave at microwave frequencies [32, 65, 12].

This thesis investigates a surface wave which is confined to the interface between air and a metal which is corrugated by a one dimensional array of grooves. The mechanism of confinement is discussed via matching electric field associated with diffraction from an incident wave to the forward and backward propagation of a waveguide mode supported within the metallic groove. This is different to the description of surface waves investigated in the 1950's wherein the impedance model was employed to describe the electromagnetic fields of the mode. The impedance model is discussed in section 2.5.3.

2.5.1 The Effective Medium Approach

Previously considered was the confinement of an electromagnetic surface wave to a metal-air interface at any frequency. This confinement was characterised by the spatial extent of the electric field into the dielectric, vertically away from the interface, which is much greater than the spatial extent of the electric field into the metal interface at the microwave frequencies. As a result, the surface wave is not confined.

By addition of subwavelength structure a confined surface wave can be supported on a metal-air interface so that the system is subject to an 'effective' permittivity rather than the large and imaginary permittivity in as is typical for this frequency regime. This section details how the effective medium approach can be applied to a subwavelength one dimensional array of grooves and an array of square holes to explain how a surface wave can be supported on these structures. This treatment has been adapted from the publication of Garcia-Vidal et al. (2005)

[51] which followed the seminal publication of Pendry et al (2004) [50] concerning the effective medium approach to support surface plasmons.

2.5.1.1 Surface Waves Supported on a One Dimensional Array of Metallic Grooves

The system considered is the same as in Section 2.3 in that a TM polarised plane wave is incident on a metal-air interface.

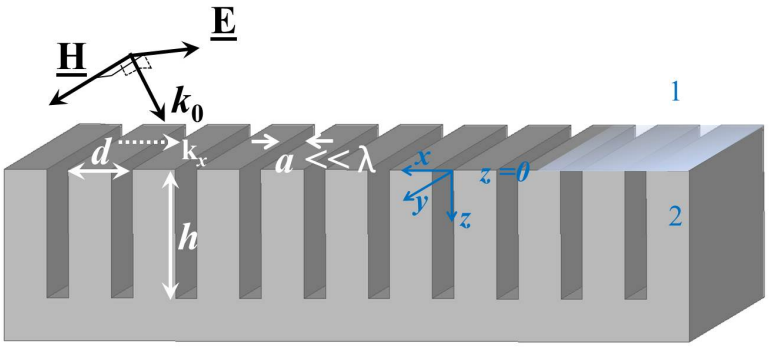

Figure 2.9: Schematic of a one dimensional array of grooves. Medium 1 is dielectric (air) and while medium 2 is composed of both metal and air. The shaded region indicates the interface between medium 1 and medium 2 at $z = 0$ and is for illustrative purposes only. The blue dotted line further illustrates the position of $z = 0$ and therefore the position of the interface. The black coordinate system indicates the direction of propagation (k_0) of the free space wave as well as the electric ($\underline{\mathbf{E}}$) and magnetic ($\underline{\mathbf{M}}$) components of that wave. The pitch of the structure and the height of each groove is indicated by d and h, respectively.

However, in this instance the surface is now considered to be corrugated by an array of grooves and medium 2 is now composed of both metal and air. This is shown schematically in Figure 2.9 where an incident free space wave is shown in black, the dimensions of the structure are stated in white and the coordinates of the system are shown in blue.

The following derivation has been adapted from Garcia-Vidal et al. (2005) [51]. The incident and reflected electric $\underline{\mathbf{E}}$ and magnetic $\underline{\mathbf{H}}$ field of the surface wave in medium 1 can be expressed as:

$$\underline{\mathbf{E}}^{inc} = \frac{1}{\sqrt{d}}[1, 0, -\frac{k_x}{k_{z1}}]\, e^{i(k_x x + k_z z - \omega t)} \tag{2.50}$$

$$\underline{\mathbf{H}}^{inc} = \frac{1}{\sqrt{d}}[0, \frac{\epsilon\mu}{k_{z1}}, 0]\, e^{i(k_x x + k_z z - \omega t)} \tag{2.51}$$

$$\underline{\mathbf{E}}^{refl} = E_{x1}^{refl}[1, 0, \frac{k_x}{k_{z1}^n}]\, e^{i(k_x^n x + k_z^n z - \omega t)} \tag{2.52}$$

$$\underline{\mathbf{H}}^{refl} = E_{x1}^{refl}[0, \frac{-\epsilon\mu}{k_z^n}, 0]\ e^{i(k_x^n x + k_z^n z - \omega t)} \tag{2.53}$$

The derivation follows the same method outlined in Section 2.3.1. Further, as the surface we are considering is a corrugated structure and not perfectly planar, the reflected wave will be subject to Huygens Principle and multiple orders of diffraction can be expected. These are denoted as (n) in the equations above where $k_x^{(n)} = k_x + 2\pi\ n/d\ (\infty \leq n \geq \infty)$ and $k_z^{(n)} = \sqrt{k_0^2 - (k_x^n)}$.

Medium 2 is comprised of both metal and air and, as previously shown in Figure 2.7, a metal's permittivity ϵ_i at microwave frequencies is large. In the case of this derivation let us now consider a metal at microwave frequencies to be a perfect electrical conductor (PEC). Subsequently ϵ_i is now considered to be infinite, instead of simply large in comparison to its real counterpart, ϵ_r, and the only electric field to consider is that found inside the groove. As the wavelength of incident radiation is much larger than the width of the groove itself we only consider the fundamental transverse electric (TE) waveguide modes supported by the corrugations:

$$\underline{\mathbf{E}_2}^{TE,\pm} = (1,0,0)\frac{1}{\sqrt{a}}e^{\pm ik_0 z)} \tag{2.54}$$

$$\underline{\mathbf{H}_2}^{TE,\pm} = (0,1,0)\frac{1}{\sqrt{a}}e^{\pm ik_0 z)} \tag{2.55}$$

where '$TE, \pm$' indicates the forward TE mode into the groove and the backward TE mode reflected from the metallic termination at the end of the groove.

Garcia Vidal et al. (2005) [51] do not consider the fields in medium 2 be subject to diffracted orders. Therefore the electric and magnetic field inside the corrugations can be considered as a combination of forward and reflected fields of the TE modes that are propagating in the positive and negative $\hat{z}$ direction due to the metal boundary terminating the end of each cavity.

$$\underline{\mathbf{E}}^2 = C^+\underline{\mathbf{E}}^{TE,+} + C^-\underline{\mathbf{E}}^{TE,-} \tag{2.56}$$

$$\underline{\mathbf{H}}^2 = C^+\underline{\mathbf{H}}^{TE,+} + C^-\underline{\mathbf{H}}^{TE,-} \tag{2.57}$$

where C is an arbitrary constant, indicative of the amplitude of the mode. The shaded region on Figure 2.9 at $z = 0$ indicates the interface between medium 1 and medium 2 and is for illustrative purposes only. This region includes a metal-air interface and an air-air interface. The matching conditions used to obtain equation 2.18 are once again applied so that E_x is continuous across the interface where z

$= 0$. However, the key difference in this treatment is that H_y is now continuous along the metallic struts which border the air filled groove and along the bottom of the groove itself. (i.e. at $z = 0$, where $x = d - a$ and $z = h$, respectively).

By applying these boundary conditions and considering that the dimensions of the corrugation are much smaller than the incident wavelength an expression for the in-plane wavevector k_x where $k_x > k_0$ can be stated thus

$$\frac{\sqrt{k_x^2 - k_0^2}}{k_0} = S_0^2 \tan(k_0 h) \tag{2.58}$$

where S_0 is the overlap integral for the zeroth diffracted order. This equation is extended in Martin-Cano et al (2010) [66] to

$$k_x = k_0 \sqrt{1 + (\frac{a}{d})^2 \tan^2(k_0 h)} \tag{2.59}$$

where k_0, the wavevector of the incident wave is defined entirely by a real value of k_z. As this expression for k_x includes a tangent function, there will be an asymptote when $k_0\, h = \frac{\pi}{2}$. As a result, if the corrugations were infinitely thin slits, the limiting frequency of the surface wave supported on the array of corrugations would occur when $h = \frac{\lambda}{4}$.

In reality the limiting frequency will occur lower than the $\frac{\lambda}{4}$ limit as the corrugations are not infinitely thin. There is an overlap between the incident field and the fields of the TE mode within the cavity resulting in a lowering of the resonant frequency of the mode.

2.5.2 Resonance

The previous section elaborated upon a surface wave supported by an array of corrugations. The boundary conditions implied by the geometrical structure of the corrugations define the characteristics of the individual resonance of each cavity; the forward and backward propagating TE waveguide modes. The surface wave is supported by a source of radiation coupling to this mode, matching the fields outside the corrugations to the waveguide modes supported within them. However, the ability to support surface waves in this manner is not unique to this structure.

Any array of cavities with subwavelength geometry that individually support a resonance, such as a waveguide mode, can be used as a metamaterial structure that will support a surface wave. The design of that cavity will dictate the limiting frequency of the supported mode. Indeed, this has been shown for a square array of infinitely deep square holes perforating a metallic slab [50], a square array of finite depth square holes [51], a square array of finite depth rectangular holes [67] and other resonant structures such as the Sievenpiper 'Mushroom' structure [68].

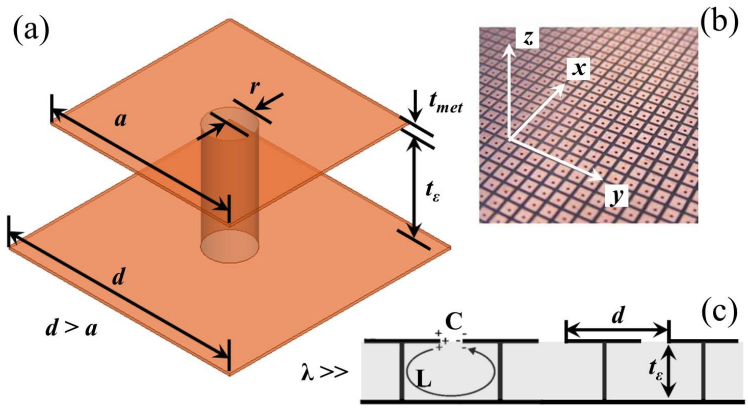

Figure 2.10: (a) Unit cell of Sievenpiper mushroom array. Pitch $d = 1.6$ mm, patch length $a = 1.3$ mm, via radius $r = 0.15$ mm, dielectric thickness $t_\epsilon = 0.787$ mm of Nelco NY-9220 ($\epsilon = 2.2$) and metal thickness $t_{met} = 0.0175$ mm. (b) Photo of a Sievenpiper mushroom array. (c) Schematic of Sievenpiper mushroom structure indicating the physical origin of the inductive (L) and capacitive (C) components of the mode. This is useful when describing a TM surface wave via the impedance (Z) model [68].

Figure 2.10 shows (a) a unit cell of the Seivenpiper mushroom structure, (b) a photo of an array of the Seivenpiper mushroom structure. Figure 2.10 (c) will be discussed in section 2.5.5 Figure 2.10 (a) shows a unit cell of the Seivenpiper mushroom structure, a combination of a metallic ground plane with a dielectric overlayer perforated by an array of metallic vias. A via can be seen in Figure 2.10 (a). The vias electrically connect the ground plane to an array of square metal patches which obtrude from the dielectric layer. This connection supports a resonance when excited by a transverse magnetic polarised wave. Figure 2.10 (b) is a photo of an array of the Seivenpiper mushroom structure. The Seivenpiper mushroom structure is an example of a structure that is not characterised by waveguide modes, unlike the array of grooves or array of holes. A further discussion of this particular structure can be found in Chapter 6

Sievenpiper originally described the resonance supported on an array of mushrooms using the impedance model, which we will now briefly detail as it has been used extensively since the 1950s to characterise surface waves investigated by radio engineers such as Barlow and Cullen [32].

2.5.3 Surface Impedance

The impedance (Z) of the surface supporting a surface wave can be expressed by its real (R) and imaginary components (χ) thus

$$Z = R + i(\chi) \tag{2.60}$$

where χ indicates reactance (Ω) and R is the resistance (Ω). The reactance χ is composed of inductive (L) and capacitive (C) components given by χ_L and χ_C respectively. In free space there is an absence of free charge so the impedance is described by R, equal to 377 Ohms and $\chi = 0$. However, when describing impedance inside a lossy medium the loss mechanisms of that medium are described by both its real (R) and imaginary (χ) components. As such, these loss components are either capacitive or inductive, given by χ_L and χ_C respectively. A surface supporting a mode is termed 'capacitive' if $X_C > X_L$ and 'inductive' if $X_C < X_L$. Figure 2.10 (c) displays the capacitive and inductive components of the Seivenpiper mushroom structure.

Surface impedance Z_s is defined as the ratio between the tangential components of electric and magnetic field at the interface at which a surface wave is confined where

$$Z_s = \frac{E_x}{H_y} \tag{2.61}$$

The concept of surface impedance can be used to derive expressions detailing the dispersion of surface waves, as is seen in

2.5.3.1 Transverse Magnetic Surface Waves

Equation 2.61 is used to describe the surface impedance with respect to a TM wave propagating on that surface. The following expressions have been adapted from 'The Field Theory of Guided Waves' by Collin (1991) [69] and will be briefly outlined here as surface impedance is referred to later in this thesis. First consider the initial boundary conditions by which a TM wave is bound to a surface where $H_x = H_z = E_y = 0$. Electric field in the direction of propagation (Figure 2.6) can be described as

$$E_x = Ce^{-i(k_x x - k_z z + \omega t)} \tag{2.62}$$

where C is a constant describing the time independent component of the mode.

Crucially, the time varying term of the electric field is described as positive ($e^{i\omega t}$), in contrast to most of the literature based in photonics where it is negative ($e^{-i\omega t}$). This positive reference is nomenclature used in most engineering literature surveyed by this author and has direct implications as regards to how a surface is described in terms of it's capacitive or inductive qualities. No physical properties of the surface wave are effected by this change of sign so this derivation continues unchanged.

By applying the Maxwell's relation defined in equation 2.6 (in the absence of

free charge) the electric and magnetic fields can be expressed as

$$i\omega\epsilon E_x = \frac{\delta H_y}{\delta z} \tag{2.63}$$

$$H_y = \frac{-i\omega\epsilon}{k_z} C\, e^{-i(k_x x - k_z z)} \tag{2.64}$$

By substituting equations 2.63 and 2.64 into Equation 2.61, Z_s can be described thus:

$$Z_s = \frac{E_x}{H_y} \quad = \frac{Ce^{-i(k_x x - k_z z + \omega t)}}{\frac{-i\omega\epsilon}{k_z} C\, e^{-i(k_x x - k_z z)}} = \quad -\frac{k_z}{i\omega\epsilon} = \quad \frac{ik_z}{\omega\epsilon} \tag{2.65}$$

By further considering that -$\frac{1}{i} = i$, Equation 2.65 can be stated thus:

$$Z_s = \frac{ik_z}{\omega\epsilon} \tag{2.66}$$

The solution is positive and imaginary therefore, with reference to the original circuit theory model outlined in 2.60 it can be stated that a surface which supports a TM surface wave is inductive as $\chi_L > \chi_C$.

2.5.3.2 Transverse Electric Surface Waves

For completeness it should be noted briefly that this analysis can be extended to describe the condition by which a transverse electric (TE) surface wave is supported. In this case $H_y = E_x = E_z = 0$ and the magnetic field is described as:

$$H_x = C\, e^{-i(k_x x - k_z z + \omega t)} \tag{2.67}$$

By applying Faraday's equation

$$\nabla \wedge \underline{\mathbf{E}} = -\mu \frac{\delta \underline{\mathbf{H}}}{\delta t} \tag{2.68}$$

to equation 2.67 the electric and magnetic components of the surface wave are obtained. However, due to the condition that the surface wave is always considered to be absorbed by the medium, the sign for the impedance (Z) describing a surface supporting a TE surface wave (Z_{TE}) changes in comparison to equation 2.66 to become:

$$Z_{\mathrm{TE}} = -\frac{E_y}{H_x} \tag{2.69}$$

Therefore Z_{TE} is given by:

$$Z_{\mathrm{TE}} = \frac{-i\omega\mu}{k_z} \tag{2.70}$$

Note that the reactance is now negative and imaginary therefore it can be stated that the surface is capacitive and does not support a TM surface wave.

2.5.4 Description of the Surface Impedance Associated with a One-Dimensional Array of Metallic Grooves

Historically, the addition of corrugation to a metallic surface in the form of a one dimensional array of grooves has been understood to support a surface wave as characterised via transmission line theory [69, 46]. This theory uses a parameter called impedance (Z), which is the ratio between tangential electric and magnetic field. Consider again Figure 2.9 and consider the case where height of each groove h is equal to $\frac{\lambda}{4}$. The shaded region noted on the schematic indicates the interface along which the surface wave is confined and consists of metal-air boundaries and air-air boundaries.

With a TM polarised wave impinging upon such a surface the magnetic field is orientated parallel to the groove and the electric field has a component in both the vertical (z) and horizontal (x) directions, as shown schematically Figure 2.9 (black coordinates). The TE mode within the groove (where groove width $a << \lambda$) will propagate to $z = h$ and be reflected by the metallic end which terminates the groove.

The reflection of an electromagnetic wave with a perfectly reflecting surface is known as a 'short' in the engineering community. At microwave frequencies metals are considered to be near perfectly reflecting. When h, the height of the groove, is equivalent to $\lambda/4$ relative to the frequency of the incident electromagnetic wave, a standing wave is set up in a metallic groove. This consists of a convolution of forward (incident) and backward (reflected) propagating waves, described thus:

$$E(z) = E^{inc}e^{-ikz} + E^{refl}e^{ikz} \tag{2.71}$$

$$H(z) = H^{inc}e^{-ikz} + H^{refl}e^{ikz} \tag{2.72}$$

The impedance is defined at the interface (where z = 0) as

$$Z = \frac{E(z=0)}{-(H(z=0)} \tag{2.73}$$

However in the grooves this must be modified to consider the forward and

backward propagation of the mode as follows:

$$\zeta = \frac{E^{inc}(z)}{H^{inc}(z)} = \frac{E^{refl}(z)}{H^{refl}(z)} \tag{2.74}$$

where ζ describes the impedance inside the groove.

Due to the termination of the groove in a short the electric field will fall to zero at z = h. Therefore $\zeta = 0$ and the electric field reverses direction. Consequently the following statement can be made:

$$E^{refl}(z = 0) = -E^{inc}(z = 0) \tag{2.75}$$

By substituting equation 2.76 into equation 2.74 a relation for impedance as a function of groove depth is obtained:

$$\frac{E_{tot}(h)}{H_{tot}(h)} = \frac{E^{inc}e^{-ikh} - E^{inc}e^{-ikh}}{H^{inc}e^{-ikh} + H^{inc}e^{-ikh}} = i\zeta \tan(kh) \tag{2.76}$$

Due to the nature of the tangent function if $h > \lambda/4$ the value of Z_S will be negative, indicative of a capacitive surface upon which TM waves are no longer supported. If h $< \lambda/4$ then the impedance will be positive imaginary and the corrugated surface supports a TM wave.

2.5.5 Physical Origin of the Lumped Circuit Model

The lumped circuit impedance model can be used to describe the surface impedance of a corrugated surface. Indeed, it can accurately be used to model the impedance of any surface which supports a surface wave that has electromagnetic field interaction in the region of space where $z \leq 0$ where z is the label for the vertical coordinate in Figure 2.9. If there are field interactions below $z = 0$, the model is no longer accurate.

The surface impedance is described by

$$Z_s = \frac{i\omega \mathtt{L}}{1 - \omega^2 \mathtt{L\ C}} \tag{2.77}$$

The resonant frequency is expressed as a function of inductance (L) and capacitance (C)

$$\omega_0 = \frac{1}{\sqrt{\mathtt{LC}}} \tag{2.78}$$

The significance of equation 2.77 and 2.78 is the that as $\omega \to \omega_0$, $Z_s \to \infty$. In practice this will never occur as when the impedance of the surface matches that of the free space (377 Ω) the mode is not longer bound to the surface and will scatter into free space. Thus Z_s will never actually be infinite. However, the impedance

model is still used in numerical calculations of the bulk response of resonant arrays as it is computationally inexpensive and is a good approximation of the response of surface wave supporting structures, except at their resonant condition.

In the case of a corrugated surface such as the one dimensional array of grooves shown in Figure 2.9 both L and C can be approximated by considering the unit cell of the groove structure. Each groove can be approximated as the gap between two metallic parallel plate capacitors, negating the end effects of the grooves, and capacitance can be calculated via

$$\mathtt{C} = \frac{\epsilon A}{d_1} \tag{2.79}$$

where A is the area of the face of the strut bordering the groove, d_1 is the separation between the metallic struts and ϵ is the permittivity of the groove medium. In the case of Figure 2.9, the groove is filled with free space only therefore $\epsilon = \epsilon_0$.

In the case of microstrip patch antennas, the capacitance of the structure is given by the fringing electric field between the adjacent metallic patches [30]. This results in a build up of charge at the edges of the patch. When a voltage is applied across the patch the charge on the edges oscillates. As previously detailed, the top layer of a Sievenpiper mushroom array is a layer of patches connected to a conducting ground plane. This is achieved with an array of connecting metallic vias, resulting in the electrical connection of the patches in the top layer.

Observe Figure 2.10 (c). When a voltage is applied across the charge on the edges of the patch layer, oscillating in time, the charge travels the electrical length of the unit cell. This is from the patch to the ground plane through the via and then up to the edge of neighbouring patch and oscillates in response to the applied voltage. This induced current results in an inductive term. Inductance (L) is described thus:

$$V(t) = \mathtt{L}\frac{\delta I}{\delta t} \tag{2.80}$$

where $V(t)$ represents time dependent voltage and I represents current. Figure 2.10 (c) schematically shows this charge build up as well as the inductive and capacitive terms of the individual Sievenpiper elements [70]. An outline of the calculations involving L and C for a Sievenpiper array is further discussed in Chapter 6.

2.5.6 Effective Surface Impedance Model

Expressions for the in-plane wavevector k_x with respect to the impedance of the surface as stated by Equation 2.77 has been derived by Collin [69] and published by Sievenpiper et al. (1999)[68] and is used as a reference for the following derivation.

Consider the form of the electric field in the z direction for a TM surface wave to be represented by Equation 2.62. Using Ampere's law (Equation 2.6 and Faraday's law (Equation 2.68), the other non-zero field components of a TM wave can be found:

$$i\omega\epsilon_0 E_x = \frac{\delta H_y}{\delta z} \tag{2.81}$$

$$i\omega\epsilon_0 E_z = \frac{-\delta H_y}{\delta x} \tag{2.82}$$

$$-i\omega\mu_0 H_y = \frac{\delta E_z}{\delta x} - \frac{\delta E_x}{\delta z} \tag{2.83}$$

These can be solved to find H_y and E_z:

$$H_y = \frac{-i\omega\epsilon_0}{k_z} C e^{-i(k_x x - k_z z) + i\omega t} \tag{2.84}$$

$$E_z = \frac{-i\omega k}{k_z} C e^{-i(k_x x - k_z) z + i\omega t} \tag{2.85}$$

where C is describing the time dependant component of the mode. Combining Equations 2.84 and 2.85 allows a solution for wavevector k_x to be derived:

$$k_x^2 = \mu_0\epsilon_0\omega^2 + k_z^2 \tag{2.86}$$

Combining Equation 2.86 and 2.68

$$Z = \frac{i}{\omega\epsilon_0}\sqrt{k_x^2 - \mu_0\epsilon_0\omega^2} \tag{2.87}$$

$$Z^2 = \frac{-(k_x^2 - \mu_0\epsilon_0\omega^2)}{\omega^2\epsilon_0^2} \tag{2.88}$$

$$\frac{k_x^2}{\omega\epsilon_0^2} = \frac{\mu_0\epsilon_0\omega^2}{\omega^2\epsilon_0^2} - Z \tag{2.89}$$

$$k_x^2 = \epsilon_0\omega^2(\mu_0 - \epsilon_0 Z^2) \tag{2.90}$$

$$k_x^2 = \epsilon_0\omega^2\mu_0(1 - \frac{\epsilon_0 Z^2}{\mu_0}) \tag{2.91}$$

$$k_x^2 = k_{TM}^2 = \frac{\omega^2}{c^2}(1 - \frac{Z_s^2}{\eta^2}) \tag{2.92}$$

where η represents free space impedance. It should be noted that the free space

impedance can be described thus:

$$\eta = \sqrt{\frac{\mu_0}{\epsilon_0}} \tag{2.93}$$

where μ_0 and ϵ_0 is the permeability and permittivity of free space.

The expression for the propagating wavevector of a TE polarised surface wave with respect to impedance can be derived in the same manner as previously seen and is expressed thus:

$$k_{TE}^2 = \frac{\omega^2}{c^2}(1 - \frac{\eta^2}{Z_s^2}) \tag{2.94}$$

where Equation 2.92 and 2.94 indicate the in-plane wavevector of the TM and TE wave with respect to impedance. By inspection of equation 2.92 it is clear that a propagating surface wave can be excited upon a corrugated surface on the condition that $Z_S < \eta$.

2.6 Chapter Summary

This background chapter investigates the origins of the electromagnetic mode known as a surface wave that can be traced through literature to the turn of the last century. Each advancement in understanding of this phenomenon has been highlighted chronologically and the relevant areas of research in association with this is elaborated upon. The mathematical derivation originally proposed as a solution to Maxwell's equations has been detailed for the general solution of a surface wave supported by a metal-air interface. The frequency dependent behaviour of the permittivity associated with a metal such as aluminium has been discussed. The consequence of this behaviour with respect to the confinement of a surface wave to the metal-air interface has been discussed with particular reference to the confinement of a surface wave to this interface at microwave frequencies. Methods for supporting a surface wave at microwave frequencies via subwavelength surface structure have been elaborated upon. This has been done by considering both the effective permittivity model and the impedance model. Expressions for relating the in-plane component of a transverse magnetic and transverse electric surface wave as a function of surface impedance and free space impedance have been detailed along with an explanation as to the origin of surface descriptors of 'inductive' and 'capacitive' surfaces.

Chapter 3

Experimental Methods

3.1 Introduction

As one dimension of a waveguide structure is changed the mode which propagates along or in that structure will be modified. This chapter outlines the experimental, analytical and numerical methods used to ascertain what, if any, effect a change in the dimension of a guiding structure has on the dispersion of the supported mode.

The experiments described in this thesis used the following apparatus: a vector network analyser (VNA); waveguide devices such as coaxial cables; radio frequency (RF) connectors and antennas which emit and receive electromagnetic radiation. The antenna used to measure the electric field of the surface wave is a stripped coaxial wire and is referred to as a 'probe' throughout this chapter. The functionality of these devices is elaborated upon. Further detailed is the architecture and operation of the VNA to highlight the attributes associated with the instrument.

The method of experimentally determining the dispersion of a surface wave supported by a metamaterial surface is detailed via the use of the aforementioned pieces of equipment. The electric field associated with the supported mode can be mapped, enabling observation of changes in amplitude and phase associated with the spatial position of the mode. A brief discussion detailing the mechanisms involved in the excitation and measurement of a surface wave is included. References as to the methods employed to excite and measure surface waves during the investigations detailed in Chapters 4, 5 and 6 are also included.

To support the conclusions reached in this thesis via experimental methods both analytical and numerical methods are used to provide comparative analysis. Both analytical and numerical methods are discussed and compared to each other.

3.2 Apparatus

3.2.1 Functionality of a VNA

Experimental investigation of laterally confined surface waves is achieved throughout this study using a Vector Network Analyser (VNA). The VNA is known as a *VectorStar MS4640A*, manufactured by Anritsu, and operates between 70 KHz and 70 GHz and is an AC source. A VNA is capable of indirectly measuring both the amplitude and phase information of an electric field associated with a surface wave. The loops of electric field associated with the supported surface wave, as previously shown in Figure 2.5, induce current in the field profile of an antenna connected to a VNA. The current generates a voltage which is measured by the VNA. The voltage generated by the induced current is assumed to be linear with field strength, hence an approximation as to the strength of the a measured field is made.

The voltage measurement is processed digitally, resulting in real and imaginary parts (I and Q pairs, respectively) of the original signal. The time-averaged electric field, otherwise known as the amplitude of the electric field ($\mathbf{A}$), can be expressed via the I and Q values thus:

$$\mathbf{A} = I^2 + Q^2 \tag{3.1}$$

Although measurement of time-average electric field is one of the many products of I and Q pair mathematics, it is used throughout this work as the primary indicator of the magnitude of the electric field strength.

A VNA internally generates a voltage resulting in a radio frequency (RF) signal that is sampled, transmitted and compared to the signal from the detected voltage. When a VNA is connected to an antenna, the voltage generated by the induced current A VNA internally generates a radio frequency (RF) signal which is sampled by the device in both the transmission and detection processes. This sampling enables comparison of transmitted and detected signals, resulting in a local phase measurement as a function of frequency. The sampling process is further elaborated upon in Section 3.2.4, as well as the production of I and Q pairs. Technical documents provided by three VNA manufacturers (Anritsu, Agilent and Rohde & Schwarz) are used as the basis for the following explanation of VNA architecture and operation and can be found in references [71, 72, 73]. Understanding of VNA functionality identifies why it is an ideal instrument for use in the investigations detailed in this thesis.

A VNA measures scattering parameters (S-parameters) on a two port system. The term 'scattering parameters' originates from transmission line terminology and describes the results of an electromagnetic wave propagating through free space

and experiencing a region of space which can no longer be considered a vacuum. This term is synonymous with the term *S*-matrix and is used to describe reflection and transmission measurements. A 'port' is the adaptor from which the RF signal internally generated by a VNA is converted into a transverse electromagnetic (TEM) mode. Specifically, the port associated with the *VectorStar MS4640A* connects to a V-type coaxial cable which transports the RF signal for use with some other device (i.e. an antenna). The path by which an RF signal is transmitted and detected, including interaction with the sample under test is further referred to as the 'electrical length'. An example of the experimental system is shown in Figure 3.1 (left) to illustrate the system during initial explanation of components. Included in this figure is the antenna used to measure the electric field associated with a surface wave: a stripped coaxial wire labelled as a 'probe'. More discussion as to the effect of the probe on measurement of the surface wave and the length of the exposed wire is included in section 3.6.2. An example of the composition of a coaxial cable has also been included (right).

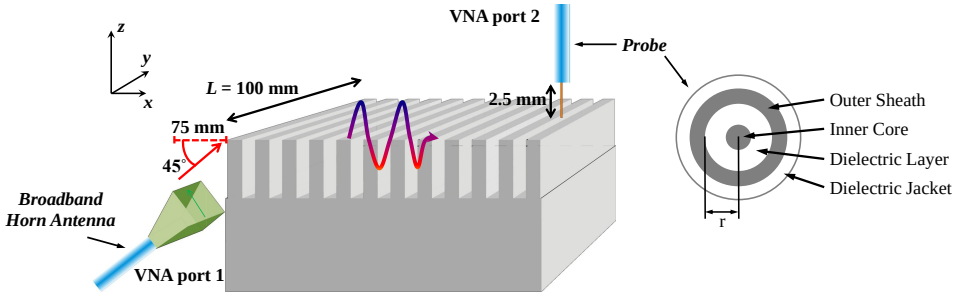

Figure 3.1: Schematic of typical measurement system (left) including detecting probe and emitting broad band horn antenna. (Right) schematic of the compositions of a coaxial wire.

3.2.2 Functionality of Equipment

Before experimentally investigating the frequency response of a surface it is vital that equipment used is specified to operate over the frequency range of interest. For example a coaxial cable connecting to a broadband horn antenna may not operate in the same frequency range, a characteristic which is dictated by the internal structure of the cable and the horn.

A coaxial cable supports a transverse electromagnetic (TEM) mode and is composed of three layers: a metallic solid cylindrical inner core, a layer of dielectric which coats the core and a metallic sheath which coats the dielectric layer [41]. These three layers are often coated once more in a dielectric jacket to protect the rigidity of the cable and the continuity of the TEM mode within. The radius between the inner core and outer sheath dictate the frequencies at which RF signal

can propagate along the cable without gross loss of signal.

RF equipment seldom operates over the large range of frequencies achievable with a VNA. It is more common to have equipment which uses a small band of possible frequencies within the spectrum produced by the VNA. Therefore signal from the 1.85 mm radius (V-type) coaxial cables which connect directly to the *VectorStar MS4640A* must be adapted for use with coaxial connectors of a different radius between the inner and outer sheaths. These connections often result in a reflection along the electrical length of the system but can be accounted for by calibration of the VNA and other equipment used in an experiment.

3.2.3 VNA Calibration

There are several sources of systematic error which are inherently present in every VNA measurement. These are:

• Crosstalk between the ports (unwanted transfer of signals between components) which bypasses interaction with the sample under test.

• Reflections from any connection along the electrical path the RF signal takes including the emitting port to coaxial cable connection and the coaxial cable connected to any other adaptor, connector or antenna.

• Loss to any amplitude measurements due to propagation along an electrical length that is not included in the architecture of the VNA. This includes coaxial cables, connectors and adaptors.

• Deformities in cables such as kinks resulting in loss of transmission at particular frequencies.

These errors result in unstable and non-repeatable amplitude measurements resolved by the VNA but can be removed from the measurement process via a calibration known as a 'SOLT', as is detailed in [72, 71] as well as the following paragraph.

A SOLT calibration normalises out systematic error by connecting calibration standards directly to the end of a coaxial cable or adaptor. The calibration standards simulate terminating boundary conditions called a 'short', 'open', 'load' and 'through' terminations. These are more commonly referred to as total reflection, free space termination, total absorption and total transmission measurements respectively. Total absorption is also known as a 'match'. The impedance (Z) inside a coaxial cable is 75 Ω where

$$Z = \frac{\mathbf{E}}{\mathbf{H}} \tag{3.2}$$

The calibration standards attached to coaxial cables are used determine the response of an electromagnetic mode travelling along the electrical length of the system to be met by the aforementioned boundary conditions. For example, the

calibration standard of a 'short' consists of a metallic termination placed a known distance from the aperture of the standard and at a known orientation. The VNA is preprogrammed with this distance and as such is also preprogrammed with the expected response of an RF signal at frequency in its range travelling this distance under lossless conditions. Therefore, when the VNA generates a frequency which will match perfectly a $\frac{\lambda}{4}$ condition and has already sampled the amplitude and phase of that generated signal, the VNA will expect to detect 100% of the RF signal reflected and a π change in phase. In practice a system is never totally without loss so the VNA will not detect 100% of the transmitted signal, there will be some offset in amplitude and phase. However, due to this process the VNA can reference how much loss is in the system via the measured offset and apply that offset to future measurements, calibrating out systematic errors. The same logic applies for the termination standards of 'open' and 'load', a separate offset is measured for each standard and applied to any further measurement the VNA records after calibration. This normalises out the systematic response of the equipment used in experiments and is polarisation independent. This normalisation is valid up to and including the ends of the cable to which the calibration standards were attached.

A broad band dual polarisation horn antenna is employed in experiments with a dynamic range of 8 and 40 GHz [74] to achieve planar excitation along a metallic edge, as is discussed in section 3.3. It is attached to a coaxial cable via a 2.4 mm connector and is composed of a square waveguide horn antenna and waveguide coaxial adaptors built as a single unit [75]. This broad band horn antenna is preferred over other standard gain horn antennas as electromagnetic modes of interest to this thesis are often measured over frequency ranges larger than the dynamic range available to a standard gain horn antenna. The historical significance of corrugated horn antennas can be found in Section 2.2.3.1.

3.2.3.1 *S*-Parameters

A VNA represents transmission and reflection measurements between two ports as *S*-parameters, a measure of the ratio between the amplitude of transmitted and detected signals noted by the constants 'a' and 'b', respectively.

The VNA used in this thesis is a two port continuous wave (CW) device which measures reflection at each port and transmission between ports. Due to the CW nature of the device, transmission and reflection can be measured simultaneously as long as the port emitting the signal is the same for both measurements. The notation S_{XY} denotes the type of measurement taking place. In this case X and Y can be integers 1 or 2 (the port number) where X indicates which port the signal is travelling to and Y indicates which port the signal is travelling from. Reflection

measurements are defined thus:

$$S_{11} = \frac{\texttt{Detected (Port 1)}}{\texttt{Transmitted (Port 1)}} = \frac{b_1}{a_1}, a_2 = 0 \tag{3.3}$$

$$S_{22} = \frac{\texttt{Detected (Port 2)}}{\texttt{Transmitted (Port 2)}} = \frac{b_2}{a_2}, a_1 = 0 \tag{3.4}$$

Transmission measurements are defined thus:

$$S_{21} = \frac{\texttt{Detected (Port 2)}}{\texttt{Transmitted (Port 1)}} = \frac{b_2}{a_1}, a_2 = 0 \tag{3.5}$$

$$S_{12} = \frac{\texttt{Detected (Port 1)}}{\texttt{Transmitted (Port 2)}} = \frac{b_1}{a_2}, a_1 = 0 \tag{3.6}$$

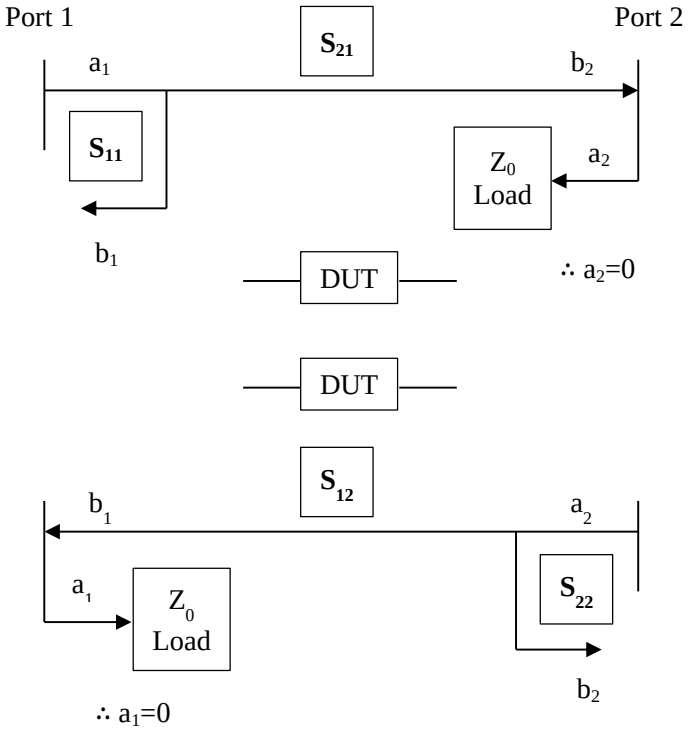

Figure 3.2: Schematic of direction of propagation between ports 1 and 2, adapted from 'Agilent Network analyzer basics' [72]. Constants 'a' and 'b' represent the magnitude of the transmitted and detected signal. The device under test (DUT) is shown as part of the electrical path between port 1 and port 2 while the direction of propagation is shown by the arrows in the schematic for measurements of S_{11}, S_{21}, S_{12} and S_{22}.

Figure 3.2 details the measurement of S_{21}, S_{11}, S_{22} and S_{12}. Note for S_{21}, signal transmitted from port 1 and detected on port 2 results in $a_1 \Rightarrow b_2$. Further, the receiving port (in this case 2) terminates the transmission signal a_2 with an absorber with impedance matched to free space (377 Ω). Signal transmitted from

port 2 and detected on port 1 undergoes the inverse of the operation previously explained.

First consider measurements of S_{21} and S_{11} and define a forward measurement as a wave travelling from port 1 to port 2. Port 1 acts as a source of radiation so that $a_1 \neq 0$. The transmitted wave is represented by the coefficient b_2 and port 2 is terminated so that there is no reflection from the port back to port 1. This termination is known as a 'load' or a 'match' and can be considered to be a perfect absorber so that $a_2 = 0$. The only reflection present in the system is from port 1, hence a measurement of S_{11} can be made. For the reverse measurements of S_{12} and S_{22}, $a_1 = 0$ and port 1 is stimulated by port 2.

Phase with respect to frequency is plotted as an S_{21} plot and labelled with the nonmenclature describing the type of parameter measured (S-parameter). The numbering system denotes which port acted as a detector (first number) and which acted as a source (second number). In this case the radiation travelled from port 1 to port 2, hence the label 'S_{21}'.

3.2.4 VNA Architecture

The *VectorStar MS4640A* is described as a heterodyne N-port network analyser where N denotes the number of ports in operation. The concept of heterodyning will be elaborated upon shortly.

A VNA has four key operational components: a generator to produce and reference an RF signal, ports which transmit and detect the RF signal, receivers for referencing the RF signal and a computer with a user interface and remote control interfaces. Section 3.2.3.1 has already discussed the measurements undertaken at the ports and the operation of a user interface is outside the scope of this thesis. However, as the phase measurement capabilities of the *VectorStar MS4640A* have been an intrinsic part of investigations detailed within this thesis a discussion now follows briefly detailing the operation of both the generator and receivers in the VNA.

3.2.4.1 Generator

Microwave radiation is generated within the *VectorStar MS4640A* using a yttrium-iron-garnet oscillator and varactor-tuned voltage oscillator or a oven controlled crystal oscillator (OCXO) for low and high frequency components present in the VNA spectrum (respectively). These voltage controlled oscillator (VCO) sources produce the sinusoidal stimulus that is the RF signal. To ensure the required frequency stability this oscillator is embedded in a phase locked loop (PLL). A PLL is composed of combining a VCO with a phase comparator so that the oscillator

maintains a constant phase angle relative to a reference signal [76, 77, 78].

In this way it is possible to maintain the generated wave (for example a_1 from Figure 3.2) within an error correction of 0 dBm $\pm$ 0.3 dBm. By using a power splitter on a signal from the generator with an amplitude $2a_1$ a reference measurement is made. The signal is split symmetrically so that half travels to a test port for outgoing S-parameter measurements while the other half is directed to a reference receiver so that the phase of a_1 on transmission is known.

3.2.4.2 Receivers

Mixing an input frequency (F_{RF}) with a known and internally generated frequency associated with a local oscillator (F_{LO}) to produce two other frequencies is a process called heterodyning and was first introduced by Reginald Fessenden in 1902 [79]. The term is composed of two greek words for 'different' and 'force'. With this method the phase and amplitude of the input signal is recorded at the receivers used to reference the transmitted signal and receivers used to reference the detected signals. Figure 3.3 is adapted from 'Fundamentals of a Vector Network analyser' published by Rohde and Schwarz and written by M Hiebel (2008) [73].

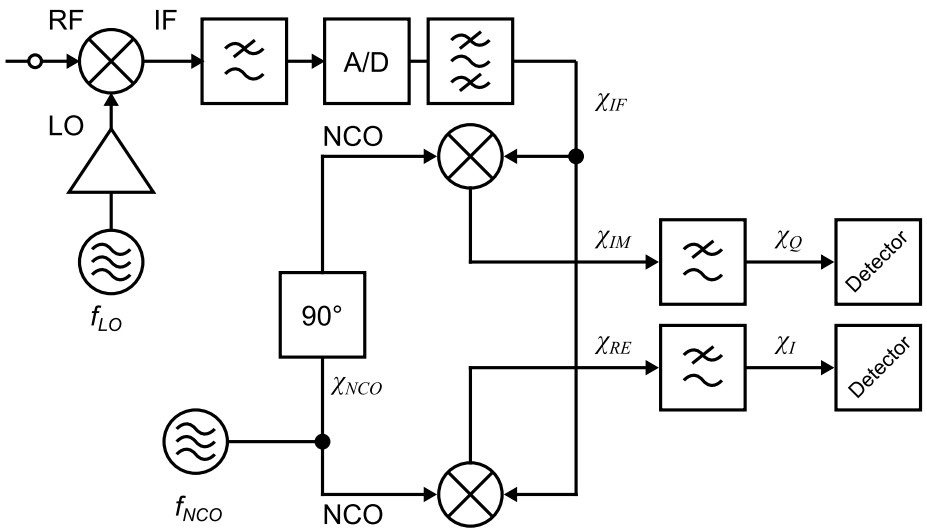

Figure 3.3: Block diagram of a heterodyne VNA reciever, adapted from 'Fundamentals of a Vector Network analyser' [73].

Figure 3.3 is adapted from [73] to show a block diagram of the operations associated with a receiver used in a VNA to produce phase measurements via the process of heterodyning. The principle states that when two frequencies A and B are combined, a product of this mixing is a signal with frequency A minus B and

A plus B [80]. This is based on the following trigonometric identity:

$$\sin\theta \sin\phi = \frac{1}{2}\cos(\theta - \phi) - \frac{1}{2}\cos(\theta + \phi) \tag{3.7}$$

In the case of heterodyne receivers the identity in Equation 3.7 is used twice, once to convert input signal F_{RF} to some intermediate frequency (F_{IF}) where F_{IF} = $|F_{RF} - F_{LO}|$ and again to produce a DC signal for analysis. In both cases the receiver filters out the higher frequency product of Equation 3.7 (i.e. the right hand side of the equation with terms $\theta + \phi$) and uses the lower frequency product. This process is known as 'down conversion'.

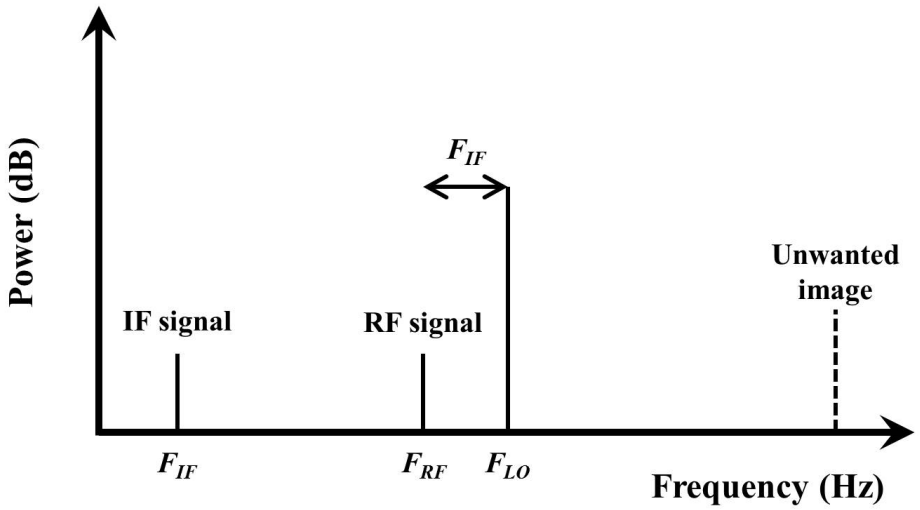

Figure 3.4: Schematic representation of F_{IF} produced when mixing F_{RF} and F_{LO}. Down conversion results in $F_{IF} = |F_{RF} - F_{LO}|$. The higher frequency component produced by the mixing is labelled as an unwanted image in this schematic. In practice, this component is suppressed with a filter.

Figure 3.4 is a schematic representation of the first use of heterodyning, clearly showing F_{IF} and an unwanted image produced when F_{RF} and F_{LO} are mixed. Once the analogue F_{IF} is produced, it is sent to an analogue to digital converter. This digital signal in indicated in Figure 3.3 as χ_{IF}.

The second use of heterodyning is now employed. A numerically controlled oscillator (NCO) generates a sinusoidal frequency (F_{NCO}) equivalent to χ_{IF}. F_{NCO} and χ_{IF} are mixed and χ_{IF} and χ_{NCO} (F_{NCO} phase shifted by 90 deg) are mixed to produce χ_{Re} and χ_{IM} thus:

$$\chi_{Re}(t) = \frac{1}{2}A_{IF}A_{NCO}\left[cos(\Phi_{IF}) + \cos[4\pi F_{NCO}t + \Phi_{IF})\right] \tag{3.8}$$

$$\chi_{IM}(t) = \frac{1}{2}A_{IF}A_{NCO}\left[\sin(\Phi_{IF}) - \sin[4\pi\chi_{NCO}t + \Phi_{IF})\right] \tag{3.9}$$

This process is known as I/Q demodulation and is typical in most digital signal processing techniques designed to measure phase. A lowpass filter suppresses the frequency components where F $\neq 0$ and the low frequency signals denoted in Figure 3.3 as the real χ_I and imaginary χ_Q are produced. They are known as the 'inphase' and 'quadrature' components respectively.

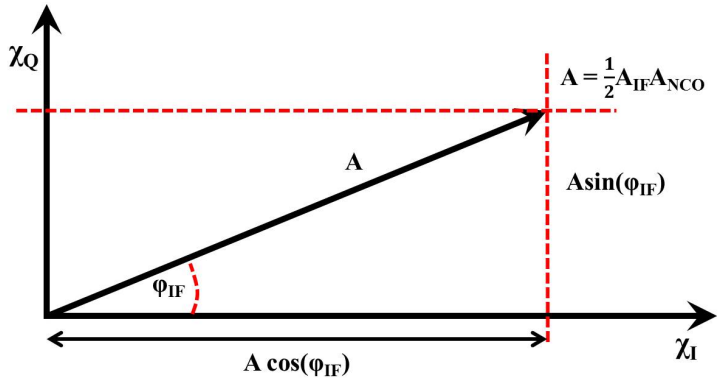

Figure 3.5: Schematic representation of real χ_I and imaginary χ_Q products of digital signal processing in a heterodyne receiver. **A** is the amplitude of the original signal a_1.

By examining Figure 3.5 the benefit of obtaining χ_I and χ_Q is clear. The phase of the intermediate frequency (Φ_{IF}) and the amplitude (**A**) of the incident wave is obtained. The phase difference obtained by receivers associated with transmission and detection ports results in a known local phase difference. The local phase difference between transmission and detection is indicative of the possible dispersive effects experience by the RF signal along the path travelled such as is present in a surface wave measurement.

Discussed thus far is the generation of an RF signal from a source, the transit of an RF signal from the generator to the ports (i.e. the test set), the interaction of that signal with a sample and a port receiving reflected or transmitted signal. The measurement and referencing of the signal received has also been detailed. Finally, the result of these processes are outputted onto a graphical interface. Graphs of amplitude and phase of electric field as a function of frequency can be displayed on the screen. Other products from the post-processing of these two fundamental measurements are also available to the user such as power, impedance and group delay [73].

3.3 Experimental Techniques

Experimental determination of dispersive behaviour associated with a surface wave supported by a metamaterial surface is detailed within this section. Further, the

spatial mapping of the electric field amplitude associated with the supported mode is discussed and employed as a tool for comparison of different methods used to excite the surface wave. The methods by which surface waves are excited and detected are discussed.

3.3.1 Experimental Setup

All measurements of the amplitude and phase of surface waves detailed in this thesis are conducted with a vertically oriented coaxial wire. This coaxial wire has an exposed inner core of wire stripped of both the surrounding dielectric layer and the outer sheath. This device is further referred to as a 'probe'. When the length of exposed inner core of wire corresponds to the $\frac{\lambda}{4}$ condition, the wire supports a resonant mode and may interfere with the measurement of the surface wave. The probe used in all measurements has been engineered so that the probe is resonant at the $\frac{\lambda}{4}$ condition above the limiting frequency of the surface wave. Therefore perturbation of the surface wave via measurement by the probe is negligible. Perturbation of the surface wave due to the scattering cross section of the probe is discussed in due course.

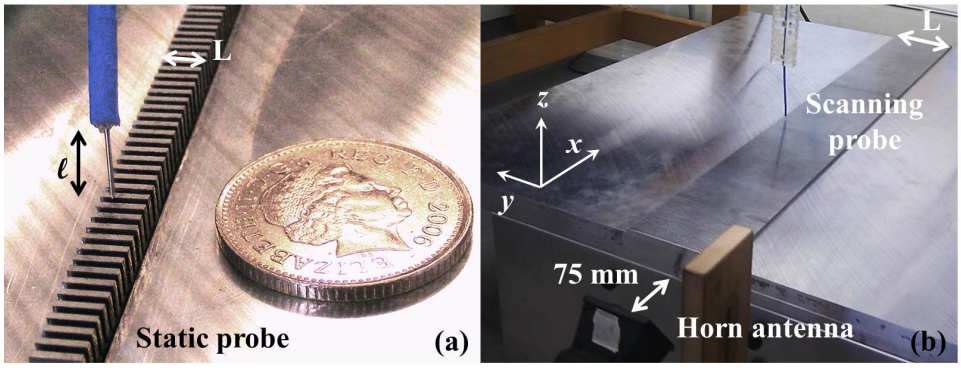

Figure 3.6: Photographs of detecting probe positioned above 1D array of grooves. Two samples of widths (a) $L = 5$ mm and (b) $L = 100$ mm are shown. (a) The method of obtaining experimentally determined dispersion measurements as detailed in Section 3.3.2 is shown. A detecting probe is maintained at a static position above the mid-point of L while the local electric field associated with the supported surface wave is measured as a function of frequency. (b) The method of detecting spatially varying fields associated with the supported surface wave. A probe varies in position in the xy-plane but remains static in z, measuring the fields associated with the supported surface wave at single frequencies as a function of distance. In both cases a broadband horn antenna is used to excite the surface wave via edge-coupling.

A *VectorStar MS4640A* VNA is used to measure S_{21} transmission between a transmitting broad band horn antenna and a detecting coaxial wire probe.

Figure 3.6 (a) and (b) are photographs of the position of the probe used for (a) experimentally determined dispersion of a surface wave and (b) direct measurement of the local electric field amplitude and phase associated with the supported surface wave at different spatial positions to achieve field mapping. The probe with exposed wire length l is oriented vertically directly above the supporting surface in both cases. To achieve mapping of electric fields with respect to spatial position, the detecting probe is simply scanned across the surface via a computer-controlled XYZ-stage in the xy-plane, remaining static in z. To ensure the probe is stationary during each measurement a lag time of 0.5 seconds is enforced between movements during the mapping process. In Figure 3.6 this surface is an array of 1-D corrugations of width $L = 5$ mm (a) and $L = 100$ mm (b).

Figure 3.6 (b) shows a transmitting microwave broad band horn antenna used to excite the surface wave via 'edge-coupling'. The horn is orientated such that it lies in the xz-plane and directs TM polarised microwave radiation at the edge of the corrugated sample and is pitched at an angle of approximately 45 deg with respect to the xy-plane. This minimises crosstalk between the horn and detector while irradiating the edge of the sample with TM polarised radiation of approximately uniform intensity. As a result diffraction occurs along the edge and evanescent field components of electric field with in-plane wavevector $k_x > k_0$ (wavevector associated with free space) become available, exciting a surface wave. The broad band horn is placed a distance of 75 mm away from the edge of the sample and irradiates the edge of the sample approximately uniformly, exciting a surface wave mode. This coupling method was successful and regardless of the width of the sample edge a surface wave was excited. Therefore no further investigations as to coupling strength were conducted with respect to the strength of the mode excited as the method proved more than adequate. Comparisons between excitation methods are made shortly in Section 3.7.

Figure 3.7 shows a schematic of this setup. The orientation of the electric field emitted from the horn as well as both the pitch and yaw of the broad band horn antenna is indicated. The possible frequency response of the cables are calibrated out of the measurement (as detailed in Section 3.2.3) so that amplitude and phase can be measured over a range of frequencies with the lowest possible level of systematic noise.

3.3.2 Dispersion Measurement

3.3.2.1 Phase as a Function of Frequency

A VNA measures phase as a function of frequency via the aforementioned processes of heterodyning and frequency mixing, previously detailed in Section 3.2.4. Due to

the calibration process outlined in Section 3.2.3, the frequency and phase response of the electrical length included in the calibration is known. However, the total electrical length of the system extends further than the point at which calibration occurred (at the end of the coaxial wires). Therefore systematic errors in the measurement process external to the VNA which effect the determination of the dispersion associated with a surface wave are not removed from the measurement via a SOLT calibration.

Figure 3.7 is a schematic of the method used to calibrate the dispersion measurement, in addition to a SOLT calibration already completed. The points at which the calibration standards were attached are noted on Figure 3.7 via the grey dotted lines. These define the calibration planes of the system via SOLT calibration.

Edge-coupling is used to excite a surface wave on an array of corrugations in the form of a metallic one dimensional array of grooves and a free space wave on an untextured metallic slab propagating from the edge of the slab to the detecting probe. These two systems are shown schematically by Figure 3.7 (a) and (b), respectively. The probe is maintained in a static position of 775 mm in the x-direction away from the edge associated with diffraction from the beam transmitted by the horn antenna. The probe is maintained at $z = 0.25$ mm above the samples in the air region as observed in Figure 3.7. By comparison of the phase response of these two systems, the effect of edge coupling and the measurement of the surface wave mode is negated. The system is calibrated over the full electrical length of the RF signal measured. This calibration is subject to the orientation of both the broad band horn antenna and the probe used to measure the surface wave remaining unchanged when used to edge-couple to either the array of corrugations or the untextured metal slab. The surface wave calibration and dispersion measurement is now detailed.

Figure 3.8 displays an example of the phase of a surface wave on a metasurface measured as a function of frequency via the method shown in Figure 3.7 (a). As the phase oscillates between $\pm\pi$ the gradient of the phase is negative due to the time dependent term of the electric field being described as $e^{i\omega t}$ as opposed to $e^{-i\omega t}$. The difference is a simple sign convention and has no bearing on the measurement of phase which, as expected, oscillates between $\pm\pi$ more frequently at higher frequencies.

Now consider Figure 3.9 where an example of the phase as a function of frequency detected by the probe from the static position over (a) a metal slab and (b) a surface wave is compared. The phase associated with the surface wave oscillates between $\pm\pi$ more frequently at a higher frequency than the phase of the free space wave over the same frequency range. This is because the wavevector measured in

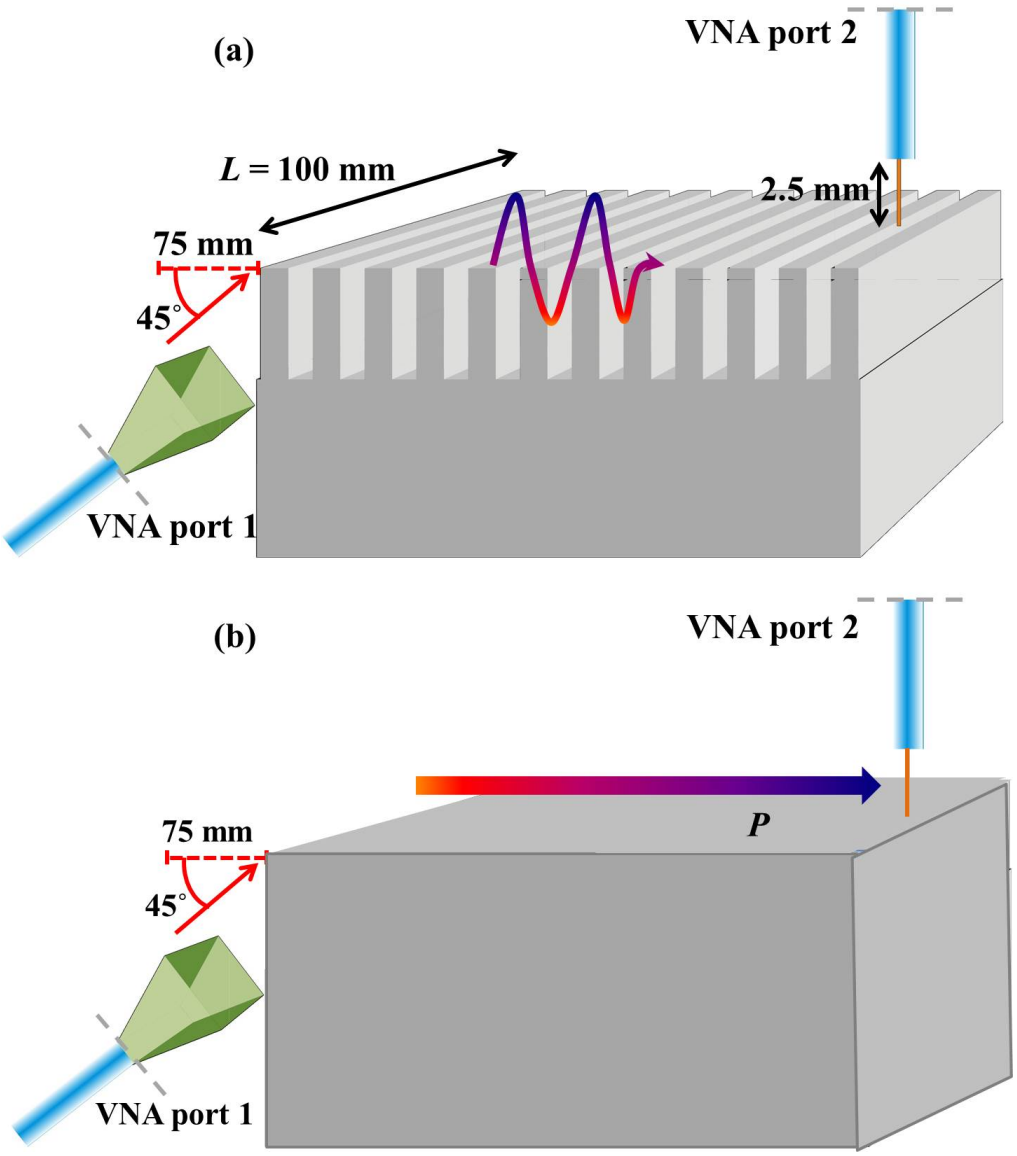

Figure 3.7: Schematic of (a) surface wave (b) free space wave (coloured arrows) reference measurement. (a) shows the excitation of a surface wave which is supported by an array of metallic corrugations via edge-coupling. (b) the excitation of an unconfined free space wave propagating along a planar, untextured metallic slab (synonymous with a grazing photon) via edge-coupling. Both surface wave and free space wave are detected by a static probe at 775 mm away from the diffracting edge maintained at a height of 0.25 mm above $z = 0$ in the air region at the mid point of L. The grey dashed lines indicate the points at which the calibration standards were attached during a SOLT calibration.

Figure 3.9 (b) is no longer associated with a free space wave and is indicative of the wavelength of the surface wave bound to the supporting interface. As a result, the wavelength of the surface wave will decrease in comparison with the wavelength of the free space wave.

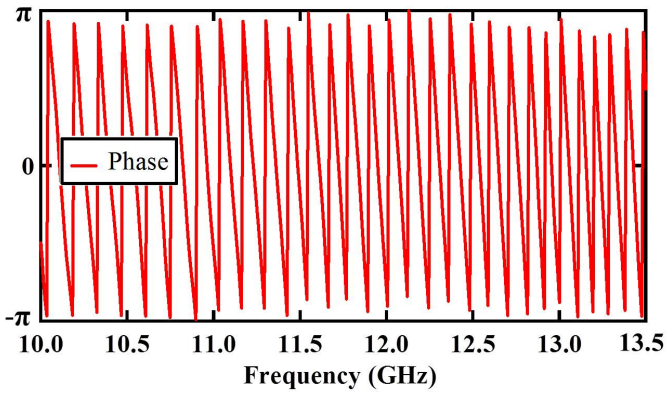

Figure 3.8: Measured phase associated with a surface wave plotted as a function of frequency. The surface wave is supported by a $L = 10$ mm array of open-sided metallic corrugations, described as a domino array in Chapter 4. The measurement is taken by a probe maintained at a static position 0.25 mm above the mid-width of the array.

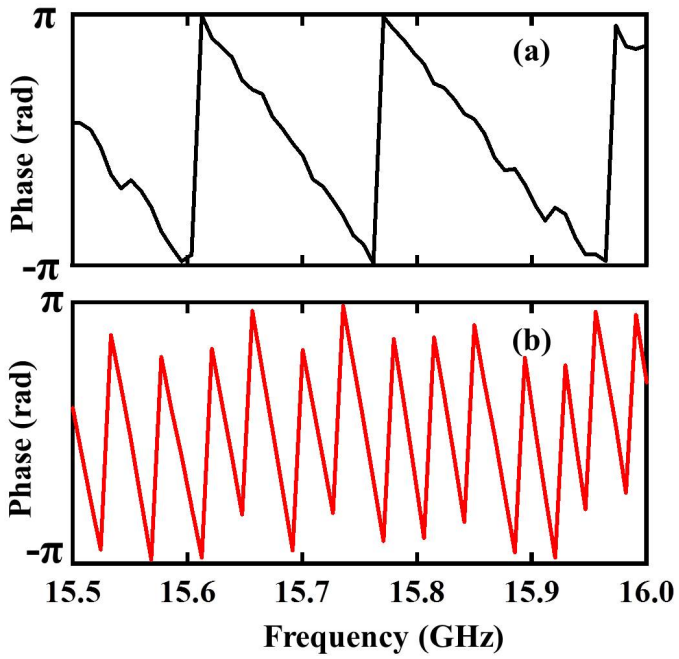

Figure 3.9: Measured phase plotted as a function of frequency associated with (a) an unconfined free space wave propagating along a planar metallic sheet and (b) a surface wave supported by a $L = 10$ mm array of open-sided metallic corrugations, described as a domino array in Chapter 4. The frequency range of 15.5 to 16.0 GHz is near the limiting frequency (18.7 GHz) of the surface wave supported by these corrugations. Both free space wave and surface wave are excited via edge-coupling and detected by a static probe at 775 mm away from the diffracting edge. The probe is maintained at a height of 0.25 mm above $z = 0$.

3.3.2.2 Modal Index

The relationship between the wavevector 'k' and phase Φ is

$$\Delta\Phi = \Delta k P \tag{3.10}$$

where $\Delta\Phi$ is the phase of the wave over some distance P and k is the wavevector associated with the wave. For the dispersion measurements detailed in Chapter 4, P = 775 mm and $\Delta\Phi \Rightarrow \Sigma\Phi$ where $\Sigma\Phi$ is the total phase of the surface wave cumulatively added over a frequency range. A full discussion of the cumulative addition of phase will follow in due course.

Figure 3.10 has been included to illustrate Equation 3.10. It is a measurement of phase associated with a surface wave supported by a metamaterial surface (as detail in Chapter 6) at a fixed frequency of 15 GHz as a function of distance from the source, which is at x = -200 mm. By inspection of Figure 3.10 it is clear that when $P = \lambda$, $\Delta\Phi = 2\pi$ since $k = \frac{2\pi}{\lambda}$.

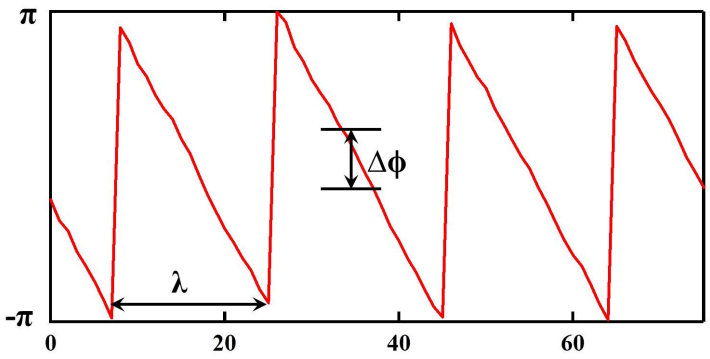

Figure 3.10: Phase of a surface wave supported by a metamaterial surface at a fixed frequency of 15 GHz as a function of distance from the source where $\Delta\Phi$ is some difference in phase and λ is surface wave wavelength. The source is positioned at x = -200 mm with a probe used to detect the surface wave scanned in the positive x-direction.

Figure 3.10 demonstrates the measurement of the wavelength of a mode. Consequently, by measuring and comparing the wavelength of a free space wave (λ_0) with that of the surface wave wavelength (λ_{SW}) the modal index (n) can be measured. Modal index is described thus:

$$n = \frac{\lambda_0}{\lambda_{SW}} \tag{3.11}$$

This measurement is later used in Chapter 5

3.3.3 Unwrapped Phase and Dispersion Measurement

A measurement of phase as a function of frequency can be used to determine the dispersive behaviour of a surface wave. First, the mode is measured over a given frequency range by a probe set at a static position in proximity to the supporting interface. The phase measurement is then 'unwrapped' in post processing. The 'unwrap' function cumulatively sums the phase as a function of frequency over the period of 2π so that it no longer oscillates between $\pm\ \pi$. The unwrap function is applied to the phase measured over the full frequency range and is further referred to as $\Sigma\Phi$. Examples of raw phase and the unwrap function will now be shown.

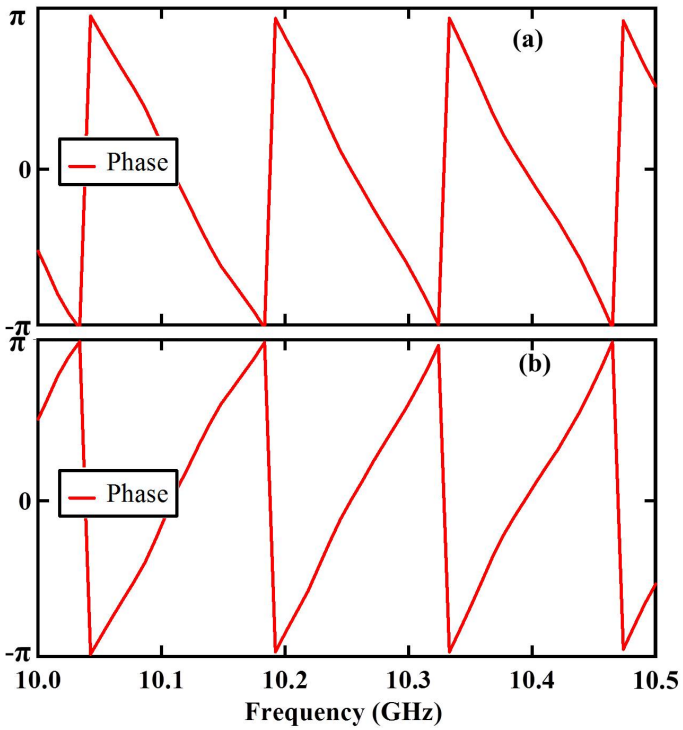

Figure 3.11: (a) Experimentally obtained phase associated with a surface wave plotted as a function of frequency. The surface wave is supported by a $L = 10$ mm array of metallic corrugations. (b) Phase of the surface wave multiplied by -1 resulting in a positive gradient of phase (between $-\pi$ to π).

Figure 3.11 displays phase as a function of frequency over a smaller frequency range than has previously been displayed in Figure 3.8. Note the negative gradient of the phase in Figure 3.11 (a). As has previously stated, this is due to the time dependent term of the electric field being defined as $e^{i\omega t}$. For the purposes of measuring dispersion, the phase is multiplied by -1 so that the change of gradient of the phase when unwrapped will be positive. This change of gradient is shown in Figure 3.11 (b).

Figure 3.12 is an example of the phase unwrap function. To measure the dispersion of the mode the phase associated with the surface wave is unwrapped

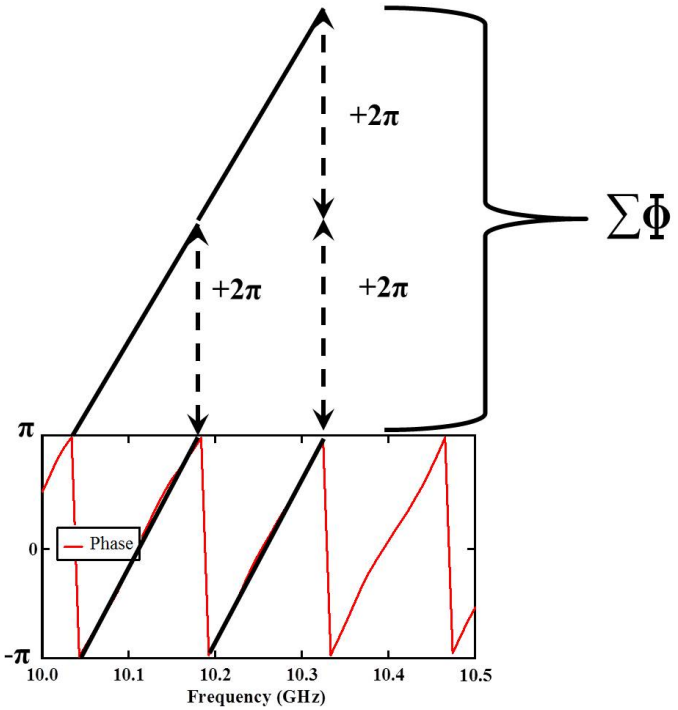

Figure 3.12: An example of a phase unwrap as a function of frequency. The overlaid black line illustrates the positive gradient of phase. Phase is cumulatively added over every period of 2π. The total phase unwrapped is noted as $\Sigma\Phi$.

and compared to the measured unwrapped phase of a free space wave propagating over a metal slab. These two systems have been shown in Figure 3.7 as schematics (a) and (b).

The phase of the wave measured with the setup shown in Figure 3.7 (b) will result in a line of constant gradient as a function of frequency, as shown in Figure 3.13 (a) (black line). Conversely, $\Sigma\Phi$ of the phase associated with the surface wave measured in setup shown in Figure 3.7 (a) will have a change of gradient as a function of frequency due to the dispersive nature of the surface wave, Figure 3.13 (a) (red line).

$\Sigma\Phi_{\texttt{Metal}}$ associated with the free space wave is subtracted from $\Sigma\Phi_{\texttt{Surface Wave}}$ associated with the surface wave. These two measurements are shown schematically in Figure 3.7 (a) and (b). The difference between the two unwrapped phases $\Sigma\Phi_{\texttt{Diff}}$ is expressed thus

$$\Sigma\Phi_{\texttt{Diff}} = \Sigma\Phi_{\texttt{Surface Wave}} - \Sigma\Phi_{\texttt{Metal}} \tag{3.12}$$

Note that the measurement of phase of both the free space wave and the surface wave includes the whole electrical length of the system, past the calibration planes of the SOLT calibration as is noted by the grey dashed lines in Figure 3.7. Therefore any phase effects directly related to initial excitation and detection

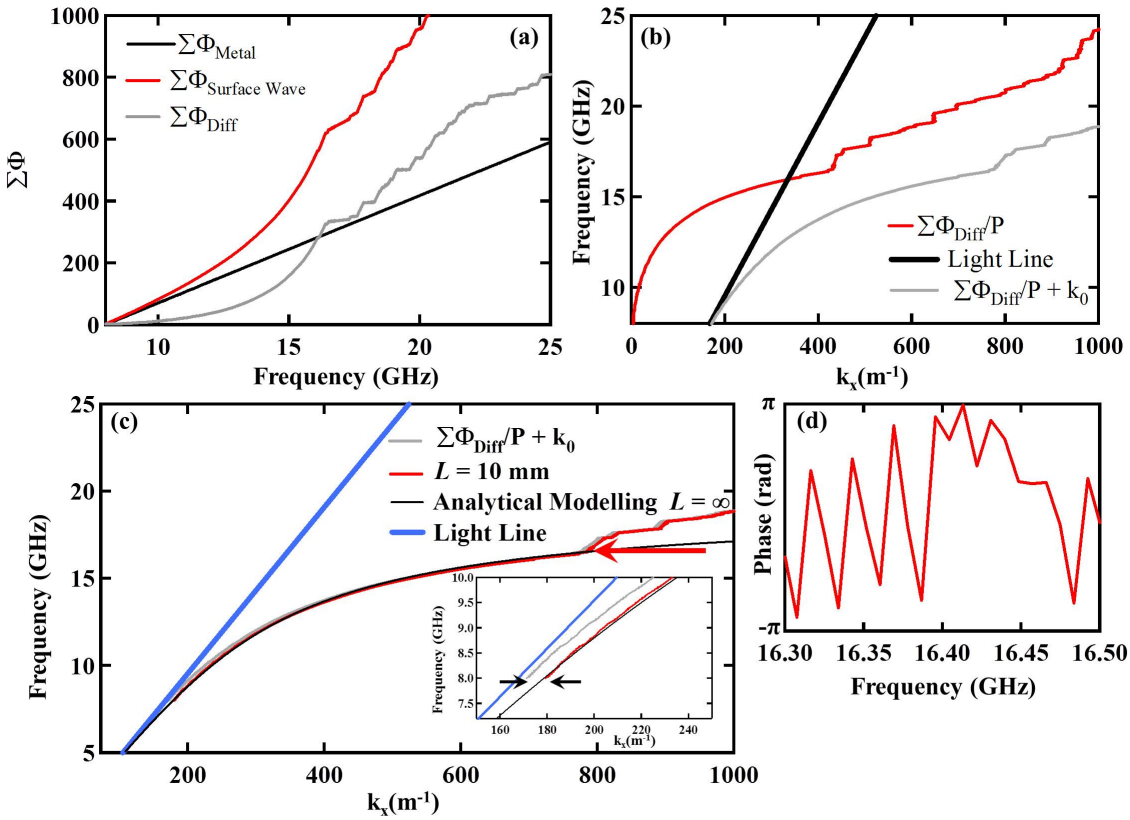

Figure 3.13: Post-processing of the phase associated with a surface wave and a free space wave to measuring the dispersion of the surface wave. Phase is measured by a probe in a static position over a range of frequencies. (a) Unwrapped phase $\Sigma\Phi$ associated with the supported surface wave (red solid line) and a free space wave propagating over an untextured metal slab (black solid line) is shown in comparison to the difference between the two unwrapped functions, $\Sigma\Phi_{\texttt{Diff}}$.(b) Converting phase $\Sigma\Phi_{\texttt{Diff}}$ to k_x. Compared is $\Sigma\Phi_{\texttt{Diff}}$ with the addition of the unwrapped phase associated with a free space photon (grey solid line). The propagation distance P of the surface wave and free space wave has been taken into account. Also compared is the light line (black solid line). (c) Displayed is the same solid grey line compared to analytical modelling of an infinite one dimensional array of grooves (solid black line). Final dispersion for a one dimensional array of grooves with $L = 10$ mm, $\pm\frac{2m\pi}{P}$ (solid red line). Inset (c) shows the addition of $\frac{2m\pi}{P}$ (where m is an integer value) to match initial unwrap position in k_x with that predicted by the analytical modelling technique. (d) Raw phase of the supported surface wave at higher frequencies. Lack of amplitude data as the surface wave approaches its limiting frequency results in a cessation of phase oscillation between $\pm\pi$ and the mode is no longer measured.

methods of both the surface wave and the free space wave have been negated by the measurement of $\Sigma\Phi_{\texttt{Diff}}$. This subtraction can be thought of as calibrating the surface wave dispersion measurement. $\Sigma\Phi_{\texttt{Diff}}$ is shown in Figure 3.13 (a) (grey line).

This difference, $\Sigma\Phi_{\texttt{Diff}}$, is related to $\Delta\Phi$ as expressed in equation 3.10 and

is a measurement of the unwrapped phase of the surface wave, total $\Delta\Phi$ of the surface wave propagating a distance $P = 775$ mm. Therefore equation 3.10 can now be applied to relate $\Sigma\Phi_{\texttt{Diff}}$ to the in-plane wavevector of the surface wave as seen in Figure 3.13 (b)(red line). The y-axis of Figure 3.13 (a) is transformed to measure k_x thus and transformed into the x-axis in Figure 3.13 (b), displaying k_x as a function of frequency.

The measurement of $\Sigma\Phi_{\texttt{Diff}}$ as detailed in equation 3.12 removed the contribution of cumulative phase associated with a free space photon travelling distance P. Therefore, the free space component of momentum (k_0) is re-added. This is plotted in Figure 3.13 (b) as the grey line to the right hand side of the light line (black line of constant gradient). Figure 3.13 (c) shows this once again as a grey line and compares it to the full expression for the in-plane component of the wavevector:

$$k_x = \frac{\Sigma\Phi_{\texttt{Diff}}}{P} + k_0 \pm \frac{2m\pi}{P} \tag{3.13}$$

where $\frac{2m\pi}{P}$ is a factor used to match the initial value of k_x associated with the derived dispersion (where m is an integer value) to the value of k_x analytically derived at that point in frequency. This is done because the exact location of the starting point of the unwrapped phase in k_x is unknown. Therefore comparison is made to the analytical model.

The analytical model detailed in Section 3.5 will reliably predict the dispersion of a surface wave supported on a 1D array of corrugations of infinite extent at all frequencies, unlike the numerical modelling which requires an HFSS model with a very high meshing volume, something which can be quite computationally expensive and will be discussed shortly. The experimental dispersion as determined by Equation 3.13 is subject to experimental error as apparatus is swapped to achieve a measurement of $\Sigma\Phi_{\texttt{Metal}}$ and $\Sigma\Phi_{\texttt{Surface Wave}}$. The array of metallic corrugations is swapped with a metallic slab which then has to be raised so that the top xy-plane of the slab is at $z = 0$. This results in very small changes to propagation distance P and error in the value of the phase initially measured at 8 GHz of within 2π radians. This is associated with $\pm$ one wavelength. Therefore, an approximation of where the initial value of experimentally determined k_x is made with possible shifts in k_x of $\frac{2m\pi}{P}$ (where m is an integer value).

The shift does not effect the rate of change of dispersion associated with the surface wave as the measured dispersion diverges from the light line. Also, it does not effect the position in frequency to which the surface wave dispersion is asymptotic. Therefore, this shift has been used to partially approximate the initial position of k_x at lower frequencies. The shift is detailed in the inset of Figure 3.13 (c) by the black arrows.

When the amplitude of the surface wave falls below the noise floor of the VNA the phase no longer oscillates in a clear period of $\pm\pi$, as noted by Figure 3.13 (d). At this point the surface wave dispersion can no longer be determined and the data is not included in final measurements representing the dispersion of the supported mode, noted by the red arrow on 3.13 (c).

3.3.3.1 Other Methods of Determining the Dispersion of a Surface Wave via Phase Measurements

Dispersion measurement via the method previously detailed is valid for approximations of the first order mode of the structure. This technique pioneers dispersion measurements of microwave surface waves using a VNA. Having understood the original work that took place by this author, it was then realised by other members of the Electromagnetic and Acoustics Materials Group at the University of Exeter that a different reference measurement could be used to obtain the dispersive properties of not only the fundamental mode of the surface wave but of higher order surface wave modes as well.

Instead of comparing two measurements of phase detected at the same position P over two different samples, as shown in Figure 3.7, two measurements of phase associated with a surface wave detected at two positions P_1 and P_2 were compared [67, 81]. The distance between P_1 and P_2 is at least five operating wavelengths in separation distance. In this case k_x is expressed as

$$k_x = \frac{2\pi}{P_2 - P_1}\left(\frac{\Sigma\Phi_2 - \Sigma\Phi_1}{2\pi} + m\right) \tag{3.14}$$

where m is an unknown integer due to the VNA measurement of phase in modulo 2π. m is calculated by comparing the experimentally determined dispersion of a surface wave to the light line at frequencies far from any resonance supported by the surface. The integer value which yields the closest comparison of the dispersion to the gradient of the light line in this frequency range is used throughout to calculate higher order modes which are not comparable to the light line. In this way any phase contributions from excitation and detection techniques are negated.

The method detailed in [67, 81] requires that the mode measured at the lowest frequency value of interest is closely matched to the light line. In the same way as the method detailed in this thesis, the position of k_x associated with the lowest frequency is gained via numerical or analytical modelling techniques. For the system of interest in Chapter 4 it is clear that the value of k_x at 8 GHz is slightly diverged from the light line, seen in inset of Figure 3.13 (c) therefore matching the mode to the light line would, for this system, be incorrect. However, once the value of m is known the dispersion (as dictated by equation 3.14) of higher order

modes can be examined with this method.

A third technique has been developed by Mr J. Dockrey [82] to directly determine the dispersion of the surface wave. As the method is unpublished it will be briefly outlined but not extensively detailed in this thesis. In contrast to the dispersion measurement previously described in Section 3.3.2, this method requires multiple position measurements of local phase as a function of distance from the source over a range of frequencies, an example of which is shown in Figure 3.10. The phase is unwrapped as a function of position and k_x is determined by analysing the gradient of the line. This is repeated for each frequency and is used in Chapter 6.

3.3.4 Termination of a Surface Wave

Thus far the experimental setup and measurement of a surface wave supported on resonant structures such as a one dimensional array of corrugated grooves has been discussed. The termination of such a surface wave mode is now considered.

Figure 3.14 is a schematic of an experimental setup where a surface wave is excited and measured. In both Figure 3.14 (a) and (b) the surface wave is supported by a one dimensional array of metallic, closed sided cavities and excited via a broadband horn antenna. In contrast to one another, the one dimensional array is terminated in free space (a), a geometrically graded absorber (b) and a metal sheet (c).

The absorber is composed of carbon loaded foam, uniformly loaded throughout the structure. As the absorber is cut into a wedge shape, the electromagnetic fields of the surface wave supported by the array of closed sided cavities gradually increases interaction with the cross section of the foam. This reduces any reflections the supported surface wave may undergo as the termination is gradual and lossy. This kind of absorber is known as geometrically graded due to the nature of the shape of the absorber, without a change of index of carbon loaded into the foam.

Figure 3.15 displays a comparison between the electric field amplitude of a surface wave supported on a 1D array of close sided grooves of width $L = 15$ mm when the terminating boundary condition at the end of the structure is modified to the three terminations shown in Figure 3.14. These include free space (solid red line), metal (solid grey line) and a geometrically graded absorber (solid black line). The period of the oscillations seen in Figure 3.15 is indicative of the surface wave wavelength. The amplitude of the oscillations in the measured field when the surface wave is terminated in an absorber is less than the amplitude of oscillations when the surface wave is terminated by a metallic boundary. The tapering of the geometrically graded absorber was optimised so that a minimum strength of

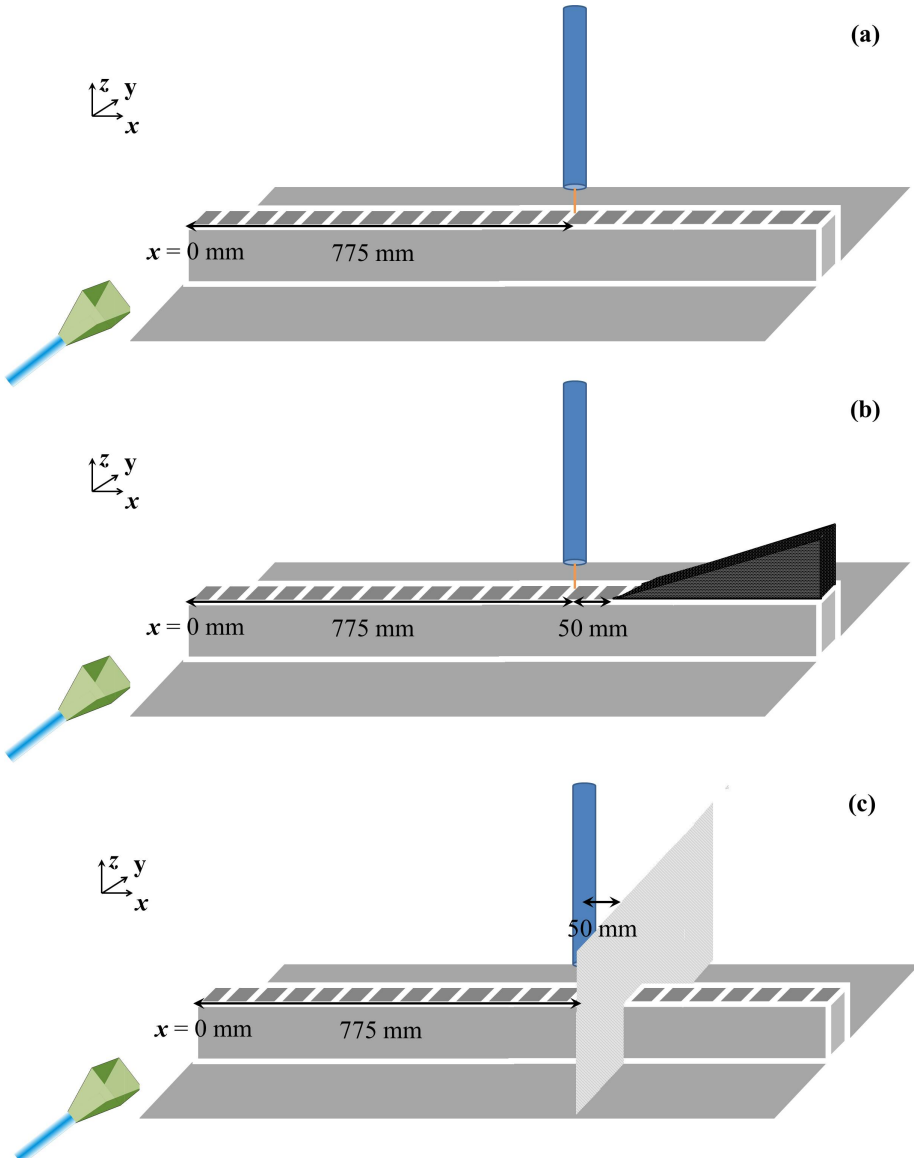

Figure 3.14: Schematic of a surface wave experiment. The surface wave is supported by a one dimensional array of metallic, closed sided cavities and excited via a broadband horn antenna. This structure is further detailed in Chapter 5. The one dimensional array is terminated in (a) free space, (b) geometrically graded absorber foam and (c) a metal screen. The surface wave is excited via edge-coupling and measured by a static probe at 775 mm away from the diffracting edge. The probe is maintained at a height of 0.25 mm above $z = 0$.

oscillation in the measured surface wave field was achieved, the result of which is displayed in Figure 3.15. As such, this absorber was used throughout all surface wave investigations detailed.

The measured system is one where a convolution of a supported surface wave is measured as there will always be some reflection of the mode from a terminating boundary condition. If this were not the case the experimental results shown in Figure 3.15 would not show any oscillation in the measured field of the surface wave

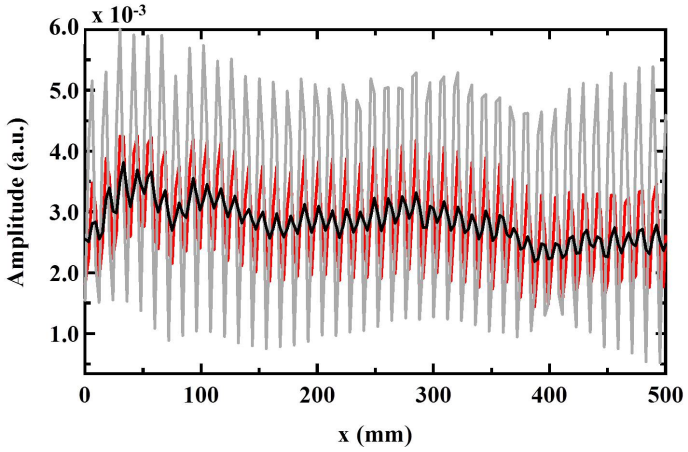

Figure 3.15: Experimental results comparing the amplitude of electric field associated with a surface wave supported on a close sided array of grooves of width L = 15 mm when the terminating boundary condition at the end of the structure is modified. These terminations include free space (red line), metal (solid grey line) and a geometrically graded absorber. The surface wave field is measured by an antenna which is scanned in along the x-direction, remaining stationary in y and z. Frequency of measurement is 11 GHz.

when the mode was terminated in absorber. Therefore the system can be described as multi-modal, with both a forward and backward surface wave mode. Initial experiments measuring the strength of the reflection of a terminating boundary were conducted in the effort to minimise surface wave reflection and investigate the possibility of a perfect microwave surface wave absorber.

These experiments included Fourier analysis of the amplitude of the supported surface wave was conducted to investigate if the strength of reflection of the surface wave could be monitored and therefore tuned. In this case, the surface wave was terminated by a metallic boundary so that a maximum reflection was analysed. However, these initial investigations failed to show any reflections at length scales that were realistic given the measurement system shown in Figure 3.14. This could have been due to the total electrical length of the system not being calibrated via the position scanning method of field detection.

The calibration planes of the system are noted by the dashed grey lines in Figure 3.7 and do not include the broadband antenna or the probe used to measure surface wave fields. This, as well as other as yet unknown effects of measuring a convolution of the surface wave and therefore a multi-modal system, was deemed the reason for the failure of the Fourier analysis. Initial investigations into surface wave absorption were discontinued in favour of continuing investigations into the lateral confinement of microwave surface waves. Indeed, the analysis of surface wave reflections is far from trivial and is the main topic investigated in 'Oblique Angle Scattering of Surface Waves from Surface Wave Absorbing Materials' by Mr

S. Berry [83] which followed this work.

3.4 Numerical Modelling

In this thesis a 3D electromagnetic simulator called HFSS (High Frequency Structure Simulator) made by Ansoft [84] is employed to compare to experimental data. HFSS is a type of Electronic Design Automation (EDA) software which, in general, provides the user with an environment for design of 3D structures and simulation of their electromagnetic behaviour over a range of frequencies [85]. Structures experimentally investigated in this thesis can be drawn directly into an HFSS 3D modeller window and assigned their constituent material properties. 'Ports' which simulate a source of excitation of the electromagnetic modes supported by the structure can be defined in a model enabling the accurate reproduction of experimental conditions. Additionally, HFSS can be set by the user to solve for all eigenmodes supported by a given structure.

3.4.1 Finite Element Method Modelling with HFSS

HFSS uses the finite element method (FEM) to simulate electromagnetic interaction associated with structures of a variety of geometries and constituent materials. The FEM method segments the volume of a model into smaller tetrahedra known as finite elements, small four-sided pyramids [86]. A collection of such elements is known as a finite element mesh. The resolution of the electrical (**E**) and magnetic (**H**) field solutions is dependent on the grade of mesh; how many segments make up a given volume of model.

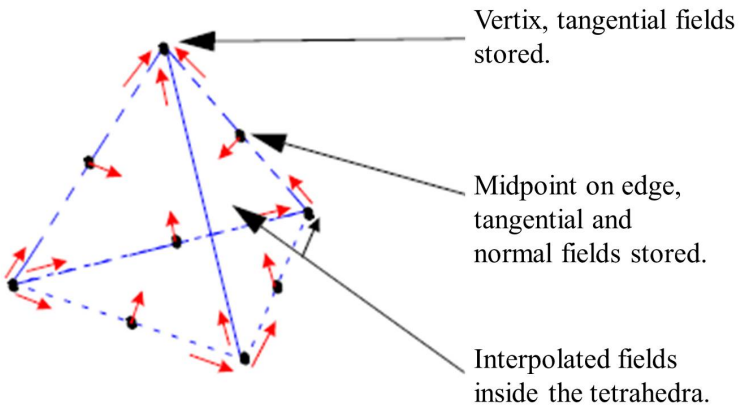

Figure 3.16: Single tetrahedron used in HFSS. Noted are points where electric and magnetic field solutions are calculated or extrapolated [87].

Figure 3.16 displays a single tetrahedron and details the regions where fields are stored or interpolated [87]. At the vertex of each tetrahedron the components of

electric field which are tangential to the three planar faces connected to the vertex are calculated and stored by the HFSS software. The components of the fields at the midpoint of the selected edges that are tangential to a face and normal to the edge are also calculated and stored. The field values in the centre of tetrahedron are interpolated from those stored from the vertex and midpoints. The electric fields are calculated for each element based on the type of excitation applied to the structure. A finite element matrix is formed from the field values associated with each tetrahedron in the mesh. Field values over the whole structure are measured by applying the wave equation below to the matrix:

$$\nabla \wedge \left(\frac{1}{\mu_r} \nabla \wedge \underline{\mathbf{E}} \right) - k_0^2 \epsilon_r \underline{\mathbf{E}} = 0 \tag{3.15}$$

where $\underline{\mathbf{E}}$ is electric field obtained from solving the finite element matrix, relative permeability $\mu_r = \frac{\mu}{\mu_0}$, relative permittivity $\epsilon_r = \frac{\epsilon}{\epsilon_0}$, $k_0^2 = \omega^2 \epsilon_0 \mu_0 = \frac{\omega^2}{c^2}$, wavevector of an electromagnetic wave propagating through free space k_0. The magnetic field $\underline{\mathbf{H}}$ is calculated by

$$\underline{\mathbf{H}} = \frac{1}{\omega \mu} \nabla \wedge \underline{\mathbf{E}} \tag{3.16}$$

Boundary conditions which may apply to the fields in the structure and port excitations used in the model are included in the finite element matrix.

3.4.2 Adaptive Iterative Solution Process

The final HFSS field solutions are not formed simply from the mesh which the model volume is initially segmented into. Instead, the whole process is repeated and the mesh is refined. The number of repetitions depends on an error calculation. This is known as an adaptive iterative solution process and will now be elaborated upon.

Initially, the model is split into a geometrically conformal mesh. Using the conformal mesh, initial electric ($E_{\texttt{initial}}$) and magnetic field ($H_{\texttt{initial}}$) components are calculated from the finite element matrix which is composed of tangential, normal and interpolated field values associated with the tetrahedra from which the mesh is composed. This process is completed at a predetermined frequency with Equations 3.15 and 3.16 and is known as 'solving'. Regions where the field solution has a high degree of error are quantified by inserting $E_{\texttt{initial}}$ and $H_{\texttt{initial}}$ into Equations 3.15 and 3.16

$$\nabla \wedge \left(\frac{1}{\mu_r} \nabla \wedge E_{\texttt{initial}} \right) - k_0^2 \epsilon_r E_{\texttt{initial}} = product \tag{3.17}$$

thus obtaining a 'product'. The 'product' of each element of mesh is evaluated

and compared with all other values of 'product' in the model. A percentage of tetrahedra with a large product value are selected and made smaller (refined). The software solves again using the refined mesh and repeats the same error analysis on the new values of $\underline{\mathbf{E}}$ and $\underline{\mathbf{H}}$. This process of solve, analyse, refine is repeated until the solutions have converged (the product value is below a set threshold for all the tetrahedra in the model) or a predetermined limit on the number of passes have been reached. Only then are other frequencies swept to find the electromagnetic response of the structure over a predetermined range.

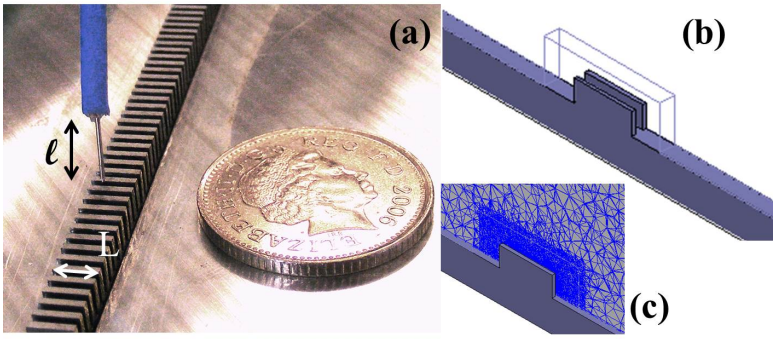

Figure 3.17: (a) A photograph of a 1D array of metallic corrugations protruding from a metallic ground plane with width $L = 5$ mm. This structure supports a surface wave. (b) A typical FEM model is displayed of a unit cell of a 1D array of metallic corrugations protruding from a metallic ground plane with a width of $L = 10$ mm. This is an example of a unit cell used to model the resonant mode of the structure in (a). (c) The same unit cell as seen in (a) however in this case the adaptive mesh of the model is overlaid. The inner cuboid has a high resolution of mesh of 202 tetrahedra per mm^3.

Figure 3.17 shows an example model used in Chapter 4. Notice that the region close to the structure of interest, the grooves, has a more refined mesh than in comparison to the surrounding region as is displayed in Figure 3.17 (c). This is due to the parameters set by the user in the adaptive iterative solution process. Specifically, the mesh is repeatedly refined to achieve a user defined convergence value. This can also be achieved by defining the maximum edge length of tetrahedra used when initially segmenting the model volume.

3.4.3 Using HFSS

In general, the method of creating and analysing any HFSS model is broken down into six steps. First, the user must draw the structure of interest in a 3D modeller window, assign it constituent material parameters and choose which solution type is most correct to use given the nature of the investigation. Second, a definition of the boundary conditions imposed on the structure is required. The software will use them to determine if the structure is a stand alone object or a periodically

repeating array as well as define how the structure is terminated. Third, assign an excitation or port to the model to excite the electromagnetic modes of interest. Fourth, make a solution setup where in the initial frequency of the model, the convergence criteria and range of frequencies of interest are defined. Fifth, analyse the model and finally sixth: post-process the results of analysis. Now that the reader understands the overall process, a more in depth description of relevant steps ensues.

3.4.3.1 Types of Solution

There are three types of solution which the software uses to obtain *S*-parameters; Driven Terminal, Driven Modal and Eigenmode. As the *S*-matrix obtained from a driven terminal solution is expressed in terms of voltages and currents it is not used in this thesis.

However, the *S*-matrix obtained from a driven modal solution is expressed in terms of incident and reflected waveguide modes for systems where two ports have been defined within the model as areas of excitation and detection. This is similar to the previously defined *S*-parameters discussed in Section 3.2.3.1. When investigations in this thesis have required the simulation of an excitation source a driven modal solution has been employed. With this type of solution the electromagnetic modes supported by the structure can be investigated over a range of frequencies, known as a 'frequency sweep' via reflection and transmission between the waveguide modes. The modes are defined by the boundary conditions associated with the 2D sheet the excitation source is defined upon (waveport) and is later discussed in 3.4.3.5.

An Eigenmode solution can deduce all possible electromagnetic modes supported by a given structure and can be used to investigate resonant photonic systems [88, 89] and modes supported by metamaterials [68, 90, 91, 92, 93, 94, 95, 96] (previously described in Section 2.2.4). The software provides the frequency at which the mode is supported as well as the the electromagnetic fields associated with each mode. It should be noted that an Eigenmode model does not require step three as the solution finds all possible modes excited by the system, regardless of excitation source therefore no excitation or port where electromagnetic radiation would enter or exit the system is required.

It should also be noted that the prediction of an Eignemode associated with a surface may not be accurate if the model has not been solved to a high enough accuracy. This is evident by inspection of the electric and magnetic fields at low values of in-plane wavevector produced in post-processing of Eigenmode models completed by this author. These modes are actually modes associated with the whole volume of the model, as they change frequency position as the geometry of

the model is changed. Eigenmodes of the electromagnetic fields associated with the surface wave at frequencies far from the limiting frequency of the supported mode can be obtained by ensuring the mesh of a model is extremely dense (as in the inset of Figure 3.17), however, this is extremely computationally expensive and still may only lead to discovery of modes associated with the whole volume of the model. Comparison between this numerical technique and other techniques such as analytical and effective medium modelling is useful in overcoming this discrepancy at low k_x values when experimentally determined values of k_x are not attainable.

3.4.3.2 Periodic Boundary Conditions

Electromagnetic solutions of infinitely large two or three dimensional arrays are achieved in HFSS by defining periodic boundary conditions. These are defined around the unit cell of the array in co-ordinate planes whose parallel planar faces are orthogonal to one another. For example this could be two faces of the outside of a model in the xz-plane, separated by some distance y. Note that these faces cannot intersect the model unit cell as infinitely repeating boundary conditions require mirror symmetry.

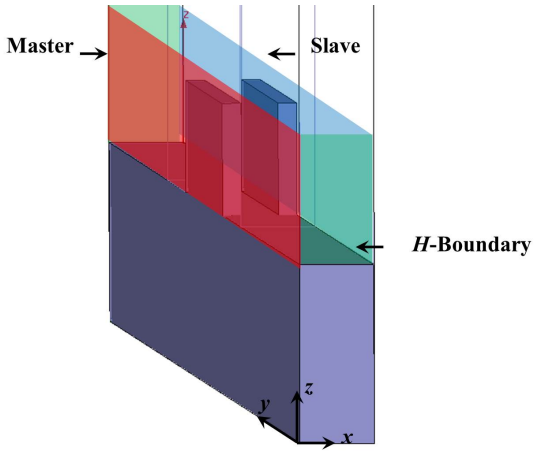

Figure 3.18: Eigenmode model where the boundaries between two yz-planes are result in a periodic condition in the x direction. This is set by the boundaries known as 'master' (red) and slave (blue) boundaries. The two xz-planes are set as perfect H-boundaries (green). In this case the structure which supports a resonance has a unit cell of a 1D array of grooves embedded in a metal sheet. xz-planes are designed to be over three wavelengths away from the supporting structure.

Figure 3.18 is an example of periodic boundary conditions placed on the yz-plane. Such boundaries are denoted as 'master ' and 'slave' and are represented on Figure 3.18 by the red and blue shaded planes (respectively). The relationship between the phase at one master boundary with respect to the phase of the

electromagnetic mode at the corresponding slave boundary can be swept as a parameter. This is true for both driven and eigenmodal solutions but is particularly useful in the latter because the dispersion of the modes obtained can be directly determined.

Conversion of an Eigenmode solution into a dispersion plot is achieved by considering the incrementation of the phase of a resonance between a master-slave boundary and relating it to k_x. The Brillouin zone of a repeating structure is $\frac{1}{2}\frac{2\pi}{\lambda_g}$ [97] where λ_g is the pitch of the structure. When the momentum of the mode as expressed by the in-plane wavevector k_x ranges from zero to $\frac{1}{2}\frac{2\pi}{\lambda_g}$, the phase change between these master-slave boundaries will range from 0 to π radians. Hence the multiple phase values of the Eigenmode solution can be converted to specific values of k_x. Subsequently, the Eigenmode solutions are detailed as frequency as a function of phase.

3.4.3.3 Symmetry Boundary Conditions

The subject of this thesis is laterally confined surface waves that are TM in character (previously discussed in Section 2.3.1) and are supported by structures which are periodic in the same dimension as the in-plane wavevector x only. Therefore periodic boundary conditions in the lateral direction are no longer desirable as the system under measurement is no longer periodic in this direction.

The Eigenmode models used in this thesis set Perfect-H boundaries at least three wavelengths away from the structure of interest in both exterior xz-planes of the models. A Perfect-H boundary is a symmetry boundary which forces the magnetic field tangential to the plane on which the boundary is set to zero. The position of the H-boundary relative to the structure of interest results in the magnetic field component of the mode supported by the structure to be greatly decayed before impinging on the boundary, and is considered negligible. Further, as the mode supported on the structure is TM in nature there will be no component of the magnetic field tangential to boundary. This decreases any possible reflection from the H-boundary which would interfere with the mode supported by the structure.

For this reason the exterior xz-planes of all Eigenmode model solutions used in this thesis to simulate a one-dimensional array, such as the 'domino' structure detailed in Chapter 4 and previewed in Figures 3.17 and 3.18 are set as 'Perfect H-boundaries'. Conversely, a 'Perfect E' boundary (otherwise known as a perfect electric conductor (PEC)) forces the electric field tangential to the boundary to be zero.

Other types of boundary conditions that are used to complete the investigations in this thesis, specifically for the driven modal solutions are 'radiation' boundaries and 'impedance' boundaries. The former acts to completely absorb electromag-

netic field which is incident upon that boundary at a direction which is normal to the surface of that boundary at all frequencies. If the electromagnetic field is incident at some angle other than normal the radiation boundaries will no longer be perfectly absorbing and the model will be subject to some reflection from this boundary.

3.4.3.4 Sheet Impedance

Impedance boundaries are employed to simulate a high impedance surface that supports a TM mode as modelled by the effective impedance model. Surface impedance Z_s is defined as the ratio between the tangential components of electric field $E_{\mathtt{Tan}}$ and magnetic field $H_{\mathtt{Tan}}$ where $Z_s = \frac{E_{\mathtt{Tan}}}{H_{\mathtt{Tan}}}$. An impedance ($Z$) can be assigned to a sheet in HFSS which is composed of resistive (R) and reactive (χ) components. To design a surface which mimics free space, the resistive component of Z is set to 377 Ω and the reactive component set to a value comparable with zero. Conversely, to simulate a surface which supports a TM mode the resistive component of the impedance is set to near zero while the reactive component is derived from the dispersion relation for a TM surface wave in the context of the effective surface impedance model [68]:

$$k_{\mathtt{TM}} = \frac{\omega}{c}\sqrt{1 - \frac{Z_s^2}{\eta^2}} \tag{3.18}$$

where $k_{\mathtt{TM}}$ is the in-plane wavevector, ω is frequency, c is the speed of light and η is the impedance of free space. Equation 3.18 can be rearranged to give

$$Z_s = \sqrt{\eta^2(1 - k_{TM}^2\frac{c^2}{\omega^2})} \tag{3.19}$$

where the value of k_{TM} is known preferably from experimental determination. The advantage of simulating a high impedance surface rather than including all structural elements of the surface is primarily due to the computational constraints associated with such a fine level of structural detail over large areas. However with a simulated high impedance surface a larger region of a supported surface wave can be investigated, a quality which is used later in Chapter 6

3.4.3.5 Excitations

The third step of using HFSS for numerical modelling requires defining an excitation source in the model. This step does not apply to an Eigenmode solution. In a driven modal solution an excitation source is used to simulate a radiative source. The electromagnetic response of a modelled structure over a user defined frequency range is then simulated, determined by the orientation of the electric

field of the source and the boundaries defined in the model as well as the geometry of the structure of interest.

Voltage and waveport excitations were used to simulate excitation sources used in experiments. A voltage excitation results in an enforced electric field pattern by projecting a static uniform field onto the surface upon which the user set the voltage line. The direction of the electric field is in the direction of the user defined voltage line. When a voltage line is set normal to two conducting plates a source with an electric field normal to those plate is achieve for the full range of frequencies as defined in the 'sweep'.

A waveport excitation is embedded on a 2D sheet structure and can achieve the same electric field profile as that set by the voltage line. The Eigenmode of that 2D structure is deduced by the software and is dependent on the geometry of the sheet and the nature of the borders to the sheet, resulting in possible quantisation of the mode. As such the direction of the electric field can be manipulated. The user selects the Eigenmode of interest to act as the excitation source.

3.4.3.6 Solution Setup

Regardless of solution type, all models in this thesis required a solution setup which includes the frequencies analysed and the convergence criteria. There are small but important differences in these setups. The frequency defined in the setup for an Eigenmode solution dictates the lowest frequency mode analysed by the system. In a driven modal solution, this frequency is the frequency at which the initial conformal mesh is solved. Frequency sweeps also need to be defined for a driven modal solution, as do the number of modes investigated by an Eigenmode solution. With the aforementioned knowledge all models in this thesis can be replicated.

3.5 Analytical Modelling

The analytical technique employed in this thesis was developed solely by Professor Hendry and adapted from his previous publication regarding the dispersion of designer surface plasmon-like modes supported by a periodic array of square holes in a perfect conductor [93].

Conversely, the software package employed for numerical modelling (HFSS) struggles to calculate the Eigenmode associating with a structure of interest at frequencies which are far less than the limiting frequency of a supported wave, at low values of the in-plane wavevector. Eigenmodes of the electromagnetic fields associated with the surface wave at frequencies far from the limiting frequency of the supported mode can be obtained by ensuring the mesh of a model is extremely

dense (as in the inset of Figure 3.17) however this is extremely computationally expensive. For this reason it is useful to compare analytically determined dispersions with those determined via numerical and experimental methods as the analytical method is frequency independent, insensitive to the meshing constraints of numerical data and is not subject to possible experimental error.

A designer surface plasmon-like mode is also known as a 'spoof' or 'pseudo' surface plasmon and is simply a surface wave supported at microwave frequencies, as is previously discussed in Section 2.2.5. The mechanism of support of the surface wave is the interaction of the waveguide modes supported in each square hole below the limiting frequency of the waveguide. Previous analytical work conducted by Pendry and co-workers [50] assumed only the fundamental mode of an infinitely deep square waveguide would be supported in each square hole where the dimensions of the hole were far less than the wavelength of incident radiation and therefore did not accurately predict the full dispersion of the surface wave supported by a real array of finite depth.

A study conducted with numerical modelling (and FEM techniques) concluded that the dispersion of a surface wave supported by the aforementioned array of holes cannot be generally derived by assuming only fundamental waveguide modes are supported in the holes [98]. Indeed, both the hole period and depth are critical in determining the precise dispersion of the surface mode supported by these structures. Hendry et al. (2008) [93] proposed an analytical technique for precisely determining the dispersion of the surface wave supported by a periodic square array of square holes for all possible depths and periods. Further noted was the interaction of evanescent diffracted orders with the supported waveguide modes, resulting in a more accurate determination of the experimentally determined dispersion when compared with previous analytical modes [99].

Professor Hendry modified his analytical technique to precisely determine the dispersion of the surface wave supported by a infinite periodic array of corrugations in a metallic slab for any value of depth or period. The technique had previously been employed to predict the Eigenmodes of the surface waves supported by an infinite array of square holes in a metallic slab with finite depth [93] and an infinite array of circular holes in a metallic plate suspended in air [100]. The technique relies on a modified modal matching approach to relate frequency to in-plane wave vector of the surface wave supported on an periodic array of corrugations in a metallic slab. The results of this technique have been published in Brock et al. (2011) [91] with Professor Hendry and is detailed in Section 4.4.3.

The modified modal matching technique can be decomposed into 4 general steps. First, the whole system is defined by either two or three regions. If analysis is performed for a finite depth array of infinite extent the two regions of interest

are: the volume of free space above the array and the cavity region in the metallic plate of finite depth. However, if the array of interest is suspended there are now two regions of free space and a cavity region embedded in the metallic plate for which the electric and magnetic fields need to be defined, resulting in three regions. Consider the periodic plane of the array to be in the xy-plane while the depth of the array is in the z-direction. For a finite depth metallic slab, consider the interface between the slab and vacuum to occur at $z = 0$ as is apparent in Figure 2.9.

Second, the time independent in-plane component of the electric field in the semi-infinite vacuum region above the structure is defined by a Fourier-Floquet expansion of diffracted orders associated with the structure. The dimensions of the expansion depend on the periodicity of the structure of being analysed. For an array of square holes in a metallic slab the expansion is expressed in two dimensions while for an array of corrugations in a metallic slab the expansion is expressed in one dimension. The number of diffracted orders included in the analytical model is specified by the user, an attribute which is not available via the numerical modelling technique employed in this thesis. Subsequently, Hendry et al. (2008) [93] commented on the importance of the inclusion of diffracted orders when analytically determining the dispersion of a designer surface plasmon in comparison other analytical measurements and those determined experimentally.

Third, the electric field inside the cavity is defined by the appropriate waveguide modes. This includes an expression for the z component of the electric field for $z < 0$ (inside the cavity) and $z < 0$ (in the vacuum region). The magnetic fields are then subsequently calculated via the following free space Maxwell equations:

$$\nabla.\underline{\mathbf{E}} = 0 \quad , \quad \nabla \wedge \underline{\mathbf{E}} = \frac{-\mu_0 \delta \underline{\mathbf{H}}}{\delta t} \tag{3.20}$$

where μ_0 denotes the permeability of free space.

Finally, appropriate boundary conditions for the tangential components of the electromagnetic fields at the vacuum-sample interfaces ($z = 0$) can then be applied and Eigenmodes of the structure can be calculated for all frequencies of interest.

Comparison between analytically determined dispersions and experimentally determined dispersions obtained for surface waves supported on structures which are periodic in two dimensions is clearly useful. However, as the electric field in the vacuum region is defined by the Fourier Floquet expansion of the diffracted orders associated with the structure the analytical model cannot be used to represent structures which can be considered periodic in one direction only.

3.6 Excitation and Detection of a Surface Wave

The studies in this thesis investigate surface waves supported by metamaterial structures via a variety of detection and excitation methods. To excite a propagating surface wave supported on a metamaterial structure there must be momentum available greater than that associated with a free space photon. Evanescent field excitation is the mechanism by which this occurs. Examples of two types of evanescent field excitation methods are discussed and contrasted in an effort to ascertain correct coupling methods.

3.6.1 Coupling Considerations

A propagating photon has a finite amount of momentum available, as described by wavevector k_0. A propagating surface wave can be described by its in-plane wavevector, k_x, where $k_x > k_0$ as discussed in Sections 2.3 and 2.3.1 where k_0 is the free space wavevector. To excite a surface wave the excitation source must have enough momentum to match k_x. Therefore a free space propagating photon will not be able to excite a surface wave directly unless an excess of momentum becomes available to the system. Conversely, a surface wave will not be able to couple out to a free space photon as it is no longer momentum matched to free space.

Diffraction or the total internal reflection (TIR) of a photon travelling in a high refractive index medium bordered by a low refractive index medium are two phenomena which result in evanescent field decay. This field will contain k components greater than that of k_0, the exact value of which will depend on the refractive index of the prism or the periodicity of the structure used in diffraction. If these two parameters are chosen correctly there will be k components present in the evanescent decay of the electric field which match k_x. It is possible to excite a surface wave if the interface upon which that mode is supported is placed in proximity to the evanescently decaying fields. Examples of prism coupling experiments can be found in references [101, 102, 92]. Examples of coupling via diffraction on a grating has previously been discussed in Section 2.2.2 and shown experimentally at microwave frequencies in [28, 19].

A brief discussion of diffraction is useful in clarifying the range of wavevectors present in evanescent decay. Diffraction occurs when a planar wave is incident on an aperture which is smaller than the wavelength associated with the incident radiation. Radiation of fields diffracted from a subwavelength aperture was first treated by Borgiotti (1963) [103], as referenced by Rhodes (1966) [104] and extended to antenna theory by Balanis (2005) [30]. The field from this diffracted aperture can be described by the Fourier expansion of the electric field after passing

through a subwavelength aperture

$$E(x,y,z) = \frac{1}{4\pi^2}\int_{-\infty}^{\infty}\int_{-\infty}^{\infty}[f(k_x,k_y)]e^{-i(k_x x+k_y y)}dk_x dk_y \tag{3.21}$$

where the cross section of the aperture is in the x and y plane and the depth of the aperture is in the z plane.

The vector amplitude of the wave is described as $\mathbf{f}(k_x,k_y))$. The radiated wave is composed of the entire spectrum of possible k vectors ($-\infty \leq k_x, k_y \leq \infty$). If $k_0^2 < k_x^2 + k_y^2$ then the wavevectors k_x and k_y will contribute to the evanescent waves associated with diffraction from the aperture. Surface mode momentum matching occurs when the wavevectors in the evanescent field of a mode radiated from an aperture is the same as k_x associated with the supported mode. Surface wave excitation can occur.

The same principle applies to an antenna such as the probe used throughout this thesis and the edge used in diffraction as outlined in Section 3.3.2, the whole spectrum of k values are available in the evanescent decay of the fields associated with these two different geometries [30]. Therefore the a probe is able to couple to a surface wave.

3.6.2 A Coaxial Probe Antenna

A coaxial probe antenna can be used to excite and couple to a propagating surface wave. However, crosstalk between source and detector will effect the measurement of the mode. This, as well as any resonance associated with the geometry of the antenna itself must be minimised to obtain an independent measure of the behaviour of the surface wave under study.

Figure 3.19 (a) shows numerically calculated time-averaged electric fields associated with a surface wave on a 1D array of corrugations with $L = 10$ mm at 14 GHz when a probe is place in the model. The probe is displaced by 1 mm in the y-direction from the edge of the supporting structure and does not significantly perturb the fields of the supported surface wave.

A stripped coaxial probe can be approximated as a $\lambda/4$ resonator [68] as is observed in Figure 3.19 when the time-averaged electric fields associated with a probe of wire length $\ell = 3.75$ mm are observed at 10 and 20 GHz. At 20 GHz $\frac{\lambda}{4} = 3.75$ mm. The fields are more confined to the wire when compared to the electric field shown at 10 GHz. Also shown in the bottom left hand corner of Figure 3.19 (a) and (c) is a grey box which is indicative of the proximity of the 1D array. By inspection it can be seen that any perturbing effect the proximity of the metallic 1D array of corrugations has on fields associated with the probe

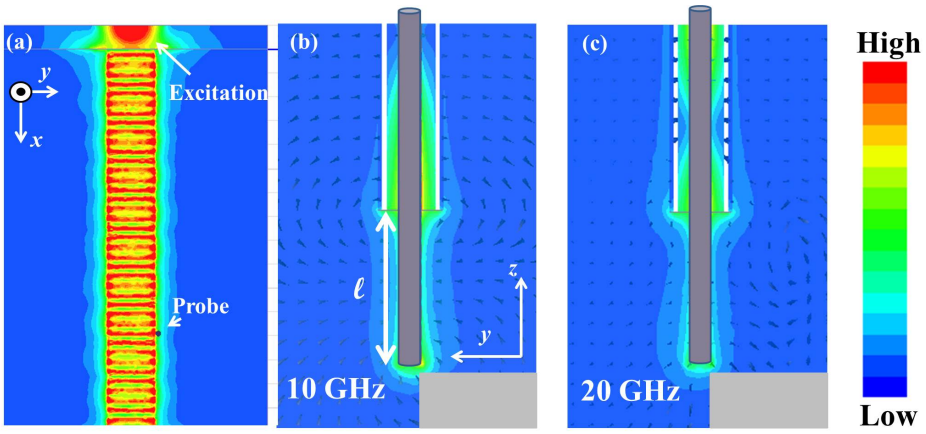

Figure 3.19: Numerical model of the time-averaged electric field associated with (a) a surface wave on an $L = 10$ mm 1D array of metallic corrugations at 14 GHz with a probe displaced 1 mm in the y-direction from the edge of the supporting structure. (b) and (c) depict numerical simulations of the time-averaged electric field associated with a coaxial probe antenna operating at two frequencies; 10 and 20 GHz. The exposed length of wire $\ell = 3.75$ mm. The grey rectangle in the bottom right hand corner of (b) and (c) represents the location of the 1D array of corrugations. The magnetic field vector of the system at these two frequencies is represented by the arrows overlaid on the plot. Excitation of the probe was achieved by a waveport placed at the top of the probe and between the inner core wire and outer sheath covering, mimicking the electromagnetic fields inside a coaxial wire.

is minimal, regardless of frequency. Therefore any perturbing effects that might be associated with the probe mapping electric field of a laterally confined surface waves is considered to be negligible as there is no significant interaction with the supporting structure. Further, to minimise any resonant effect, all detecting probes throughout this thesis are engineered so that the $\frac{\lambda}{4}$ condition is at a higher frequency that that of the investigated mode.

3.7 Different Excitation Methods

Experimental plots of the local electric field amplitude are displayed throughout this thesis. They are achieved by measurement of the local electric field with a detecting probe, the position of which is modified by an automated XYZ stage. A high amplitude of local electric field is expected to be measured in areas which are in close proximity to a surface wave supported on a metamaterial structure. When the probe is not in proximity of such a structure, the electric field is expected to be negligible in amplitude when compared to the amplitude associated with the supported mode.

Electric field measurements recorded in regions more than five wavelengths

away from a surface wave supporting structure and compared with the amplitude of electric field associated with the supported surface wave. Surprisingly in some cases these measurements were only separated by an order of magnitude. Two types of coupling techniques were investigated so that the source of these 'stray' fields could be ascertained and minimised.

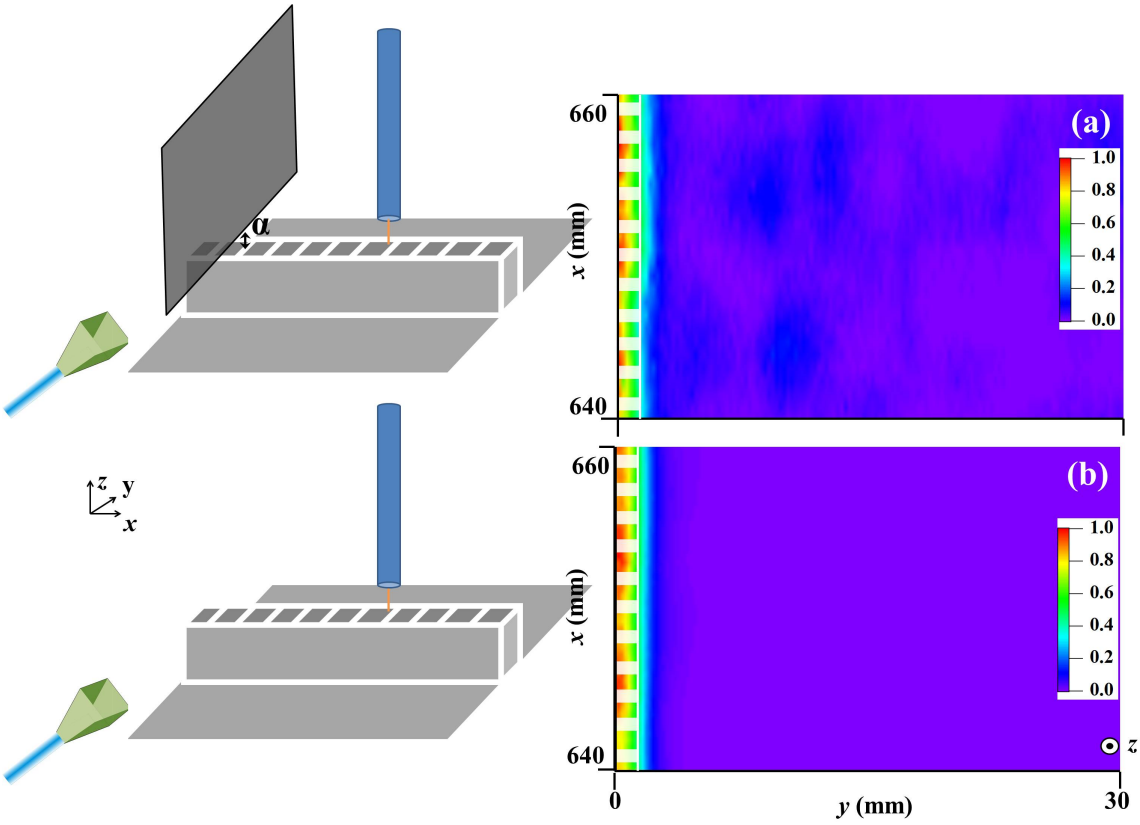

Figure 3.20: Experimental data showing the amplitude of the electric field associated with a surface wave supported on a 1D array of close sided cavities using two separate coupling in techniques to excite the mode, measured via a vertical antenna. All data is normalised and at a finite frequency of 17 GHz. (a) Blade-coupling (left) and the amplitude of electric field plot (right) in the xy-plane of the surface wave.(b) Edge-coupling (left) and the amplitude of electric field plot (right) in the xy-plane of the surface wave. All detection regions plotted are 640 mm from the excitation point (at $x = 0$ mm) with $y = 0$ mm, mid-width of the array.

Figure 3.20 displays the result of these investigations. The amplitude of the measured electric field associated with a surface wave supported by a one dimensional array of closed sided metal cavities is displayed in field plots. These plots are indicative of the amplitude of the electric field measured in the xy-plane. The white line and box structure outline a schematic representation of the supporting structure beneath the field plot but are not reflective of the pitch of the structure and are for illustrative purposes only. The field plots are measured by a probe at a constant vertical distance of 0.25 mm above the array of closed sided metal

cavities at a starting position of $y = 0$, mid-width of the array. The surface wave is excited via edge or blade-coupling. Both plots are normalised with respect to the maximum amplitude of electric field associated with the supported surface wave, enabling comparison to the amplitude of electric field strength measured in regions which are not in proximity to the supporting surface wave structure.

Edge-coupling, as seen in Figure 3.7 relies on the edge of a sample to diffract incident radiation incident from a broad band horn antenna. Blade-coupling as schematically shown in Figure 3.20 (a) and used in a previous publication [105] also relies on diffraction of radiation from the same horn antenna. However this diffraction now occurs through an aperture of width α where $\alpha < \lambda$ and should decrease excitation of fields from other sources. Further, the ratio between width of gap and operating wavelength is a method of ensuring a greater number of higher wavevector components result from the diffraction through the aperture in comparison to an edge.

Figure 3.20 (a) and (b) show that when blade and edge-coupling are compared, a surface wave excited via blade-coupling clearly results in stray fields with amplitude of electric field within a tenth of that associated with the surface wave supported by the 1D array of cavities. In contrast to this, the stray fields measured when a surface wave is exited via edge-coupling are less than a tenth of the amplitude of electric field associated with the supported mode. For the purposes of investigating laterally confined surface waves this evidenced the edge-coupling technique as a preferred method of surface wave excitation.

From these investigations it is concluded that surface wave experiments will never be totally independent of stray fields which can be attributed to free space waves. However the technique preferred in this thesis is, in general, edge-coupling as it uniformly excites along edges up to 100 mm in length and minimises the stray fields in comparison to the blade coupling technique shown in Figure 3.20.

3.7.1 Surface Wave Launcher

When a excitation source was required to uniformly excite surface waves along length greater than 100 mm, a lens device known as a 'surface wave launcher' was used. This has been designed recently by Mr S. Berry and will appear in 'Oblique Angle Scattering of Surface Waves from Surface Wave Absorbing Materials' [83].

The device resembles a parallel plate capacitor structure with a pin in the cavity between the two plates. The pin, as indicated by the black arrow (left) acts as dipole source, emitting a radial field pattern within the two conducting plates (labelled PEC) with electric field parallel to the z-plane. The interaction of the electric field within the launcher with a perspex lens can be seen in Figure 3.21

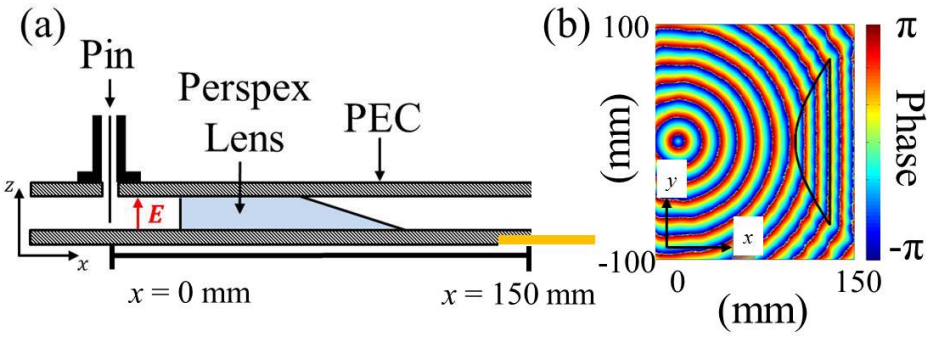

Figure 3.21: Adapted from 'Oblique Angle Scattering of Surface Waves from Surface Wave Absorbing Materials' by Mr S. Berry [83]. (a) Schematic of surface wave launcher in the xz-plane. The lens is composed of two parallel metallic plates separated by a cavity. The plates are considered to be PEC at microwave frequencies. The aperture of the lens occurs when $x = 150$ mm and rests on the metamaterial surface, schematically represented by the orange box. A coaxial cable connects an RF source such as a VNA to the lens where a metallic pin protrudes into the cavity, exciting a transverse electromagnetic (TEM) mode within the cavity. This mode propagates radially away from the pin and results in spherical wavefronts with an electric field polarised in the xz-plane (red arrow in (a)). (b) Numerically calculated phase of the electric field in the xy-plane inside the surface wave launcher associated with the mode within the cavity. The pin is located at coordinates (0,0), the centre of the spherical wavefronts. The perspex lens inside the cavity is noted in (a) and the interaction of the mode within the cavity with perspex is observed when the spherical wavefronts associated with the cavity mode become planar at $x = 150$ mm, the aperture of the lens.

(b) as represented by the numerically modelled phase of the electric field (without reflections considered from the sides of the lens). As a result the beam is collimated within the launcher. The wavefronts associated with the phase of the electric field of the mode within the cavity are spherical at the pin location but are planar at $x = 150$ mm, the aperture of the lens.

The pin indicated on the photograph is connected to a coaxial cable so that a TM mode is excited and guided within the lens by the tapped semi-transparent perspex and the black absorber. This lens is used to launch microwave radiation with planar wavefronts along a distance of over 300 mm, polarised so that the electric field is polarised in the xz-plane and can excite TM modes on a metamaterial surface such as a Sievenpiper mushroom array. The electric field is not totally polarised in the z-plane due to diffraction at the aperture of the lens. The surface is placed directly underneath the lens device, so that the lens aperture rests along the surface uniformly. The surface is represented schematically by the orange box in Figure 3.21 (a). The dynamic range of the lens is 10 to 30 GHz. In comparison to previous methods of excitation, the surface wave launcher can

excite a mode uniformly along distances of greater that 100 mm. Edge-coupling, which relies on excitation from a broad band horn antenna, cannot be guaranteed to uniformly excite over 100 mm width due to curvature of the beam profile from the horn antenna.

The coupling efficiency of the launcher when used to excite a surface wave on the Sievenpiper mushroom array was not investigated. This is due primarily to the fact that a uniform excitation over distances greater than that of 100 mm was required for investigations detailed in Chapter 6, therefore coupling constraints were not analysed. Further, there was never any experimental issues encountered as regards to the strength of the mode excited on the Sievenpiper mushroom array surface so an investigation was not warranted at that time.

3.8 Conclusions

The method of measuring the dispersion of the fundamental mode of a surface wave supported by a metamaterial surface has been outlined in this chapter. Further, mapping the electric field of surface waves supported by a metamaterial and excitation methods used to induce a surface wave are elaborated upon. The method of termination of surface wave experiments has also been discussed. All of the aforementioned experimental data is collected with a vector network analyser (VNA) whose operation, functionality and calibration has been detailed. To support the conclusions reached in this thesis via experimental measurements, both analytical and numerical methods are used therefore have been discussed.

Chapter 4

Lateral Confinement of Microwave Surface Waves

4.1 Introduction

Experimental verification of the 'domino plasmon,' proposed by Cano et al. (2010) [66] is presented. Using microwaves, it is demonstrated that this mode propagates along a periodic chain of metallic cuboids protruding from a planar metallic ground plane. The structure used to support the surface wave resembles a chain of dominos placed on a flat metallic sheet therefore the mode has been referred to as a 'domino plasmon'. The dispersion of the surface wave is determined experimentally and compared with the predictions of analytical and numerical models. This mode is found to be surprisingly insensitive to the lateral width of the chain. This is found to be the case even when the lateral width of the chain is less than the wavelength of microwave radiation used to excite the mode. This limit is further referred to as subwavelength. Having such tight confinement, 'domino plasmons' show considerable promise for one-dimensional subwavelength guiding and focusing of electromagnetic fields. Confinement of the domino plasmon to the supporting structure is shown by measurement of the local field amplitude along a constant height in the yz-plane. The amplitude of the local electric field of the surface wave in the xy-plane is shown for two different heights above the supporting domino structure to further illustrate confinement.

4.2 Background

The plethora of electromagnetic (EM) surface-wave studies since the early 1900s [6] have largely focused on the propagation of non-radiative modes along the interface between two dissimilar media [32]. At optical frequencies, a surface plasmon

polariton (SPP) is one such wave, existing at the interface between a metal and a dielectric.

This mode can be described as the hybridisation of a grazing photon with the density oscillation of the electrons at the metal surface, and whose dispersion is asymptotic to the surface plasma frequency, ω_{SP}. These electron density oscillations have dipolar and multi-polar charge distributions [106] that strongly enhance the fields at the interface [107]. The propagating surface mode is bound to the interface with fields decaying exponentially away. This behaviour has been previously discussed in Section 2.4.

Propagation of a SPP may be characterised by the real (resistive) and imaginary (reactive) components of the impedance of the interface, Z_s along which it travels. When this interface is bounded by a metal in the visible regime, Z_s is dominated by a positive reactance [69]. The surface can be described as naturally inductive [108] with the SPPs supported being transverse magnetic (TM) polarized waves. The impedance associated with a surface is discussed further in Section 2.5.3.

At visible frequencies the fundamental modes of metallic waveguides, such as channel [109, 110], or corrugated-wedge [111] structures are considered as SPP modes hybridized with the geometric resonances of the structure itself. Therefore it is usual for the dispersion of a SPP mode supported by such waveguide structures to experience a dependence dictated by either the transverse or vertical dimension of that structure, or even both. For reference, Sections 2.2.2.2 and 2.2.5 contain explanations of the dispersion of a surface wave supported in both the optical and the microwave regime so will not be further elaborated on in this chapter.

In contrast to the visible regime, at microwave frequencies a strongly bound surface wave, such as the SPP in the visible, is no longer naturally supported on a metallic planar surface because the fields are almost completely excluded i.e. the imaginary component of the permittivity with respect to the real component is very large and positive. Consequently the decay length of the electric ($\underline{\mathbf{E}}$) field into the dielectric is many orders of magnitude larger than the incident wavelength. Hence the SPP becomes essentially an almost unconfined surface wave described as a surface current [28]. A discussion of the confinement of the surface wave in relation to the decay length of electric field penetrating into a metal can be found in Section 2.4.1.1

Previous studies have shown that the addition of a dielectric overlayer [32] on to a metal surface, or a corrugation [18] introduced to that surface will result in an enhanced positive surface reactance, allowing a confined TM-polarised surface wave to be supported.

4.3 Experimental Setup

The present study investigates a surface mode at microwave frequencies supported by a metallic waveguide composed of an array of grooves. This modes asymptotic frequency is dictated primarily by the height of the grooves, h, even when the transverse dimension of the waveguide is subwavelength. The waveguide consists of a chain of metal cuboids (dominos) with uniform separation (cavities) that protrude from a large metal sheet. Figure 4.1 shows a schematic of the supporting surface which can also be described as a 1D array of corrugations and physically resemble a chain of dominos with the lateral width (domino dimension along y), L. This structure will be known henceforth as the 'domino array'.

The cavity between each cuboid along the chain is analogous to a truncated transmission line, which for a perfect conductor (the approximation for a metal at microwave frequencies), is perfectly reflecting at its closed end (in the negative z-direction) though it remains open at each side end (in the transverse direction) and top. Consequently, the surface impedance at the top of the dominoes becomes very high at frequencies close to the resonant condition of the cavities. The frequency at which the resonant condition of the cavities occurs is defined as:

$$f_{\mathtt{res}} \sim \frac{c}{4h} \tag{4.1}$$

where c is the speed of light and h is the height of the cavity. As a result, the group velocity of the surface mode support at the interface between the top of the cavities and the free space region tends towards zero at this limit [34]. This mode, which is bound to the waveguide via the boundary conditions imposed by the structure (and not the constituent material properties), is henceforth referred to as a 'Domino Plasmon' (DP).

Consider the surface wave waveguide structure presented in Figure 4.1. In contrast to the optical SPP mode, the localization of energy is here achieved via the hybridisation between a grazing photon and the resonant mode of the cavities. On resonance, the top of each cavity supports an electric dipole and, when all these dipoles interact collectively, provide the mechanism for the DP to be supported. The time-averaged electric field and vector direction of a surface wave supported on an array of grooves near resonance can be observed in Figure 4.2 (a) and (b) respectively. The DPs dispersion exhibits many similarities to a SPP, but in contrast, due to its dependence on geometry, it can be engineered to occur at almost any wavelength [50].

Through a series of experimental measurements, we show a surprising insensitivity of the dispersion of the DP to the lateral width L, exhibited even in the subwavelength limit, as proposed in reference [66]. To be specific, a surface wave

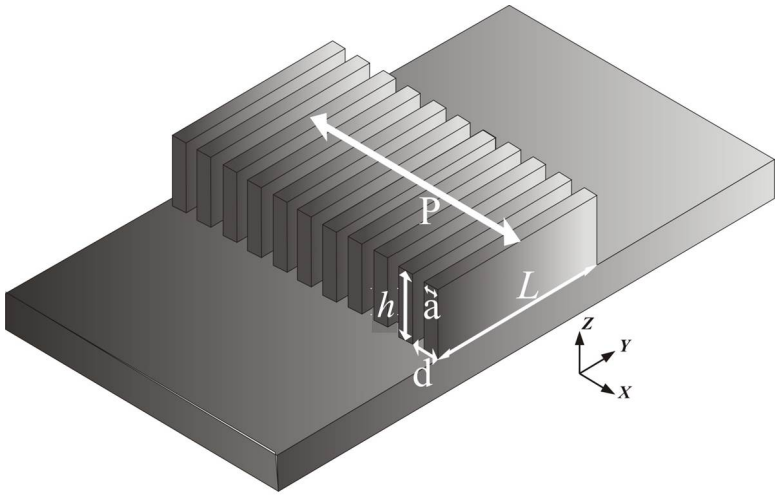

Figure 4.1: Schematic of dimensions of the proposed domino structure where the pitch (d) is 1.6 mm, the width of the domino (a) is $\frac{d}{2}$, height (h) is 3.75 mm and L denotes the lateral width of the structure which is varied.

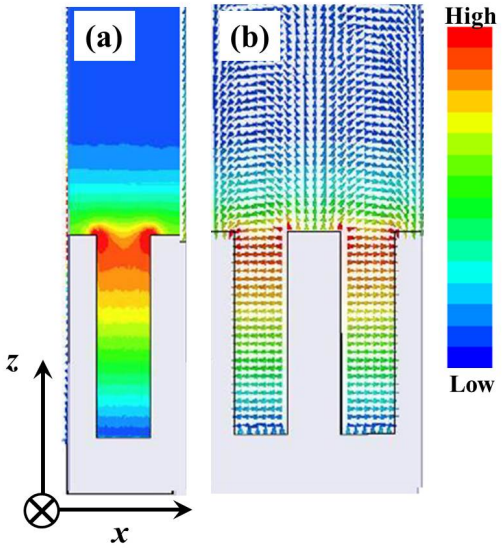

Figure 4.2: Numerically calculated time-averaged electric field (a) and vector distribution of electric field (b) of the surface wave supported on a domino structure near resonance. These solutions were obtain via FEM modelling.

is excited on domino arrays of six different widths $L = 100$ mm, 19 mm, 15 mm, 10 mm, 5 mm and 1.60 mm ($\pm$ 0.05 mm). A photograph of five of the experimental samples can be viewed in Figure 4.4. The metallic ground plane from which the dominos protrude is not shown for clarity.

In our experiments, edge coupling at the end of the waveguide is employed to excite the DP. Figure 4.5 is a schematic representation of the experimental setup. A Vector Network Analyser (VNA) is used to measure S_{21} transmission between a transmitting microwave horn antenna and a detecting coaxial-wire probe antenna, providing measurement of both magnitude and phase of the local field. The horn

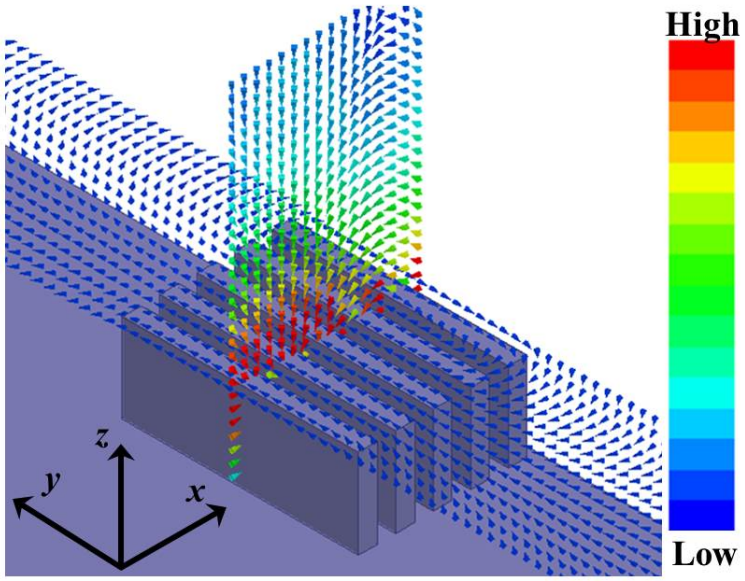

Figure 4.3: Numerical simulations of time-averaged field on resonance of the domino waveguide consisting of open-ended cavities. The coloured arrows bisecting the xz-plane are representative of the vector electric field while the coloured arrows in the xy-plane are representative of the vector magnetic field.

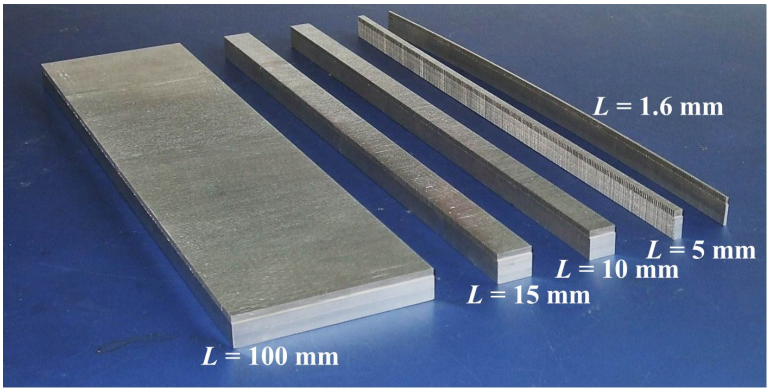

Figure 4.4: Photograph of non-embedded experimental samples of lateral widths L = 100 mm, 15 mm, 10 mm, 5 mm, 1.6 mm ($\pm$ 0.05 mm).

is orientated such that it lies in the xz-plane (Figure 4.1) and directs microwaves with polarization in that plane towards the end of the sample at an angle of approximately 45° with respect to the horizontal xy-plane.

This setup minimizes direct transmission between the horn and detector while irradiating the end of the waveguide with TM-polarised radiation of approximately uniform intensity. This edge diffraction provides a range of effective in-plane incident momentum values (evanescent near field source) for excitation of the DP. The distance between this source and the receiving antenna, length P, is many times larger than the wavelength ($P > 50\frac{c}{f_{\text{res}}}$). Subsequently, the signal detected by the coaxial probe can be attributed solely to the DP and not any surface modes

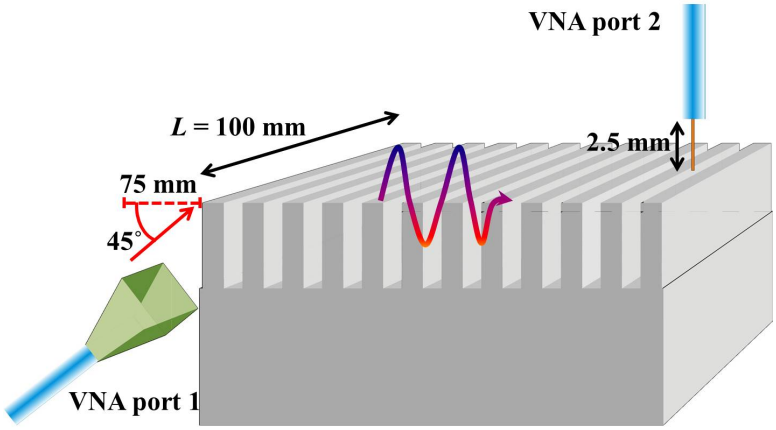

Figure 4.5: Schematic of experimental setup. Broad band horn irradiates the side of the sample at 45° with respect to the horizontal. Direction of radiation is noted by the red arrow. Surface wave is excited and propagates across the sample, radiation direction is represented by the multicoloured sinusoidal curve. It should be noted that this curve is not representative of the amplitude of the electric field of the surface wave and is for illustrative purposes only. The detecting coaxial-wire probe antenna is also shown connected to port 2 of the VNA. The exposed length of the wire of the probe is 2.5 mm in this experiment.

associated with the surrounding metal ground plane. This setup is also discussed in Section 3.3. All surface waves in this experiment have been terminated in a geometrically graded absorber placed at the end of the array supporting the mode. This has been discussed previously in Section 3.3.4.

4.4 Results

The cumulative phase of the detected signal associated with the DP supported by the waveguide is compared with that expected from a free space wave excited from the diffraction at the edge of the sample which then propagates over a planar metal sheet for the same distance P. The coaxial probe used in detection is placed at the same height above both types of surface so that the phase difference between the waveguide DP and the surface current on a flat metal substrate is obtained, allowing the dispersion of the DP to be directly determined. The method for obtaining the dispersion of a surface wave has been previously explained in Section 3.3.2 so will not be further elaborated upon in this chapter.

4.4.1 Dispersion over Multiple Widths

The dispersion of a surface wave has been experimentally obtained for domino arrays of six different widths $L = 100$ mm, 19 mm, 15 mm, 10 mm, 5 mm and 1.60 mm. Figure 4.6 compares these dispersions for all six variations of the domino

array to analytically obtained data for an array of lateral width $L = \infty$ but with otherwise similar dimensions. The analytical technique used to calculate dispersion for comparison with experimental data will be elaborated upon shortly.

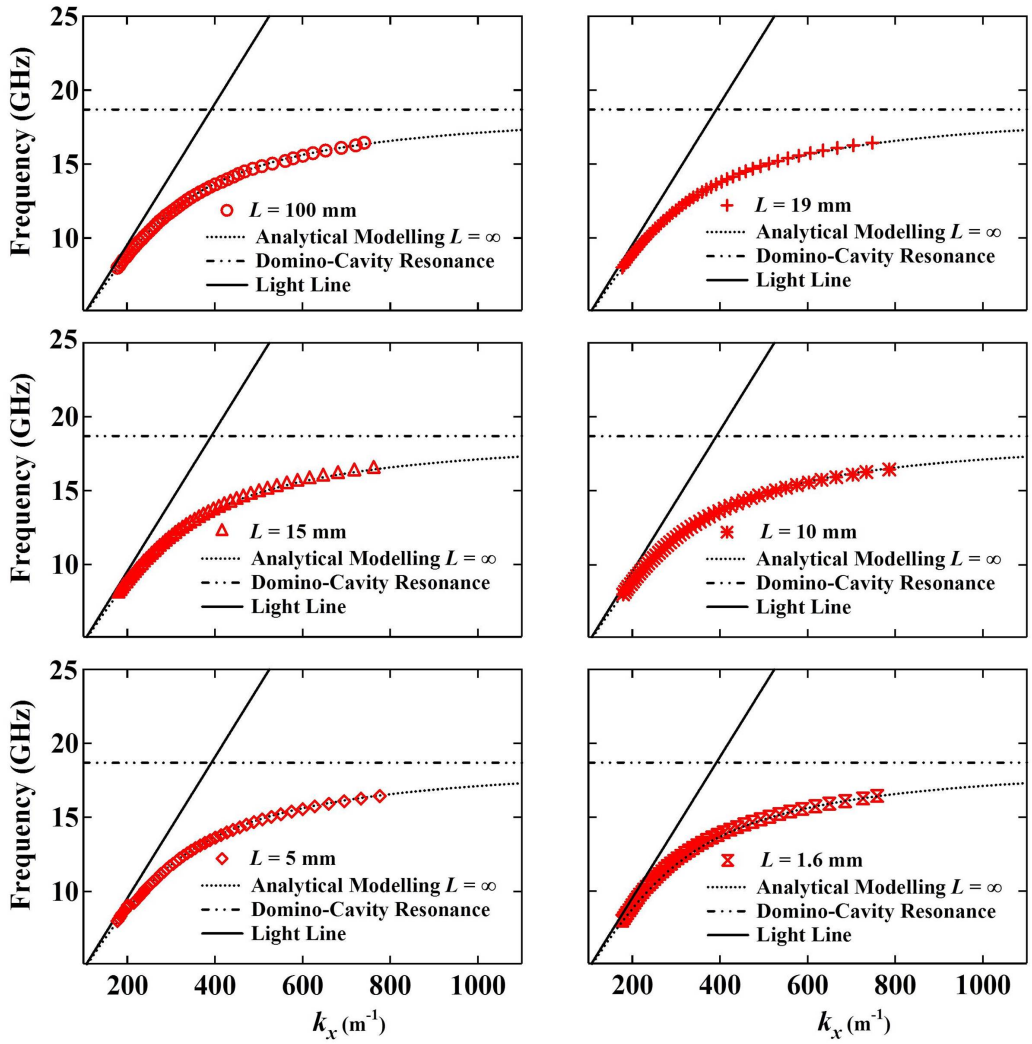

Figure 4.6: Experimentally obtained dispersion curves (red symbols) of surface mode supported by samples with $L = 100$ mm, 19 mm, 15 mm, 10 mm, 5 mm and 1.60 mm compared with analytically derived dispersion.

Each graph in Figure 4.6 compares the dispersion of a surface wave supported on a domino array with an analytically derived dispersion associated with a surface wave supported on a 1D array of grooves of infinite lateral width. Also compared is the frequency at which domino cavity is expected to be resonant labelled as the domino cavity resonance. This is less than the resonant condition of the cavities previously stated in Equation 4.1 as the cavities are a width of $a = 0.8$ mm ($\pm$ 0.05 mm) and not infinitely thin. By inspection of Figure 4.6 it is clear to see that the width of the supporting domino array can be decreased until it is far subwavelength while the supported surface wave mode remains insensitive

to geometric change. Further, the mode remains similar to the dispersion of the surface wave analytically calculated for an array of infinitely wide dominos. This is true for both the limiting frequency of the mode and the rate of change in k_x associated with the surface wave as a function of frequency. Therefore, given the previous discussion in Section 2.2.2.2 it can be stated that the confinement of the mode to the interface as a function of frequency remains insensitive to geometrical changes.

4.4.2 Local Electric Field Amplitude with Respect to the Guiding Structure

Figure 4.7 depicts the experimental and numerical measurement of local electric field amplitude of a surface wave supported by a domino array. This is measured as a function of distance y from mid-width of the array, at $y = 0$, illustrating the confinement of the mode to the domino array.

The starting position of the probe in x is at $P = 350$ mm, y = 0 mm (mid width of the array) and $z = 1$ mm above the array. The x and z coordinates remain unchanged throughout the measurement. The measurement of electric field amplitude via the probe was varied in distance y from the starting location, mid-width of the array, past the end of the supporting domino array at $\frac{L}{2}$ and over the flat untextured metal surface from which the array protrudes from. The experiment was conducted for a surface wave supported by a domino structure of lateral width $L = 1.6$ mm and 19 mm (black and red lines, respectively).

Figures 4.7 (b) shows a numerical FEM measurement of the same experiment for domino widths of $L = 1.6$ mm, 5 mm and 10 mm (red, grey and black lines, respectively). The end of the supporting domino structure is noted in Figure 4.7 (a) and (b) by the vertical dashed lines for the surface wave supported by each domino array. Figure 4.7 (c) illustrates the measurement detailed in (a) and (b) via a schematic. The probe used in measurement is shown at starting position y = 0 mm. The red rectangle in the schematic in Figure 4.7 (c) is representative of the $L = 19$ mm domino structure while the black rectangle represents the $L = 1.6$ mm domino structure

As seen in Figure 4.7, the local electric field amplitude of the supported surface wave on a domino array decreases as a function of distance from mid-width of the array, irrespective of domino width.

The confinement of the electric field to the supporting structure is further illustrated by the experimentally measured field plots in Figure 4.8 of the local electric field amplitude associated with the supported surface wave. The field plots were obtained by a detecting probe attached to a motorised XYZ scanning

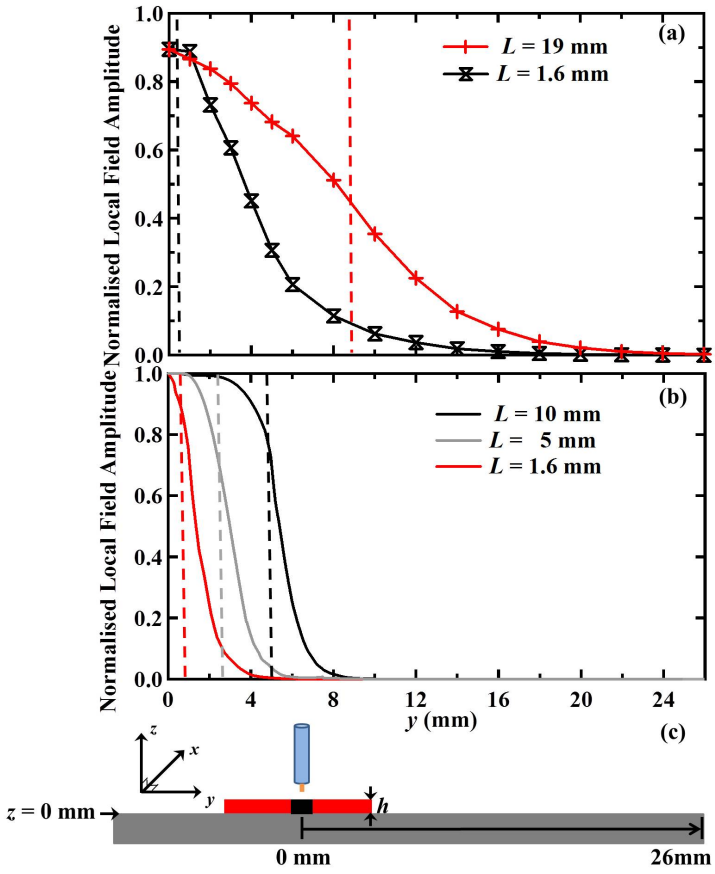

Figure 4.7: (a) Experimentally obtained local electric field amplitude associated with a surface wave supported by an array of open sided dominos as a function of distance in y away from the mid-width of the supporting structure. This is measured for domino arrays of $L = 1.6$ mm (black) and $L = 19$ mm (red). The starting position of the probe in x is at $P = 350$ mm, y $= 0$ mm (mid width of the array) and $z = 1$ mm above the array. The x and z coordinates remain unchanged throughout the measurement.(b) Numerically obtained local electric field amplitude associated with a surface wave supported by a domino array as a function of distance y away from the mid-width of the supporting structure. This measurement was observed for domino arrays of widths $L = 1.6$ mm (red), $L = 5$ mm (grey) and $L = 10$ mm (black). The vertical dashed lines in (a) and (b) are representative of the position of the probe at y $= \frac{L}{2}$ above the supporting domino array. (c) Schematic depicting the starting position of the measuring probe, mid-width of the array at $y = 0$ mm. The red and black rectangles denote the position of an open sided domino array with widths $L = 19$ mm (red) and 1.6 mm (black) with respect to the starting position of the probe. This schematic is for illustrative purposes only.

stage and sampled the electric field of the supported surface wave in the xy- plane at two constant heights, $z = 4.0$ mm (left) and $z = 4.5$ mm (right). Figure 4.8 is shown at the single frequency of 15 GHz and scans an area of 100 mm^2 at a resolution of 0.2 mm. While no smoothing was preformed on this image, it is still subject to the limit of accuracy of measurement of the motorised XYZ stage of

$\pm$ 0.2 mm. Both data sets are represented on the same scale. By inspection of Figure 4.8 it is evident that when the detecting probe is moved further from the supporting structure in height, there is less intensity of local electric field detected. This illustrates surface wave confinement of the electric field with respect to the supporting the domino structure.

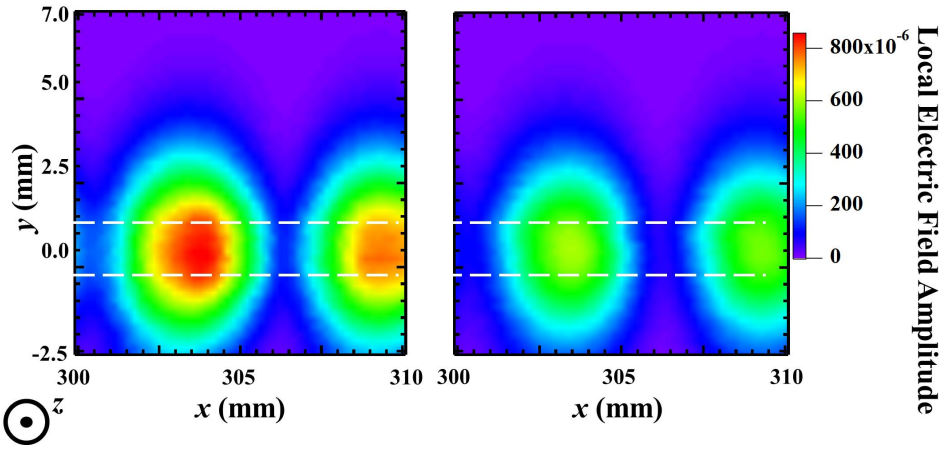

Figure 4.8: Experimentally obtained field plot of the local field amplitude of a surface wave supported on a $L = 1.6$ mm domino array, height = 3.75 mm above the planar metallic surface from which it protrudes. The surface wave is excited via edge-coupling at $x = 0$ mm. The field plots were obtained by measurement of a probe attached to a motorised XYZ scanning stage. The amplitude of the electric field was sampled in the xy- plane at two constant heights, $z = 4.0$ mm (left) and $z = 4.5$ mm (right) where $z = 0$ mm is defined at the top of the planar metallic surface from which the array protrudes. The probe length $l = 2.5$ mm, with the tip of the probe position at (left) $z = 4.0$ mm or (right) $z = 4.5$ mm above the domino array. The white dashed lines are indicative of the structure supporting the surface wave, beneath the xy-plane of either and is illustrative of the position of the edge of the domino array only. Both left and right experimental data sets are plotted on the same scale and at the single frequency of 15 GHz. The plots were obtained at the same distance $x = 300$ mm along the domino array and at a resolution of $\pm$ 0.2 mm.

4.4.3 Analytical Modelling

The dispersion curves of the DP obtained experimentally are compared in Figure 4.10 to those predicted from a modal matching method developed by Professor Hendry and similar to that presented by Hendry et al. (2008) [93] and employed in Edmunds et al. (2011) [100]. This approach obtains the dispersion relation expected for an array of dominoes of infinite width ($L = \infty$). The domino array is considered to be a PEC structure filled with air and at an interface with air.

The analytical method functions by first defining the in-plane component of the electric field in the semi-infinite vacuum region as a one dimensional Fourier-Floquet expansion of the form

$$E_x^{vac} = \sum_N A_N e^{(i(k_x + 2N\pi/d)x)} e^{-ik_z(N)z} \tag{4.2}$$

where N is the order of diffraction, k_x is the in-plane component of the wavevector and d is the pitch of the domino structure. The out of plane component of the wavevector, k_z is described by the component of electric field in the z plane and is given by:

$$E_z^m = \sqrt{(k_0)^2 - (k_x 2N\pi/d)^2} \tag{4.3}$$

where k_0 is the wavevector of light in vacuum and A_N is the Fourier amplitude of order N. Equations 4.2 and 4.3 describes a mode whose electric field is polarised in the xz-plane, a TM polarised mode which has previously been depicted in Figure 2.6.

The number of orders of diffraction has been shown by Hendry et al. (2008) [93] to be crucial when determining the limiting frequency of a surface wave. Before some critical value is reached, the dispersion calculated by the analytical code will vary. This is in comparison to previous work by Pendry et al. (2004) [50] where the diffracted orders associated with a supported surface wave were considered to be negligible. As a result, Pendry et al. predicted the dispersion of supported surface waves to have a limiting frequency which was less than the experimentally measured mode whereas the analytical predictions of Hendry et al. (2008) described the measured mode far better. However, as the domino array of infinte width is considered to be infinite in extent, there are an infinite number of diffracted orders that could be included to measure the dispersion of the mode supported.

The analytical code provided by Professor Hendry to analytically measure the dispersion of an infinitely wide domino array was initially tested to investigate the number of diffracted orders up to which the measurement of the dispersion was no longer sensitive to. Up to N = 5 was tested before the values for the dispersion of the mode calculated by the analytical code remained insensitive to a change of

diffracted orders (within 1% standard deviation).

Inside the domino cavities the in-plane component of the electric field is represented by the fundamental waveguide mode:

$$E_x^{cav} = B(e^{(ik_0 z)} - e^{(ik_0(2h-z))}) \tag{4.4}$$

where h is the height of the domino cavity and B is the amplitude of the mode. One can then obtain the z-components of the electric field inside and outside the domino cavity, and subsequently expressions for the magnetic field, by applying Maxwells relations.

$$\nabla.\underline{\mathbf{E}} = 0 \quad , \quad \nabla \wedge \underline{\mathbf{E}} = \frac{-\mu_0 \delta \underline{\mathbf{H}}}{\delta t} \tag{4.5}$$

where μ_0 denotes the permeability of free space. The boundary conditions at the vacuum-domino interface (defined here as $z = 0$) is such that at the vacuum-vacuum interface the field inside the domino cavity must match the field in free space, the bordering medium. At the domino-vacuum interface tangential electric field is forced to zero and magnetic field is maximal. By applying these boundary conditions the unknowns A_N and B can be eliminated. The dispersion relation for a surface wave supported on a domino array of infinite width can be stated thus:

$$k_0 \cot(k_0 h) = i \sum_N \frac{Q^+(N)Q^-(N)}{ad} \frac{k_0}{k_z(N)} \tag{4.6}$$

Where

$$Q^{\pm}(N) = \int_0^a (e^{\pm i(k_x + \frac{2N\pi}{d})} x dx \tag{4.7}$$

is the mode overlap integral. A mode overlap integral describes how well the fields at an interface match spatially, in intensity and in phase.

To aid in understanding of modal overlap, Figure 4.9 is considered. Numerical models of the time-averaged electric field of a surface wave on resonance supported by (a) a domino array and (b) a closed-sided domino array are displayed. Both arrays have a width $L = 10$ mm. (b) is supporting a second order resonance within the closed-sided cavity while (a) is supporting a fundamental mode. Now inspect mid-width of both arrays.

At this position, as illustrated by the dashed white line, Figure 4.9 (a) is at an anti-node and the time-averaged electric field is maximal. Conversely, the time-averaged electric field shown in Figure 4.9 (b) at the same position mid-width of the array is experiencing an node and is minimal. Therefore, if these structures were placed in proximity to one along, in a 1D uniform array, there would be no modal overlap between the two modes mid-width of the array and one mode would

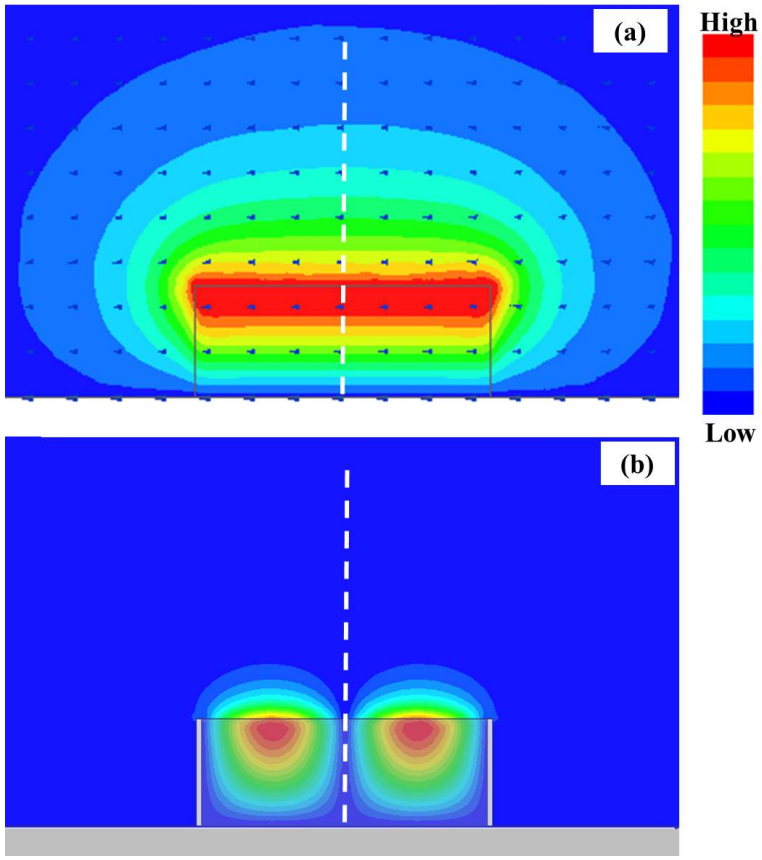

Figure 4.9: Numerical models of the time-averaged electric field of a surface wave on resonance supported by (a) a domino array and (b) a closed-sided domino array. Both arrays have a width $L = 10$ mm. (b) is supporting a second order resonance within the closed-sided cavity while (a) is supporting a fundamental mode. The arrows in (a) are indicative of the magnetic field of the mode. The dashed white line is used for comparison of the mid-width of both arrays and is used for comparison only.

not couple to the other.

The analytical technique detailed here has been previously discussed in Section 3.5 in context with other publications that have used analytical methods to calculate dispersion.

4.5 Discussion

Figure 4.10 shows the experimentally determined dispersion of the domino structures of lateral widths of $L = 100$ mm ($\gg$ c / $f_{\mathtt{res}}$) and $L = 1.60$ mm ($\ll$ c / $f_{\mathtt{res}}$) compared to the analytically calculated dispersion for $L = \infty$ where $f_{\mathtt{res}}$ is the limiting frequency of the surface wave.

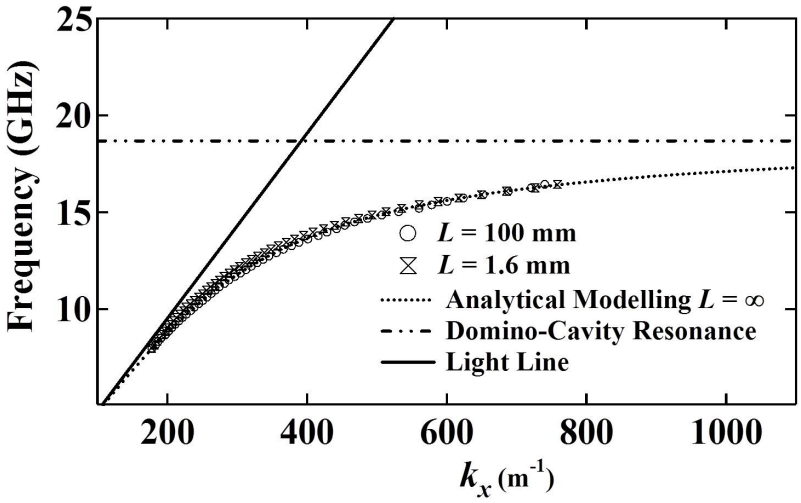

Figure 4.10: Experimentally obtained dispersion curves (symbols) of surface mode supported by samples with $L = 100$ mm and 1.60 mm compared with analytically derived dispersion (lines) for a structure represented by inset schematic. Pitch $d = 1.6$ mm, Height $H = 3.75$ mm, $a = d/2$, near field source to detector length $P = 775$ mm, lateral widths L are varied.

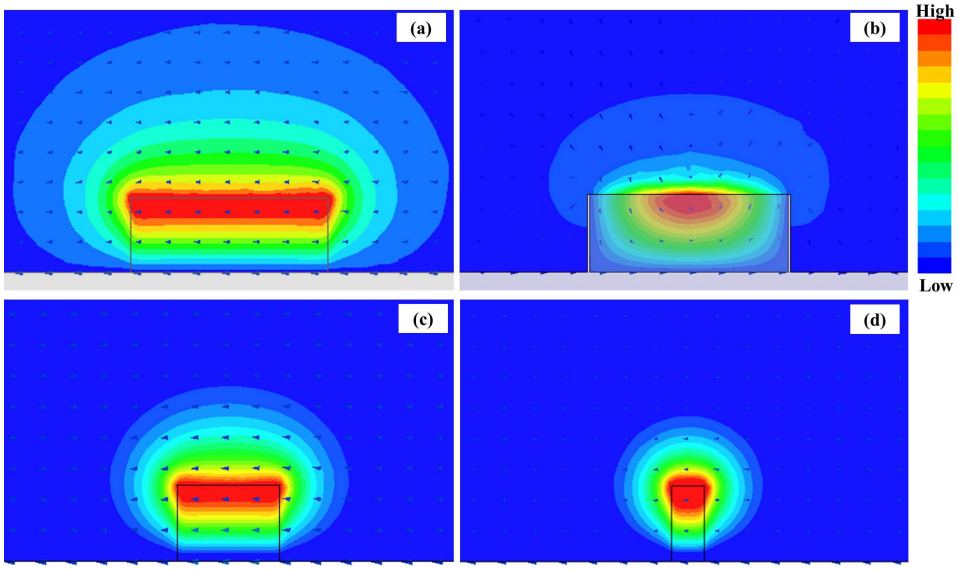

Figure 4.11: Numerical simulations of time-averaged electric field (regions of high to low field represented by the colour scale, arbitrary units) and vector magnetic field (arrows) on resonance of the domino waveguide consisting of (a) open-ended cavities, $L = 10$ mm and (b) closed-ended cavities, $L = 10$ mm. The slice of field in the middle of the cavity in the yz-plane is clearly seen to be quantised by boundary conditions imposed upon it by the closed ended structure (b). (c) and (d) display simulations of $L = 5$ mm and $L = 1.6$ mm open-ended cavities, respectively. The mode remains unquantised, even when the width of the supporting structure is subwavelength.

4.5.1 Boundary Conditions

In Figure 4.11 we plot field profiles for a surface mode on an $L = 10$ mm sample with open and closed sides (left and right respectively). It is apparent from the arrows overlaid on Figure 4.11 (left) that the magnetic field is polarized parallel to the edge of the domino and remains unquantized in the y-direction. The vector of the magnetic and electric fields of the supported surface wave on resonance is plotted in Figure 4.3. The magnetic field loops associated with the surface wave can be observed, however within the domino cavity the magnetic field is seen to be polarized parallel to y-axis.

Therefore it presents no significant contribution to the total wavevector of the cavity mode. The insensitivity of the dispersion and, in particular the asymptotic limit of the DP mode to L is therefore due to the open-ended nature of cavity sides parallel to the xz-plane. This total wavevector k_0 is a sum of the components of the wavevector in three dimensions express thus

$$k_0^2 = k_x^2 + k_y^2 + k_z^2 \tag{4.8}$$

As there is no boundary condition imposed on the field in the y-direction there is no component of k_y which will contribute to the in-plane wavevector k_x where $k_x^2 = k_0^2$ - k_z^2. Therefore the domino structure can be decreased in width until it is far subwavelength without perturbing the supported surface wave.

4.5.2 Closed-Ended Cavities

To substantiate this hypothesis, we have carried out dispersion measurements and FEM modelling for waveguides comprised of cavities with open ends and closed metallic (perfect electrical conductor, PEC) ends each with lateral domino width of $L = 10$ mm as represented by the insets of Figures 4.10 and 4.12 respectively.

Changing this boundary condition from open-ended to a metal reflecting plate (PEC) results in a lateral quantization of the electromagnetic field within the cavity, shown by the FEM model presented in Figure 4.11. This significantly affects the mode dispersion as shown by comparison of the $L = 10$ mm and $L = 100$ mm DP results displayed in both the experimental and FEM data (Figure 4.12). It is clear that for the closed-ended waveguide, even a modest lateral confinement (of order c / $f_{\mathtt{res}}$) due to the lateral domino width results in a drastically different dispersion of the surface mode compared to that of a mode supported by cavity widths of infinite extent ($L = \infty$).

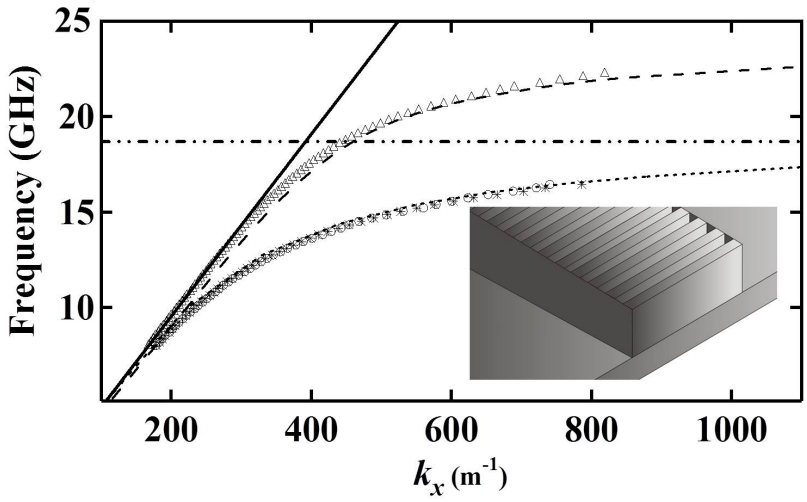

Figure 4.12: Dispersion curves obtained experimentally are represented by the symbols ◯, ∗ and △ which indicate data from the $L = 100$ mm closed-ended, $L = 10$ mm open-ended and $L = 10$ mm closed-ended structures respectively. Data obtained numerically (FEM) are represented by the short dotted line and long dashed line for the $L = 10$ mm open and closed-ended structures, respectively. The solid black line represents the light line and the intermittently dotted black line is the domino-cavity resonance. Inset is a schematic of the modified domino structure, the gray sides representing the closed boundary condition.

4.6 Conclusion

Present in this chapter is compelling experimental evidence that the domino waveguide supports a surface wave whose dispersion (including its asymptotic limit) is surprisingly insensitive to the lateral width of the structure. The surface wave supported by such a domino array structure has been shown to be confined to that structure both laterally and vertically. The dispersion of DPs for a range of lateral widths from 100 mm to 1.60 mm is measured, the latter being subwavelength compared to the excitation wavelength. Even for such narrow dominos, good agreement is found between the experimentally measured dispersion and the analytical relation expected for cavity widths of infinite extent. The reason for this insensitivity lies in the absence of a lateral quantization condition for the mode when the waveguide is comprised of open-ended cavities. This is compared and contrasted to experiments conducted on domino waveguide structures with close-ended cavities to affirm our understanding of the mechanism responsible.

Chapter 5

Microwave Surface Waves Supported by a Tapered Geometry Metasurface

5.1 Introduction

This chapter demonstrates the spatially dependent reduction of group velocity associated with a microwave surface wave. The metasurface supporting this mode is composed of a linear array of rectangular cavities whose lateral widths are varied as a function of distance from the point of excitation. This variation results in modification to the dispersion of the supported mode and, therefore, a spatially dependent modal index. Previous investigations of slowing propagating electromagnetic modes and further literature concerning stopping such phenomena are highlighted and compared with the present investigation. Both local electric-field and phase measurements are used to probe this condition, the latter of which is shown to be a more accurate identification of the trapping location of the surface wave. The reflectivity of the mode supported by two tapered metasurfaces close to this point is discussed and the effects of modifying the rate of taper is noted. The concurrent excitation and support of a family of higher order modes on the tapered metasurfaces in each experiment is explored and discussed. A large proportion of the contents of this chapter has been recently been published by the author of this thesis in Applied Physical Letters [95].

5.2 Background

The prospect of slowing and completely stopping light is an attractive focus for many areas of physics due to the number of technological applications that would

benefit from such control. The characteristic that defines slow light is a reduced group velocity, v_g in comparison to the speed of light, c. Equation 5.1 defines group velocity

$$v_g = \frac{d\omega}{dk} < c \tag{5.1}$$

where ω and k are the angular frequency and wavevector of the electromagnetic mode, respectively.

Applications where a reduced group velocity would be advantageous range from the fields of nonlinear optics such as Raman spectroscopy [112] and quantum optics to the fields of optical storage and switching in microwave photonics. Practically, slowing light results in stronger light-matter interactions as, by definition, the electromagnetic wave under investigation has a lower group velocity than if that same mode were travelling in free space. This can also be discussed in terms of the density of states of a system.

As previously discussed in Section 2.2.2.2, the dispersion of a surface wave is defined the relationship between propagating wavevector k of the mode as a function of frequency (ω). This can also be thought of as a change in the density of states of the system [64] and is described as $\frac{\delta k}{\delta \omega}$. At frequency far below that of the limiting frequency of the surface mode, there is a low density of states as the dispersion of the surface wave resembles that of a free space propagating photon. As the limiting frequency of the surface wave is approached the density of states increases, as there are more k states available per frequency component. The higher k components decay more rapidly into the surrounding medium and this systematic loss results in a width of the mode in frequency approaching resonance. There is a higher concentration of energy via these higher k values at the interface of the supported mode, resulting in stronger light-matter interactions [113].

Control of the bandwidth of these interactions is possible via the manipulation of the band gap of a photonic crystal waveguide and allows delay and temporary storage of optical signals [114].

A seminal example of slowing light to 17 ms^{-1} using electromagnetic induced transparency (EIT) has been achieved by Hau et al [115] over a very narrow bandwidth. Other methods include guiding a transverse electromagnetic mode along waveguides composed of different insulator-metal combinations or guides with a negative-index core clad in dielectric (insulator-negative-index-insulator) design [116, 117, 118, 119, 120] or indeed through photonic crystal (PhC) waveguides [121, 122, 123, 124, 125, 126].

5.2.1 Photonic Crystal Waveguides

A photonic crystal (PhC) waveguide is composed of a periodic array of dielectric layers, each with a different permittivity associated with it. The path of an electromagnetic (EM) mode through a PhC is dependent on both the layer arrangement and the changing refractive index experienced by the photon when propagating between the layers. This is analogous to the study of electron propagation through a semiconductor crystal; a periodic arrangement of atoms or molecules. The spatial position of electrons associated with the constituent atoms or molecules in the crystal form periodic potentials with clear allowed energy states. Therefore both the conduction properties and the lattice geometry of the crystal dictate the range of energy within each state. As such energy band gaps, i.e. the range of energy above or below the allowed states, may be engineered. The path of an electron through such a crystal is dictated by its interactions with these periodic potentials.

In the PhC case it is the refraction and reflection between the dielectric layers that define the allowed frequencies and directions of propagation of the mode through the system, creating band gaps. The bandwidth over which light can be slowed in a PhC waveguide is defined by the width of its bandgap; a result of the crystals periodicity. At these frequencies, delay and temporary storage of optical signals is possible [126].

The total thickness of such slow light waveguide structure is of the same scale as the wavelength of light itself and therefore larger than the electrical components required to connect to it, limiting minimum geometric size. However, surface plasmons polaritons (SPPs) [25] have provided a route to circumnavigate this limitation. SPPs are a resonant collective excitation of free electrons strongly localised at the interface between a metal and a dielectric, oscillating longitudinally and in coherence with incident visible light.

They are intrinsically slow transverse-magnetic (TM) polarised modes, whose electromagnetic fields exponentially decay into each bounding medium. Importantly, the mode can be manipulated on subwavelength structures; an aspect that has recently been exploited in slow wave devices including miniaturized photonic circuits, enhancement of Raman spectroscopy and sensing.

A photonic circuit would rely on using the subwavelength channelling properties of surface plasmons. Such a circuit would convert light into surface plasmons, which would then propagate along subwavelength channels to be processed by logic elements [25]. Another application of the slow light characteristic of surface plasmons is the electric field enhancement of the surface plasmon at a dielectric-metal interface. This is used to manipulate light-matter interactions and boost nonlinear phenomena. For example, surface-enhanced Raman spectroscopy (SERS)

relies on massive signal enhancement from structures much smaller than the wavelength of light. This enhancement could be greatly increased if these structures were supporting surface plasmons [26, 27].

5.2.2 Slow Light and the Dispersion Relation

It is known that light can be slowed down in dispersive materials near resonances [97]. The gradual decrease in velocity of an electromagnetic mode can be observed when plotting the frequency of the mode as a function of its propagating wavevector, the dispersion relation. Dispersion and the limiting frequency associated with a mode have already been discussed in Section 2.3. Specifically, the gradient of a tangent to the dispersion relation of the mode under inspection indicates its group velocity (Equation 5.1). Figure 5.1 is a schematic representation of the dispersion (a) of a surface wave (red line). Noted on each figure are two frequencies ω_1 and ω_2 and the tangent to the dispersion associated with those frequencies.

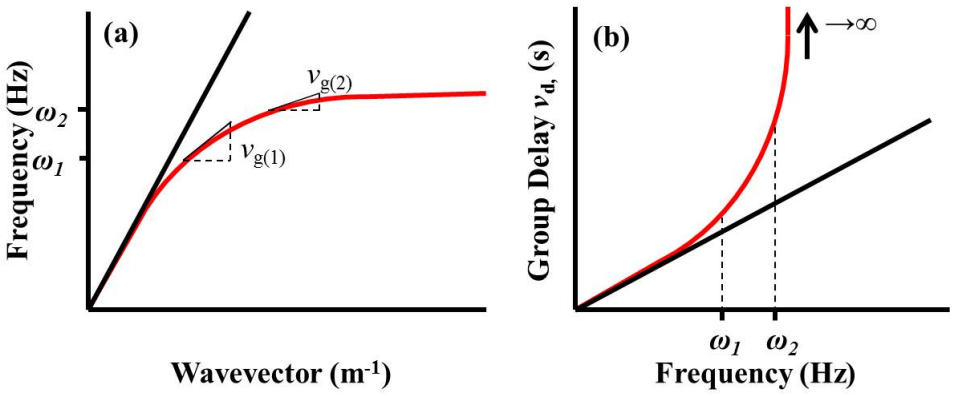

Figure 5.1: Schematic of dispersion (a) and group delay (b) of a surface wave approaching a resonant limit. (a) notes the group velocity at two specific frequencies by drawing a tangent to the dispersion at ω_1 and ω_2, illustrating the decrease in gradient of the dispersion curve (red) between these two points in frequency. (b) shows the behaviour of the group delay at these two frequencies and illustrates the reciprocal relationship between v_g and d_g, per unit length.

Clearly, the group velocity of the mode at frequency ω_1 is greater than that associated with the mode at ω_2. As the wavevector increases the gradient of the dispersion tends to zero. The frequency associated with this condition is known as the limiting frequency and has already been discussed in Section 2.2.4. Figure 5.1 also displays a schematic representation of the group delay (d_g, per unit length) of the surface wave in (b) and is described thus:

$$d_g = \frac{1}{v_g} \tag{5.2}$$

Equation 5.2 shows the reciprocal nature of the relationship between v_g and d_g, per unit length. By inspection of this relationship it is clear that the group delay of the mode will become infinite (i.e. the mode is stationary) when the group velocity falls to zero. Also, it is clear that group delay d_g is in fact a measurement of the density of states of a systems, $\frac{\delta k}{\delta \omega}$, and becomes infinite at the resonant frequency of the mode.

Strictly any electromagnetic mode cannot be completely stopped before Ohmic losses become dominant [127], an example of which is an SPP supported by a Drude-like metal. As previously stated during the discussion of density of states, on approach to the resonant frequency more k states become available at greater values of k, decaying into the surrounding media. Therefore an actual 'stopping' location for a surface wave will never actually be measured. Practically, the tangent to a measured dispersion curve, as is seen in Figure 5.1 for the highest value of k measured with respect to frequency will result in a measurement of the velocity of a supported surface wave such as an SPP.

However, it has been shown that a somewhat analogous mode to the SPP, with a similar dispersion, can be supported at microwave frequencies on metals patterned with subwavelength features [50]. Such structures are known as metasurfaces [59] and can be described as a single layer of periodically arranged subwavelength elements arranged in a dielectric host which gain their electromagnetic properties from geometric design and not their constituent materials. Without such surface structure a metal would be unable to support a confined microwave surface wave due to its near-perfectly conducting nature in this frequency regime [32, 128].

The collective resonant frequency of these metallic elements is synonymous with the surface plasma frequency of the aforementioned case because it is this limiting frequency, below which the necessary boundary condition (inductive surface impedance [69]) is induced for TM-polarised surface waves to be supported. The surface plasma frequency and the confinement of a surface wave has previously been discussed in Section 2.4.

At frequencies much lower than this limit, the surface wave is photon-like, however on approach to this limiting frequency it becomes highly localised to the metasurface, and its group velocity reduces to zero. Such behaviour has been experimentally demonstrated on metasurfaces for a range of geometries, including open-ended grooves[91] , holes [67],[28] and Sievenpiper mushrooms [68].

5.2.2.1 Radar Beam Sharpening

The localisation of a mode supported by a metasurface and the dispersive properties of that mode can be utilised for pulse compression during Doppler radar

operations [129]. This application results in the radar transmitting what is commonly referred to as a 'long pulse' while gaining the potential benefits of the transmission of a 'short pulse', a pulse transmitted over a time duration which is less than that of a long pulse. Typical long pulse and short pulse values are 2μ seconds and 0.5μ seconds respectively.

The benefits of transmitting a short pulse are greater range resolution and accuracy, better multipath resolution and therefore better target classification. However, if a radar transmitter is peak-power limited, the shorter the pulse the less energy transmitted. Therefore transmission of a short pulse results in a range limited measurement in comparison to a long pulse measurement.By compressing a long pulse, the benefits of greater range resolution and accuracy, better multipath resolution and therefore better target classification is regained and the measurement is not range limited.

Pulse compression can be described as applying some modulation to the transmitted waveform such as another known waveform at a different frequency. The response is analysed after the frequency modulated pulse is passed through a pulse-compression filter. An example of this would be to send a waveform of a sine wave whose frequency is increased linearly over the duration of the pulse. This is known as 'chirp' pulse compression. The modulated sine wave is then passed through a pulse compression filter which is designed so that the velocity of propagation through the filter is proportional to frequency. The filter acts as a dispersive delay line in that the velocity components of the wave are separated so that the higher frequency components of the waveform increase in velocity at the trailing edge of the pulse relative to the lower frequencies at the leading edge, sharpening the pulse.

A metamaterial surface which supports surface waves is described as a dispersive device, with the mode on the surface exhibiting a wavelength which decreases as a function of frequency faster than the wavelength of a free space mode. It is suggested that such a surface could be used to modulated the transmitted and received waveform from the a radar and result in pulse sharpening.

5.2.3 The Proposed Experiment

In this study, we experimentally demonstrate the spatial separation of frequency components associated with a microwave surface wave supported on a tapered metasurface. This slow-wave structure is composed of a linear array of constant depth, closed-sided air-filled rectangular cavities obtruding from a planar metal sheet. Two samples of this description are fabricated with their lateral widths tapering from $L_{\texttt{Start}}$ to $L_{\texttt{Finish}}$ (where $L_{\texttt{Start}} \ll L_{\texttt{Finish}}$), the dimensions of which

are schematically depicted in Figure 5.2. By increasing the lateral width of each cavity as a function of distance from the point of excitation, we modify the dispersion of the surface wave by lowering its limiting frequency. In this way, frequency components of the surface wave are slowed (due to an increase of their modal index, $n = c/v_g$), and consequently trapped so that they cease to propagate further along the array. We demonstrate that local electric-field observations alone are not sufficient to determine the trapping point of the mode, however utilisation of the local phase provides a more accurate method to probe this condition.

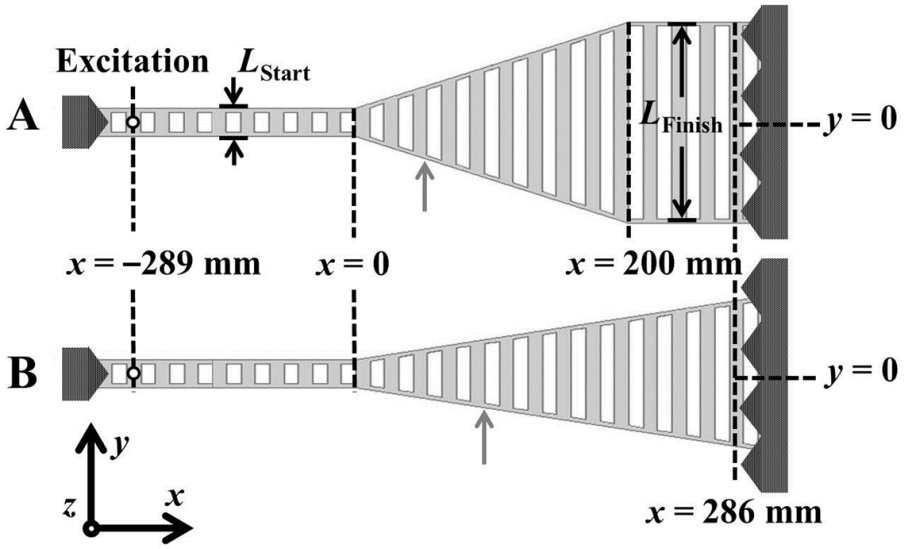

Figure 5.2: (a) Schematic of Samples A (top) and B (bottom) as viewed from above (white regions detailing internal structure are for illustrative purposed only). On both samples the tapering begins at $x = 0$ with lateral width $L_{\texttt{Start}} = 1.6$ mm. The taper ends with $L_{\texttt{Finish}} = 48.5$ mm at $x = 200$ mm for sample A, and $x = 399$ mm for sample B with $L_{\texttt{Finish}} = 50$ mm. The position of the coaxial probe providing near field excitation is also shown. Microwave foam absorber is used to prevent reflections at each end ($x = 297$ mm and $x = 286$ mm) of samples A and B. The small grey arrows indicate the x-position on the sample where $L = 16.8$ mm.

5.3 Experimental Setup

A vertically orientated antenna (2.5 mm of unshielded core) provides near-field excitation of the surface wave. This is used instead of the edge coupling method previously defined in Section 3.3 as comparitively larger amplitude of the mode supported on the tapered array of larger and small width of the structure results in the probe being able to approximately uniformly excite the surface modes. The probe attached to port 1 of a vector network analyser (VNA) via a coaxial cable

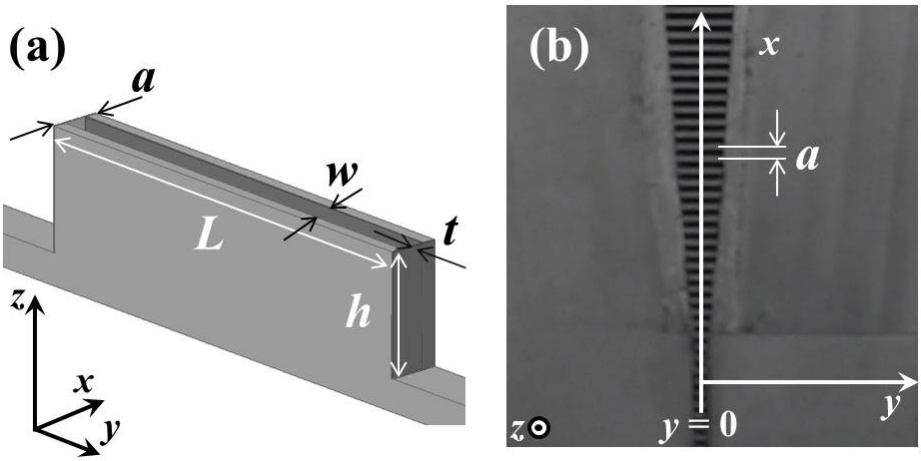

Figure 5.3: (a) A schematic illustration of a unit cell of the samples, where L is the lateral width of the cavities, cavity height $h = 3.75$ mm, wall thickness $t = 0.1$ mm, periodicity $a = 1.59$ mm and cavity width $w = a/2$. (b) An photograph of a small section of the sample as viewed from above, the position of the white arrow indicates where $y = 0$ along the x-direction.

and is driven between the frequencies of $8 - 40$ GHz. The probe remains in a static position throughout the experiment at $x = 289$ mm, $y = 0$ mm (mid-width of the array), and height $z' = 0.25$ mm (above the obtruding metallic cavities).

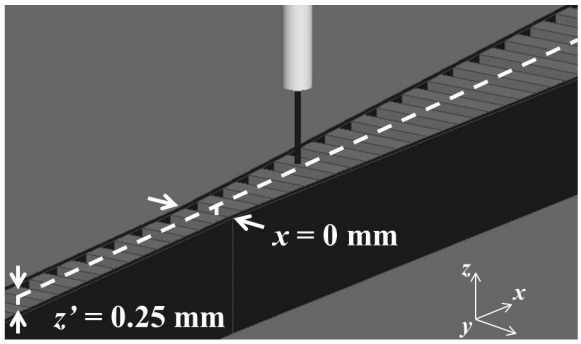

Figure 5.4: Schematic measuring probe, a vertically oriented antenna, above the tapered array. The white dashed line represents the path of the detecting antenna above the tapered metasurface at $y = 0$ mm. Notice the path is at a height z' = 0.25 mm above the metasurface. The position of $x = 0$ mm is also noted. At x¿ 0 the width of the taper starts to increase.

A second identical probe is also positioned at the same coordinates in y and z but is scanned along the length of the array (x) via operation of a computer controlled motorised stage. Figure 5.4 is a schematic representation of this second probe. Noted in this figure is the height, z, of the probe and the position along the tapered array where x has been defined as 0. The local electric field amplitude and phase of the surface wave is detected via connection of this second probe to port 2 of the VNA.

5.3.1 Spatially Dependent Dispersion

In order to fully understand the slow light phenomenon associated with the surface wave excited on tapered samples A and B, it is first useful to study the dispersion of surface modes associated with one-dimensional periodic array of rectangular cavities with uniform widths. Figure 5.5 (b) displays the predicted dispersion of surface waves supported by a one-dimensional array of cavities of uniform widths $L = 1.6$, 16.8 and 48.5 mm.

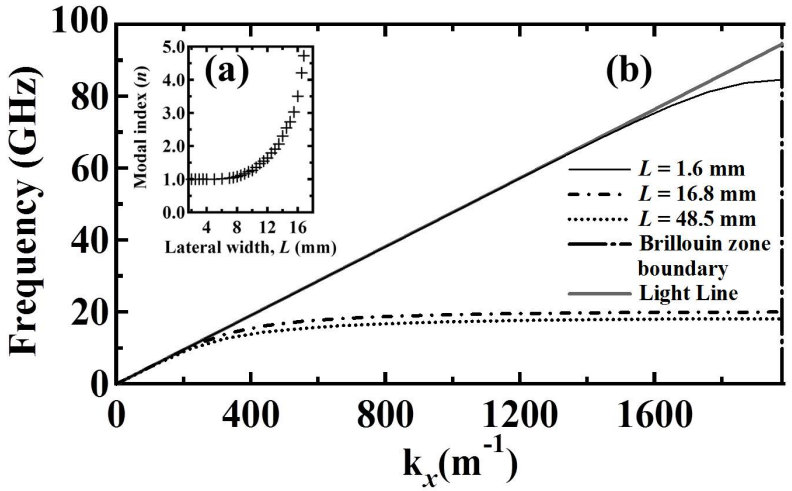

Figure 5.5: Predicted dispersion of surface wave supported by a linear array of identical cavities of height $h = 3.75$ mm, periodicity $a = 1.59$ mm and cavity width $w = a/2$ in instances of $L = 1.6$, 16.8 and 48.5 mm. Inset: Predicted modal index of the supported wave at different lateral widths L for 20.0 GHz. These predictions have been obtained via FEM modelling [130] to find the eigenmodes of a unit cell of the structure bounded by periodic boundary conditions in the xz-planes). Since the modes of interest are TM polarised, and the unit cell is infinite in the y-direction, perfect-magnetic boundary conditions are utilised on yz-planes to limit the unit cell dimension. The model geometry is bounded 45 mm above the metasurface by a free space boundary. The predictions of modal index are calculated thus: $n = c/v_g$.

5.3.1.1 An Array Composed of Finite Depth Cavities

Consider the regions defined by x ∈ [297, 0] and x ∈ [200, 285.25] (in units of mm) along sample A that have a lateral width L of 1.60 and 48.5 mm respectively. In both of these regions the width is constant and hence the modal index (n) of the supported surface wave is dependent on frequency only. The surface mode dispersion is asymptotic to a frequency, to a first approximation, dictated by the lowest order Fabry-Perot resonance of the transverse electric (TE_{01}) waveguide mode supported in the cavity [67, 131, 132, 93].

5.3.1.2 Modal index of the Tapered Metasurface

The exact limiting frequency is numerically determined via FEM modelling for arrays of constant width L = 1.6 mm, 16.8 mm and 48.5 mm to be 84.6 GHz, 20.0 GHz and 16.4 GHz respectively (Figure 5.5(b)), i.e. we would expect the 20 GHz component of the surface mode to have $v_g = 0$ and be trapped when L = 16.8 mm.

5.3.1.2.1 Far below each limiting frequency, the surface mode is photon-like (i.e. lies close to light line), with a modal index n $\sim$ 1. However the surface mode supported by the tapered array propagates from the narrow width region (higher limiting frequency) to the wider width region (lower limiting frequency). Therefore the modal index is dependent on both frequency and x-position along the sample. Consequently, frequency components of the surface wave between these limits will be spectrally separated and prevented from propagating further with the highest frequencies being slowed and trapped closest to the start of the taper. Further to this we consider two samples with different gradients of taper ($\Delta L/\Delta x$) and contrast the reflection of the surface mode in each case.

5.4 Discussion

Figure 5.6 illustrates measurements of local amplitude and phase of the electric field as a function of position in x along Samples A and B at 20, 25 and 30 GHz. Note that the VNA measures local phase by sampling the fields of the detected surface wave and excitation source. By comparing these values a local phase difference is obtained, limited to the range π to π radians, which is periodic in x and indicative of the surface mode wavelength $\lambda_{\mathtt{SW}} = \lambda_0/n$ where λ_0 is the excitation wavelength.

Consider the global peak in the field amplitude data at x = 43 mm for Sample A, and x = 77 mm for Sample B (Figure 5.6 (a) and (b)). These peaks are indicative of an increase in the energy density of the surface mode associated with a reduction in its group velocity as the sample is traversed. Naively, these peaks may be viewed as an indication of the positions along the array at which the surface mode is trapped [133], after which it is no longer supported. However it should be remembered that the increase in the modal index (and propagation constant, k_x) is accompanied by a reduction in the decay length ($\frac{1}{2k_z}$) of the mode above the surface, in order to conserve momentum. It is therefore clear that any measurement of the field magnitude at a fixed height above the sample (where z' = 0.25 mm, Figure 5.4) will be unable to accurately probe the exact trapping location of a surface wave. After this peak, the locally measured field amplitude

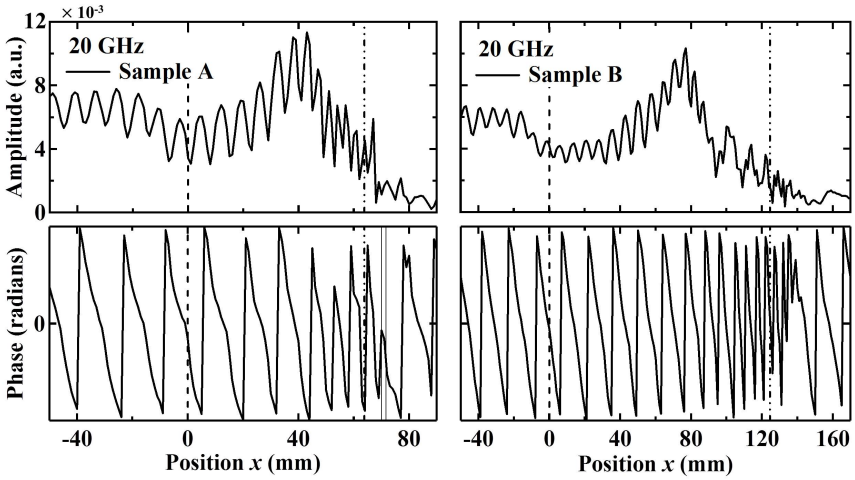

Figure 5.6: Experimental observations of local field amplitude (top) and phase (bottom) of the surface wave at fixed frequency of 20.0 GHz as a function of distance x along sample A (left) and sample B (right). Vertical black dashed line indicates the position of the start of the taper ($L = L_{\texttt{Start}}$). The dot-dash line indicates the x-position of $L = 16.8$ mm along sample A where, for a 1D array of fixed width cavities, 20.0 GHz is the limiting frequency. This position is indicated by the grey arrow in Figure 5.2. The position of $L = 16.8$ mm on sample B is indicated in the same fashion as on sample A; a dot-dash line. Thin vertical black lines on the lower part of (a) indicate the spatial extent of the pitch.

gradually falls to zero, indicative that the mode eventually ceases to propagate [128, 133, 127, 134] due to a combination of Bragg diffraction from the periodicity of the array and dissipative loss into the metal. Subsequently the exact trapping location of the surface wave is ambiguous as this zero condition occurs at some distance after the field peak. However, by measuring the local phase of the surface wave this condition can be more accurately observed and commented upon, as can the increasing modal index of the surface wave on approach to this location.

It is clear from the periodicity of the oscillation in the phase data in Figure 5.6 that $\lambda_{\texttt{SW}}$ has a value that is associated with the free space wavelength ($\lambda_0 =$ 15 mm at 20 GHz) at $x = 0$ where $L = L_{\texttt{Start}} = 1.6$ mm (Figure 5.8(a)) and the mode is photon-like (Figure 5.5). Beyond this position, $\lambda_{\texttt{SW}}$ gradually decreases (n increases) until some minimum value is reached. This recorded minimum occurs at $x = 70$ mm and 135 mm on samples A and B respectively (Figures 5.6 (a), (b) and 5.8(b)). Whereas the measured amplitude of the surface wave fields also reduce to the noise floor at a similar position (i.e. propagation of the mode is forbidden), the phase data is more resilient at low signal levels and is less sensitive to variations in the background signal level. The phase information can therefore be used to pinpoint the trapping location of the surface mode more precisely.

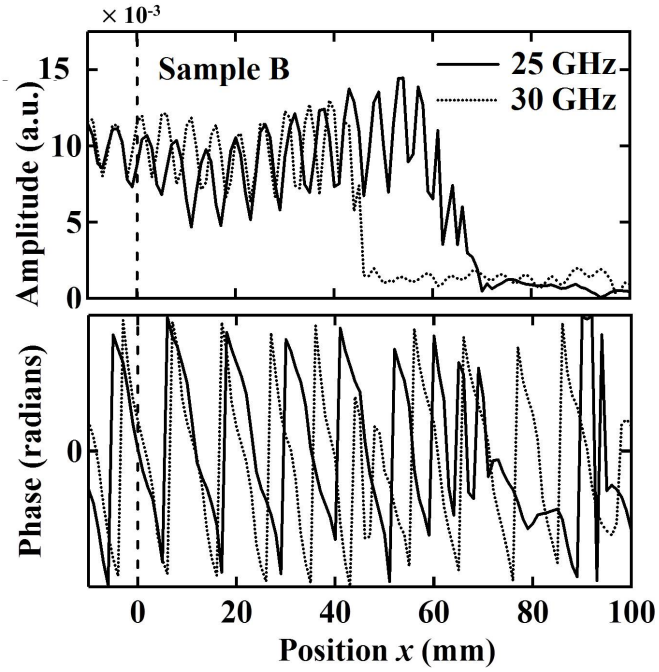

Figure 5.7: Experimental observations of local field amplitude and phase of the surface wave at fixed frequencies as a function of distance x along sample B at 25 and 30 GHz.

5.4.1 Modal Index Approaching the Limiting Frequency of the Mode

Note that on approach to the trapping location modal index increases (Figure 5.9), but is limited by the Brillouin zone boundary because the surface wave wavelength becomes comparable to the pitch of the supporting structure. The pitch of the structure in comparison to the locally measured phase of the surface wave can be seen in Figure. 5.6). At this condition the surface wave is subject to Bragg reflections due to this photonic effect. In addition, our probe is no longer able to spatially resolve the phase in this limit due to its finite scattering cross section, and the phase does not reach π. The observant reader will note that, after this position, the periodicity of the phase data recovers its free space value, a subject addressed in due course.

5.4.2 The Trapping Location of a Surface Wave

Also apparent in Figure 5.6 is that the trapping position occurs at a distance along the sample beyond that which we would expect from our previous numerical modelling. Experimentally (Figure 5.6) we observe this to occur at $x = 70$ mm and $x = 135$ mm along Samples A and B respectively for the 20 GHz component of the surface wave. In both cases, the trapping position corresponds to a lateral cavity

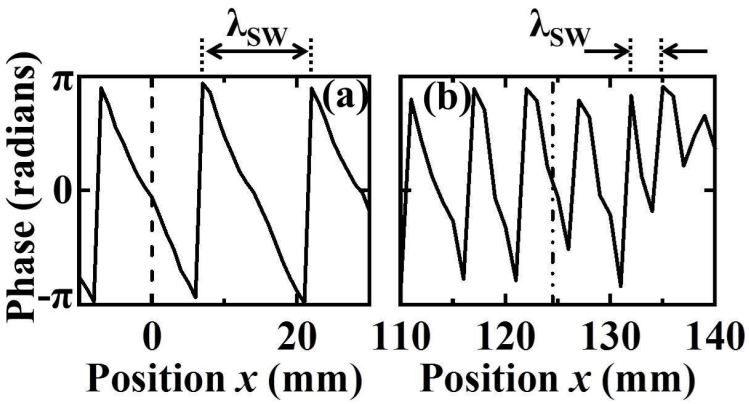

Figure 5.8: Experimental observations of local field amplitude and phase of the surface wave at a fixed frequency of 20 GHz as a function of distance x along sample B. (a) and (b) Closer inspection of the local phase measured from the mode supported by sample B on Figure 5.6. The periodicity of oscillation in recorded phase corresponding to surface wave wavelength ($\lambda_{\mathtt{SW}}$) supported on two regions in x along Sample B at 20 GHz is highlighted by the arrows.

width of $L = 18.0$ mm on a non tapered sample. However numerical predictions of the limiting frequency (inset Figure 5.5) suggest that this limit should occur on a region of the waveguide corresponding to $L = 16.8$ mm.

To explore this discrepancy further, the experiment was replicated in two numerical model. Figure 5.10 compares experimental data of locally measured amplitude with numerical data obtained via FEM modelling of a surface wave supported on sample B. Both data sets are normalised. A probe is used to excite a surface wave in both of the numerical cases presented (red and grey curves). However, the red data is indicative of the time-averaged electric field measurement in a model where a probe is drawn at $x = 127$ mm, mimicking the location of the probe in the actual experiment. The grey data represents the same system where the surface wave is excited via a probe. However, in contrast to the previous numerical model, the probe used to mimic the measuring probe in the experiment is not drawn into the model. Comparison of these two models with experimental data is used to ascertain what, if any, effect the scattering cross section of the probe used to measure the fields of the surface wave might have on the supported surface wave.

The modelled data is obtained by defining a line at height $z = 0.25$ mm above the metasurface, sampling the modelled electric field amplitude at a height level with the tip of the detecting probe. The experimental data is obtained by a probe of exposed coaxial wire of length 2.5 mm therefore samples a larger volume in z of the amplitude of the fields supported by the surface wave. The difference in the spatial position of the overall peak in the experimental data in comparison to the

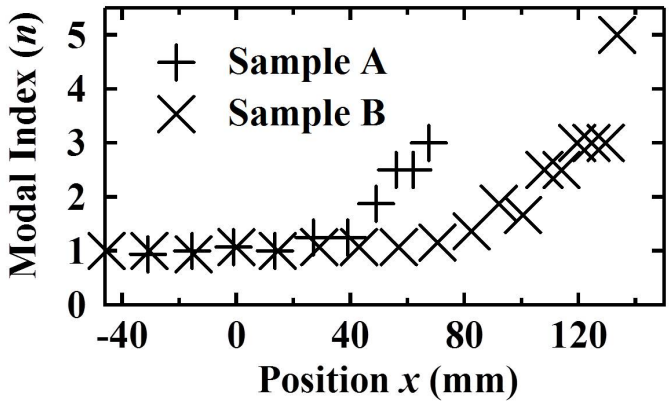

Figure 5.9: Experimentally derived modal index as a function of distance along samples A and B at 20 GHz illustrating an increasing modal index (decreasing group velocity) with reduction of the asymptotic frequency. For both samples the surface mode is supported at 20 GHz until the width of the supporting structure becomes $L = 18.0$ mm.

numerical data can be attributed to this aforementioned difference in detection. Further, the sharp spike in the red data at $x = 127$ mm after the overall peak can be attributed to the tip of the detecting probe interacting with the electric field of the supported surface wave. This spike is noted by the black arrow in Figure 5.10. There is no spike of this nature in the grey data as the model was solved without a detecting probe in the geometry. In the experimental data this effect is incorporated in the measurement of the surface wave and cannot be observed directly.

By observation of the extension of the field associated with the surface wave without a probe in comparison to the measured field with a probe it is clear that there is a small extension of the local field amplitude due to near field coupling between the detecting probe and the propagating surface wave. However, it is too small a contribution to completely account for this discrepancy. Therefore we propose this discrepancy is associated with the intrinsic width of the mode itself.

This conclusion is supported by the observation that the spatial separation of cavities corresponding to $L = 16.8$ mm and $L = 18.0$ mm is different for the two tapered samples.

5.4.2.1 Loss Mechanisms

The finite width of the mode can be attributed to three radiative decay channels and one intrinsic loss mechanism that all surface waves supported by metamaterial structures are subject to; ohmic loss. The three radiative decay channels include the scattering of the mode out of the surface due to mode shape mismatch, Bragg

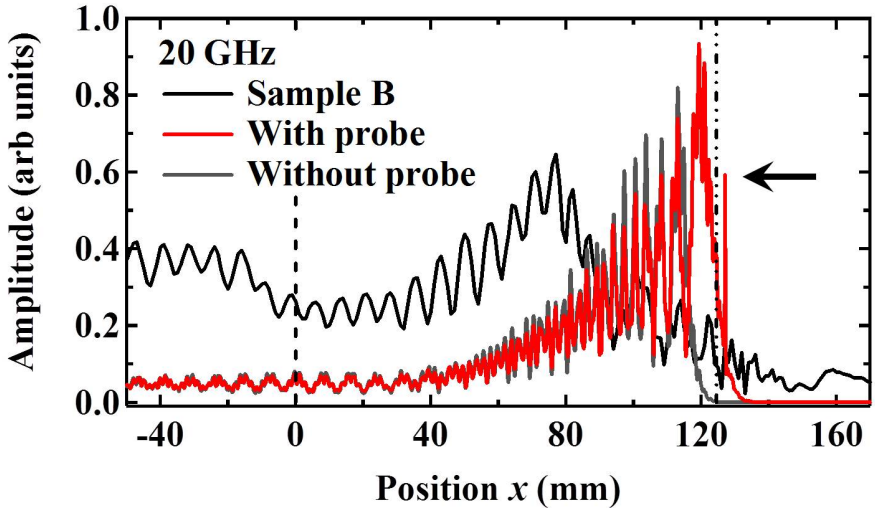

Figure 5.10: Experimental (black) and numerical (red and grey) observations of a surface wave supported on Sample B at 20 GHz. Numerical observations obtained via FEM modelling and compare the amplitude of the surface wave at $z = 0.25$ mm above sample B, with(red) and without (grey) a measurement probe present in the modelled system. The trapping location previously shown in Figure 5.6 is also marked with a vertical black dot-dash line. The arrow indicated the spike in the red numerical data illustrates the position of the measuring probe drawn into the model and is due to the proximity of the probe.

reflection and loss due to coupling to the probe.

Consider the first mechanism, scattering of the mode out of the surface. A microwave surface wave is supported by a coherent oscillation of resonant elements, such as cavities. If the geometry of one element differs significantly from a neighbouring element, the shape of the electric fields supported by the element will be modified with respect to that of the neighbour. In this case, the overall resonant response of the array will be effected. In an extreme case, when there is no modal overlap (as discussed previously in Section 4.4.3) or when a the medium through which the surface wave is propagating changes suddenly (for example, a terminating metallic boundary) there will be a reflection. At this point the surface wave will be scattered into free space, as well as back in the direction of propagation and energy is dissipated.

The second mechanism, Bragg reflection, occurs when the period of the surface wave becomes comparable to that of the pitch of the supporting structure. Therefore, a reflection occurs.

Loss due to coupling to the probe can be due to a lack of field overlap between the detected field and the measuring probe or excitation of the resonant condition of the probe. This is minimised by ensuring the first resonant condition of the probe occurs far above the frequency of measurement.

Ohmic loss is due to the interaction of the electric field decay of the surface

wave into the supporting metallic structure and, for a real material is unavoidable. At microwave frequencies a metal can be approximated to behave like a perfect electrical conductor with and infinite conductivity, therefore electric field will not penentrate into the surface. However, on approach to the resonant condition of the surface wave structure this approximation fails and there is loss, due to an increased density of states, into the metal.

5.4.3 Amplitude of Oscillations in Local Field Intensity

Consider next the oscillations in the local field amplitude data (Figures 5.6 and 5.7). They arise from a forward propagating surface wave mixing with a reflected mode, to produce an oscillation with period of $\lambda_{\mathtt{SW}}/2$. This reflection is due to Bragg reflection, and also a mismatch in the overlap of the fields of the surface wave, which is more significant for the shorter taper with a larger gradient ($\delta L/\delta x$). The amplitude of these oscillations is indicative of the strength of reflection experienced by the surface mode [127]. Therefore by inspection of Figure 5.6 it is clear that a 20 GHz surface wave supported by sample A experiences a reflection amplitude that is over twice that of a surface wave supported by sample B. This is unsurprising as the rate of change of limiting frequency and modal index in sample A occurs spatially at more than twice the rate of sample B.

5.4.4 Oscillation Insensitivity

To ensure the amplitude of oscillations of the supported surface wave is not dictated by the termination of the surface wave an experiment was carried out wherein the terminating boundary condition at the end of a sample was changed.

Figure 5.11 presents the amplitude of the electric field associated with the surface wave supported on sample A at 15 GHz. A comparison can be made between the amplitude of the surface wave when sample A is terminated with absorber and when the mode is terminated with a metallic sheet. This is represented by the solid red and pink lines respectively. By inspection of both red and pink data sets it is apparent that the terminating boundary at the end of the taper does not effect the measured oscillations.

To contrast this the electric field associated with a surface wave supported by a one-dimensional array of rectangular cavities of uniform lateral width $L = 1.6$ mm was measured. When the array was terminated by an orthogonal metal wall the oscillations in the measured field were large in comparison to the case of the same supported surface wave terminated with an absorber boundary the oscillations, as seen by the grey and black data sets respectively. The oscillations are much greater when the surface wave is terminated by a metallic boundary supported by

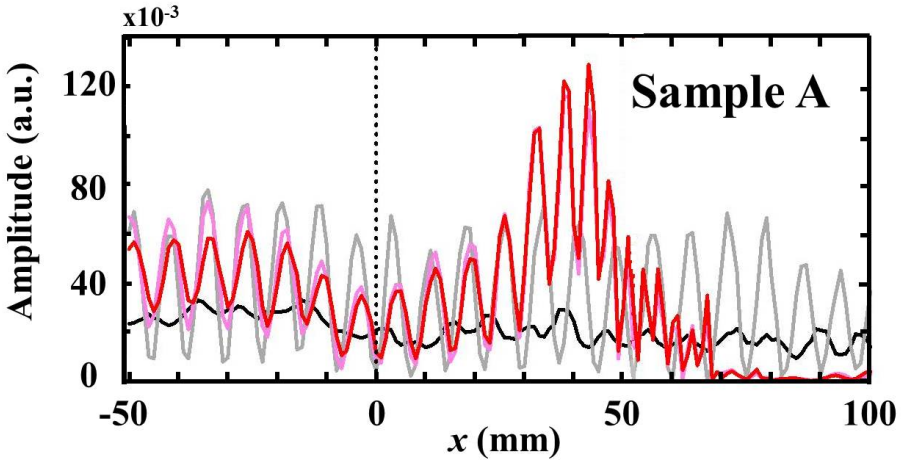

Figure 5.11: Experimental observation of the amplitude of the electric field associated with the surface wave supported by sample A. The pink and red data depict measurement of a surface wave supported on sample A terminated in a metal wall or an absorbing boundary, respectively. In contrast to this the black and grey data depict a measure of the amplitude of electric field associated with a surface wave supported by a 1D array of close-sided cavities with uniform width $L = 1.6$ mm. The former (black) is terminated by absorber and the latter (grey) is terminated by a metal wall, orthogonal to the propagation direction of the surface wave.

a uniform array and is shown to be sensitive to its termination boundary condition.

Therefore, the oscillations observed when measuring the amplitude of the electric field associated with the surface wave supported by samples A and B can be attributed to both Bragg reflections and the non-adiabatic nature of each taper. The oscillations are insensitive to the terminating boundary condition of the sample.

5.5 Multi-Modal Excitation

Now inspect the local field amplitude and phase of the surface wave after the trapping point is observed (Figure 5.6 and 5.12).

Quite unexpectedly the spatial periodicity of the oscillations in the phase recover their free space value ($n = 1$) whereas we would expect there to be no data beyond this point since the forward propagation of the fundamental mode is forbidden. Figure 5.12 (a) shows an experimental field plot in the xy-plane just above the top of the cavities while (c) shows field predictions obtained from FEM numerical modelling of the entire geometry of sample A. The model geometry is surrounded by absorbing ('radiation') boundaries positioned over one wavelength away from the tapered cavity structure in the xz-planes and used as termination boundaries in the yz-planes, similar to the microwave foam absorber in experiment.

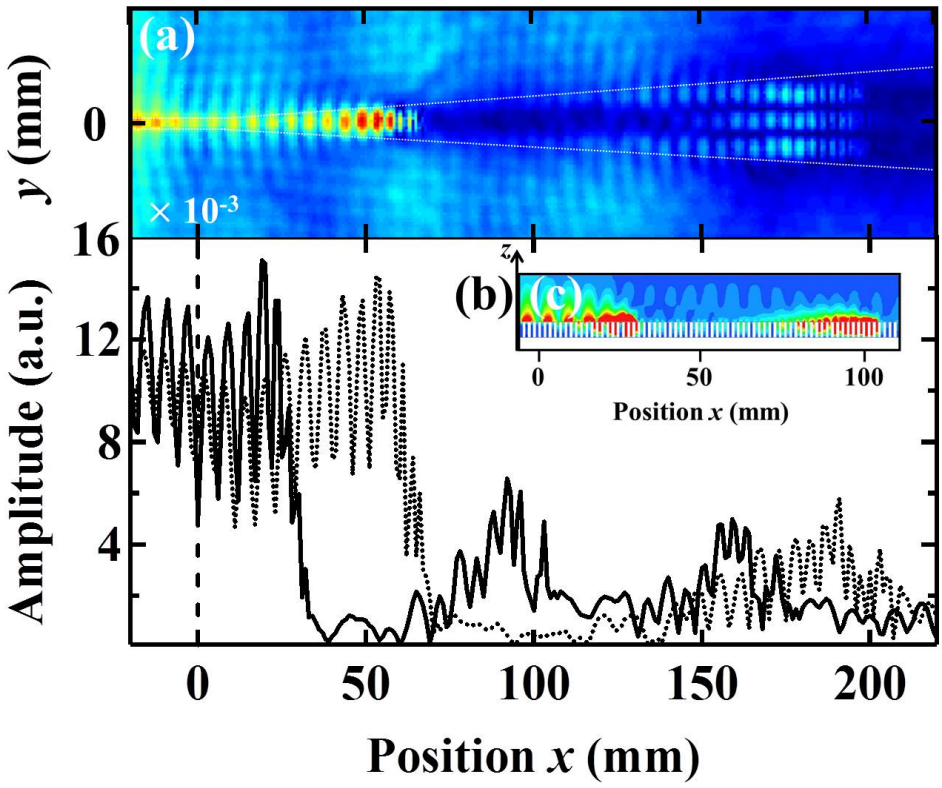

Figure 5.12: (a) Experimental field plot in the xy-plane (i.e. top down view) of electric field amplitude at 25 GHz on sample B. White dashed line indicates the edge of Sample B. (b) Experimental observations of local field amplitude of the surface wave at 25 GHz as a function of distance x along samples A (solid black line) and B (dotted black line). Vertical black dashed line indicates the position of $L_{\texttt{Start}}$. Both (a) and (b) are at the same fixed height above the sample, 0.25 mm. (c) Predictions of time-averaged electric field of the supported mode at 25 GHz on sample A in the xz-plane, note the re-radiation of the lowest order mode. Regions of high and low field are red and blue respectively for (a) and (c).

Termination boundaries are further detailed in Chapter 3.

Figure 5.12 clearly illustrates that there exists a mode further along the array with higher quantisation in lateral width (three antinodes). This is a surface wave associated with the lowest order Fabry Perot resonance of the TE_{03} waveguide mode in the cavities [100], with a limiting frequency greater than that of the original TE_{01} mode. It is excited by fields scattered into free space at the original trapping point (Fig. 5.12 (c)), and therefore both the fundamental and the higher order surface mode of the array can be observed at the same fixed frequency. Further experimental field plots of both sample A and B are observed in Figure 5.13 at 20 GHz, 25 GHz and 30 GHz which illustrate the concurrent excitation of multiple modes of the supported surface wave. The excitation of the surface wave associated with the TE_{05} waveguide is also apparent from inspection of the amplitude data from Sample A in Figure 5.12 (b) at $x = 163$ mm and Figure 5.13,

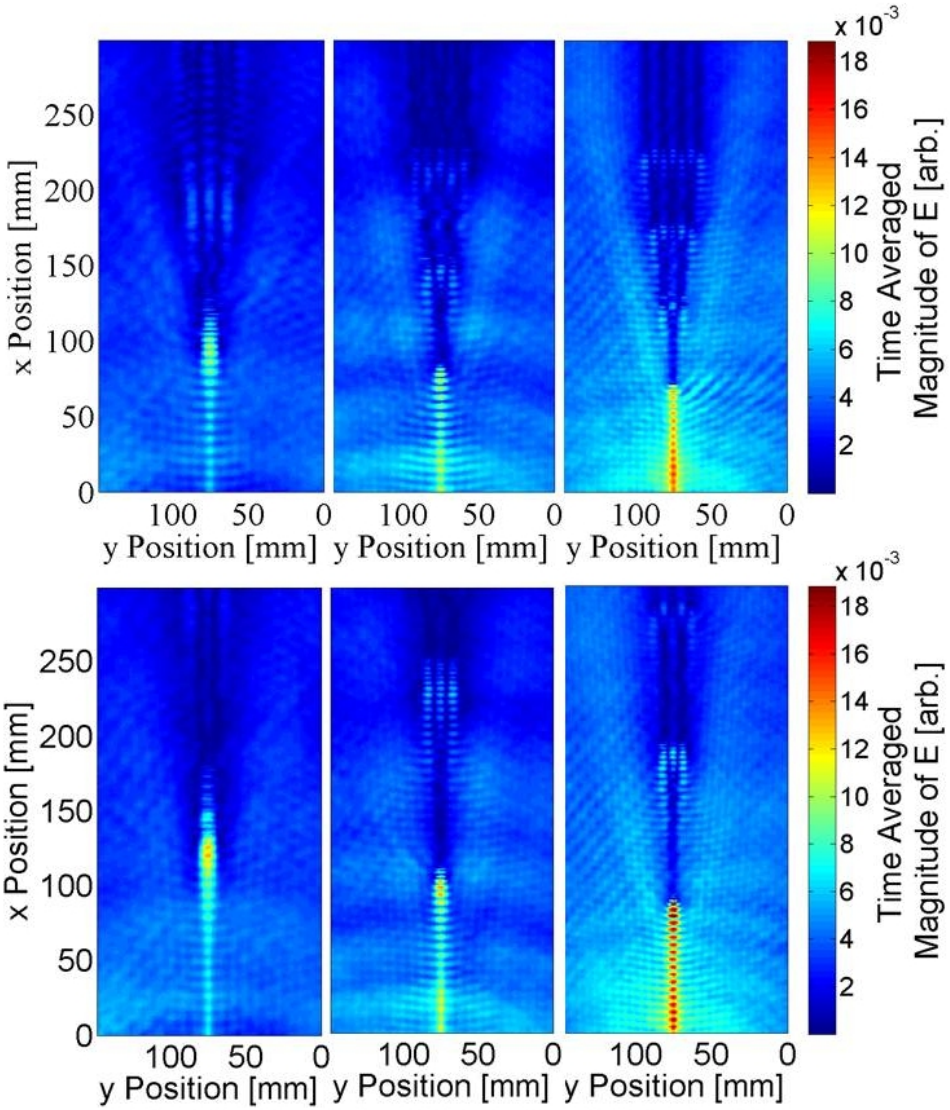

Figure 5.13: Experimentally obtained electric field maps at 20, 25 and 30 GHz (left to right). The top three show the field of the surface wave excited on sample A, the bottom three show the surface wave excited on sample B at the aforementioned frequencies.

top right field plot.

5.5.1 Higher Order Mode excitation

Excitation of a mode requires the symmetry of the modal fields to match that of the excitation source. In the case of samples A and B the excitation source is probe or the previously excited mode. Consider the field associated with TE_{01}, TE_{02}, TE_{03} in Figure 5.14.

Clearly, TE_{02} does not have an antinode at the mid-width of the cavity. As the excitation source is a probe mid-width of the cavity, the field overlap of the source means the mode that will be excited must also have an antinode at it's

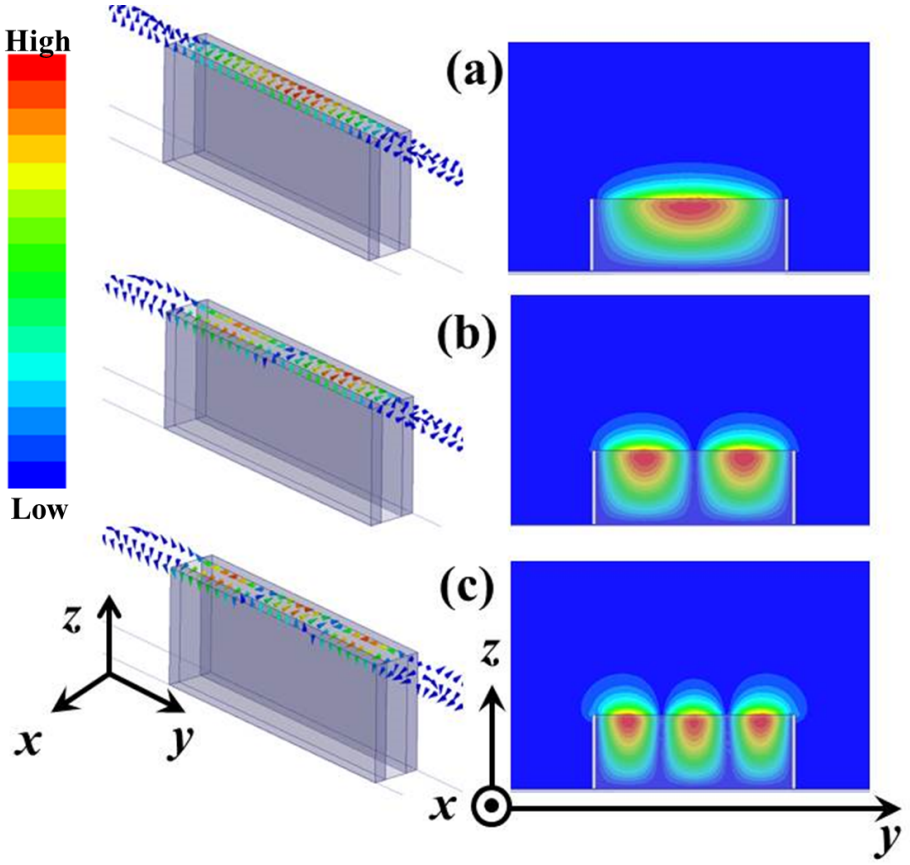

Figure 5.14: Left: Electric field vector associated with the (a) TE_{01}, (b) TE_{02} and (c) TE_{03} supported in a rectangular cavity of $h = 3.75$ mm, pitch $d = 1.6$ mm and width $L = 10$ mm. The plane of measurement is in the xy-plane and is equidistant to the top of the closed-sided cavity. Right: Time-averaged electric field in the xz-plane for the same three modes.(a), (b), (c) are measured on approach to the resonant condition of the supported modes and are numerically calculated via eignemode FEM modelling.

centre. Therefore surface modes associated with even lateral-quantisations of the waveguide mode (e.g. TE_{02}) cannot be excited.

Further consider the numerically calculated dispersion of a one-dimensional array of cavities with uniform widths of $L = 1.6$ and 10 mm in Figure 5.15.

The first order quantisation of the surface wave supported on such a structure is associated with the TE_{01} waveguide mode, the second order is associated with the TE_{02} mode and the third order surface wave is associated with the TE_{03} mode. At 30 GHz, when $L = 10$ mm, only the second order mode is excited. This can be seen from the dotted red line in Figure 5.15, intersecting with the TE_{02} mode in the propagating region of the dispersion curve. This is above the cut-off of the fundamental mode and before the third order quantisation of the surface wave has been excited.

To show that the second order mode cannot be excited by a probe in the

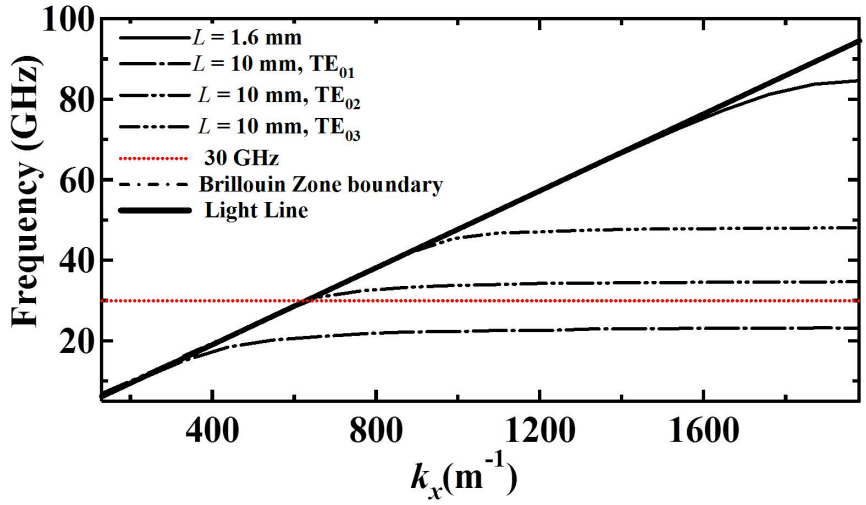

Figure 5.15: Numerically calculated dispersion of one-dimensional array of cavities with uniform widths of L = 1.6 and 10 mm. The dispersion associated with the TE_{01}, TE_{02} and TE_{03} modes of the L = 10 mm width of cavity are shown by the dashed lines in comparison to L = TE_{01} mode shown by the thin solid black line.

experiment, numerical modelling of the system was carried out. Figure 5.16 shows two electric field maps of the supported surface wave on (left) sample A ($L_{\texttt{Start}}$= 1.6 mm) and (right) on a sample with $L_{\texttt{Start}}$= 10 mm. The white dotted lines are an indication of the outline of the supporting structure underneath the field map only.

It is clear that the excitation of higher order modes is limited when $L_{\texttt{Start}}$= 10 mm to excitation from residual far field effects of the probe only. Also, the second order surface wave mode remains unexcited by the probe. By considering the variation of the electric field and poytning vector (S) in x at mid-width of each sample in Figure 5.17 and 5.18 the lack of higher order quantisations is clearly observed. In particular, the direction of power across the top of a surface as is shown by the Poynting vector is indicative of a propagating surface wave. Therefore the complete lack of any magnitude of Poynting vector in the black data in Figure 5.18 is even more indicative that the mode is not supported. Therefore, the main mechanism of excitation of higher order modes must primarily be scattering from the reflection of the first mode approaching a stopping point.

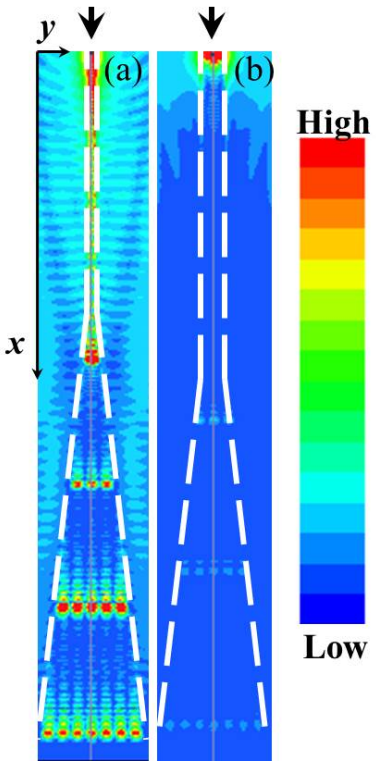

Figure 5.16: Top down view of numerically calculated time-averaged electric field plots of a surface wave supported by a taper with a feed width of (a) $L = 1.\ 6$ mm in comparison to a feed width (b) of 10 mm at 30 GHz. The black arrows note the position and excitation surface wave. Excitation is achieved with a probe drawn into the model. The length of the model is directly comparable to dimensions of sample A and is terminated in radiation boundaries and the white dashed lines are illustrative of the position of the supporting structure only.

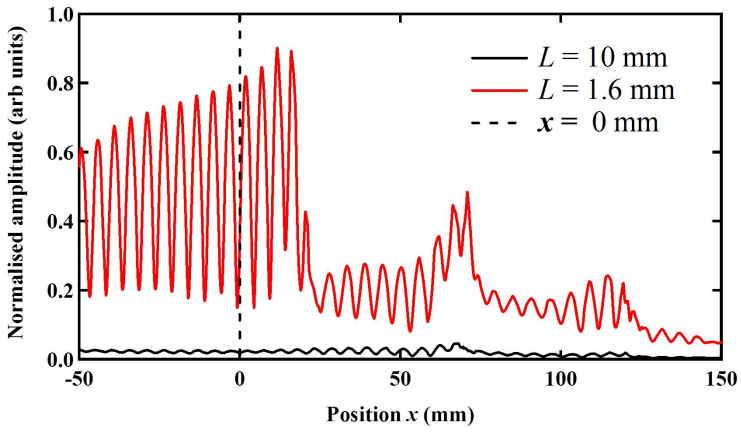

Figure 5.17: Local electric-field amplitude of the surface wave supported by a taper with a feed width of $L_{\texttt{Start}} = 1.\ 6$ mm in comparison to a taper with $L_{\texttt{Start}} = 10$ mm at 30 GHz (black).

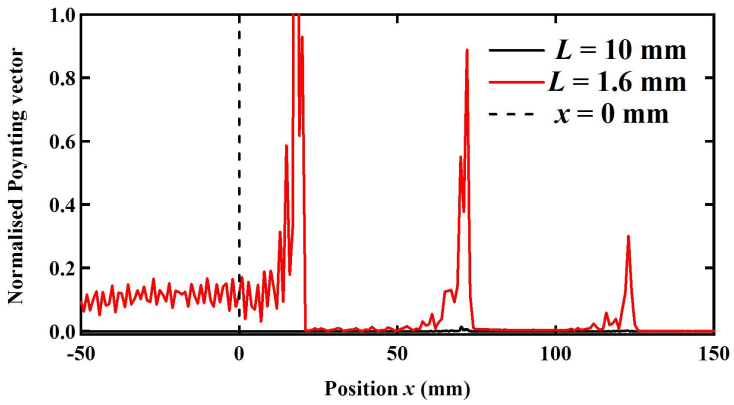

Figure 5.18: Normalised magnitude of the Poynting vector associated with the surface wave supported by a taper with $L_{\texttt{Start}} = 1.\ 6$ mm (red) in comparison to a taper with $L_{\texttt{Start}} = 10$ mm (black).

5.6 Conclusion

In conclusion, the spatial dependence of the group velocity associated with a microwave surface wave supported across a metasurface with a graded geometry is studied. The metasurface consists of an array of closed-sided rectangular cavities obtruding from a ground plane whose lateral widths are increased as a function of distance from the point of excitation. This variation in cavity width results in a spatially dependent modal index. Subsequently, frequency components of the surface wave are slowed and trapped at different positions along the tapered metasurface.

The use of a metamaterial surface as a dispersive device used for beam sharpening of a Doppler radar has been highlighted. Notably, the structure investigated in this Chapter results in a spatially dependent modal index. A dispersive device can be used to interact with a pulse transmitted by the radar. However, the dispersion of that device will be tuned to a single frequency. If the radar was transmitting pulses at two different frequencies, as is often the case for the purposes of velocity unfolding [129], more than one dispersive device would be required for beam sharpening. The structure outlined in this chapter is not limited by this constraint and could be applied to sharpen the beam of a Doppler radar which transmits pulses at different frequencies.

The trapping position and the behaviour of the supported mode approaching this location have been experimentally observed with both local field amplitude and phase data. Four notable aspects of this data have been discussed. Primarily, the phase of the electric-field data provides a more accurate identification of the trapping location compared to amplitude measurements alone. Secondly, the exact stopping location of the surface wave does not correspond with numerical predic-

tions obtained for a fixed-width one-dimensional array of cavities. Thirdly, the oscillations observed in the local amplitude of the surface wave provide insight as to the magnitude of reflection experienced by the surface mode close to this point. The origin of the reflection mechanism is considered. Finally, higher order lateral quantisations of the surface mode have been experimentally observed excited by scatter of the fundamental mode from the trapping point.

Chapter 6

Channelling a Microwave Surface Wave

6.1 Introduction

The channelling of surface waves via the addition of dielectric overlayers to a metamaterial surface is investigated in this chapter. The metamaterial surface is composed of mushroom elements of a Sievenpiper array [68]. The Sievenpiper array is designed such that it supports a TM surface wave both with and without a dielectric overlayer placed directly upon the structure. However the dispersive properties of the supported mode are modified by the addition of an overlayer, resulting in a lower limiting frequency.

Initially, the dispersion of surface waves supported by an uncovered Sievenpiper mushroom surface is analysed and measured. Then, a planar dielectric overlayer is placed on the surface, covering it completely and the dispersion of the supported TM mode of the modified system is measured. A lower limiting frequency of the supported mode is observed in comparison to the limiting frequency of the mode supported by an uncovered Sievenpiper mushroom array. The dispersions of the TM mode supported by the covered and uncovered Sievenpiper mushroom surface are compared and used to contrast to measurements concerning the channelling of surface waves via the addition of dielectric overlayers to the Sievenpiper mushroom surface supporting the mode. In the channelling case, the dielectric overlayers no longer completely cover the Sievenpiper mushroom array.

Instead, the Sievenpiper surface is covered by a planar dielectric overlayer except for a small central region, an uncovered channel of width L. The mode associated with the uncovered region will continue to be supported at frequencies above that of the mode associated with the surrounding covered regions. In this way a TM surface wave is channelled across the metamaterial. By progressively

narrowing the width of the channel, the interaction of the fields of the supported mode within the surrounding dielectric overlayer increases.

The local electric field amplitude and phase of the supported mode in the covered and uncovered regions of the Sievenpiper surface are experimentally and numerically recorded. This data is compared with numerically and experimentally determined dispersion measurements to gain insight as to the minimum possible channel width before which perturbations due to the proximity of the bordering overlayers are observed. Comment is made regarding the mechanism that dictates the minimum width (L) of the uncovered channel.

6.2 Background

The addition of a dielectric overlayer to a conducting surface such as a metal provides a mechanism by which a TM microwave surface wave can be confined to the interface between the surface and free space [51]. This phenomenon was extensively studied in the 1950's ([33, 49, 135]) during the pursuit of more efficient antennas composed of a metal wire coated in dielectrics [15]. More recently this concept has been extended in the pursuit of surface wave Luneberg and Eaton lens devices in the microwave [136] and optical wavelength regimes [137]. In these cases the modal index varies as a function of radius from the centre of the lens by varying the height of the dielectric overlayer. Modal index (n) has previously been defined in Section 2.3.1.1 and measured in both Section 3.3.2.2 and in Chapter 5.

However, a dielectric overlayer is not the only mechanism by which a TM surface wave can be confined to a metallic surface in the microwave regime. Indeed, as discussed in Section 2.5.1, surface structures such as a 1D array of grooves, 2D holes or an array of 'Sievenpiper mushrooms' [18, 32, 51, 68] also provide the necessary boundary conditions to support TM surface waves. These modes exhibit limiting frequencies that are synonymous with a surface plasma frequency in that the dispersion of the mode is limited by geometrically engineered resonances in the same way a surface plasmon resonance is limited by the surface plasma frequency. These structures have previously been described as metamaterials as they gain their electrical properties from their geometric design and not their intrinsic properties.

Dockrey et al. (2013) [94] recently demonstrated an example of an application of designed surface structure via the fabrication of a Luneberg lens device, operating in the microwave regime. The limiting frequency of the mode supported on the lens was spatially varied by engineering the dimensions of mushroom elements of a Sievenpiper array. Consequently, the modal index (n) (discussed previously

in Section 3.3.2.2) was spatially varied. Modal index can be described thus:

$$n = \frac{\lambda_0}{\lambda_{\mathtt{SW}}} \tag{6.1}$$

where λ_0 and $\lambda_{\mathtt{SW}}$ are representative of the wavelength of a free space mode and the wavelength of the surface wave respectively. As the modal index was varied, control of the propagation of the supported TM wave on the modified structured was gained, resulting in Luneberg lens fabrication.

Anther application to result from of the study of a Sievenpiper mushroom array includes beam steering of microwave patch antenna arrays via the control of surface wave scattering off the array [138]. The resonant condition of the surface defines the reflected phase from the surface, as is described shortly, and can be engineered so that the collective response of the patches results in an antenna with a directed beam profile.

Here, the fundamental mode supported by an array of the Sievenpiper 'mushroom' structure with, without and in the proximity of dielectric overlayers is investigated experimentally. This mode is a TM surface wave, supported by the structure at microwave frequencies [68]. The mode is a coherent oscillation of the electric field associated with the mode supported by each element of the array, the thickness of which is much less than $\lambda_{\mathtt{SW}}$. The geometry of a Sievenpiper mushroom structure and mechanism by which an array of such mushrooms support a surface wave is discussed initially.

Highlighted in this discussion is the presence of a 'band gap' wherein propagating modes are suppressed. The presence of a dielectric overlayer on the metamaterial surface modifies the lower band edge, a property which is subsequently utilised to laterally confine the surface wave.

6.3 Sievenpiper 'Mushroom' Structure

The structure originally proposed by Sievenpiper et al. (1999) [68] is a three layered system composed of a layer of dielectric sandwiched between a conducting ground plane and a square array of square patches. Each patch is connected to the conducting ground plane by a metallic via which perforates the dielectric layer. The via connects to the mid-point of the patch, which in itself protrudes from the layer of dielectric. Figure 6.1 (a) details the dimensions of the unit cell of the Sievenpiper structure used in this chapter. The side length of the patch $a < d$ and resembles a mushroom when connected to the ground plane with a via, hence the name Sievenpiper 'mushroom' structure. The two dimensional array composed of the Sievenpiper unit cell used in this investigation is manufactured using standard

printed circuit board (PCB) techniques with a dielectric core of Nelco NY-9220 (ϵ = 2.2). An example of a Sievenpiper mushroom array is shown in Figure 6.1 (c).

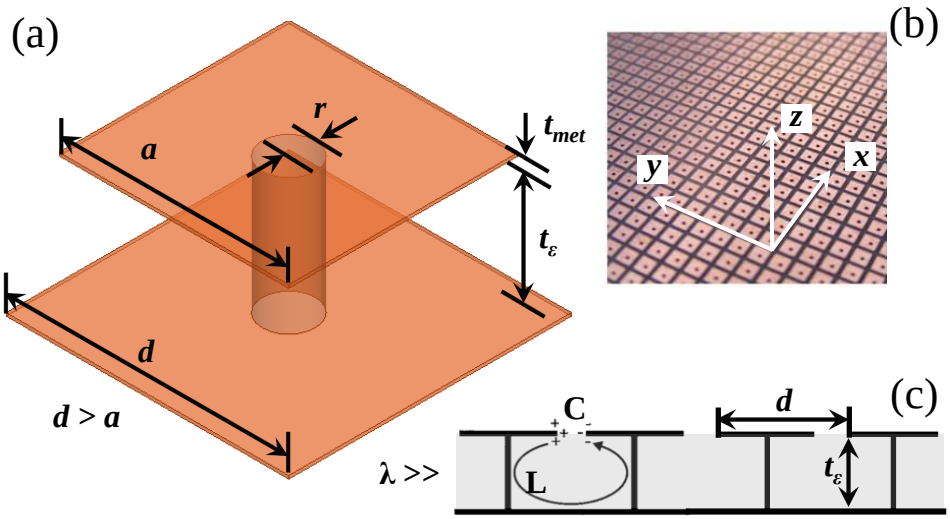

Figure 6.1: (a)Unit cell of Sievenpiper mushroom array. Pitch $d = 1.6$ mm, patch length $a = 1.3$ mm, via radius $r = 0.15$ mm, dielectric thickness $t_\epsilon = 0.787$ mm of Nelco NY-9220 ($\epsilon = 2.2$) and metal thickness $t_{\mathtt{met}} = 0.0175$ mm. (b) Photo of a Sievenpiper mushroom array (c) Schematic of Sievenpiper mushroom LC model [68].

The Sievenpiper mushroom array is frequently described as a high-impedance surface. The general equation for impedance (Z) is given by the ratio between the electric ($\mathbf{E}$) and magnetic ($\mathbf{H}$) fields.

$$Z = \frac{\mathbf{E}}{\mathbf{H}} \tag{6.2}$$

propagating through a bulk medium. This is modified when describing the impedance associated with a surface Z_s which is specifically dependent on the ratio between the tangential components of $\mathtt{E}$ and $\mathtt{H}$ in the air region above the structure only.

6.3.1 Application of the LC model to the Sievenpiper Mushroom Structure

The Sievenpiper mushroom structure can be modelled as a parallel resonant circuit and by considering the impedance of each element acting in parallel, the overall impedance of the surface Z_s is described. As such, the inductive (L) and capacitive (C) contributions to the impedance can be identified by considering the interactions of an individual unit cell with incident electromagnetic radiation.

First consider the operation of the radio frequency (RF) source, a Vector Network Analyser (VNA) used to generate microwave radiation, previously detailed

in Section 3.2.1. A VNA is used as a microwave source to excite surface waves on the Sievenpiper mushroom surface and is an AC source [71]. Therefore, the nature of the therefore the direction of the electric field will oscillate in time. The source is connected to a secondary device, which emits radiation with electric field polarised in the xz-plane. Consider this excitation applied to a Sievenpiper mushroom structure. Initially, the electric field component in the z-direction will diffract in the gaps between the patches, inducing current in the top patch layer of the Sievenpiper mushroom structure. The current induces a voltage which interacts with the component of the electric field in the x-direction and charge becomes concentrated at the edges of the patch.

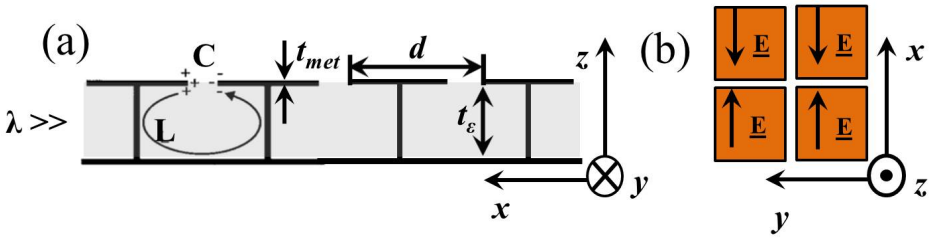

Figure 6.2: (a) Schematic of Sievenpiper mushroom LC model [68]. Dimensions include pitch $d = 1.6$ mm, patch length $a = 1.3$ mm, , dielectric thickness $t_\epsilon = 0.787$ mm of Nelco NY-9220 ($\epsilon = 2.2$) and metal thickness $t_{\mathtt{met}} = 0.0175$ mm. Wavelength of incident radiation $\lambda >> t_\epsilon$ (b) Schematic of the electric field direction on the top of the patches when a TM surface wave is excited on an array of Sievenpiper mushroom structures.

The resulting concentration of charge results in a capacitance, and is shown in Figure 6.2 (a). The electric field interaction in the x-direction are shown in Figure 6.2 (b).

Due to the time dependent nature of the excitation field the capacitive charge at the edge of the patches will oscillate back and forth, flowing around the longer electrical path of the unit cell (i.e. through the vias and conducting metal ground plate). Capacitance C is defined as

$$\mathtt{C} = \frac{Q}{V} \quad = \frac{Q}{E(d-a)} \quad = \frac{Q\epsilon}{\sigma(d-a)} \quad = \frac{A\epsilon}{(d-a)} \tag{6.3}$$

where Q is the charge on the patch, V is the voltage induced on the patch, ϵ is the permittivity of the dielectric layer, E is the amplitude of the electric field, σ is the charge density on the patch and A is the area of the side of the patch where $A = at_{\mathtt{met}}$). a is patch length and d is the pitch of the unit cell, shown in Figure 6.1. Therefore $(d-a)$ is the separation distance between the patches.

To calculate the capacitance associated with one unit cell of the Sievenpiper

array many variables must be considered. The voltage across the patch would depend on the strength of the electric field emitted by the source, and the strength of diffraction of the field in the gap between the patches. This, as well as the charge density σ on the edge of the patch and total charge on the patch would also be subject to variations depending on any resonant condition supported by an array of Sievenpiper mushrooms, such as a TM mode. As such, the calculation is non-trivial.

The charge oscillating around the longer electrical path length of the unit cell has a magnetic field associated with it and therefore an inductive component due to this resonance can be identified. Inductance (L) is described thus:

$$\mathtt{V}(t) = \mathtt{L}\frac{\delta I}{\delta t} \tag{6.4}$$

where V(t) is time dependent voltage and I is current. The calculation of inductance is non-trivial, for the same reasons as detailed Equation 6.3.

Due to the collection of charge at the edges of each patch the layer of metallic patches in a Sievenpiper mushroom array act as a capacitive frequency selective surface (FSS) [139].

The individual component contributions of capacitance and inductance associated with an individual Sievenpiper mushroom have been defined. As an array of these structures are connected by a conducting metallic ground plane, the response of the Sievenpiper array is described as analogous to a parallel resonant circuit when they are irradiated with a plane wave. A complex surface impedance (Z_s) associated with the Sievenpiper mushroom array is defined thus:

$$Z_s = \frac{i\omega\mathtt{L}}{1 - \omega^2\mathtt{LC}} \tag{6.5}$$

The surface is inductive at low frequencies and capacitive at high frequencies. Consider now the resonant condition associated with the inductance and capacitance of a system, defined thus:

$$\omega_0 = \frac{1}{\sqrt{\mathtt{LC}}} \tag{6.6}$$

where ω_0 is the resonance frequency of the mode. By substitution of Equation 6.6 into Equation 6.5 it is observed that the surface impedance Z_s will increase on approach to the resonant condition of a mode supported by the Sievenpiper mushroom array, hence the description of the array as a high-impedance surface. However, according to Equation 6.5, Z_s is infinite when the Sievenpiper mushroom array supports a mode it's resonance frequency ω_0. In practice this will never happen, impedance is maximal at 377 Ω. The surface impedance model does not take

into account the whole system and is an approximation of field interaction tangential to the interface and does not include any consideration as to the interaction of the electromagnetic fields in the dielectric overlayer of the Sievenpiper mushroom structure.

However, the channelling experiment detailed in this chapter studies surfaces with an area many times greater than the dimensions of the unit cell of an individual Sievenpiper mushroom element. As such, the impedance model is utilised for numerical modelling of the channelling experiment. The resonant frequency of the modes supported by the Sievenpiper mushroom array are measured, therefore the wavevector as a function of frequency associated with the supported TM surface wave, $k_{\mathtt{TM}}$, is known.

The dispersion relations of the modes supported on such an surface as described using the effective surface impedance model is described thus:

$$k_{\mathtt{TM}} = \frac{\omega}{c}\sqrt{1 - \frac{Z_{\mathtt{TM}}^2}{\eta^2}} \tag{6.7}$$

$$k_{\mathtt{TE}} = \frac{\omega}{c}\sqrt{1 - \frac{\eta^2}{Z_{\mathtt{TE}}^2}} \tag{6.8}$$

where η is the impedance of free space (377 Ω), $Z_{\mathtt{TM}}$ the impedance associated with the surface supporting a TM wave, $Z_{\mathtt{TE}}$ the impedance associated with the surface supporting a Transverse Electric (TE) wave and $k_{\mathtt{TM}}$ and $k_{\mathtt{TE}}$ are the wavevectors of the mode. This has been discussed previously in Section 2.5.3. By using Equations 6.7 and 6.8, the surface impedance at a given frequency is known. This value can be assigned to a sheet in a model used to numerically calculate mode resonances during FEM modelling, a process previously defined in Section 3.4.3.4. Numerical modelling with an impedance sheet is computationally less expensive and far more achievable than trying to represent a full Sievenpiper array structure. Therefore this method is used for comparative purposes to investigate the fields of surface waves above the top of the supporting array only.

6.3.2 The Band Gap

The Sievenpiper mushroom structure is used to investigate lateral confinement of a TM surface wave primarily because it exhibits a 'band gap' in the dispersion relation of the supported surface wave. In other words, there is a range of frequencies over which surface waves are not supported by the structure. Consider Figure 6.3, reproduced with permission from Sievenpiper et al. (1999) [68]. Figure 6.3 (a) depicts the dispersions numerically calculated using effective surface impedance

model and (b) finite element method (FEM) modelling. The surface wave band gap is labelled on Figure 6.3 (b) with a red box. Notice that the vias in Figure 6.3 (a)(inset) are cuboid, in comparison to the unit cell in Figure 6.1 (a) where they are cylindrical. The surface wave band gap is insensitive to this change of shape, as is discussed later in this chapter. The patch layer of the original array as presented in [68] and the array composed of the unit cell represented in Figure 6.1 (a) are composed of square patches. Figure 6.3 was achieved via an eigenmode model, a solution type that has been discussed previously in Chapter 3.

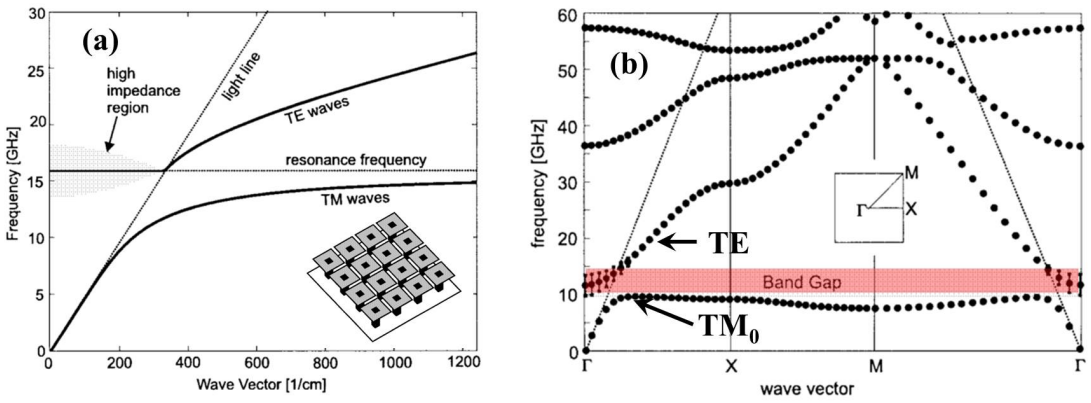

Figure 6.3: Figures reproduced with permission from D. Sievenpiper publication [68]. (a) Dispersion diagram of the TM_0 and TE surface wave predicted by the effective surface impedance model. A schematic of the Sievenpiper mushroom array investigated is inset.(b) Dispersion diagram of the modes supported by the array as calculated by Finite Element Method (FEM) modelling. The presence of the band gap above the first mode is marked by a red box. The array dimensions are: pitch $d = 2.4$ mm, patch length $a = 2.1$ mm, width of square vias $= 0.36$ mm and total thickness of structure $= 1.6$ mm. The volume between the patches was filled with a dielectric of permittivity $\epsilon = 2.2$.

Both TM and TE surface modes are represented on the dispersion diagram in Figure 6.3 (b). The fundamental mode supported by the structure is TM and can be seen to follow the light line at low frequencies. However, when the frequency approaches 10 GHz the dispersion curve is seen to diverging perceptibly and quite rapidly from the light line. The TE mode begins at a higher frequency within the radiative region to the left of the light line. Consequently, there is a broadening of the TE mode as indicated by the error bars. The TE_0 mode continues to slop upwards and crosses the light line whereupon it becomes a bound non-radiative surface mode.

The band gap is defined as the frequency range over which no bound surface waves are supported. In this case, the band occurs between the maximum frequency at which the TM_0 mode is supported and the frequency at which the TE_0 mode crosses the light line. The resonant frequency as predicted by the effective

surface impedance model (ω_0) is centred in this surface wave band gap region. An example of the electric and magnetic fields associated with the TM modes supported by an isotropic Sievenpiper array will follow shortly in Section 6.4.

6.3.3 Disadvantages Associated with the Effective Surface Impedance Model

Sievenpiper's original paper [68] highlights the lack of comparison between the effective surface impedance model and both experimental and numerical analysis of the dispersion of the surface modes supported by the Sievenpiper array. Experimental and numerical analysis of the modes supported by the array clearly show the presence of a band gap whereas the effective surface impedance model does not predict one.

Previous investigations regarding the tuning of the band gap by Clavijo et al. (2003) [140] reveal that the lower band edge as defined by the asymptotic limit of the TM_0 mode is sensitive to the periodicity of the via layer and thickness of the via layer. The TE mode which defines the upper band edge is only sensitive to the FSS layer. Conversely, the TE mode was shown to be insensitive to the dimensions of the array of vias and the TM_0 insensitive to the FSS patch layer. This conclusion was reached by approximating the Sievenpiper structure to an effective medium (with effective permittivity $\epsilon_{\mathtt{eff}}$ and permeability $\mu_{\mathtt{eff}}$) and is detailed in Clavajo et al. [140]. Rance 2013 [141] experimentally investigated these dependencies by measuring the dispersion of the surface waves supported by an array of rectangular Sievenpiper mushrooms. The position of the lower band edge was shown to result from the relative power flow of the surface wave on resonance in the dielectric layer, a result of the frequency dependent effective permittivity ($-\epsilon_{\mathtt{eff}}$), in comparison to the power flow of the mode in the region above the Sievenpiper array ($+\epsilon$). The band gap is not due to interaction with the Brillouin zone boundary imposed by the periodicity of the structure, as is typical in photonics.

The effective surface impedance model for TM and TE surface waves as defined by Equations 6.7 and 6.8 relies on the ratio between the tangential components of electric and magnetic field above the surface of the structure. The model cannot predict the band gap as it does not account for the interaction between the electric and magnetic fields in the layer of vias surrounded by dielectric and the FSS layer (patch array).

6.3.3.1 The Characteristics of the Sievenpiper Mushroom Array

The literature that evolved from Sievenpiper's original publication refers the band gap as a surface wave 'suppression band' [140, 142, 143, 144, 145, 146] and shall

hence forth be referred to as such in this thesis. These publications focus on both the position of the surface wave suppression band in frequency and the frequency dependent characteristic of the phase on reflection from a Sievenpiper mushroom structure. While it is not an attribute used in this chapter it has generated enough interest to be worthy of a brief note.

The reflection of the electric field from the surface of a perfect electric conductor (PEC) at which the tangential component of the electric field is forced to zero exhibits phase shift of π radians relative to the incident field. Conversely, the electric field reflection from a surface which acts as a perfect magnetic conductor (PMC) exhibits no phase shift relative to the incident field. The PEC surface is described as 'low impedance' as the ratio between the tangential components of the electric and magnetic fields with respect to the plane of the surface is small (Equation 6.2). For a PMC surface this ratio is very large, hence description of the surface as 'high impedance'.

The 'in-phase reflection band' associated with a Seivenpiper array describes a range of frequencies between which the phase shift on reflection is $\pm\frac{\pi}{2}$ and occurs close to the PMC condition. Hence a Sievenpiper mushroom array can be described as a high impedance surface. This is surprising as a large percentage of the surface of a Sievenpiper array is composed of the metallic layer of patches. The in-phase reflection band and the suppression band are not forced to occur over the same range of frequencies. The ability to design each band by modifying the geometry of the structure is a highly valued attribute of the Sievenpiper mushroom structure in the pursuit of low gain antennas.

6.4 Addition of a Dielectic Overlayer

The addition of a dielectric overlayer to a structure that supports a surface wave reduces the limiting frequency of that mode. When the Sievenpiper mushroom array is uncovered, the electric field associated with the fundamental mode supported by the array extends from the top of the surface structure and penetrates into free space. After the addition of the covering overlayer, the electric field of the surface wave penetrate into the dielectric overlayer where $\epsilon_{\texttt{Dielectric}} > \epsilon_{\texttt{Free Space}}$. By inspection of Equation 6.3, this will result in an increase in the capacitance of the array structure. By considering Equation 6.6 it is clear that the increased capacitance will result in a lower resonant frequency.

The time-averaged electric and magnetic fields associated with the first two TM surface modes supported by the Sievenpiper array are shown in Figure 6.4. The fundamental mode, TM_0, is represented in (a) and (c) and the TM_1 mode is represented in (b) and (d). The electric field is polarised parallel to the xz-plane

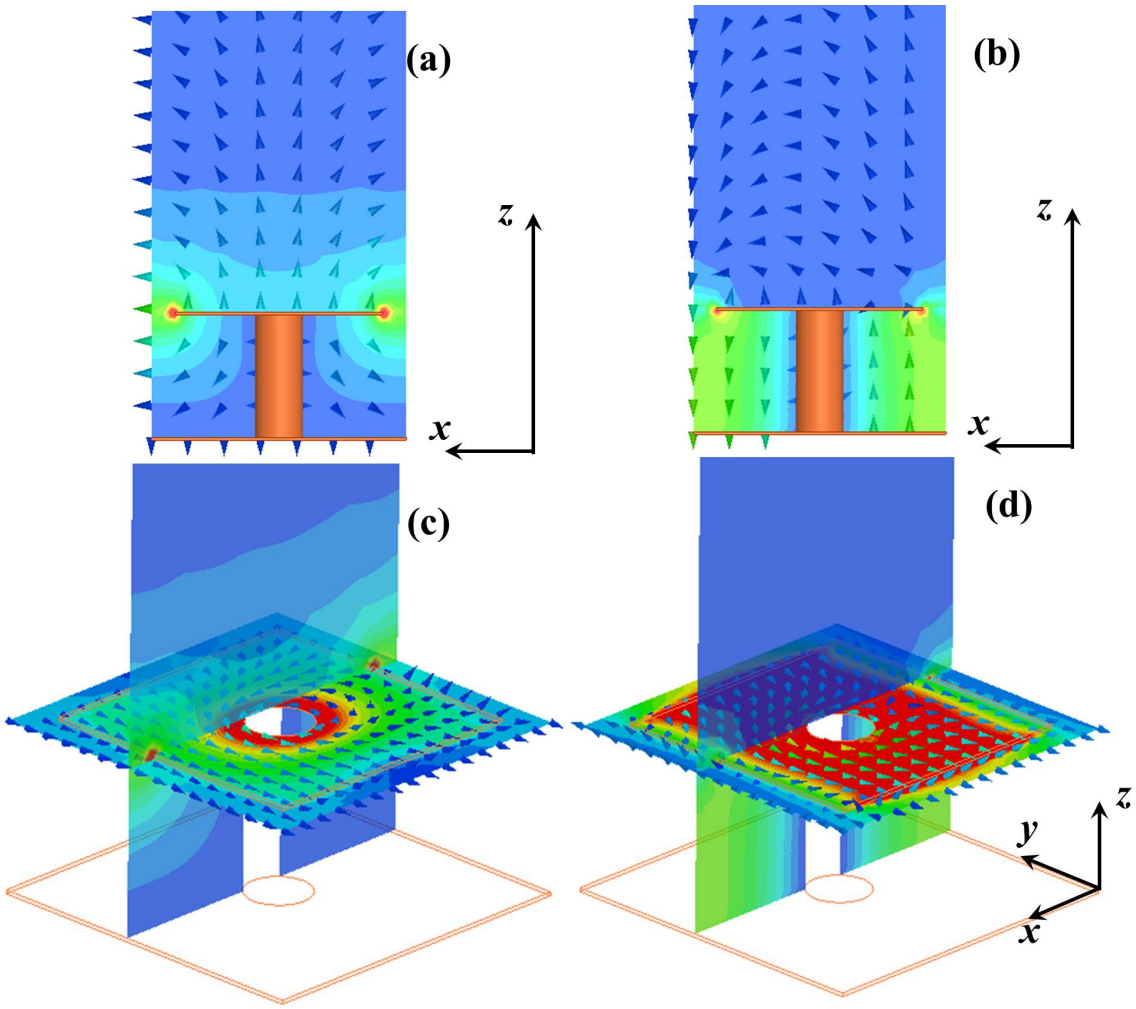

Figure 6.4: Field profiles of TM_0((a) and (c)) and TM_1 ((b) and (d)) modes of the Sievenpiper array near resonance. The colour maps in (a) and (b) are indicative of the time-averaged electric field strength, and arrows indicate the direction of the instantaneous electric field. The colour maps in the *xy*-plane in (c) and (d) represent the time-averaged magnetic field of the supported mode, and the arrows are indicate the direction of the instantaneous magnetic field. The *xy*-plane bisects the unit cell directly below the patch layer, within the Neltec 9220 dielectric. The time-averaged electric field in the *xz*-plane previously displayed in (a) and (b) is overlayed onto (c) and (d). Relative field strength is indicated by a range between the colours of red (high field) and blue (low field).

for both modes. The time-averaged magnetic field and vector direction is shown in Figures 6.4 (c) and (d) for the TM_0 and TM_1 modes respectively. The magnetic field is plotted on a plane parallel to the *xy*-plane, directly beneath the patch layer (FSS) of the Sievenpiper structure. The time-averaged electric field is overlaid onto Figure 6.4 (c) and (d) in the *xz*-plane.

6.4.1 The TM Suppression Band

A TM_0 can only be excited with an electric field vector component normal to the plane of the FSS layer. The method of excitation used here is a surface wave launcher, detailed previously in Section 3.7.1. The launcher has a component of electric field polarised primarily in the vertical direction, normal to the plane of the FSS layer therefore will excite TM modes. By their very nature a TE mode requires excitation via electric field polarised parallel to the horizontal y-direction. Subsequently, no TE modes will be excited via the surface wave launcher device so are not detailed. As a result, the TM_0 and TM_1 modes form the lower and upper edges of the suppression band for the proposed investigation into surface wave channelling.

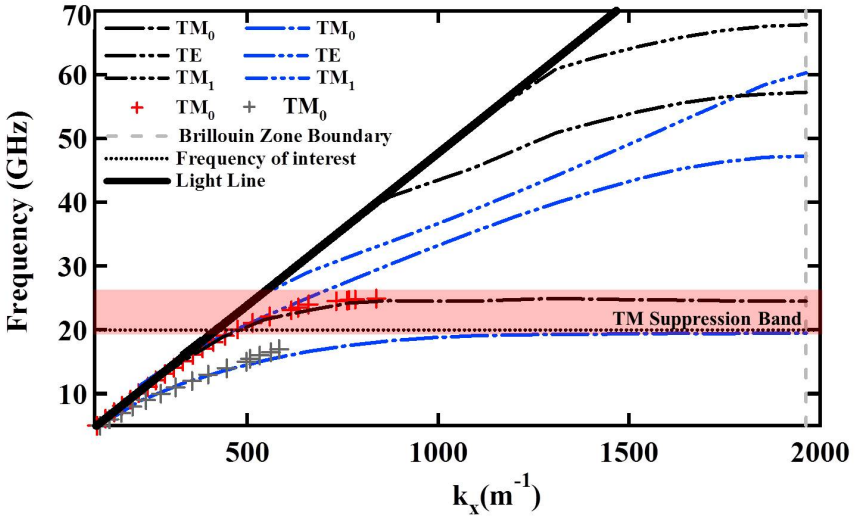

Figure 6.5: Dispersion relation of the TM_0, TE and TM_1 modes of the Sievenpiper array of dimensions described in Figure 6.1. Represented by the dot long-dash line, the double-dot long-dash line and the triple-dot-long-dash line are the TM_0, TE and TM_1 (respectively) as numerically calculated by FEM modelling. All dotted black lines are representative of the modes supported by a Sievenpiper array of infinite extent. All dotted blue lines represent the same array with a dielectric overlayer $\epsilon = 2.6$ of thickness 2.95 mm. The experimentally obtained dispersions for a Sievenpiper array with and without a dielectric overlayer are plotted as red and grey crosses (respectively). The suppression band associated with the Sievenpiper array with a dielectric overlayer is noted by a band of red and the Brillouin zone edge of the structure is marked by the vertical grey dashed line.

Figure 6.5 shows the dispersion of the first three modes of the Sievenpiper mushroom array numerically obtained from finite element method modelling (FEM) calculations via an Eigenmode solution. The dimensions of the modelled structure are the same as previously stated in Figure 6.1. The TM_0, TE and TM_1 are represented by the black dot long-dash line, double-dot long-dash line and triple-

dot long-dash line respectively. Overlaid on this plot are the first three modes supported by the Sievenpiper mushroom array completely covered by a dielectric overlayer of permittivity $\epsilon = 2.6$ and thickness $w = 2.95$ mm. The TM_0, TE and TM_1 modes supported by the Sievenpiper structure are represented by the blue dashed lines on Figure 6.5.

Crucially, the dispersion relation of the TM_0 mode after the addition of an overlayer has been is shifted down in frequency. Dielectric overlayers on top of the Sievenpiper mushroom structure reduce the limiting frequency of the structure as the vertical component of electric field associated with the TM surface wave (k_z) is now propagating through a medium of permittivity $\epsilon > 1$.

6.5 Experimental Setup

6.5.1 Addition of a Dielectric Overlayer Completely Covering the Sievenpiper Mushroom Array

Consider again Figure 6.5. The red and grey crosses overlaid onto the numerical data represent experimentally measured dispersions for the modes supported by an uncovered Sievenpiper array and an array that is completely covered by a dielectric overlayer. Figure 6.6 (a) and (b) schematically show the two experimental setups associated with the dispersion measurement represented in Figure 6.5.

The numerical modes in Figure 6.5 agree well with the experimentally determined dispersions of the surface waves supported on Sievenpiper structure with and without the dielectric overlayer. These initial measurement are later compared to the measurements of a surface wave supported in an uncovered channel region on the Sievenpiper mushroom array, which is surrounded by dielectric overlayers. The experimental setup associated with the dispersion measurement of the channel mode is shown schematically in Figure 6.6, (a) and (b).

6.5.2 TM Surface Wave Channel Using a Sievenpiper Mushroom Array and Dielectric Overlayers

To investigate the lateral confinement of a TM surface wave, two regions of the sample are each covered by a dielectric overlayer placed directly on top of the Sievenpiper array surface with an uncovered region, of width L, in between the layers. Figure 6.6 (c) and (d) shows schematics of this setup with two different widths L of uncovered channel. The dielectric overlayer is a material known as perspex.

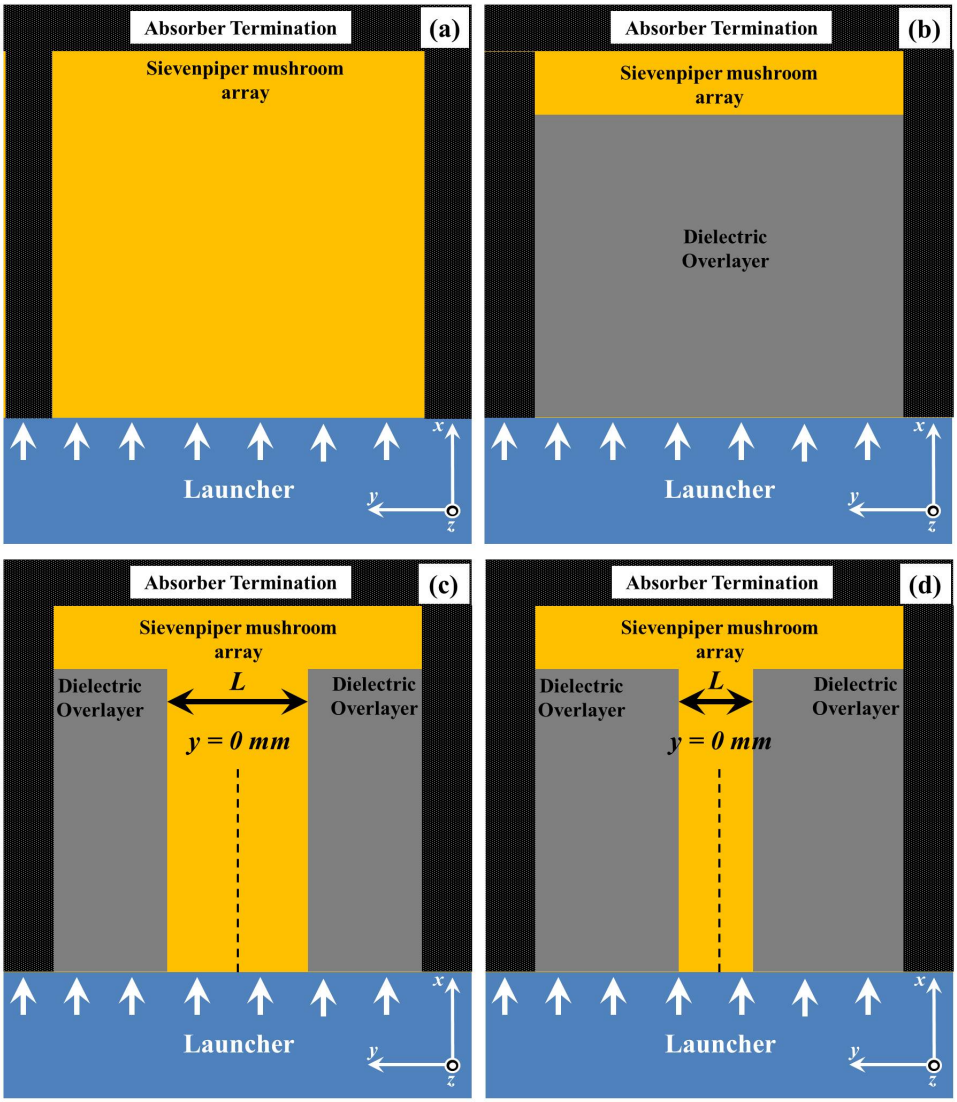

Figure 6.6: Schematics of four separate experimental setups, top down view. (a) An uncovered Sievenpiper mushroom array (orange). (b) A Sievenpiper mushroom array covered with a dielectric overlayer (grey). (c) A Sievenpiper mushroom array with two dielectric overlayers covering the array. The region between the overlayers remains uncovered, resulting in a channel. The width L between the two dielectric layers (grey) on top of the Sievenpiper mushroom array (orange) is shown. (d) Same experiment as (c) except that channel width L is smaller. The direction of propagation of radiation from the excitation source, the surface wave launcher (blue), is noted by the white arrows. Geometrically graded microwave absorber lines the edges of the Sievenpiper mushroom array, with and without dielectric overlayers to minimise reflections from the edge of the array. All dielectric overlayers used are described by $\epsilon = 2.6$ and have a thickness of $w = 2.95$ mm. They are a material known as perspex.

The metamaterial surface supports a TM surface wave with a different limiting frequency in the covered and uncovered regions respectively. Therefore the frequency of the lower band edge of the TM suppression band will also differ with respect to the covered and uncovered regions. Consequently, between these

two overlayers, there is an uncovered region where the surface mode will continue propagating at frequencies above that of the limiting frequency of the surrounding region. In this section experiments investigate how narrow a channel between overlayers can be made until the mode supported in the uncovered region is effected by the proximity of the bordering dielectric layers.

6.5.2.1 Excitation and Measurement

A surface wave with planar wavefronts is excited by a microwave 'surface wave launcher' as designed by Mr S. Berry. A top down view of the launcher has been labelled in Figure 6.6 as a blue box with the direction of excitation of radiation from the launcher noted by the white arrows. A schematic of the surface wave launcher's composition and details of its operation has been previously been detailed in Section 3.7.1. However, it is now useful to briefly detail the launcher's operation when used to excite a surface wave on a Sievenpiper array covered by a perspex overlayer.

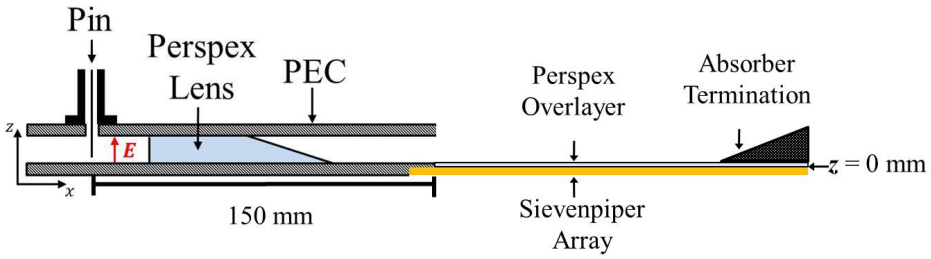

Figure 6.7: Schematic of experiment for illustrative purposes, adapted from 'Oblique Angle Scattering of Surface Waves from Surface Wave Absorbing Materials' by Mr S. Berry [83]. Schematic of surface wave launcher in the xz-plane. The lens is composed of two parallel metallic plates separated by a cavity with a perspex lens placed inside the cavity. The plates are considered to be PEC at microwave frequencies. The aperture of the lens occurs when $x = 150$ mm and rests on the Sievenpiper array, schematically represented by the orange box. A coaxial cable connects an RF source such as a VNA to the lens where a metallic pin protrudes into the cavity, exciting a transverse electromagnetic (TEM) mode within the cavity. This mode propagates radially away from the pin and results in spherical wavefronts with an electric field polarised in the z-plane (red arrow in (a)). Interaction with the perspex lens results in the mode's transformation from spherical wavefronts to planar wavefronts, resulting in uniform excitation of the mode supported by the array. The perspex dielectric overlayer and the absorber used to terminate the surface wave are also illustrated.

Figure 6.7 illustrates the surface wave launcher used to excite surface waves on a Sievenpiper mushroom array covered by a perspex overlayer. The launcher consists of a point source placed orthogonal to a pair of parallel metallic plates.

The point source is marked by the pin in Figure 6.7. The radiation emitted by the source is focused by a perspex lens so that emission from the aperture is approximately collimated between the operating frequency range of 10 to 30 GHz. The aperture of the lens is a distance of 150 mm away from the pin.

The launcher can excite surface waves approximately uniformly in the y-direction via evanescent field associated with diffraction from the aperture between its operating frequencies. This will allow investigation of the phase of the mode supported in the uncovered channel. Crucially, the electric field associated with the excitation is oriented vertically (parallel to z-direction).

With respect to measurement of the supported surface waves, consider that the position of the aperture of the launcher is at position $(x,z) = (0 \text{ mm}, 0 \text{ mm})$ and is parallel the y-direction. The launcher is place upon the metamaterial surface and aligned so that the intersection between array elements is parallel to and in proximity of the edge of the aperture. Surface waves are excited and propagate in the x-direction approximately uniformly as a result of careful alignment. This alignment is subject to a small amount of experimental error through misalignment of the aperture of the launcher by $\pm(d-a)$. The edges of the dielectric overlayers shown in Figure 6.6 (c) and (d) are straight and aligned along the intersection of neighbouring elements of the array layer. Therefore, the width of the channel between the overlayers will remain constant regardless position in the x-direction.

Transmission of energy is mediated by the excitation of these modes and their local electric field amplitude and phase are measured by connecting a vertically oriented antenna to a Vector Network Analyser (VNA). This antenna is a coaxial wire with the outer sheath and dielectric coating removed from the end of the wire, leaving 2.5 mm of exposed core to detect the electric field allowing spatial variation of the fields to be determined. The position of the detecting antenna is modified by a computer controlled motorised stage. This method of field detection has been previously elaborated upon in Chapter 3.

6.5.3 Measurement of Spatially Dependent Phase

The phase of the measured electric field as a function of position on the xy-plane is shown in Figure 6.6 for (a) an uncovered Sievenpiper array and (b) a Sievenpiper array with a dielectric overlayer. The two systems are shown schematically in Figure 6.6 (a) and (b). The xy-plane of measurement is maintained at $z = 3$ mm in height above the metamaterial surface for both Figures 6.6 (a) and (b). The posistion of $z = 0$ mm has been noted previously on Figure 6.7 for clarity. The dielectric overlayer placed upon the Sievenpiper array in Figure 6.6 (b) is with perspex with $\epsilon = 2.6$ and has a thickness $w = 2.95$ mm. Both plots are obtained

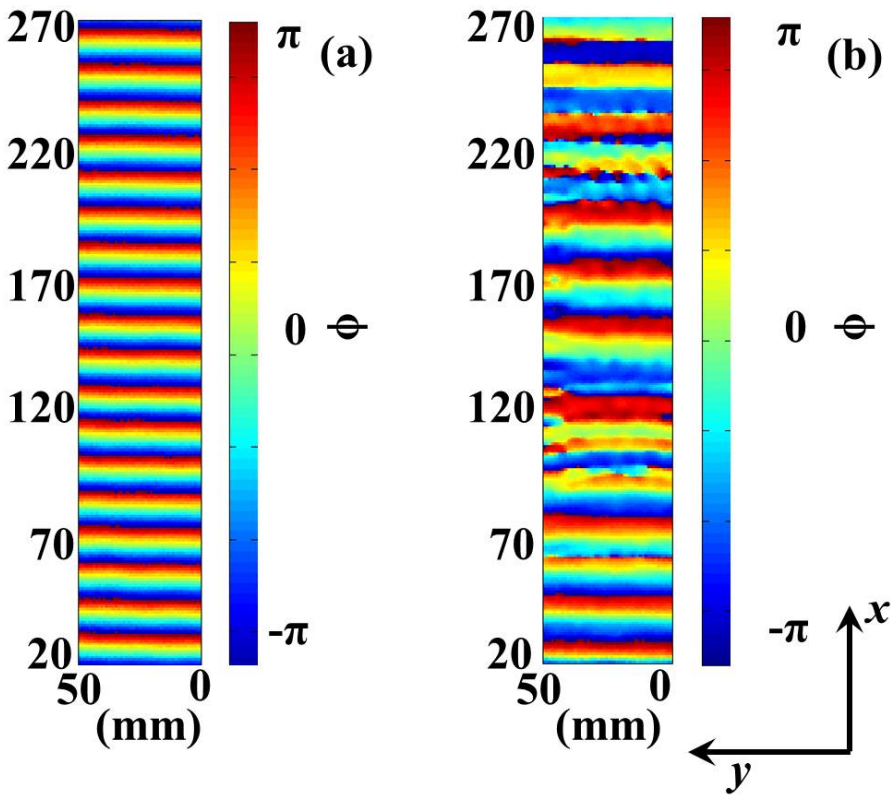

Figure 6.8: Experimentally determined local phase of the electric field (Φ) detected at 20 GHz over (a) the uncovered Sievenpiper array and (b) a Sievenpiper array with a dielectric overlayer of permittivity $\epsilon = 2.6$ and thickness $t = 2.95$ mm. The detecting antenna is at a constant height of $z = 3$ mm above the surface so that the overlayer can be placed underneath the antenna without modifying the position of the probe. The surface wave launcher is used to uniformly excite the mode. The launcher is placed at $x = 0$ mm and is not included in this figure.

at a frequency of 20 GHz and the starting point of the scanning antenna for both measurements is at position (x,y,z) of (20 mm, 0 mm, 3 mm). Notice that the lines of constant phase in Figure 6.6 are approximately parallel to the y-axis, indicating that the launcher is exciting surface waves uniformly.

As a surface propagates across a surface, the phase of the supported mode will vary spatially and oscillate between $\pm\pi$. The frequency of this oscillation is indicative of wavelength of the surface wave. This has been shown previously in Chapter 3, Figure 3.10. Comparison of Figure 6.6 (a) and (b) reveals that the phase of the supported modes measured as a function of distance differ significantly in wavelength for the covered and uncovered Sievenpiper array.

Figure 6.5 displays the experimentally measured dispersion for both systems. 20 GHz has been marked on this graph and can be seen to lie in the suppression band for a Sievenpiper mushroom with an overlayer. Therefore, a surface wave is not expected to be supported. The electromagnetic mode detected in Figure 6.6

is in fact a free space wave.

Inspection of Figure 6.6 (b) reveals the period of the wave is approximately 15 mm which is equal to $\lambda_{20\ \mathrm{GHz}}$ in free space. Notably, the wave being measured simply corresponds to that of a grazing photon, and not that of a surface wave. The wavelength of the field in Figure 6.6 (a) is observed to be much less than that of a grazing photon (b) as without a dielectric overlayer this surface still supports a TM_0 surface wave at 20 GHz. This is crucial to the investigations of channelling detailed further in this chapter.

6.5.3.1 Measuring Dispersion

Measurements of the dispersion of a surface wave supported by a Sievenpiper mushroom array with and without a dielectric overlayer is achieved with the setup schematically represented in Figure 6.6. In addition to measuring the dispersion of the surface wave on the covered and and uncovered systems (Figure 6.6 (a) and (b)), the same technique is used to measure the dispersion of surfaces waves laterally confined between overlayers (Figure 6.6 (c) and (d)). Two perspex overlayers of dimension (x,y,z) = (250 mm, 150 mm, 2.95 mm) are placed on top of the array such that the width, L, between the overlayers can be varied. The detecting antenna maintains a constant height of 0.25 mm $\pm$ 0.2 mm above the uncovered Sievenpiper array and is located centrally in the channel between the overlayers. It remains equidistant to the two overlayers as it is scanned in the x-direction away from the lens source, directly above the intersection between two neighbouring elements of the Sievenpiper array. The tip of the antenna extends beyond the surface of the dielectric overlayers with a starting position of (20 mm, 25 mm, 0.25 mm) and final position of (270 mm, 25 mm, 0.25 mm)

The technique used to measure the dispersion of the surface wave within the uncovered channel was developed by Mr J. Dockrey [82] and evolved from the initial dispersion measurement technique as described in Section 3.3.2. The phase of the surface wave is measured at a single frequency as a function of distance along the supporting surface and is unwrapped as a function of position. k_x is determined by analysing the gradient of the unwrapped phase. This is repeated for each frequency. Phase unwrapping has been discussed previously in Section 3.3.3 so will not be further detailed.

6.6 Results and Analysis

Experimentally obtained dispersion of a TM_0 mode supported in a channel between two dielectric overlayers are presented in Figure 6.9 (blue circles). The width of

the channel L is varied between 3.2 mm and 25.6 mm in step sizes of 3.2 mm, twice the pitch (d) of a Sievenpiper mushroom unit cell.

Figure 6.9 compares measurements of a mode supported in an uncovered channel between overlayers to the experimentally and numerically determined dispersions of a surface wave supported by a Sievenpiper array completely covered and completely uncovered by a dielectric overlayer. The differences in these setups has been shown schematically in Figure 6.6 and has been presented previously in Figure 6.5. Experimental data has been overlaid as purple and black crosses detailing the dispersion of the surface wave supported by the completely covered and completely uncovered Sievenpiper array (respectively) and the numerical data is represented by grey and red lines for the same two systems (respectively). At 20 GHz the TM_0 mode is expected to be supported by a completely uncovered Sievenpiper surface but not supported by a Sievenpiper surface covered with a dielectric overlayer, as is depicted in the previous measurement displayed in Figure .

As previously shown in Figure 6.4, the electric field of the TM_0 mode extends out of the surface in large loops in the xz-plane. The magnetic field remains contained within the plane of the surface, parallel with the xy-plane and in the dielectric layer of the Sievenpiper mushroom structure. The confinement of the surface mode between two dielectric overlayers onto the surface of the array does not change the boundary condition experienced by the magnetic field contained in the dielectric layer, and the mode remains purely TM in character. If the edges of the dielectric overlayers are aligned with the intersection between elements of the array as well as invariant in thickness, there is no change of boundary condition experienced by the electric field in the x-direction. In practice there will be a small margin of experimental error concerning both the smoothness of the edges of the layers and their placement on the array but this will be limited to the size of the gap in between elements ($\pm\ (d - a)$).

6.6.1 Frequency Dependent Dispersion Characteristics

One might naively expect the dispersion of the mode supported in the channel to strongly resemble the dispersion of an uncovered Sievenpiper mushroom array until, at some critical width L, the presence of the bordering overlayers perturbs the supported surface wave. By observation of Figure 6.9 one can see this is not the case. The dispersion of the mode measured at a single channel width strongly resembles both the dispersion of the mode associated with the uncovered Sievenpiper mushroom array and the dispersion of the mode associated with the covered Sievenpiper mushroom structure, for two different frequency ranges.

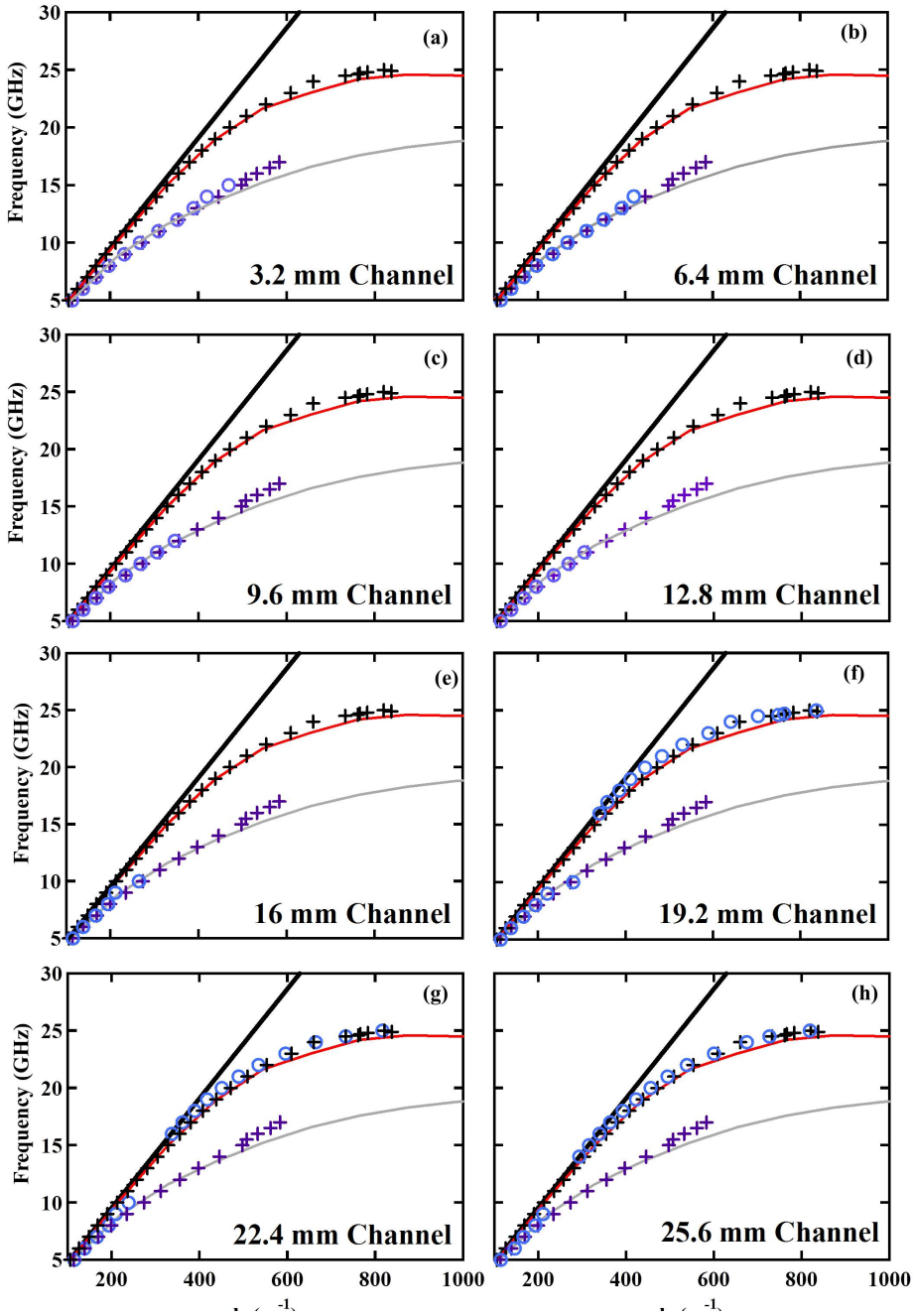

Figure 6.9: Dispersion plots of a TM_0 mode supported on a Sievenpiper mushroom array in an uncovered channel between two dielectric overlayers at separation distance L (blue circles). Separation distance L is modified so that modes supported in channels of widths 3.2 mm, 6.4 mm, 9.6 mm, 12.8 mm, 16 mm, 19.2 mm, 22.4 mm and 25.6 mm are measured. The dispersions of a mode supported on a completely covered (black crosses) and uncovered Sievenpiper array (purple crosses) are compared to the dispersion associated with the channelled mode. Numerically determined dispersions for the completely covered and uncovered cases are plotted as solid red and grey lines (respectively). The solid black line represents a grazing photon.

At small channel widths the dispersion measured strongly resembles that of the dispersion of the TM_0 mode supported by a Sievenpiper array covered by a dielectric overlayer. This is strong resemblance is consistent up to and including the dispersion measured at 15 GHz, beyond which there are no longer any modes measured. As the channel width is increased, this maximum frequency at which a TM_0 mode is supported reduces until the channel width $L = 19.2$ mm at which point something quite unexpected is observed. To highlight this Figure 6.10 replicates the dispersion shown in Figure 6.9 (f) in greater detail.

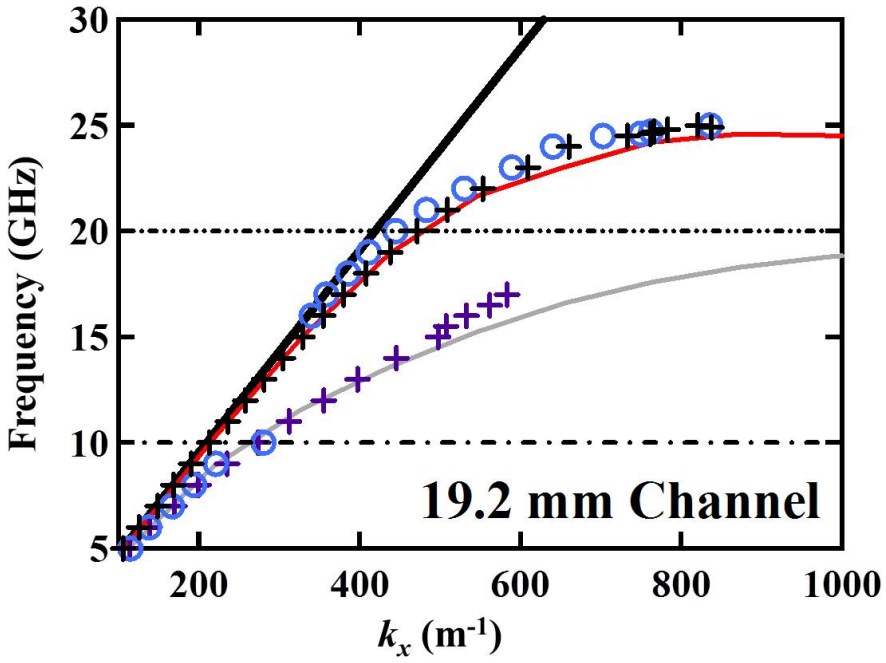

Figure 6.10: Measured dispersion of a TM_0 mode supported on a Sievenpiper mushroom array in a channel between two dielectric overlayers (blue circles). The separation distance L between the two overlayers is 19.2 mm. The overlayers are invariant in thickness ($w = 2.95$ mm and place such that the edge of the layer is parallel to the intersection between two lines of neighbouring elements in the x-direction. Also shown is the numerically calculated dispersion of the TM_0 mode supported by a Sievenpiper array with (grey) and without (red) a dielectric overlayer of the aforementioned thickness. Experimentally determined dispersions for the same two systems are represented by purple and black crosses (respectively).

Inspect Figure 6.10. Over the frequency range of 5 to 10 GHz, the mode supported in the uncovered channel of width 19.2 mm has a dispersion which strongly resembles the dispersion of a mode supported by a Sievenpiper array completely covered by a dielectric overlayer. The solid grey line and purple crosses denoted the numerically calculated and measured dispersion for the covered system, respectively. A schematic of the completely covered array and the array with an uncovered channel region is shown in Figure 6.6 (b) and (c).

As the frequency becomes greater than 10 GHz, the dispersion of the mode supported by the channel is not measured again until 17 GHz. At this frequency the dispersion in the uncovered channel strongly resembles the dispersion of a mode supported by a completely uncovered Sievenpiper mushroom array. The solid red line and black crosses denoted the numerically calculated and measured dispersion for the covered system, respectively. A schematic of the completely uncovered array and the array with an uncovered channel region is shown in Figure 6.6 (a) and (c). The comparative similarity of the measured dispersion continues as the frequency increases, ceasing when the mode is no longer measured on approach to the resonant condition of the surface wave. Numerical modelling is achieved via the FEM technique and has previously been discussed in conjunction with Figure 6.5.

The measurement of the dispersion of the mode supported in the channel is clearly frequency dependent. Inspection of Figure 6.10 reveals that at lower frequencies it compares well with the mode supported by the Sievenpiper mushroom surface covered with an overlayer while at higher frequencies it resembles a mode supported by an uncovered metasurface. The dispersion of the TM modes supported in channels with $L > 19.2$ mm continues to exhibit similar character however this chapter will now continue to focus on the measurements of the surface waves supported in a channel of width $L = 19.2$ mm.

6.6.2 Comparison of Numerical and Experimental Measurements of Electric Field Amplitude and Phase

Figures 6.11 and 6.12 show numerically obtained phase (a) and time-averaged electric field (b) compared with experimentally obtained local phase (c) and time-averaged electric field (d) associated with the modes supported in an uncovered channel region of a Sievenpiper mushroom array, surrounded by regions of the Sievenpiper array which are covered by dielectric overlayers. This setup has previously been shown schematically in Figure 6.6 (c).

For both Figures 6.11 and 6.12, width of channel $L = 19.2$ mm, thickness dielectric overlayers $t = 2.95$ mm with a permittivity $\epsilon = 2.6$. Both the time-averaged electric field and phase associated with the supported surface wave are measured in the xy-plane, 3 mm above the top of the Seivenpiper mushroom structure. This is similar to the previous measurement detailed for Figure 6.6.

In the numerical case, a plane is defined in the FEM model at $z = 3$ mm so that time-averaged electric field and phase can be numerically calculated. In the experimental case, the tip of the probe used to sample the field of the surface wave is at $z = 3$ mm. In both Figures 6.11 and 6.12 the position of the white

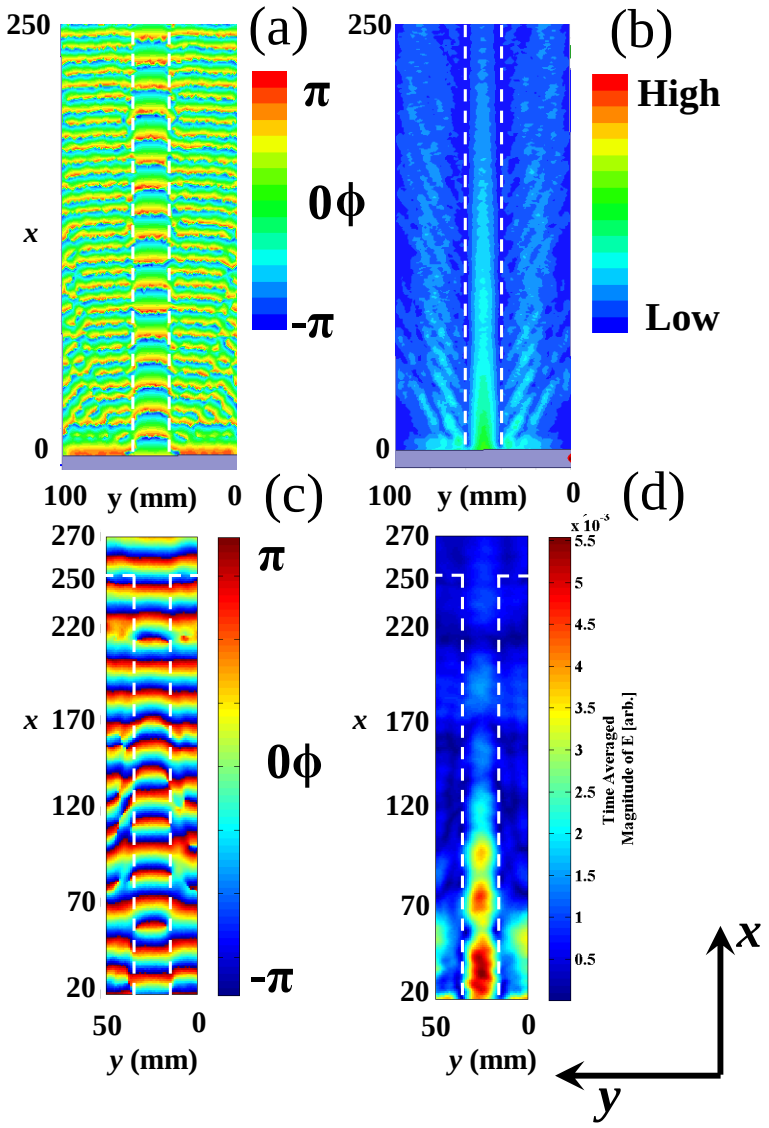

Figure 6.11: Numerical and experimental data of the local time-average electric field and phase of a surface wave supported in an uncovered channel of a Sievenpiper mushroom array, measured at 20 GHz. The channel is surrounded by the Sievenpiper mushroom array covered by two dielectric overlayers of length 250 mm and thickness $t = 2.95$ mm The uncovered channel between the two overlayers $L =$ 19.2 mm. (a) and (b) are numerically calculated phase and time-averaged electric field of the mode supported by the system. (c) and (d) display the experimentally measured local phase and time-averaged electric field. The measurement is taken in the xy-plane at a distance z = 3 mm above the Sievenpiper mushroom array The location of the channel beneath the measurement plane is shown schematically by the dashed white lines. The grey box at the bottom of (a) and (b) indicate the position of the excitation source in the numerical FEM models. The surface wave in (c) and (d) is terminated by geometrically graded absorber.

dashed line is indicative of the dielectric overlayers present beneath the xy-plane of measurement.

The data presented in Figure 6.11 is measured when frequency is equal to 20

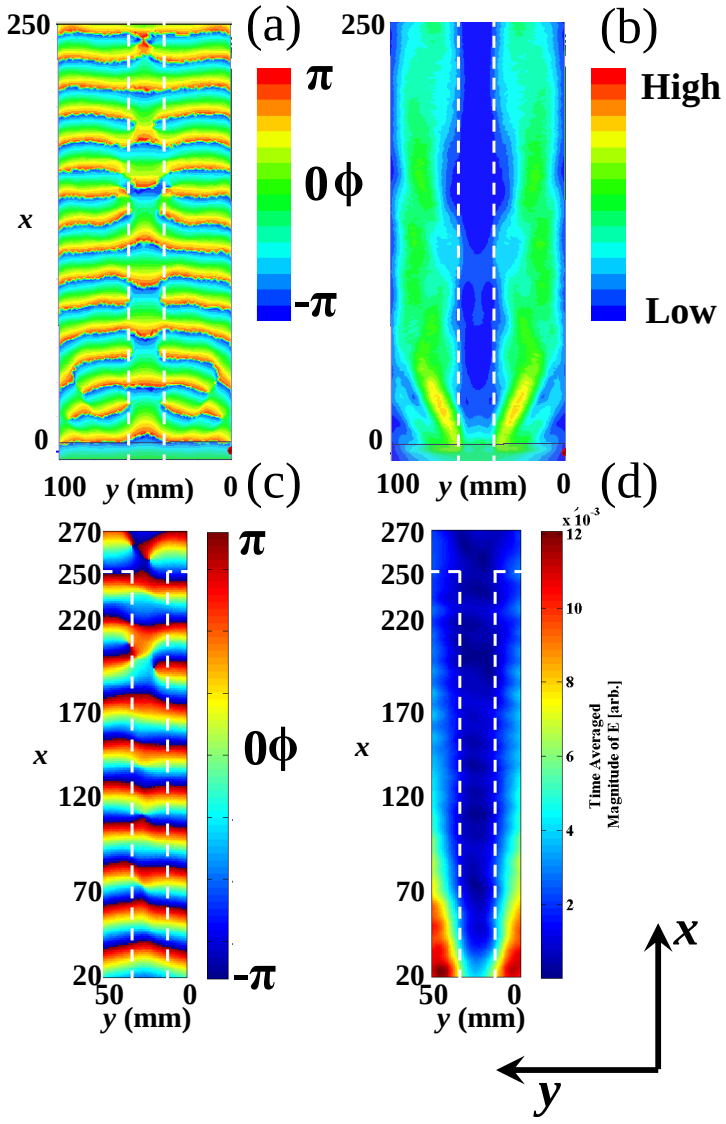

Figure 6.12: Numerical and experimental data of the local time-average electric field and phase of a surface wave supported in an uncovered channel of a Sievenpiper mushroom array, measured at 10 GHz. The channel is surrounded by the Sievenpiper mushroom array covered by two dielectric overlayers of length 250 mm and thickness $t = 2.95$ mm The uncovered channel between the two overlayers $L = 19.2$ mm. (a) and (b) are numerically calculated phase and time-averaged electric field of the mode supported by the system. (c) and (d) display the experimentally measured local phase and time-averaged electric field. The measurement is taken in the xy-plane at a distance z = 3 mm above the Sievenpiper mushroom array The location of the channel beneath the measurement plane is shown schematically by the dashed white lines. The grey box at the bottom of (a) and (b) indicate the position of the excitation source in the numerical FEM models. The surface wave in (c) and (d) is terminated by geometrically graded absorber.

GHz. The data presented in Figure 6.12 is measured when frequency is equal to 10 GHz.

Figures 6.11 (a) and (b) are achieved via FEM modelling by assigning a single

sheet with an effective impedance, as previously outlined in Chapter 3. Two dielectric overlayers of thickness $w = 2.95$ mm and length 250 mm are then added with an uncovered region between the overlayers of width $L = 19.2$ mm. Exact duplication of the experiment in the model is impractical due to computational constraint. For example over the spatial distance of 250 mm, as modelled in Figure 6.11, there are over 156 Sievenpiper unit cells. The length scales of the model are such that modelling such individual elements is simply not practical. However, the effective impedance model produces similar dispersive behaviour as presented in Figure 6.10.

The value of the surface impedance Z_s is obtained via the effective impedance model for a TM mode previously stated in Equation 6.7, using the value of k_x experimentally determined in Figure for 6.10 for an uncovered Sievenpiper array. This method has been previously detailed in Section 3.4.3.4.

The entire geometry of Figure 6.11 (a) and (b) is surrounded by absorbing ('radiation') boundaries in the xz-planes. These are used as termination boundaries in the yz-planes. The length of the numerical model in the x direction is 250 mm, up to and including the whole length of the uncovered channel region. The microwave surface wave launcher is modelled by assigning a waveport excitation inside a waveguide so that the fundamental mode of the system has a vertically polarised electric field vector only. Waveport excitations have been previously discussed in Chapter 3 therefore will not be further elaborated upon. The position of the launcher in the models is $(x, y, z) = (0, 0, 3\text{mm})$ and can be observed as the grey box at the bottom of Figures 6.11, (a) and (b).

Figures 6.11 (c) and (d) show measurement of the time-averaged electric field and phase of a surface wave supported in an uncovered channel region of a Sievenpiper mushroom array. As previously stated, the channel has a width $L = 19.2$ mm and is surrounded by planar dielectric overlayers of thickness $t = 2.95$ mm and $\epsilon = 2.6$. The measurement technique using a probe and a VNA to sample the surface wave fields has previously been detailed in Section 6.5.2.1, and shown in Figure 6.6, so will not be reiterated here. The fields are sampled by the probe over an area of 250 mm x 50 mm.

The measured time-averaged electric field and phase plots do not show the position of the microwave lens and begin at coordinate (20 mm, 0 mm, 3 mm). The dielectric layers cease to cover the metasurface when $x = 250$ mm. Consequently, Figure 6.11 (c) and (d) measure the supported mode over the region directly above the dielectric overlayers and 20 mm after they terminate.

By inspection of Figure 6.11, it is clear that the surface wave supported by the uncovered channel is confined to the channel at 20 GHz. The phase of the surface wave shown in Figure 6.11 (a) and (c) is indicative of this as the distance between

the oscillation in phase between $\pm\pi$ is shorter within the channel in comparison to this distance between the same oscillation for the mode measured above the dielectric overlayer. The time-average electric field measured in (b) is also noticeably greater in the uncovered channel in comparison to the surrounding overlayer regions. This is less noticeably in Figure 6.11 (d). This could be due to (b) being a model which uses a sheet impedance to mimic a surface which supports a surface wave and is not subject to loss in the structure. Conversely, the experimental measurement in (d) is subject to loss due to the dielectric layer between the patches and the ground plane of the Sievenpiper mushroom array structure.

Figure 6.12 is a measure of the same experiment detailed for Figure 6.12, measured at 10 GHz. The time-averaged electric field of the mode of the mode is most highly concentrated in the dielectric overlayer region of the system, in contrast to Figure 6.11.

6.7 Discussion

By inspection of Figures 6.11 and 6.12 a difference in the concentration of energy of the supported mode is observed. At lower frequencies (10 GHz) the mode is confined to the dielectric, at higher frequencies (20 GHz) there is a concentration of energy in the non-dielectric region.

One would expect the dispersion of the channel mode to be similar to that of either the metasurface covered by a dielectric overlayer *or* the dispersion of the uncovered metasurface. However the mode is observed to propagate in both, for two different frequency ranges. This is possible due to phase matching of the electric field observed at the interfaces of the covered and uncovered regions. The location of these interfaces is illustrated by the white dashed lines in Figures 6.11 and 6.12.

Thus far the reason for the dispersive character of the mode supported by the uncovered channel at a lower frequency regime are not yet known. The data presented in Figure 6.13 (reproduced from Figure 6.10 with only experimentally determined data for clarity) shows the mode ceases to propagate at frequencies higher than that of 10 GHz. If indeed two modes are supported simultaneously then one would expect the mode associated with the covered metamaterial surface to be detected up to 17 GHz, similar to the dispersion of the surface wave supported on the metamaterial surface in the completely covered case. This region is indicated by the purple shaded region. However, both modes are not measured within the indicate region. This could be due to coupling constraints or decay of the mode in the perspex layer and is not investigated further.

The dispersion of the mode supported by an uncovered channel of a Seiven-

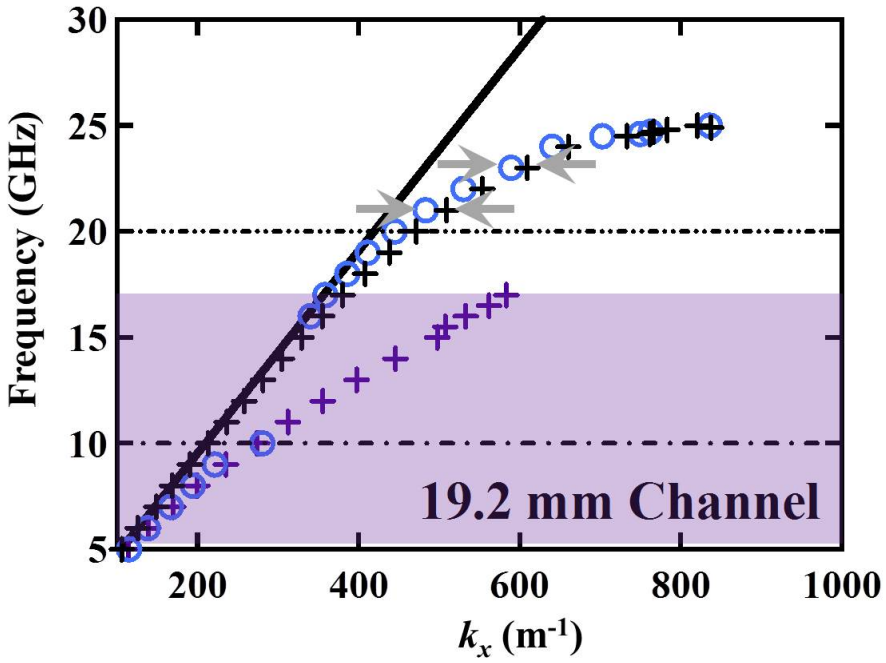

Figure 6.13: The experimental dispersion of a TM_0 mode supported on a Sievenpiper mushroom array in a channel $L = 19.2$ mm between two dielectric overlayers (blue circles). The separation distance L between the two overlayers is 19.2 mm. Overlaid is the experimentally determined dispersion of the TM_0 mode supported by a Sievenpiper array that is complete covered (purple crosses) or completely uncovered (black crosses) by a dielectric overlayer. The semi-transparent purple region highlights the frequency region where both a completely covered and completely uncovered Sievenpiper array will support a TM mode. The grey arrows highlight the contribution of k_y to the mode supported in the channel.

piper mushroom array of width $L = 19.2$ mm closely resembles that of the mode supported by the completely uncovered Sievenpiper array above 16 GHz. However, inspection of the measured dispersion of these two systems reveals that the whole profile of the dispersion of the channel mode has been shifted in the negative k_x direction, as highlighted by the arrows in Figure 6.13. This author suggests the shift is due to the mode propagating in the uncovered channel being subject to quantisation associated with a lateral boundary condition imposed on it by the proximity of the dielectric overlayer.

Consider the lines of constant phase shown in Figure 6.11 (a) and (c). The phase of the mode supported over the regions covered by dielectric compared to the phase of the mode supported in the uncovered regions show that different wavelengths are supported at different spatial positions on each region. Therefore, lines of constant phase and amplitude occur at different positions and are dependent on the region measured. At the boundary between the covered and uncovered regions the electric field values must be matched. By forcing the amplitude to zero at the

boundary between the two regions this matching becomes possible.

Inspection of the experimental data at 20 GHz in Figure 6.11 is indicative if this conclusion. The time-averaged electric field in (d) drops to zero at the boundary between the covered and uncovered Sievenpiper array, noted by the white dashed line in Figure 6.11. The phase within the uncovered channel in (c) changes from a linear profile to a bent one in order to meet this boundary condition.

Figure 6.12 displays the local time-averaged electric field and phase of the supported mode within the uncovered channel at 10 GHz. Figure 6.12 (c) and (d) are not greatly effected by this boundary condition as the mode propagates only in the dielectric region.

Numerically determined data of the phase over a covered and uncovered high impedance sheet is presented in (a) and (b) in Figures 6.11 and 6.12. This shows the lines of constant phase in the channel bending to match an isocontour of similar value in close proximity at the boundary between the covered and uncovered region. The postition of the boundary is once again illustrated by the dashed white line.

Therefore, the fields associated with the phase are matching across the boundary. The time-averaged electric field in Figure 6.11 (b) falls to zero at the boundary. The impedance sheet shows the boundary between the covered and uncovered regions forcing time-average electric field to zero as well as the subsequent bending of the phase in the channel associated with the supported modes to zero more clearly than the experiment. A suggestion as to why this might be the case is that the model is not subject to the influence of any free space propagating wave which may be a source of interference.

The boundary condition outlined previously forces a quantisation of the mode in the y-direction. The wavevector (k_0) of an electromagnetic mode is described as

$$k_0^2 = k_x^2 + k_y^2 + k_z^2 \tag{6.9}$$

where k_x is the wavevector of the mode in the x-direction and k_y and k_z represent the wavevectors of the mode in the y and z direction respectively. For a TM surface wave propagating in the x-direction on a Sievenpiper array, $k_x > k_0$ and the contributions from k_y and k_z to k_0 are considered to be zero. However, as the mode under consideration is subject to a field matching boundary condition, there is some contribution to the overall mode in k_y. This effect is observed by the bending of the phase fronts in the channel. As k_y increases k_x must decrease. This results in k_x being shifted to a lower value as highlighted by the grey arrows in Figure 6.13.

The uncertainties associated with the present study are worthy of note. They include surface wave scattering to higher order modes and measurement of a multi-

modal system due to the cessation of the dielectric overlayers before the end of the sample was reached as well as possible coupling constraints of associated with the excitation source. The cessation of the dielectric layers before the end of the sample was an experimental oversight. From inspection of Figure 6.11 it is clear that the time-averaged field associated with the supported mode is not negligible at $x = 250$ mm, therefore there may be reflections measured in this experiment due to this boundary condition.

The coupling efficiency of the launcher when used to excite a surface wave on the Sievenpiper mushroom array was not investigated. This is due primarily to the fact that a uniform excitation over distances greater than that of 100 mm was required for investigations detailed in Chapter 6, therefore coupling constraints were not analysed. Further, there was never any experimental issues encountered as regards to the strength of the mode excited on the Sievenpiper mushroom array surface so an investigation was not warranted at that time.

Further, as the surface wave is supported on a Sievenpiper array or confined with a single layer of dielectric to that surface it is dissimilar to a photonic crystal device. A photonic crystal is composed of multiple periodic layers of different refractive index which is relied upon to guide a mode and as such is a closed system. The mode guided by the photonic crystal is also inherently lossy. It is the structure of the Seivenpiper array which results in the support of a surface wave, not a change of refractive index. As such, it is not considered to be comparable to a photonic crystal waveguide. Further, although a surface wave supported on the Sievenpiper array is subject to loss from the dielectric layer, it is not comparable to the amount of loss a mode propagating through a photonic crystal is subject to as the surface wave penetrates into free space which is considered as lossless. This constraint also results in greater confinement of the surface wave mode to the interface in comparison to the mode supported in the photonic crystal device [26].

Investigations on the subject of guiding surface waves can be read in the publication of Gregoire et al. (2011) [147] and most recently Quarfoth et al. (2013) [148] numerically predicting the presence of a surface wave guided along a high impedance region surrounded by free space impedance. To be exact, the work in these publications focus on surface waves guided in regions where the imaginary component of the surface impedance is greater than that of 377 Ω and is surrounded by a region of surface impedance equal to 377 Ω.

The investigation detailed in this chapter is somewhat more complex as the surface impedance varies depending on which mode is supported in the channel. For example, a mode supported on a Sievenpiper array with an uncovered channel of width $L = 19.2$ mm has a magnitude of surface impedance of less than 377 Ω while the surface impedance of the surrounding covered region is 377 Ω for frequen-

cies associated with the suppression band of the covered region. At frequencies of less than the suppression band it is possible to support both modes. However, the relative strength of one mode in comparison to other may make detection more difficult. While eigenmode modelling of such a channel system has yet to be completed both in this investigation and in the wider literature as read by this author, these experimental results show a promising step towards understanding of a complex system.

Another application to result from of the study of a Sievenpiper mushroom array includes beam steering of microwave patch antenna arrays via the control of surface wave scattering off the array [138].

6.8 Conclusions

This chapter investigates surface wave channelling between two dielectric overlayers placed on a Sievenpiper mushroom array. The overlayers cover the metamaterial surface which supports a surface wave. The lower edge of the suppression band enforced on surface waves supported on the Sievenpiper surface is lowered due to the presence of the overlayer. A region between the two overlayers is left uncovered, and the lower edge of the suppression band is increased in frequency in this uncovered region. Therefore there is a frequency regime in which surface waves will only be supported on the uncovered channel region and not in the region associated with the overlayers. Below this frequency regime surface waves will be supported in both regions.

Experimental and numerical observations of the dispersion of the mode supported with and without the overlayer are compared. Experimental measurements of the dispersion of the mode supported in the channel are conducted for a range of channel widths including 3.2 mm, 6.4 mm, 9.6 mm, 12.8 mm, 16 mm, 19.2 mm, 22.4 mm and 25.6 mm. The smallest width for which a surface wave is supported in the uncovered channel is experimentally determined to be 19.6 mm. Subsequent investigation of the propagation of electric fields through materials of different permittivity is discussed as well as the concept of electric field matching across a boundary between two regions which support surface waves of different values of k_x.

Chapter 7

Conclusions and Future Work

7.1 Introduction

7.2 Summary of Thesis

Presented is compelling experimental evidence that the domino waveguide supports a surface wave whose dispersion (including its asymptotic limit) is surprisingly insensitive to the lateral width of the structure. It is shown that the surface wave supported by such a domino array structure is confined to that structure both laterally and vertically. The dispersions of DPs for a range of lateral widths from 100 mm to 1.60 mm are experimentally determined, the latter being subwavelength compared to the excitation wavelength. Even for such narrow dominos, good agreement is found between the experimentally measured dispersion and the analytical relation expected for cavity widths of infinite extent. The reason for this insensitivity lies in the absence of a lateral quantization condition for the mode when the waveguide is comprised of open-ended cavities. This is compared and contrasted to experiments conducted on domino waveguide structures with close-ended cavities to affirm the understanding of the mechanism responsible.

The spatial dependence of the group velocity associated with a microwave surface wave supported across a metasurface with a graded geometry is studied. The metasurface consists of an array of closed-sided rectangular cavities obtruding from a ground plane whose lateral widths are increased as a function of distance from the point of excitation. The variation in cavity width results in a spatially dependent modal index. Subsequently, frequency components of the surface wave are slowed and trapped at different positions along the tapered metasurface. The trapping position and the behaviour of the supported mode approaching this location have been experimentally observed with both local field amplitude and phase data. Four notable aspects of this data have been discussed. Primarily, the phase of the

electric-field data provides a more accurate identification of the trapping location compared to amplitude measurements alone. Secondly, the exact stopping location of the surface wave does not correspond with numerical predictions obtained for a fixed-width one-dimensional array of cavities. Thirdly, the oscillations observed in the local amplitude of the surface wave provide insight as to the magnitude of reflection experienced by the surface mode close to this point. The origin of the reflection mechanism is considered. Finally, higher order lateral quantisations of the surface mode have been experimentally observed excited by scatter of the fundamental mode from the trapping point.

Surface wave channelling between two dielectric overlayers is investigated. The overlayers cover a metasurface which supports a surface wave and enforces a surface wave suppression band on the modes supported. A region between the two overlayers is left uncovered, thereby making a channel through which surface modes are supported at the same frequency as the uncovered isotropic metasurface. The surface wave supports a modified mode on the regions covered with a dielectric overlayer. Therefore the modified mode is subjected to a suppression band which is at a lower frequency in comparison to the suppression band associated with the mode supported by an uncovered metasurface. Experimental and numerical observations of the dispersion of the mode suppported with and without the overlayer are compared. Experimental measurements of the dispersion of the mode supported in the channel are conducted for a range of channel widths including 3.2 mm, 6.4 mm, 9.6 mm, 12.8 mm, 16 mm, 19.2 mm, 22.4 mm and 25.6 mm. The smallest width for which a surface wave is supported in the uncovered channel is experimentally determined to be 19.6 mm. Subsequent investigation of the propagation of electric fields through materials of different permittivity is discussed as well as the concept of field matching across a boundary between two regions which support surface waves of different values of k_x.

This thesis concludes that a microwave surface wave can be laterally confined if there is no boundary condition present to quantise the mode. The phase of the surface wave is found to be more indicative of the behaviour of the mode in comparison to measurements of electric field amplitude as the modal index and direction of propagation are more obvious.

7.3 Recent Publications Relating to this Work

The subject of this thesis, laterally confined microwave surface waves, is an active area of research. As such, during the course of this PhD there were several publications that which were closely linked to the work presented here. The first is a paper by Ma et al. (2011) [149] wherein power splitting of a surface wave

mode is investigated. The structure used to support the surface wave mode in the study conducted by Ma et al. has been investigated in Chapter 4 and consists of a periodic array of metallic cuboids protruding from a flat metallic ground plane. The investigation in Chapter 4 outlines the insensitivity of the supported surface wave mode to lateral confinement and is discussed forthwith. Ma et al. (2011) used the structure to demonstrate power transfer over an array of metallic cuboids which are arranged so that the supported mode propagated along 90 degree bends in the supporting array and so investigated beam steering.

This was extended to investigate directional couplers and waveguide ring resonators, the later of which was estimated by Ma et al. to be 60 % efficient. This was attributed to radiative loss in the system and manufacturing flaws in positioning of the metallic cuboids on the metallic ground plane. The amount of radiative loss due to rate of change of direction to achieve a 90 degree bend in the supporting waveguide was not investigated or optimised.

Surface wave guiding was recently taken to the extreme by Shen et al. (2013) [150] when a mode was shown to be supported on an ultrathin flexible dielectric film patterned with an ultrathin layer of metal. The metal printed onto the film is an thin array of grooves so that the whole pattern resembles that of a two dimensional comb. The film can be folded and wrapped around objects over multiple 360 degree turns while still supporting a surface wave mode. Such a mode was shown numerically and experimentally to maintain a time-averaged power density at the output side of the film of 95% in comparison to the input after one such 360 degree turn of direction, all at a frequency of 10 GHz. The surface wave mode investigated by Shen et al. has a different modal shape in comparison to the study presented in Chapter 4 due to a lack of ground plane. However lateral insensitivity of the supported surface wave has been verified and successfully utilised for beam steering with little loss and so is included in this literal study of laterally confined surface waves.

Other publications concerning a surface wave supported on an array of cuboids protruding from a metallic ground plane include the by Wu et al. (2013) [151] where open waveguide geometry is discussed and Shen et al. (2013) [150] where the grooves between each cuboid are bent to a 90 degree angle. However, the work presented by Shen et al. (2013) [150] clearly shows the strongest evidence of subwavelength confinement of a surface wave mode via good comparison of both experimental and theoretical data as the dimensions of the supporting waveguide in comparison to the operating wavelength is the most extreme.

7.4 Future Work

The publications previously detailed occurred throughout the investigations detailed in this work. Future work proposed on the topic of laterally confined microwave surface waves is now detailed with respect to these publications and suggestions as to the advancement and the potential impact of each chapter is outlined.

7.4.1 Surface Wave Data Transfer

Of all the work presented, the subject of Chapter 4 has the highest potential impact with regards to the design of wireless communication devices. Turner et al. (2012) [152] have recently designed a device for surface wave data transfer. The device operates at 60 GHz and is composed of a one-dimensional array of corrugations. In contrast to the structure studied in Chapter 4, the array is fabricated on a flexible material. A surface wave is supported on the corrugations. Coupling to and from the near field of the surface wave allows data to be transferred. As the material is flexible and the device is low loss, such devices could be worn on the body. One example of the potential advancement this device could offer is possible improvement of health monitoring. A patient's vital statistics could be stored as information on the body of the patient and transferred to a monitoring device in close proximity to the corrugated surface.

Notably, the smallest lateral width of surface wave device tested in Turner et al. [152] is 90 mm. Further, a publication used in reference to the work of Turner by Hendry el a. (2010) [153] suggests that the corrugated device should not be fabricated so that its lateral width is less than the depth of the corrugations or the surface will not support a mode. Chapter 4 details a surface wave supported on a one-dimensional array of corrugations of width $L = 1.6$ mm while the depth of corrugation, height $h = 3.75$ mm. A surface mode is supported even though L ¡ h, directly contradicting the statement made by Hendry el a. (2010) [153]. Subsequent work previously detailed by [150] supports the investigation detailed in Chapter 4, the supported mode is insensitive to the lateral width of the supporting structure. As a result it may be possible for the device designed by Turner et al. [152] to be much less than 90 mm in width.

7.4.2 Beam Sharpening

The subject of Chapter 5 presents another potential application; beam sharpening of a radar pulse. Notably, the structure investigated in this Chapter results in a spatially dependent modal index. A dispersive device can be used to interact with

a pulse transmitted by the radar. However, the dispersion of that device will be tuned to a single frequency. If the radar was transmitting pulses at two different frequencies, as is often the case for the purposes of velocity unfolding [129], more than one dispersive device would be required for beam sharpening. The structure outlined in Chapter 5 is not limited by this constraint and could be applied to sharpen the beam of a Doppler radar which transmits pulses at different frequencies. As of yet no references have been found regarding this application, other than details of utilising surface acoustic wave (SAW) devices for beam sharpening [129]. Therefore an investigation as to the feasibility of this application is suggested as an extension to the work presented in Chapter 5.

7.4.3 Further Investigation of Surface Wave Channelling

The work detailed in Chapter 6 can be expanded. Initially suggested is an investigation as to the sensitivity of the mode supported in the uncovered channel region of the Sievenpiper mushroom structure to the edges of the bordering dielectric layers.

Figure 7.1 is a schematic of the experimental setup used to investigate channelling of the surface wave between dielectric overlayers. Suggested initially is the modification of the sides of the dielectric overlayer from a square sided layer of uniform thickness $w = 2.95$ mm to a layer that is not uniformally thick at the edges. Suggested is an investigation as to the gradual tapering of thickness w from 0 mm to 2.95 mm as a function of distance from the edge of the layer. The measured dispersion of the mode supported in the uncovered channel could be compared and contrasted for different rates of dielectric tapering.

The confinement of the TM surface wave supported by the Sievenpiper mushroom array covered by the overlayer is modified as a function of thickness of the dielectric overlayer. As such, if the edge of a bordering dielectric overlayer as is depicted in Figure 7.1 is tapered, the boundary condition at the edge of the layer will result in a gradual change in the limiting frequency of the mode supported in this covered region. This is in contrast to the sudden change in limiting frequency of the mode that occurs when the taper sides remains square, as is presented in Chapter 6. It is suggested that tapering the edge of the bordering dielectric overlayer will modify the dispersion of the mode supported in the uncovered channel so that more closely resembles a mode supported by an uncovered Sievenpiper array and will not exhibit the shift in k_x previously depicted in Figure 6.13.

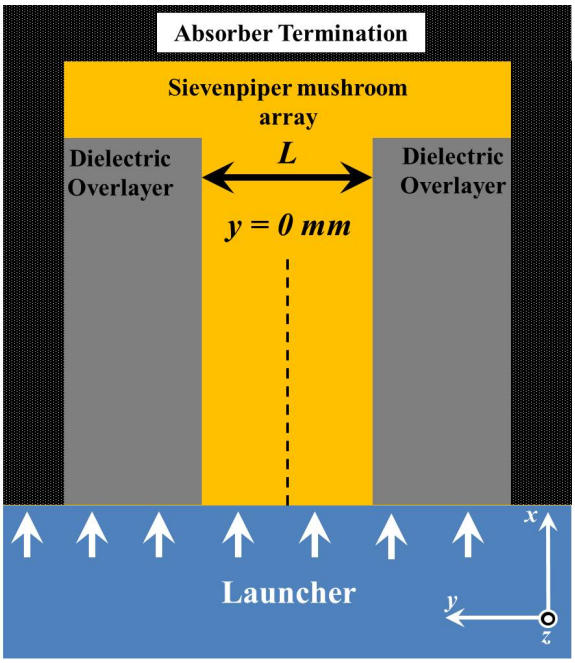

Figure 7.1: A Sievenpiper mushroom array (orange) with two dielectric overlayers (grey) covering the array. The region between the overlayers remains uncovered, resulting in a channel. The width L between the two dielectric layers (grey) on top of the Sievenpiper mushroom array (orange) is shown. The direction of propagation of radiation from the excitation source, the surface wave launcher (blue), is noted by the white arrows. Geometrically graded microwave absorber lines the edges of the Sievenpiper mushroom array, with and without dielectric overlayers to minimise reflections from the edge of the array. All dielectric overlayers used are described by $\epsilon = 2.6$ and have a thickness of $w = 2.95$ mm. They are a material known as perspex.

7.4.4 Quantifying the Reflections of a Surface Wave by Measurement of Local Phase

Suggested is the characterisation of the magnitude of reflection experienced by a surface wave when terminated by a metal or absorber via measurement of the local phase associated with a surface wave.

Figure 7.2 schematically shows the experimental setup of a surface wave experiment where the position of the terminating boundary is modified. The surface wave is supported on an array of open-sided metallic corrugations of width $L = 5$ mm, a domino array and is excited via edge-coupling. Constants A_1, A_2 and A_3 represent the forward (blue), reflected(red) and total (green) surface wave amplitudes, respectively. The solid black line illustrates the initial position of the terminating boundary. The position of the probe mid-width of the array is noted by the red circle.

Initial data of the local phase associated with the surface wave supported on the domino array as a function of distance from the source is shown in Figure 7.3.

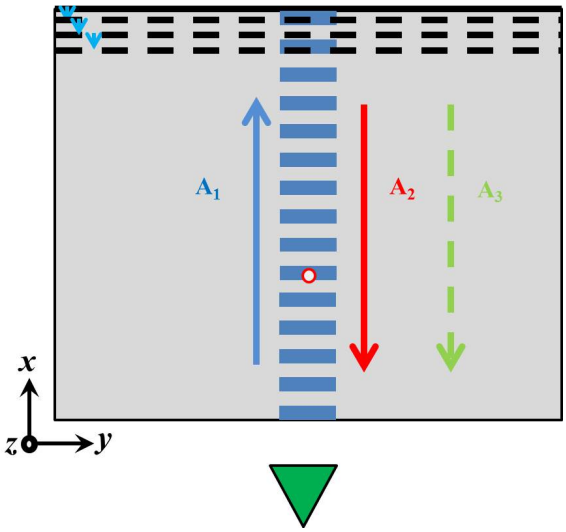

Figure 7.2: Schematic of experimental setup used to excite a surface wave on an $L = 5$ mm domino array protruding from a metallic sheet. The blue boxes are illustrative of the position of the array and not the dimensions of the structure. Constants A_1, A_2 and A_3 represent the forward (blue), reflected(red) and total (green) surface wave amplitudes, respectively. The solid black line illustrates the initial position of the terminating boundary. The dashed black lines and white arrows denote the shifted position of the terminating boundary. The position is always modified in the x-direction at a step size of $\frac{\lambda}{4}$. For a frequency of 15 GHz, $\frac{\lambda}{4}$ = 5 mm. The probe used to measure the electric field associated with the surface wave is noted by the red circle and the surface wave is excited via edge-coupling. The broadband horn used for excitation is noted by the green triangle.

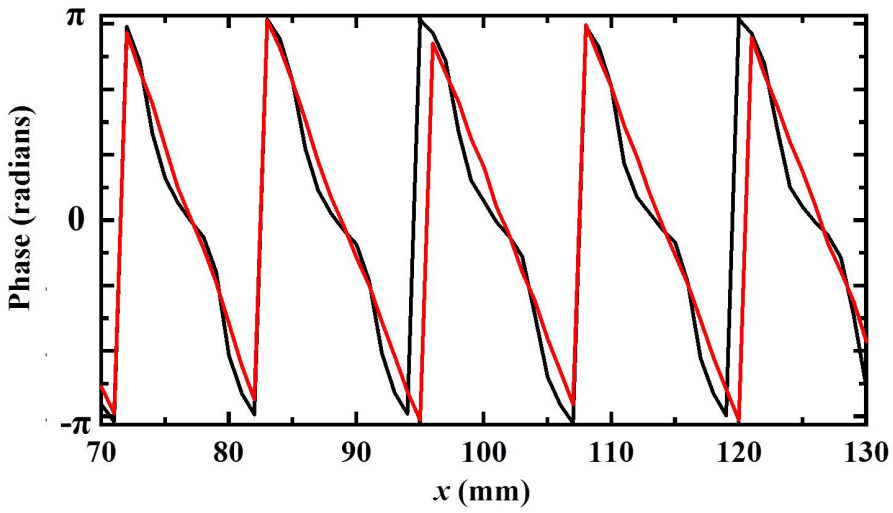

Figure 7.3: Phase as a function of distance of the electric field associated with a 1D array of corrugations of width $L = 5$ mm, as studied in Chapter 4. The supported surface wave is terminate by a metal (black) and an absorber (red) and the data is representative of the mode at 15 GHz.

In this case, the surface wave was terminated with geometrically graded absorber

(red) or a metallic boundary (black) at the position noted by the solid black line. Of interest to this author is the characterisation of the phase of surface wave measured as a function of distance when the supported mode is terminated by a metal or by an absorber. The phase is measure at 15 GHz.

Notice that when the surface wave is terminated by an absorber boundary the profile of the phase as a function of distance between the limits of $\pm\ \pi$ is linear. Conversely, the profile of the phase as a function of distance of a surface wave terminated by a metal boundary results in two sharp turning points in the profile measured between $\pm\ \pi$.

The sharp turning points observed on Figure 7.2 and are clearly indicative of the surface wave's reflection from a metallic boundary and is indicative of the contributions of A_1 and A_2 (the forward and reflected amplitude of the surface wave) to and A_3, the total amplitude of the surface wave. Section 3.3.4 has already noted the surface wave measured as an multi-modal system. The measurement of the strength of reflection and therefore the contributions of A_1 and A_2 to the overall amplitude of the mode A_3 is proposed as a further investigation of this work.

The loss mechanisms of a surface wave supported by a domino array include absorption into the supporting media or ohmic heating, absorption at termination and scattering into free space at the termination of the surface wave. It is suggested that the proposed analysis of the profile of the local phase of the surface wave would result in a measure of the losses due to the boundary terminating the surface wave absorbing the supported mode and a measurement of the energy lost to scattering at a terminating boundary. Only after these two loss mechanisms have been assessed can a calculation as to loss of energy of the surface wave due ohmic heating be made.

This investigation was further continued by once again measuring the phase of the surface wave reflected from a metal boundary. However, in this instance the metal boundary was placed $\lambda/4$ increments closer to the source and the phase was remeasured. Figure 7.2 depicts the starting position of the metallic boundary as represented first by the solid black line. The the increments of $\lambda/4$ are indicated by the dashed black lines and blue arrows in the upper right hand corner of Figure 7.2. The surface wave is measured at 15 GHz. As a result, the metallic boundary in this investigation is moved at increments of 5 mm in the x-direction.

The results of this initial investigation show a clear period of the sharp turning points in the phase measured as a function of distance. This is due to the reflecting boundary being moved incrementally by a factor of $\lambda/4$ for every measurement. Suggested is the use of the observed characteristic to measure the phase on reflection from a boundary, as well as the phase change of reflection of the surface wave as dictated by that boundary.

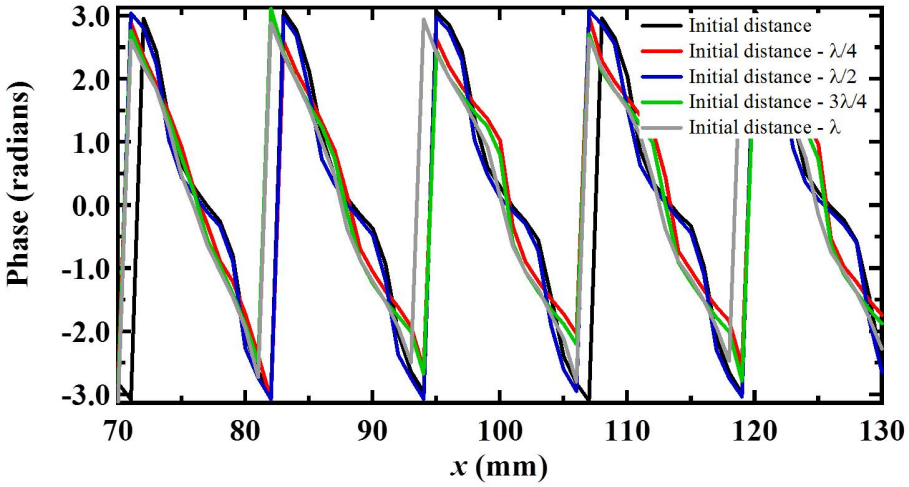

Figure 7.4: Phase as a function of distance of the electric field associated with a 1D array of corrugations of width $L = 5$ mm, as studied in Chapter 4. The supported surface wave is terminate by a metal boundary and moved in $\lambda/4$ increments closer to the emitting antenna. Measurement of the surface wave was achieved at 15 GHz, therefore $\lambda/4 = 5$ mm. The surface wave is measured for five different propagation lengths (in the x-direction), with the metallic boundary moved closer to the source of excitation by $\lambda/4$ for each measurement. Notice the profile of the locally measured phase of the surface wave is repeated when the metallic boundary is incremented a distance of $\lambda/2$.

7.4.5 Impedance Matching Compared to Field Overlap

When a propagating mode is travelling from one impedance region to another and those regions are matched, one might expect the mode not to be reflected. However, the electric field of the mode between the two regions must also overlap or reflection will occur. For example, Chapter 4 showed that the dispersion of surface waves supported on an array of 1D corrugations were similar for a mode propagating on an $L = 100$ mm array compared to an $L = 1.6$ mm.

Figure 7.5 shows the experimental measurement of the surface wave supported by a domino array of width $L = 1.6$ mm and width $L = 100$ mm. The dispersions are very similar, implying that the impedance of the mode as a function of frequency would also be similar. This is true for all domino widths and is shown in Chapter 4.

The similarity in dispersion between the surface wave supported on one domino array is comparison to another of different width would suggest that the mode could propagate between one array to another without reflection. However, the mode overlap between one surface wave supporting structure and another would also have to match or the result would be a reflection of the supported mode.

Figure 7.6 (a) displays the measured time-averaged electric field (left) and

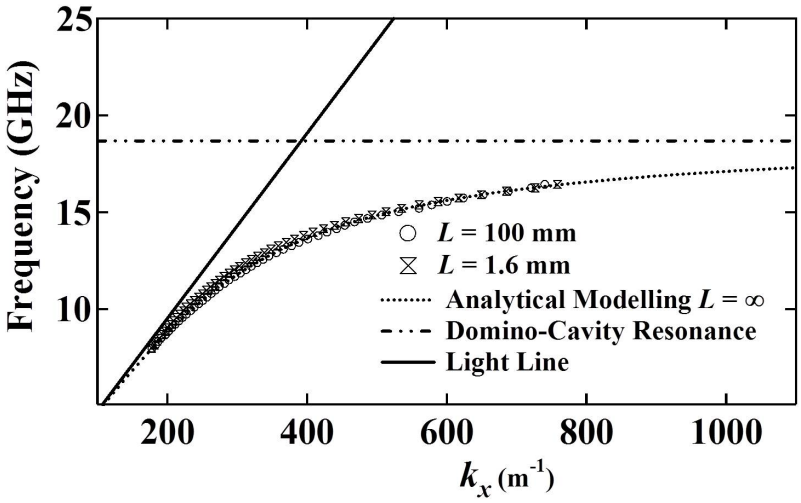

Figure 7.5: Measured dispersion of a surface wave supported on a domino array of width $L = 1.6$ mm and $L = 100$ mm. Reproduced from Chapter 4.

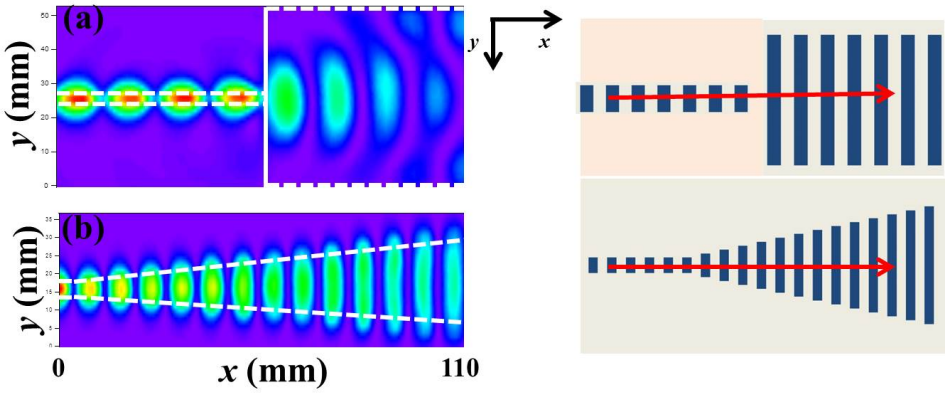

Figure 7.6: (a) Measured time-averaged electric field (left) and schematic of supporting structure (right) for two domino arrays aligned centrally. The two widths are $L = 5$ mm and $L = 100$ mm. Propagation of the surface wave from one array to the other is illustrated by the red arrow. (b) Measured time-averaged electric field (left) and schematic of supporting structure (right) for a domino array that is tapered in width as a function of distance from the start of taper. The width at the start of the taper $L = 1.6$ mm and the propagation direction is once again noted in (b). Both measurements are for a surface wave supported at 13 GHz.

schematic of supporting structure (right) for two domino arrays aligned centrally. The two widths are $L = 5$ mm and $L = 100$ mm. Propagation of the surface wave from one array to the other is illustrated by the red arrow. (b) Measured time-averaged electric field (left) and schematic of supporting structure (right) for a domino array that is tapered in width as a function of distance from the start of taper. The width at the start of the taper $L = 1.6$ mm and the propagation direction is once again noted in (b). Both measurements are for a surface wave supported at 13 GHz.

Preliminary data is shown in Figure 7.6 (a) indicates that the mode overlap of the surface wave between the domino of width $L = 5$ mm and $L = 100$ mm is small, hence the non-uniform distribution of the time-averaged electric field over the $L = 100$ mm. However, field distribution of the surface wave supported by the tapered structure shown in Figure 7.6 (b) is mush more uniform. Proposed is an investigation into the rate of change of taper of a tapered open-sided domino array to so that the surface wave is not reflected via a change in modal overlap.

Thus concludes the future work proposed as an extension to the investigations of laterally confined microwave surface waves.

7.5 Presentations and Publications

Elizabeth M. G. Brock, Alastair P. Hibbins
Experimental investigation of laterally confined microwave surface waves
Poster Presentation at the Royal Society conference, Theo Murphy International Scientific Meeting on Metallic Metamaterials and Plasmonics, Chicheley Hall, United Kingdom, 2^{nd} June 2010.

Ansoft's HFSS user conference, Basingstoke, United Kingdom, October 2010

Elizabeth M. G. Brock, Celia A. M.Butler, and Helen J. Rance
Experimental Microwave Photonics
Poster Presentation at Functional Materials conference, University of Exeter, United Kingdom, 1^{st} December 2010.

Elizabeth M. G. Brock, Euan Hendry, Alastair P. Hibbins
Laterally confined microwave surface waves
Poster presentation at ONYX conference, The University of Bristol, Clifton, 8_{th} July 2011.

Elizabeth M. G. Brock, Euan Hendry, Alastair P. Hibbins
Laterally confined microwave surface waves
Poster presentation at Nanometa, Seefeld, Austria, 2^{nd} January 2011.

Elizabeth M. G. Brock, Euan Hendry, Alastair P. Hibbins
Subwavelength lateral confinement of microwave surface waves
Applied Physics Letters, (2011), **99** (5), 051108

Elizabeth M. G. Brock, Euan Hendry, Alastair P. Hibbins
On the lateral confinement of surface waves in the microwave regime
Oral Presentation at CIMTEC conference, Montecantini Terme, Italy, 9^{nd} June 2012

Elizabeth M. G. Brock, Alastair P. Hibbins
Microwave surface waves supported by a tapered geometry metasurface
Applied Physics Letters, (2013), **103** (11), 111904

References

[1] S. Tretyakov, *Analytical modelling in Applied Electromagnetics*. Norwood, MA: Inc, Artech House, 2003. 3

[2] U. Fano, "The Theory of Anomalous Diffraction Gratings and of Quasi-Stationary Waves on Metallic Surfaces (Sommerfelds Waves)," *Journal of the Optical Society of America*, vol. 31, p. 213, Mar. 1941. 3, 6

[3] Julius Adams Stratton, *Electromagnetic Theory*. McGraw-Hill, New York, 1941. 4

[4] F. Zucker, "Theory and applications of surface waves," *Il Nuovo Cimento (1943-1954)*, vol. IX, no. 1902, 1952. 4, 5

[5] G. John, "Electromagnetic surface waveguides a review," *I.E.E.-I.E.R.E.*, no. V, 1977. 4

[6] J. Zenneck, "Zenneck - 1907 - Uber die Fortpflanzung ebener elektromagnetischer Wellen langs einer ebenen Leiterflache und ihre Beziehung zur drahtlosen Telegraphie," *Ann. der Physik*, vol. 23, p. 846, 1907. 4, 10, 11, 13, 16, 82

[7] E. Cohn, *Das elektromagnetiche Feld. Vorlesungen uber die Maxwell'sche Theorie*. Leipzig, S. Hirzel, 1900. 4

[8] K. Uller, *Beitrage zur Theorie der elektromagnetischen Strahlung*. PhD thesis, Rostock, 1903. 4

[9] A. Sommerfeld, "Uber die Ausbreitung der Wellen in der drahtlosen Telegraphie," *Annalen Der Physik*, vol. 28, no. 4, pp. 665–736, 1909. 4

[10] H. Weyl, "Ausbreitung elektromagnetischer Wellen uber einem ebenen Leiter," *Annalen Der Physik*, vol. 60, pp. 481–500, 1919. 4, 9

[11] K. Norton, "Propagation of radiowaves over a plane earth," *Nature*, p. 954, 1935. 4, 9, 13

[12] C. Burrows, "Existence of a surface wave in radio propagation," *Nature*, 1936. 4, 9, 27

[13] K. F. Neissen, "Zue Entscheidung den Zwischen den beiden Sommerfeldschen Formelin fur Fortpflanzung von drahtlosen Wellen," *Annalen Physik Lpz*, vol. 29, no. 585, 1937. 5

[14] A. Sommerfeld, "Ueber die Fortpflanzung elektrodynamischer wellen langs eines Drahtes," *Annalen Der Physik*, vol. 303, no. 2, pp. 233–290, 1899. 5, 10, 13

[15] G. Goubau, "Surface Waves and Their Application to Transmission Lines," *Journal of Applied Physics*, vol. 21, no. 11, p. 1119, 1950. 5, 10, 13, 123

[16] G. Toraldo di Francia, "No Title," *Ottica*, vol. 7, no. 117, p. 197, 1942. 5, 10

[17] J. M. Guerra, "Super-resolution through illumination by diffraction-born evanescent waves," *Applied Physics Letters*, vol. 66, no. 26, p. 3555, 1995. 5

[18] C. Cutler, "Genesis of the corrugated electromagnetic surface," *Proceedings of IEEE Antennas and Propagation Society International Symposium and URSI National Radio Science Meeting*, vol. 3, pp. 1456–1459, 1944. 5, 9, 83, 123

[19] M. Schaffner and G. T. di Francia, "Microonde evanescenti generate per diffrazione," *Il Nuovo Cimento (1943-1954)*, vol. VI, no. 2, 1949. 5, 74

[20] R. Ulrich, "Submillimeter waveguiding on periodic metal structure," *Applied Physics Letters*, vol. 22, no. 5, p. 251, 1973. 5

[21] R. Wood, "XLII. On a remarkable case of uneven distribution of light in a diffraction grating spectrum," *The London, Edinburgh, and Dublin Philosophical . . .*, vol. 269, 1902. 6

[22] L. Rayleigh, "On the dynamical theory of gratings," *Proceedings of the Royal Society of London. Series A, Containing Papers of a Mathematical and Physical Character*, vol. 79, no. 532, pp. 399–416, 1907. 6

[23] J. Strong, "Effect of Evaporated Films on Energy Distribution in Grating Spectra," *Physical Review*, vol. 49, no. 1902, 1936. 6

[24] Y. Teng and E. Stern, "Plasma radiation from metal grating surfaces," *Physical Review Letters*, vol. 19, no. 9, 1967. 6

[25] W. Barnes, A. Dereux, and T. Ebbesen, "Surface plasmon subwavelength optics," *Nature*, vol. 424, no. August, pp. 824–830, 2003. 7, 100

[26] E. Ozbay, "Plasmonics: merging photonics and electronics at nanoscale dimensions.," *Science (New York, N.Y.)*, vol. 311, pp. 189–93, Jan. 2006. 7, 101, 150

[27] S. Kawata, *Near-Field Optics and Surface Plasmon Polaritons*. Berlin-Heidelberg-New York: Springer, 2001. 7, 101

[28] A. P. Hibbins, B. R. Evans, and J. R. Sambles, "Experimental verification of designer surface plasmons.," *Science (New York, N.Y.)*, vol. 308, pp. 670–2, Apr. 2005. 9, 16, 27, 74, 83, 102

[29] W. Wise, "The Physical Reality of Zenneck's Surface Wave," *Bell. Sys. Tech. J*, 1937. 9

[30] C. A. Balanis, *Antenna Theory*. New Jersey: John Wiley & Sons, third ed., 2005. 10, 36, 74, 75

[31] F. Zucker, "Surface-wave antennas," *Antenna engineering handbook*, pp. 1–32, 2007. 10, 11

[32] A. L. Cullen and H. M. Barlow, "Surface waves," *IEEE Transactions on Microwave Theory and Techniques*, vol. 10, no. 1482, pp. 329–341, 1953. 10, 11, 13, 16, 27, 31, 82, 83, 102, 123

[33] S. S. Attwood, "Surface-Wave Propagation Over a Coated Plane Conductor," *Journal of Applied Physics*, vol. 22, no. 4, p. 504, 1951. 11, 123

[34] W. Rotman, "A study of single-surface corrugated guides," *Proceedings of the IRE*, vol. 21, no. September 1948, 1951. 11, 84

[35] R. Elliott, "On the theory of corrugated plane surfaces," *Transactions of the IRE Professional Group on Antennas and Propagation*, vol. 2, pp. 71–81, Apr. 1954. 11

[36] J. C. Slater, "Theory of the Magnetron Oscillator," tech. rep., MIT Radiation Lab Report, 1941. 12

[37] H. Goldstein, *Cavity Resonators and waveguides Containing Periodic Elements*. PhD thesis, MIT, 1943. 12

[38] H. Goldstein, "The Theory of Corrugated Transmission Lines and Waveguides," tech. rep., MIT, 1944. 12

[39] W. Walkinshaw, "Theory of Corrugated Waveguide for linear Accelerator," tech. rep., British TRE Report T2037, 1946. 12

[40] W. Walkinshaw, "Theoretical design of linear accelerator for electrons," *Proceedings of the Physical Society*, no. March, 1948. 12

[41] D. Pozar, *Microwave engineering*. 4 ed., 2009. 12, 25, 42

[42] A. F. Kay, *The Scalar Feed*. Boston: Ft. Belvoir Defense Technical Information Center, 1964. 12

[43] A. D. Olver and P. Clarricoats, *Corrugated Horns for Microwave Antennas*. London, UK: Peter Periginus Ltd., 1984. 12

[44] A. Olver, P. Clarricoats, A. Kishk, and L. Shafai, *Microwave Horns and Feeds*. Piscataway, NJ, USA: IEEE Press, 1994. 12

[45] J. E. McKay, D. a. Robertson, P. a. S. Cruickshank, R. I. Hunter, D. R. Bolton, R. J. Wylde, and G. M. Smith, "Compact Wideband Corrugated Feedhorns With Ultra-Low Sidelobes for Very High Performance Antennas and Quasi-Optical Systems," *IEEE Transactions on Antennas and Propagation*, vol. 61, pp. 1714–1721, Apr. 2013. 13

[46] B. A. L. Cullen, D. Ph, B. Sc, and A. Member, "The excitation of plane surface waves," *IEEE Transactions on Microwave Theory and Techniques*, vol. 13, no. 93, 1954. 13, 34

[47] A. Harvey, "Periodic and guiding structures at microwave frequencies," *Microwave Theory and Techniques, IRE ...*, pp. 30–61, 1960. 13

[48] J. Wait, "Excitation of surface waves on conducting, stratified, dielectric-clad, and corrugated surfaces," *Journal of Research of the National Bureau of Standards*, vol. 59, p. 365, Dec. 1957. 13

[49] F. Zucker, "Theory and applications of surface waves," *Il Nuovo Cimento (1943-1954)*, vol. IX, no. 1902, 1952. 13, 123

[50] J. B. Pendry, L. Martín-Moreno, and F. J. Garcia-Vidal, "Mimicking surface plasmons with structured surfaces.," *Science (New York, N.Y.)*, vol. 305, no. 5685, pp. 847–8, 2004. 13, 15, 28, 30, 72, 84, 92, 102

[51] F. J. Garcia-Vidal, L. Martín-Moreno, and J. B. Pendry, "Surfaces with holes in them: new plasmonic metamaterials," *Journal of Optics A: Pure and Applied Optics*, vol. 7, pp. S97–S101, Feb. 2005. 13, 15, 28, 29, 30, 123

[52] V. G. Veselago, "The electrodynamics of surfaces with simultaneously negative values of permittivity and permeability," *Soviet Physics Uspekhi*, vol. 10, pp. 509–514, 1968. 14

[53] J. B. Pendry, "Negative Refraction Makes a Perfect Lens," *Physical Review Letters*, vol. 85, no. 18, pp. 3966–3969, 2000. 14

[54] D. R. Smith, W. J. Padilla, D. C. Vier, and S. Schultz, "Composite Medium with Simultaneously Negative Permeability and Permittivity," *Physical Review Letters*, vol. 84, pp. 4184–4187, 2000. 14

[55] R. a. Shelby, D. R. Smith, and S. Schultz, "Experimental verification of a negative index of refraction.," *Science (New York, N.Y.)*, vol. 292, pp. 77–9, Apr. 2001. 14

[56] J. B. Pendry, A. J. Holden, D. J. Robbins, and W. J. Stewart, "Magnetism from Conductors and Enhanced Nonlinear Phenomena," *IEEE Transactions on Microwave Theory and Techniques*, vol. 47, no. 11, pp. 2075–2084, 1999. 14

[57] C. M. Soukoulis and M. Wegener, "Past achievements and future challenges in the development of three-dimensional photonic metamaterials," *Nature Photonics*, pp. 1–8, July 2011. 14

[58] E. Shamonina and L. Solymar, "Metamaterials: How the subject started," *Metamaterials*, vol. 1, pp. 12–18, Mar. 2007. 14

[59] S. Maci and G. Minatti, "Metasurfing: Addressing waves on impenetrable metasurfaces," *Antennas and Wireless Propagation Letters*, vol. 10, pp. 1499–1502, 2011. 14, 102

[60] Ian Richard Hooper, *The Optical Response of Short-Pitch Surface- Relief Gratings*. PhD thesis, University of Exeter, 2002. 17, 20

[61] A. P. Hibbins, *Grating Coupling of Surface Plasmon Polaritons at microwave and visible frequencies*. PhD thesis, University of Exeter, 1999. 20

[62] F. Yang, J. Sambles, and G. Bradberry, "Long-range surface modes supported by thin films.," *Physical review. B, Condensed matter*, vol. 44, pp. 5855–5872, Sept. 1991. 21

[63] M. J. Lockyear, *Electromagnetic surface wave mediated absorption and transmission of radiation at microwave frequencies*. PhD thesis, University of Exeter, 2004. 21, 26

[64] C. Kittel, *Introduction to solid state physics*. John Wiley & Sons, 8th editio ed., 2005. 23, 24, 99

[65] A. W. Lines, G. R. Nicoll, and A. M. Woodward, "Some properties of waveguides with periodic structure," *IEEE*, no. 941, 1949. 27

[66] D. Martin-Cano, M. L. Nesterov, a. I. Fernandez-Dominguez, F. J. Garcia-Vidal, L. Martin-Moreno, and E. Moreno, "Domino plasmons for subwavelength terahertz circuitry.," *Optics Express*, vol. 18, pp. 754–64, Jan. 2010. 30, 82, 84

[67] H. J. Rance, I. R. Hooper, A. P. Hibbins, and J. Roy Sambles, "Structurally dictated anisotropic designer surface plasmons," *Applied Physics Letters*, vol. 99, no. 18, p. 181107, 2011. 30, 60, 102, 106

[68] D. Sievenpiper, R. Broas, N. Alexopolous, and E. Yablonovitch, "High-impedance electromagnetic surfaces with a forbidden frequency band," *IEEE Transactions on Microwave Theory and Techniques*, vol. 47, no. 11, pp. 2059–2074, 1999. 30, 31, 36, 67, 70, 75, 102, 122, 123, 124, 125, 126, 128, 129, 130

[69] R. E. Collin, *Field Theory of Guided Waves*. McGraw-Hill, New York, second ed., 1991. 32, 34, 36, 83, 102

[70] Daniel Frederic Sievenpiper, *High-Impedance Electromagnetic Surfaces*. PhD thesis, University of California, 1999. 36

[71] Anritsu, *The Essentials of Vector Network Analysis*. Anritsu Company, first ed., 2009. 41, 43, 126

[72] Agilent, "Agilent Network analyzer basics," tech. rep., Agilent Technologies, Inc. 2004, 2004. 41, 43, 45

[73] M. Hiebel, *Fundamentals of Vector Network Analysis*. Rohde & Schwarz, third ed., 2008. 41, 47, 49

[74] F. Microwave, "Flann Microwave: Microwave Products," tech. rep., Bodmin, United Kingdom, 2010. 44

[75] C. A. M. Butler, *The Microwave Response of Square Mesh Metamaterials*. PhD thesis, University of Exeter, 2012. 44

[76] M. Curtin and P. O. Brien, "Phase-Locked Loops for High-Frequency Receivers and Transmitters Part 1," *Analog Dialogue*, vol. 33-3, pp. 3–6, 1999. 47

[77] M. Curtin and P. O. Brien, "Phase-Locked Loops for High-Frequency Receivers and Transmitters Part 2," *Analog Dialogue*, vol. 33-5, pp. 1–5, 1999. 47

[78] M. Curtin and P. O. Brien, "Phase Locked Loops for High-Frequency Receivers and Transmitters Part 3," *Analog Dialogue*, vol. 33-7, pp. 1–5, 1999. 47

[79] J. Belrose, "Reginald Aubrey Fessenden and the birth of wireless telephony," *Antennas and Propagation Magazine, IEEE*, vol. 44, no. 2, 2002. 47

[80] Fredrik Nebeker, *Dawn of the Electronic Age: Electrical Technologies in the Shaping of the Modern World*. John Wiley & Sons, 2009. 48

[81] S. J. Berry, T. Campbell, a. P. Hibbins, and J. R. Sambles, "Surface wave resonances supported on a square array of square metallic pillars," *Applied Physics Letters*, vol. 100, no. 10, p. 101107, 2012. 60

[82] J. Dockrey, *Manipulation of Microwave Surface waves supported on Metamaterials*. PhD thesis, University of Exeter, 2015. 61, 139

[83] S. Berry, *Oblique Angle Scattering of Surface Waves from Surface Wave Absorbing Materials*. PhD thesis, University of Exeter, 2014. 64, 78, 79, 136

[84] M. Kopp, "An Introduction to HFSS : Fundamental Principles , Concepts and Use," tech. rep., Ansoft, 2009. 64

[85] O. Donadio, *G-band waveguide to microstrip transition for MMIC integration*. PhD thesis, University of Glasgow, 2012. 64

[86] J.-f. Lee, D.-k. Sun, and Z. J. Cendes, "Full-wave analysis of dielectric waveguides using tangential vector finite elements - Microwave Theory and Techniques, IEEE Transactions on," vol. 39, no. 8, pp. 1262–1271, 1991. 64

[87] Ansoft, "Ansoft HFSS - Technical Notes," tech. rep., Ansoft, 2001. 64

[88] D. F. G. Gallagher and T. P. Felici, "Eigenmode Expansion Methods for Photonics - Pros and Cons," *Photonics West*, pp. 1–14, 2003. 67

[89] E. Noponen and J. Turunen, "Eigenmode method for electromagnetic synthesis of diffractive elements with three-dimensional profiles," *Journal of the Optical Society of America A*, vol. 11, p. 2494, Sept. 1994. 67

[90] D. Martin-Cano, O. Quevedo-Teruel, E. Moreno, L. Martin-Moreno, and F. J. Garcia-Vidal, "Waveguided spoof surface plasmons with deep-subwavelength lateral confinement.," *Optics Letters*, vol. 36, pp. 4635–7, Dec. 2011. 67

[91] E. M. G. Brock, E. Hendry, and A. P. Hibbins, "Subwavelength lateral confinement of microwave surface waves," *Applied Physics Letters*, vol. 99, no. 5, p. 051108, 2011. 67, 72, 102

[92] M. Lockyear, A. Hibbins, and J. Sambles, "Microwave Surface-Plasmon-Like Modes on Thin Metamaterials," *Physical Review Letters*, vol. 102, p. 073901, Feb. 2009. 67, 74

[93] E. Hendry, a. Hibbins, and J. Sambles, "Importance of diffraction in determining the dispersion of designer surface plasmons," *Physical Review B*, vol. 78, p. 235426, Dec. 2008. 67, 71, 72, 73, 92, 106

[94] J. a. Dockrey, M. J. Lockyear, S. J. Berry, S. a. R. Horsley, J. R. Sambles, and a. P. Hibbins, "Thin metamaterial Luneburg lens for surface waves," *Physical Review B*, vol. 87, p. 125137, Mar. 2013. 67, 123

[95] E. M. G. Brock and A. P. Hibbins, "Microwave surface waves supported by a tapered geometry metasurface," *Applied Physics Letters*, vol. 103, no. 11, p. 111904, 2013. 67, 98

[96] A. P. Hibbins, M. J. Lockyear, and J. R. Sambles, "Otto coupling to a transverse-electric-polarized mode on a metamaterial surface," *Physical Review B*, vol. 84, p. 115130, Sept. 2011. 67

[97] L. Brillouin, "Wave guides for slow waves," *Journal of Applied Physics*, vol. 19, p. 1023, 1948. 69, 101

[98] Y.-c. Lan and R.-L. Chern, "Surface plasmon-like modes on structured perfectly conducting surfaces," *Optics Express*, vol. 14, no. 23, pp. 670–672, 2006. 72

[99] F. García de Abajo and J. Sáenz, "Electromagnetic Surface Modes in Structured Perfect-Conductor Surfaces," *Physical Review Letters*, vol. 95, p. 233901, Nov. 2005. 72

[100] J. D. Edmunds, E. Hendry, A. P. Hibbins, J. R. Sambles, and I. J. Youngs, "Multi-modal transmission of microwaves through hole arrays.," *Optics Express*, vol. 19, pp. 13793–805, July 2011. 72, 92, 115

[101] E. E. Hall, "E. E. Hall," *Physical Review*, vol. 15, no. 73, 1902. 74

[102] S. Zhu, A. Yu, D. Hawley, and R. Roy, "Frustrated total internal reflection: a demonstration and review," *American Journal of Physics*, vol. 54, no. 601, 1986. 74

[103] G. Borgiotti, *Fourier Transforms Method of Aperture Antennas*. 1963. 74

[104] D. Rhodes, "On the stored energy of planar apertures," *IEEE Transactions on Antennas and Propagation*, vol. 14, pp. 676–683, Nov. 1966. 74

[105] J. Saxler, J. Gómez Rivas, C. Janke, H. Pellemans, P. Bolívar, and H. Kurz, "Time-domain measurements of surface plasmon polaritons in the terahertz frequency range," *Physical Review B*, vol. 69, p. 155427, Apr. 2004. 78

[106] A. Sihvola and I. V. Lindell, "Bridging the Gap Between Plasmonics and Zenneck Waves," *IEEE Antennas and Propagation Magazine*, vol. 52, pp. 124–136, Feb. 2010. 83

[107] H. Raether, *Surface Plasmons*. Berlin: Springer, 1988. 83

[108] D. Sievenpiper, *Metamaterials: Physics and Engineering Explorations*. New Jersey: Wiley-Interscience, 2006. 83

[109] S. I. Bozhevolnyi, V. S. Volkov, E. Devaux, J.-Y. Laluet, and T. W. Ebbesen, "Channel plasmon subwavelength waveguide components including interferometers and ring resonators.," *Nature*, vol. 440, pp. 508–11, Mar. 2006. 83

[110] J. Dintinger and O. J. F. Martin, "Channel and wedge plasmon modes of metallic V-grooves with finite metal thickness.," *Optics Express*, vol. 17, pp. 2364–74, Feb. 2009. 83

[111] a. I. Fernández-Domínguez, E. Moreno, L. Martín-Moreno, and F. J. García-Vidal, "Terahertz wedge plasmon polaritons.," *Optics Letters*, vol. 34, pp. 2063–5, July 2009. 83

[112] R. L. Espinola, J. I. Dadap, and R. M. Osgood, "Raman amplification in ultrasmall silicon-on-insulator wire waveguides," vol. 12, no. 16, pp. 2489–2494, 2004. 99

[113] R. S. T. Jacob B. Khurgin, *Slow Light: Science and Applications*. Taylor and Francis Group, 2009. 99

[114] T. F. Krauss, "Slow light in photonic crystal waveguides," *Journal of Physics D: Applied Physics*, vol. 40, pp. 2666–2670, May 2007. 99

[115] L. V. Hau, S. E. Harris, Z. Dutton, and C. H. Behroozi, "Light speed reduction to 17 metres per second in an ultracold atomic gas," *Nature*, vol. 397, no. February, pp. 594–598, 1999. 99

[116] K. L. Tsakmakidis, A. D. Boardman, and O. Hess, "'Trapped rainbow' storage of light in metamaterials.," *Nature*, vol. 450, pp. 397–401, Nov. 2007. 99

[117] M. S. Jang and H. Atwater, "Plasmonic Rainbow Trapping Structures for Light Localization and Spectrum Splitting," *Physical Review Letters*, vol. 107, p. 207401, Nov. 2011. 99

[118] S. Savo, B. D. F. Casse, W. Lu, and S. Sridhar, "Observation of slow-light in a metamaterials waveguide at microwave frequencies," *Applied Physics Letters*, vol. 98, no. 17, p. 171907, 2011. 99

[119] W. T. Lu, Y. J. Huang, B. D. F. Casse, R. K. Banyal, and S. Sridhar, "Storing light in active optical waveguides with single-negative materials," *Applied Physics Letters*, vol. 96, no. 21, p. 211112, 2010. 99

[120] J. Park, K.-Y. Kim, I.-M. Lee, H. Na, S. Y. Lee, and B. Lee, "Trapping light in plasmonic waveguides," *Optics Express*, vol. 18, pp. 598–623, July 2010. 99

[121] M. Santagiustina and G. Eisenstein, "Slow Light Devices and Their Applications to Microwaves and Photonics," *IEEE Photonics*, vol. 26, no. February, pp. 6–13, 2012. 99

[122] H. Gersen, T. Karle, R. Engelen, W. Bogaerts, J. Korterik, N. van Hulst, T. Krauss, and L. Kuipers, "Real-Space Observation of Ultraslow Light in Photonic Crystal Waveguides," *Physical Review Letters*, vol. 94, p. 073903, Feb. 2005. 99

[123] S. Ha, M. Spasenović, A. a. Sukhorukov, T. P. White, C. M. de Sterke, L. K. Kuipers, T. F. Krauss, and Y. S. Kivshar, "Slow-light and evanescent modes at interfaces in photonic crystal waveguides: optimal extraction from experimental near-field measurements," *Journal of the Optical Society of America B*, vol. 28, p. 955, Mar. 2011. 99

[124] Y. a. Vlasov, M. O'Boyle, H. F. Hamann, and S. J. McNab, "Active control of slow light on a chip with photonic crystal waveguides.," *Nature*, vol. 438, pp. 65–9, Nov. 2005. 99

[125] M. Spasenović, T. P. White, S. Ha, A. a. Sukhorukov, T. Kampfrath, Y. S. Kivshar, C. M. de Sterke, T. F. Krauss, and L. K. Kuipers, "Experimental observation of evanescent modes at the interface to slow-light photonic crystal waveguides.," *Optics Letters*, vol. 36, pp. 1170–2, Apr. 2011. 99

[126] J. D. Joannopoulos, S. G. Johnson, J. N. Winn, and R. D. Meade, *Photonic Crystals: Molding the flow of light*. Princeton University Press, Princeton, NJ, second ed., 1995. 99, 100

[127] S. He, Y. He, and Y. Jin, "Revealing the truth about 'trapped rainbow' storage of light in metamaterials.," *Scientific Reports*, vol. 2, p. 583, Jan. 2012. 102, 108, 113

[128] J. Suckling, a. Hibbins, M. Lockyear, T. Preist, J. Sambles, and C. Lawrence, "Finite Conductance Governs the Resonance Transmission of Thin Metal Slits at Microwave Frequencies," *Physical Review Letters*, vol. 92, p. 147401, Apr. 2004. 102, 108

[129] M. L. Skolnik, *Introduction to Radar Systems*. Singapore: McGraw-Hill Book Co., 1981. 103, 120, 157

[130] "HFSS, Ansoft Corporation, Pittsburgh, PA, USA." 106

[131] M. Qiu, "Photonic band structures for surface waves on structured metal surfaces," *Optics Express*, vol. 13, no. 19, pp. 7583–7588, 2005. 106

[132] Z. Ruan and M. Qiu, "Slow electromagnetic wave guided in subwavelength region along one-dimensional periodically structured metal surface," *Applied Physics Letters*, vol. 90, no. 20, p. 201906, 2007. 106

[133] J. Zhu, Y. Chen, X. Zhu, F. J. Garcia-Vidal, X. Yin, W. Zhang, and X. Zhang, "Acoustic rainbow trapping," *Scientific Reports*, vol. 3, pp. 1–6, Apr. 2013. 107, 108

[134] Y. J. Zhou and T. J. Cui, "Multidirectional surface-wave splitters," *Applied Physics Letters*, vol. 98, no. 22, p. 221901, 2011. 108

[135] J. H. Richmond, "Reciprocitiy theorems and plane surface waves. Part I. Scattering by dielectric and metal objects. Part II. Surface waves on plane dielectric sheets and sandwiches. Part III. Excitation of surface waves on plane dielectric sheets," Columbus, Engineering Experiment Station, College of Engineering, Ohio State University, 1959, 1963. 123

[136] C. Walter, "Surface-wave Luneberg lens antennas," *Antennas and Propagation, IRE Transactions on*, no. 667, pp. 508–515, 1960. 123

[137] T. Zentgraf, Y. Liu, M. H. Mikkelsen, J. Valentine, and X. Zhang, "Plasmonic Luneburg and Eaton lenses.," *Nature Nanotechnology*, vol. 6, pp. 151–5, Mar. 2011. 123

[138] S. Podilchak, A. Freundorfer, and Y. Antar, "Surface-Wave Launchers for Beam Steering and Application to Planar Leaky-Wave Antennas," *IEEE*, vol. 57, no. 2, 2009. 124, 151

[139] B. A. Munk, *Frequency selective surfaces: Theory and Design*. New York: Wiley, 2 ed., 2000. 127

[140] S. Clavijo, R. E. Díaz, and W. E. Mckinzie, "Design Methodology for Sievenpiper High-Impedance Surfaces : An Artificial Magnetic Conductor for Positive Gain Electrically Small Antennas," *IEEE Antennas and Propagation Magazine*, vol. 51, no. 10, pp. 2678–2690, 2003. 130

[141] H. Rance, *Surface waves supported by Anisotropic surfaces at microwave frequencies*. PhD thesis, University of Exeter, 2013. 130

[142] A. Feresidis, G. Goussetis, S. W. S. Wang, and J. Vardaxoglou, "Artificial magnetic conductor surfaces and their application to low-profile high-gain planar antennas," *IEEE Transactions on Antennas and Propagation*, vol. 53, 2005. 130

[143] L. Li, Q. Chen, and Q. Yuan, "Surface-wave suppression band gap and plane-wave reflection phase band of mushroomlike photonic band gap structures," *Journal of Applied ...*, pp. 1–10, 2008. 130

[144] T. Nguyen, D. Kim, S. Kim, and J. Jang, "Design of a Wideband Mushroom-like Electromagnetic Bandgap Structure with Magneto-Dielectric Substrate," *resonance*, vol. 1, no. Icita, pp. 130–135, 2009. 130

[145] F. Yang and Y. Rahmat-samii, "Reflection Phase Characterizations of the EBG Ground Plane for Low Profile Wire," *IEEE Antennas and Propagation Magazine*, vol. 51, no. 10, pp. 2691–2703, 2003. 130

[146] O. Luukkonen, "Effects of spatial dispersion on reflection from mushroom-type artificial impedance surfaces," *Microwave Theory ...*, pp. 1–11, 2009. 130

[147] D. Gregoire and A. Kabakian, "Surface-wave waveguides," *Antennas and Wireless ...*, vol. 10, pp. 1512–1515, 2011. 150

[148] R. Quarfoth and D. Sievenpiper, "Artificial Tensor Impedance Surface Waveguides," *IEEE Antennas and Propagation Magazine*, vol. 61, no. 7, pp. 3597–3606, 2013. 150

[149] Y. G. Ma, L. Lan, S. M. Zhong, and C. K. Ong, "Experimental demonstration of subwavelength domino plasmon devices for compact high-frequency circuit.," *Optics Express*, vol. 19, pp. 21189–98, Oct. 2011. 154

[150] X. Shen and T. Cui, "Conformal surface plasmons propagating on ultrathin and flexible films," *Proceedings of the National Academy of Sciences of the United States of America*, vol. 110, no. 1, pp. 1–6, 2013. 155, 156

[151] J. J. Wu, "Open Waveguide Based on Low Frequency Spoof Surface Plasmon Polaritons," *Journal of Electromagnetic Analysis and Applications*, vol. 05, no. 02, pp. 58–62, 2013. 155

[152] J. E. Turner, M. S. Jessup, and K.-F. Tong, "A Novel Technique Enabling the Realisation of 60 GHz Body Area Networks," *2012 Ninth International Conference on Wearable and Implantable Body Sensor Networks*, pp. 58–62, May 2012. 156

[153] J. Hendry, "Isolation of the zenneck surface wave," *Antennas and Propagation Conference (LAPC), ...*, vol. 0, no. 10, pp. 2–5, 2010. 156